Programa de Doctorado en Ingeniería Matemática, Estadística e Investigación Operativa por la Universidad Complutense de Madrid y la Universidad Politécnica de Madrid





Delay-differential equations, Hopf bifurcations and the Ginzburg-Landau formalism in multi-scale stability analysis of vehicular traffic

DRAFT 22/07/25

Tesis Doctoral

JOSÉ ENRÍQUEZ GABEIRAS

Director:

JUAN FRANCISCO PADIAL MOLINA

Año 2025



UNIVERSIDAD POLITÉCNICA DE MADRID
Escuela Técnica Superior de Arquitectura

Doctoral Degree in Mathematical Engineering, Statistics and Operations Research

Delay-differential equations, Hopf bifurcations and the Ginzburg-Landau formalism in multi-scale stability analysis of vehicular traffic

DOCTORAL THESIS

Submitted for the degree of Doctor by:

José Enríquez Gabeiras
Ingeniero Superior de Telecomunicación

Under the supervision of:
Dr. Juan Francisco Padial Molina (Supervisor)

Madrid, 2025

Title: Delay-differential equations, Hopf bifurcations and the Ginzburg-Landau formalism in multi-scale stability analysis of vehicular traffic

Author: José Enríquez Gabeiras

Doctoral Programme: Mathematical Engineering, Statistics and Operations Research

Thesis Supervision:

Dr. Juan Francisco Padial Molina, Departamento de Matemática Aplicada, Escuela Técnica Superior de Arquitectura, Madrid.(Supervisor)

External Reviewers: <delete this text to leave this field blank>

Thesis Defense Committee: <delete this text to leave this field blank>

Thesis Defense Date: <delete this text to leave this field blank>

< If the thesis has received funding from any competitive call, please state it here by writing: "This thesis has been partially supported by...". Otherwise, delete this text to leave this section blank >

<Dedication (optional)>

Acknowledgement

<Optional >

Abstract

Since the early 20th century there has been increasing interest in the mathematics and physics community to study and characterize the vehicular traffic as a physical system obeying predictable laws. Road traffic has been modelled either as a multi-particle system or as a continuous flow, resembling the features of well known physical systems amenable to be analyzed with existing mathematical techniques. A number of mathematical models have been proposed to represent the dynamics of vehicular traffic, predominantly the car-following models, which have been applied both to the inter-vehicles dynamics (*microscopic* modelling) and to the aggregated traffic process (*macroscopic* modelling). Even though these models accurately represent phenomena observed in real roads, like congestion and wave propagation, they are sometimes based on narrow assumptions that do not match the behaviour of real drivers and vehicles. On the other hand, the relevance of these models is specially important now that new communication technologies like 5G and V2X (Vehicle-to-Everything) are intended to be a key part of the future road infrastructure and will require stringent latency requirements so that the driving decisions are taken in a timely manner.

The mathematical models to be applied have to factor in some way the influence of this response time in the system equations. This has been traditionally achieved by introducing the delay as a sensitivity factor in standard (i.e. non retarded) ODEs or PDEs. Nevertheless, this is not the adequate approach if one wants to investigate the nonlinear effects associated to reaction times, most importantly the Hopf bifurcation, which demands to apply the theory of Delay Differential Equations (DDEs). Moreover, in addition to the nonlinear effects introduced by the reaction times, the interaction between vehicles and the environment can be quite complicated, resulting in differential equations that are highly nonlinear. To adequately analyze these nonlinearities, another key mathematical tool has been the use of perturbation methods to calculate approximate solutions to the mobility equations. One of the main contributions of this work is the introduction of new approaches of application of DDEs and perturbation methods in order to obtain results not available before.

Finally, one important objective of this thesis is to provide a unified view of the traffic behaviour, starting from the individual vehicle up to the global traffic flow, linking the results of one finer scale with the results of a coarser one. To do this an intermediate scale, the *mesoscale*, is introduced such that it bridges the gap between the *micro* and *macro* scales. In this sense, of particular importance is the introduction of the Wirtinger calculus and the Complex Ginzburg-Landau formalism in the study of this mesoscale, for which there were not previous existing results.

In summary, this thesis contains new application methods of nonlinear analysis to study the instability that reaction times and communication delays introduce in the road traffic process. The research has been mostly focused on determining the limits of the reaction times inherent to the driver, vehicles and algorithms governing the driving decisions, and on quantifying the impact of these delays on the emergence of traffic oscillations and density waves at the different physical scales. It is worth noting that some of these methods can also be applied to other research fields, and some examples of this are provided in the text.

Resumen

Desde principios del siglo XX, la comunidad matemática y física ha mostrado un interés creciente en el estudio y la caracterización del tráfico vehicular como un sistema físico sujeto a leyes predecibles. El tráfico rodado ha sido modelado con frecuencia como un sistema de partículas o como un flujo continuo, con características similares a las de sistemas físicos bien conocidos, y por tanto susceptibles de ser analizados mediante técnicas matemáticas existentes. Distintos modelos se han propuesto para representar la dinámica del tráfico vehicular, entre los que destacan los modelos de seguimiento de vehículos, que se aplican tanto a la dinámica intervehicular (modelado microscópico) como al proceso de tráfico agregado (modelado macroscópico). A pesar de que estos modelos representan con precisión fenómenos observados en entornos de tráfico reales, como la congestión y la propagación de ondas de tráfico, con frecuencia las premisas en las que se basan no se ajustan al comportamiento real de los conductores y vehículos. Por otro lado, la relevancia de estos modelos es especialmente significativa ahora que nuevas tecnologías de comunicación, como el 5G y V2X (*Vehicle-to Everything*), están destinadas a ser un componente clave de la infraestructura vial del futuro y requerirán estrictos requisitos de latencia para que las decisiones de conducción se tomen a tiempo.

Los modelos matemáticos deben tener en cuenta de algún modo la influencia de este tiempo de respuesta en las ecuaciones del sistema. Esto se ha logrado tradicionalmente introduciendo el retardo como un factor de sensibilidad en EDOs o EDPs convencionales (no retardadas). No obstante, este enfoque no es el mejor si buscamos investigar los efectos no lineales asociados a los tiempos de reacción, en particular la bifurcación de Hopf, que requiere aplicar la teoría de Ecuaciones Diferenciales con Retardo (DDEs). Además, la interacción entre vehículos y el entorno puede llegar a ser bastante compleja, requiriendo modelos de ecuaciones diferenciales altamente no lineales. Para analizar adecuadamente estas no linealidades, otra herramienta matemática esencial son los métodos de perturbación para calcular soluciones aproximadas a las ecuaciones de movilidad. Una de las principales contribuciones de este trabajo es la introducción de nuevos enfoques de aplicación de las DDEs y métodos de perturbación para obtener resultados no disponibles previamente.

Finalmente, otro objetivos importante de esta tesis es proporcionar una visión unificada del comportamiento del tráfico, desde un vehículo individual hasta el flujo de tráfico global, vinculando los resultados de una escala más detallada con los resultados de una escala mayor. Para ello, se introduce una escala intermedia, la *mesoescala*, que sirve para relacionar coherentemente las escalas micro y macro. En este sentido, es de particular importancia el uso del cálculo de Wirtinger y el formalismo del Ginzburg-Landau Complejo en el estudio de esta mesoescala, algo no realizado anteriormente.

En resumen, esta tesis contiene nuevos métodos de análisis no lineal para estudiar la potencial inestabilidad que pueden introducir los tiempos de reacción y los retrasos de comunicación en el proceso de tráfico rodado. La investigación se ha centrado principalmente en determinar los límites de los tiempos de reacción debidos al conductor, los vehículos y los algoritmos que gobiernan las decisiones de conducción, y en cuantificar el impacto de estos retrasos en la formación de oscilaciones y ondas de densidad a las diferentes escalas físicas. Cabe destacar

que algunos de estos métodos también pueden aplicarse a otros campos de investigación, y algunos ejemplos de esto se proporcionan en el texto.

Contents

Acknowledgement . . . iii
Abstract . . . iv
Resumen . . . v
List of Figures . . . xi
List of Tables . . . xiv
Abbreviations . . . xvi

1 Introduction **1**
1.1 Road traffic and the impact of communications delay in automated driving . 1
1.2 The relevance of the scale: micro-, macro- and meso- scales . . . 2
1.3 The mathematics behind vehicular traffic theory . . . 3
1.4 Outline of this Thesis . . . 5
1.5 Notation . . . 6

2 Background **9**
2.1 Mathematical techniques relevant to this research . . . 9
2.1.1 Perturbation methods for nonlinear equations . . . 9
General procedure . . . 10
Asymptotic series . . . 10
Uniformity, straightforward expansion and secular terms . . . 10
Method of strained coordinates/parameters . . . 12
Method of multiple scales . . . 13
2.1.2 Delay Differential Equations . . . 13
Formal definition . . . 14
A simple scalar example . . . 14
The Hopf Bifurcation . . . 15
2.1.3 The Complex Ginzburg-Landau equation (CGLE) . . . 17
Spectral assumptions . . . 18
The linear part (dispersion) . . . 18
The nonlinear part (modulation) . . . 19
Complete CGLE and scaling . . . 21
Linear stability of the CGLE . . . 22
2.1.4 The Wirtinger derivative . . . 22
2.2 Models for vehicular traffic dynamics . . . 24

2.2.1 General overview of microscopic car-following models 25
Linear model 25
General Motors (GM) model 26
The Optimal Velocity Model (OVM) 28
The Intelligent Driver Model (IDM) 29
The new DDE model (nDDE) 30
2.2.2 General overview of macroscopic models 31
Lighthill-Whitman model 32
Burgers equation 33
Modern macroscopic models 33
Microscopic to macroscopic link for the OVM 34
2.2.3 Cellular automata model 36
2.3 Communications traffic modeling 36
2.3.1 Performance evaluation in network design and management 36
2.3.2 Evolution of network technologies and usage patterns 37
2.3.3 Mobile network standards evolution 37
2.3.4 New network paradigms in the 2020s 38
2.3.5 Communication models for V2X technologies 39
2.4 Motivational example: V2V network supporting traffic coordination 40

3 Simulation platform **43**
3.1 Development of simulation model on *ns-3* platform 43
3.1.1 *ns-3* platform characteristics 43
3.1.2 Enhancement of the existing mobility models 44
3.1.3 Communication models 47
3.2 Validation of existing traffic models 48
3.2.1 General Motors (GM) model validation 48
3.2.2 Optimal Velocity Model (OVM) validation 50
3.2.3 nDDE model validation 53
3.2.4 nDDEa model development and evaluation 54
3.2.5 First evaluation of the coupled system vehicles - network 59
Microscopic behaviour of nDDE model with variable delay 59
Macroscopic behaviour of nDDE model with variable delay 61
3.3 Final comments 63

4 The Hopf bifurcation in the microscopic modelling **65**
4.1 Problem statement 66
4.2 Poincaré-Lindstedt method applied to DDEs 67
4.2.1 General overview of the method 67
4.2.2 System of equations transformation 68
4.2.3 Solutions as series expansion 70
Equation for order j of ε 71
Asymptotic validity of the solution 73
4.3 Procedure to obtain a explicit solution of a desired order 74
4.3.1 General expression for the solution of order j 74

4.3.2 Solution $\mathbf{z}_j(\tau)$ of DDE_{z_j} . . . 76
4.3.3 Complete solution . . . 77
4.3.4 Error estimation . . . 77
4.4 Numerical examples . . . 78
4.4.1 nDDE car-following model . . . 78
System of equations and equilibrium solution . . . 79
Explicit expression of periodic solutions . . . 80
Error estimation . . . 83
4.4.2 SIR Epidemic model . . . 84
System of equations and equilibrium solution . . . 85
Explicit expression of periodic solutions . . . 86
4.4.3 Macroeconomic model . . . 90
System of equations and equilibrium solution . . . 90
Explicit expression of periodic solutions . . . 91
4.5 Final comments . . . 96

5 Stability and the Complex Ginzburg-Landau Equation (CGLE) in mesoscopic modelling 97
5.1 Problem statement . . . 97
5.2 Linear stability: calculation of the bifurcation point . . . 98
5.3 Mesoscopic model using the Complex Ginzburg-Landau equation (CGLE) formalism . . . 103
5.3.1 The CGLE in mesoscopic scale of traffic . . . 103
Asymptotic expansion of the solution . . . 103
5.3.2 Some comments on the calculation of coefficient γ . . . 105
Expressions for $\mathbf{M}_{l,m}$ and $\mathbf{N}_{l,m,n}$ . . . 105
Straightforward or singular expansion . . . 106
Validation of the calculation of γ . . . 107
5.3.3 Stabilty and the formation of modulating waves . . . 107
Metastability and criticality of the CGLE . . . 107
Impact of constant drift in metastability . . . 109
5.3.4 A simple example: the nDDE mesoscale . . . 110
5.4 Final comments . . . 114

6 General long-wavelength PDE for macroscopic modelling 115
6.1 Construction of the *long-wavelength* macroscopic equations . . . 115
6.1.1 Linearly relevant terms . . . 117
6.1.2 Continuity equation . . . 117
6.1.3 Momentum equation . . . 118
6.2 Expression for the macroscopic acceleration . . . 120
6.2.1 Managing delay in the microscopic equation . . . 120
6.2.2 Series expansion of the acceleration function . . . 120
Relative distance $\langle \Delta y_n(t) \rangle$ . . . 121
Relative velocity $\langle \Delta \dot{y}_n(t) \rangle$ . . . 123
Relative acceleration $\langle \Delta \ddot{y}_n(t) \rangle$ . . . 125

6.3 Final PDE system for the macroscopic process . . . 126
6.4 Linear stability analysis . . . 127
6.4.1 Long wavelength approximation linear equation . . . 127
6.4.2 Linear stability limit in the long-wavelength regime . . . 129
6.5 Examples of macroscopic stability . . . 129
6.5.1 Macroscopic linear instability of the Optimal Velocity Model . . . 129
6.5.2 Macroscopic linear instability of the nDDE Model . . . 130
6.6 Final comments . . . 134

7 Comparative results for existing driving models 135
7.1 Optimal Velocity Model (OVM) . . . 136
7.1.1 OVM microscopic analysis . . . 136
7.1.2 OVM mesoscopic analysis . . . 137
7.1.3 OVM macroscopic analysis . . . 141
7.2 Intelligent Driver Model (IDM) . . . 143
7.2.1 IDM microscopic analysis . . . 144
7.2.2 IDM mesoscopic analysis . . . 145
7.2.3 IDM macroscopic analysis . . . 148
7.3 New DDE model (nDDE) . . . 149
7.3.1 nDDE microscopic analysis . . . 149
7.3.2 nDDE mesoscopic analysis . . . 150
7.3.3 nDDE macroscopic analysis . . . 154
7.4 Final comments . . . 155

8 Conclusion 157
8.1 Original contributions of the thesis . . . 157
8.2 Future directions of research . . . 159

References 161

A Simulator diagrams 167

B Maple programs pseudocode 171
B.1 Calculation of Hopf limit cycles in DDEs . . . 171
B.2 Calculation of mesoscopic bifurcation and CGLE coefficients . . . 171

List of Figures

1.1 Micro, meso and macro scales. 3

2.1 Solutions for $u(\tau)$ in the simple DDE example with initial condition $u(0) = 1$. 15
2.2 Fundamental diagram relating the vehicle density ρ with the density current (flow) q (source: [48]). 24
2.3 Relationship of flow (in graph q_n) and density (in graph $\frac{k}{k_j} \equiv \frac{\rho}{\rho_{max}}$) for $m = 0$ and different values of l (Source: [24]) 27
2.4 V2X standards evolution 39
2.5 DSRC scheme 40
2.6 Interference as the source of main delay 41

3.1 Flow diagram of the simulator 47
3.2 Evolution of 2 vehicles dynamic for linear GM model in [61] for $C = e^{-1}$ (Figure 4.2 in the original). 49
3.3 Evolution of 2 vehicles dynamic for linear GM model calculated with *ns-3* simulator. 49
3.4 Evolution of the follower vehicle for linear GM model in [61] for several values of C (Figure 4.3 in the original). 50
3.5 Evolution of the follower vehicle for linear GM model and for several values of C, calculated with *ns-3* simulator. 50
3.6 Evolution of macroscopic scenario with delay under the stability limit ($\tau = 0.4s$). 51
3.7 Evolution of macroscopic scenario with delay over the stability limit ($\tau = 0.7s$). 51
3.8 Macroscopic simulation of the difference equation (3.2) with $\tau = 0.5s$ [48] . . 52
3.9 Macroscopic simulation of the difference equation (3.2) with $\tau = 0.5s$ [48] . . 52
3.10 Oscillatory and stable solution for $\tau = 1.2s$ in nDDE in [56]. 53
3.11 Oscillatory and stable solution for $\tau = 1.2s$ in nDDE using the *ns-3* simulation. 54
3.12 Oscillatory and unstable solution for $\tau = 6.2s$ in nDDE in [56]. 54
3.13 Oscillatory and unstable solution for $\tau = 6.2s$ in nDDE using the *ns-3* simulation. 55
3.14 A typical nDDE function (the equilibrium line $g(s, s') = 0$ in dashed red line). 55
3.15 Example of acceleration diagram (from [63]) 56
3.16 Maximum acceleration function 56
3.17 nDDE model with maximum acceleration dependent on velocity (the equilibrium line $g(s, s') = 0$ in dashed red line). 57
3.18 Distance and velocity evolution for OVM simulation. $\tau = 0.5s$, $t = 100s, 120s$. 57

3.19 Distance and velocity evolution for nDDE model simulation. $\tau = 3s$, $t = 100s, 120s$. 58
3.20 Distance and velocity evolution for nDDEa model simulation. $\tau = 3s$, $t = 100s, 120s$. 58
3.21 Micro evolution for delay depending on vehicle density. Density change from 0.0225 veh./m to 0.04275 veh./m. 60
3.22 Micro evolution for delay depending on vehicle density. Density change from 0.0225 veh./m to 0.04725 veh./m. 60
3.23 Micro evolution for delay depending on vehicle density. Density change repeatedly from 0.0225 veh./m to 0.04725 veh./m. 61
3.24 Macro evolution with density 0.03 veh./m and constant delay $\tau = 0.5s$. . . . 62
3.25 Macro evolution with density 0.03 veh./m and and variable delay dependent on the density. 63
3.26 Macro evolution with density 0.03 veh./m and and variable delay dependent on the density. 63

4.1 Bifurcation diagram of s and s' in the nDDE model (4.50). 82
4.2 Asymptotic stable solution of u_1 and u_2 for $r = 1.4s$ in nDDE (4.51). 83
4.3 Asymptotic stable solution of $u_1(t)$ and $u_2(t)$ for $r = 1.6s$ in nDDE (4.51). . 84
4.4 Asymptotic stable solution of $u_1(t)$ and $u_2(t)$ for $r = 1.8s$ in nDDE (4.51). . 84
4.5 Bifurcation diagram of I, R and S in the SIR model (4.55). 89
4.6 Asymptotic stable solution of I, R and S for $r = 120$ days in model in eq. (4.55). 89
4.7 Asymptotic stable solution of I, R and S for $r = 140$ days in model in eq. (4.55). 90
4.8 Asymptotic stable solution of $R(t)$, $I(t)$ and $P(t)$ for $r = 0.1s$ in model in eq. (4.58). 94
4.9 Asymptotic stable solution of $R(t)$, $I(t)$ and $P(t)$ for $r = 0.3s$ in model in eq. (4.58). 95
4.10 Bifurcation diagram for the macroeconomic model (4.58). 95

5.1 Position and distance of the vehicles in the microscopic view of traffic. 98
5.2 Example of neutral stability line ($\kappa(r)$ such that $\Re(\lambda(r, \kappa)) = 0$). 102
5.3 Evolution of distance and velocity of the vehicles with nDDE for $r = 0.55s$. . 112
5.4 Evolution of distance and velocity of the vehicles with nDDE for $r = 0.6s$. . 112
5.5 Detailed view of the evolution of the vehicles with nDDE for $r = 0.6s$. 113
5.6 Evolution of distance and velocity of the vehicles with nDDE for $r = 0.8s$. . 113
5.7 Detailed view of the evolution of the vehicles with nDDE for $r = 0.8s$. 114

6.1 Position and distance of the vehicles in the microscopic view of traffic. 116
6.2 Examples of coarse-graining functions. 116
6.3 Evolution of distance and velocity of the vehicles with OVM for $r = 0.055s$. . 131
6.4 Evolution of distance and velocity of the vehicles with OVM for $r = 0.1s$. . . 131
6.5 Evolution of distance and velocity of the vehicles with OVM for $r = 0.2s$. . . 131
6.6 Evolution of distance and velocity of the vehicles with nDDE for $r = 0.6s$. . 133
6.7 Evolution of distance and velocity of the vehicles with nDDE for $r = 0.9s$. . 134
6.8 Evolution of distance and velocity of the vehicles with nDDE for $r = 1s$. . . 134

7.1 Bifurcation diagram of s and s' for the OVM model. 138
7.2 Asymptotic stable solution of u_1 and u_2 for $r = 0.2s$ in OVM scenario. 138
7.3 Neutral stability line ($\kappa(r)$ such that $\Re(\lambda(r, \kappa)) = 0$) in OVM scenario. . . . 139
7.4 Evolution of distance and velocity of the vehicles with OVM for $r = 0.051s$. . 140
7.5 Evolution of distance and velocity of the vehicles with OVM for $r = 0.055s$. . 140
7.6 Evolution of distance and velocity of the vehicles with OVM for $r = 0.055s$. . 142
7.7 Evolution of distance and velocity of the vehicles with OVM for $r = 0.1s$. . . 142
7.8 Evolution of distance and velocity of the vehicles with OVM for $r = 0.2s$. . . 142
7.9 Bifurcation diagram of s and s' for the IDM model. 145
7.10 Asymptotic stable solution of u_1 and u_2 for $r = 0.2s$ in IDM scenario. 145
7.11 Neutral stability line ($\kappa(r)$ such that $\Re(\lambda(r, \kappa)) = 0$) in IDM scenario. 147
7.12 Evolution of distance and velocity of the vehicles with IDM for $r = 0.56s$. . . 148
7.13 Evolution of distance and velocity of the vehicles with IDM for $r = 0.6s$. . . 148
7.14 Bifurcation diagram of s and s' in the nDDE model. 150
7.15 Asymptotic stable solution of $u_1(t)$ and $u_2(t)$ for $r = 1.1s$ in nDDE. 151
7.16 Neutral stability line ($\kappa(r)$ such that $\Re(\lambda(r, \kappa)) = 0$) for nDDE scenario. . . 152
7.17 Evolution of distance and velocity of the vehicles with nDDE for $r = 0.35s$. . 153
7.18 Evolution of distance and velocity of the vehicles with nDDE for $r = 0.4s$. . 154
7.19 Detailed view of the evolution of the vehicles with nDDE for $r = 0.4s$. 154
7.20 Evolution of distance and velocity of the vehicles with nDDE for $r = 0.6s$. . 155
7.21 Evolution of distance and velocity of the vehicles with nDDE for $r = 0.9s$. . 156
7.22 Evolution of distance and velocity of the vehicles with nDDE for $r = 1s$. . . 156

A.1 C++ structure of the main simulator program 168
A.2 C++ structure of the car-following model implementation. 169

B.1 Pseudocode of the Maple 2024 program for the calculation of limit cycles in Hopf bifurcation in DDEs (I). 172
B.2 Pseudocode of the Maple 2024 program for the calculation of limit cycles in Hopf bifurcation in DDEs (II). 173
B.3 Pseudocode of the Maple 2024 program for the calculation of the nDDE mesoscopic approximation (I). 174
B.4 Pseudocode of the Maple 2024 program for the calculation of the nDDE mesoscopic approximation (II). 175

List of Tables

3.1 nDDE parameters used in the simulations. 53

4.1 General overview of Chapter 4 notation. 68
4.2 nDDE parameters for the evaluated scenario [56]. 80
4.3 Coefficients for series expansion of $\hat{r}$ and $\hat{T}$. 81
4.4 Coefficients for space u_1. 81
4.5 Coefficients for relative velocity u_2. 82
4.6 Relative errors for the different values of r. 84
4.7 Parameters used in the study of the SIR model (4.55). 86
4.8 Coefficients for series expansion of r and $\hat{T}$. 87
4.9 Coefficients for Infected variable I. 87
4.10 Coefficients for Susceptible variable S. 88
4.11 Coefficients for Recovered variable R. 88
4.12 Relative errors (%) for the SIR model scenario. 90
4.13 Parameters used in the study of the financial model (4.58) 92
4.14 Coefficients for series expansion of λ and T 92
4.15 Coefficients for Interest Rate variable R. 93
4.16 Coefficients for Investment variable I. 93
4.17 Coefficients for Price Index variable P. 94
4.18 Relative errors (%) for the macroeconomic model scenario. 95

7.1 OVM parameters for the evaluated scenario. 136
7.2 Coefficients for series expansion of $\hat{r}$ and $\hat{T}$ for the OVM scenario. 137
7.3 IDM parameters for the evaluated scenario. 143
7.4 Coefficients for series expansion of $\hat{r}$ and $\hat{T}$ for the IDM scenario. 145
7.5 nDDE parameters for the evaluated scenario [56]. 149
7.6 Coefficients for series expansion of $\hat{r}$ and $\hat{T}$. 150

Abbreviations

1G : First Generation of mobile communications (AMPS, NTM, TACS).

2G : Second Generation of mobile communications (GSM, CDMA).

3G : Third Generation of mobile communications (UMTS, CDMA2000).

3GPP : Third Generation Partnership Project.

4G : Fourth Generation of mobile communications (LTE, WiMAX).

5G : Fifth Generation of mobile communications (NR).

CA : Cellular Automata.

CGLE : Complex Ginzburg-Landau Equation.

CSMA-CA : Carrier Sense Multiple Access - Congestion Avoidance.

DDE : Delay Differential Equation.

DFE : Disease-Free Equilibrium.

DSRC : Dedicated Short Range Communications.

EE : Endemic Equilibrium.

GM : General Motors.

GSMA : Global System for Mobile communications Association.

IDM : Intelligent Driver Model.

IEEE : Institute of Electrical and Electronics Engineers.

IoT : Internet of Things.

IP : Internet Protocol.

IPv4 : Internet Protocol version 4.

IPv6 : Internet Protocol version 6.

LTE : Long Term Evolution.

M2M : Machine to Machine.

MAC : Medium Access Control.

nDDE : new DDE car following model

NG-V2X : Next Generation Vehicle to everything.

ns-3 : network simulator version 3.

ODE : Ordinary Differential Equation.

OVM : Optimal Velocity Model.

PDE : Partial Differential Equation.

RFDE : Retarded Functional Differential Equation.

SIR : Susceptible - Infected - Recovered epidemic model.

TCP : Trnsport Control Protocol.

V2I : Vehicle to Infrastructure.

V2V : Vehicle to Vehicle.

V2X : Vehicle to Everything.

Chapter 1

Introduction

1.1 Road traffic and the impact of communications delay in automated driving

Since the early 20th century, when automotive traffic gained importance as one of the cornerstones of modern economies, there has been increasing interest in the mathematics and physics community to study and characterize the traffic process as a physical system obeying predictable laws. Vehicular traffic was seen either as a multi-particle system or as a continuous flow whose features resemble well known physical systems, and were therefore amenable to be studied using existing mathematical techniques employed in modern physics. Road traffic, as a system of interacting particles, present phenomena similar to those observed in complex physical systems, like phase transitions, wave propagation and metastability, so methods coming from thermodynamics, fluid dynamics and gas kinetics have been adapted to study traffic phenomena [48, 31]. In addition, the new simulation capabilities offered by modern computing platforms allowed to build and test approximate models whose performance could be compared to measurements in real roads.

The most successful models that have emerged in this area of research have been mostly centered in modelling the behaviour of the driver and its interaction with the environment, specially the dynamics of other vehicles. These models approximately explain the genesis of congestion formation observed in real roads in typical circumstances, but on occasions they are unable to reproduce the behaviour of real drivers and vehicles in more intricate environments. Moreover, the analysis is now further complicated because a significant number of vehicles with some kind of automatic driving assistance is expected to appear in the roads in the coming years. Given the different degrees of predictability of the behaviour of these vehicles, we can expect an increasing complexity in the mobility models to be used.

In this regard, the different forms of automatic driving systems that are expected to be introduced shortly (assisted, remote or autonomous self-driving) will certainly rely on one or several communication technologies - e.g. vehicle-to-vehicle (V2V) or vehicle-to-infrastructure (V2I) - to acquire or share information relevant to the driving management functions. The mechanisms to establish and manage these communication channels have indeed been included

in the specifications of the most recent versions of the telecommunication standards (either in the IEEE or GSMA standards), but, for the time being, have had a very limited use due to a perceived lack of reliability. In particular, this is specially the case of the time taken by transmission or reception of the information, that are required to be in very strict limits so that the driving decisions are taken in a timely manner. It is only now that the assisted driving functions in the last generation of mobile network standards (5G), called vehicle-to-everything communications (V2X), are capable to offer latencies low enough to enable delay critical driving assistance over mobile connections. This is considered a fundamental cornerstone for safely deploying self-autonomous driving systems.

Therefore, paramount for the successful adoption of these services is the understanding of the challenges and risks derived of these new mobility scenarios. This will be especially critical for applications highly dependent on strict timing, which will be affected by both network traffic and road traffic conditions. We think that this is not being addressed appropriately in current research, where, even in mobility and dynamic scenarios, the patterns of the vehicular traffic and the communications traffic can be an input for each system analysis, but are not studied like a single, coupled system. Therefore the objective of this thesis is to provide new mathematical methods to evaluate the impact of the delays and reaction times inherent to these interactions in the main dynamics of the road traffic process.

1.2 The relevance of the scale: micro-, macro- and meso-scales

Given the wide array of problems and applications in the field of vehicular traffic, it is necessary to clearly determine what is the relevant physical domain of an investigation to decide what kind of modelling is more suitable for the problem. For instance, the tools for determining the best algorithm for the management of acceleration and braking in a self driving car would focus in a physical scale that involves the individual vehicle and its immediate surrounding area, while the tools for studying the best admission control in an incoming ramp to a main road would see the traffic of many vehicles as an aggregated entity. It is then essential to define from the onset the relevant scale, which will determine the mathematical tools to use.

Following this principle, two main physical scales have been traditionally considered in road traffic investigations: the *microscopic* scale, involving one vehicle and its environment and interested in the individual dynamics of the vehicle (velocity, acceleration), and the *macroscopic* view, in which the traffic is seen as a continuous flow described by the global continuous variables density $\rho(x,t)$ (vehicles/m) and velocity $v(x,t)$ (m/s). An intermediate view derived from gas kinetic techniques has also been proposed, mixing the aggregate variables of the macroscopic view with assumptions on the interactions of individual vehicles. Nevertheless this approach, though useful to model different states of congestion of the traffic, is limited to a stochastic modelling of the driver behaviour, and does not allow for a specific driver modelling ([31, 48]).

One important objective of this thesis is to provide a unified view of the traffic behaviour, starting from the individual vehicle up to the global traffic flow, linking the results of one

finer scale with the results of a coarser one. To do this we will introduce an intermediate scale, the *mesoscale*, that bridges the gap between the *micro* and *macro* scales. As we will see, some of the most important results of this thesis are concerned with this *mesoscale*, for which there were not previous existing results.

Thus, formal definitions of the physical scales considered in this thesis follows.

- **Microscopic scale**: the traffic is seen as individual interacting particles, and the focus is on an individual vehicle dynamics (space, velocity and acceleration) as determined by its immediate environment (typically, the surrounding vehicles). The spatial validity of these models is in the order of $50\,m - 500\,m$.
- **Mesoscopic scale**: traffic is seen as interacting particles, but in this case obeying global dynamics that define the collective behaviour (typically, wavelike motion in space and time). This collective behaviour is the result of the aggregation of the individual interactions at *micro* scale. The applicability of these models is in the order of $100\,m - 5000\,m$.
- **Macroscopic scale**: traffic is seen as a compressible fluid, and is described by the continuous average variables density $\rho(x,t)$ (vehicles/m) and velocity $v(x,t)$ (m/s). The equations describing these average quantities are the result of the individual and collective behaviour of the smaller scales. Therefore the typical validity of the models at this scale is in the order of $1\,km - 50\,km$.

Figure 1.1 gives a visual representation of the different scales defined above.

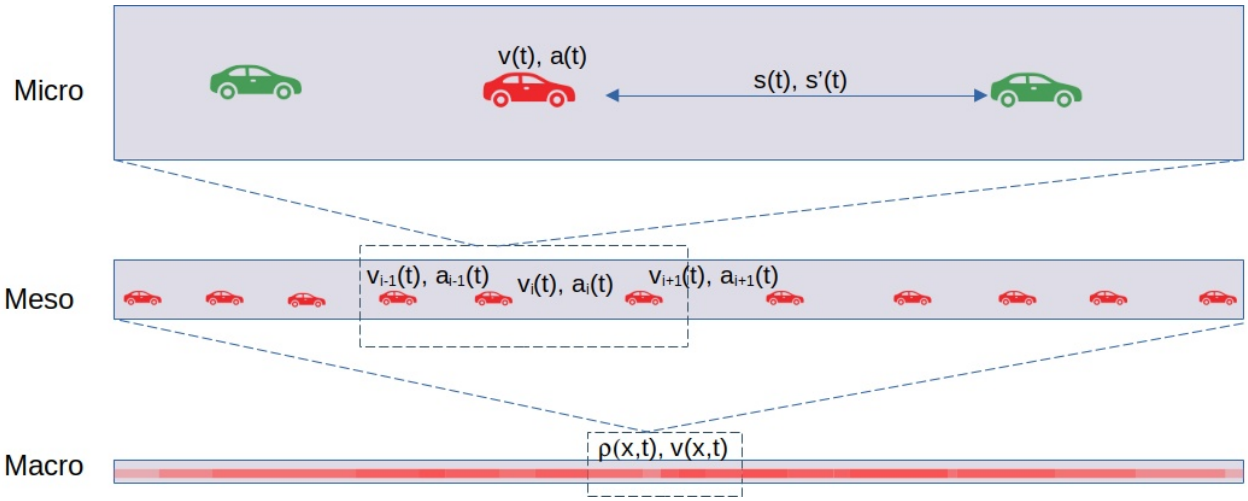


Figure 1.1: Micro, meso and macro scales.

1.3 The mathematics behind vehicular traffic theory

Every scale of interest requires specific mathematical tools for its analysis. The method of choice is determined by the classical physical system that best resembles the scale of the target mobility scale. The *microscopic* models are normally expressed as equations of classical

mechanics describing the kinetics of the vehicle under study in the spatial frame of reference relative to its equilibrium speed, in the form of Ordinary Differential Equations (ODEs). Mesoscopic and macroscopic models, on the other hand, need to consider the absolute spatial frame of reference, and see the traffic process as a continuous flow, thus they are usually expressed in terms of Partial Differential Equations (PDEs). Standard linear stability analysis techniques are normally employed to determine the reaction time stability limit is a specific situation.

In any case, all of the models have to factor in some way the influence of the response time in the system equations. This has been traditionally achieved by introducing the delay as a sensitivity factor in non retarded ODEs or PDEs. For example one may model that a driver wants to set the velocity of the vehicle to a specific optimal velocity after a certain reaction time, e.g.:

$$y'(t+r) = v_{opt}, \tag{1.1}$$

where y is the position of the vehicle and r is the reaction time. This way, we can approximate this "retarded" velocity as

$$v_{opt} = y'(t+r) = y'(t) + ry''(t) + O(r^2), \tag{1.2}$$

where the prime symbol indicates differentiation with respect to time t. Then the acceleration to apply $a(t) = y''(t)$ is approximated by:

$$a(t) = y''(t) = \frac{1}{r}(v_{opt} - y'(t)) = \alpha(v_{opt} - y'(t)), \tag{1.3}$$

thus embedding the reaction time in a sensitivity parameter $\alpha = 1/r$. This kind of approximation has been the preferred way of dealing with delays in the equations of vehicular traffic models. Nevertheless, as we will see, this is not the adequate approach if one wants to investigate the nonlinear effects associated to reaction times. To do this, it is necessary to rely on the theory of Retarded Functional Differential Equations (RFDE) [29], most frequently referred to as Delay Differential Equations (DDEs), of which equation (1.1) is a simple example. This branch of differential calculus will be one of the basis of the methods introduced by this thesis.

In addition to the nonlinear effects introduced by the reaction times, the interaction between vehicles and the environment can be quite complicated, resulting in differential equations that are highly nonlinear. To adequately analyze these nonlinearities, another key mathematical tool employed in this thesis is the use of perturbation methods [52] to calculate approximate solutions to the mobility equations. These methods look for approximate solutions in the form of asymptotic series over an expansion parameter, usually related to the deviation with respect to the limiting delay that introduces oscillations in the dynamics of the system. Different types of application of this technique, like strained coordinates or multiple scales, have been used in the past in the literature and have been a key tool for this research. In this sense, one of the main contributions of this thesis is the introduction of new approaches of application of these mathematical methods in order to obtain results not available before in vehicular traffic studies.

1.4 Outline of this Thesis

This thesis contains new application methods of nonlinear analysis to study the instability that reaction times and communication delays introduce in the road traffic process. The research has been mostly focused on determining the limits of the reaction times inherent to the driver, vehicles and algorithms governing the driving decisions, and on quantifying the impact of these delays on the emergence of traffic oscillations and density waves. It is worth mentioning that some of these methods could also be applied to other research fields, as shown by some examples included in chapter 4.

The results are presented according to the following outline:

- Chapter 2 provides background material, with a brief introduction and references to the mathematics that supports the methods employed in this research. It also includes a summary of the state of the art of the research in vehicular traffic dynamics, and an introduction to the network technologies that bring new challenges to traffic management. The chapter is completed with an illustrative example of interaction of vehicular and communications dynamics to motivate the pertinence of this research.
- Chapter 3 introduces the simulation platform that has been used to validate the main results of the research. Given that the investigation is centered in the interaction of mobility and communications, we have extended an existing simulation platform for telecommunications (*network simulator ns3*) to support the vehicular mobility models under study.
- The research carried out for *microscopic* models is included in chapter 4. The main result is the development of a novel methodology to derive explicit expressions for limit cycles in instabilities due to bifurcations in car-following models. This method is also applicable to other nonlinear phenomena, as is illustrated with additional examples from the fields of immunology and economics.
- The results obtained for the *mesoscopic* scale of traffic are the object of chapter 5. This traffic scale is lacking of an adequate modelling in the current state of research. This is addressed by the introduction of an original perspective in the characterization of the interaction of a set of vehicles by using the Wirtinger calculus to obtain the set of exact, closed-form equations that describe the vehicle dynamics at this scale. In addition, approximate solutions to these equations are obtained by means of the Complex Ginzburg-Landau Equation (CGLE) formalism. These methods are general enough to be applicable to any standard microscopic acceleration model in the published research.
- Chapter 6 presents the results obtained for the *macroscopic* scale. This consists of a novel *long-wavelength* approximation of the continuous flow in the macroscopic view that is again applicable to any standard microscopic model. The PDEs obtained by this approximations can then be used to study the large scale traffic process stability and the formation of density waves and stop-and-go traffic patterns.
- To provide a coherent view of the applicability of the mathematical methods introduced

in this thesis, chapter 7 contains examples of characterization of several existing traffic models. Starting from the most basic model at *micro* scale, the equations that describe the *meso* and *macro* scales are formulated. The theoretical results are then validated with simulations using the simulation tool introduced before.

- Finally, the last chapter contains a summary of the results of this thesis. The generality of the methods introduced in the different chapters allows for the characterization at all scales of existing mobility models, and sets the path for future investigations in the current challenges and directions in this field.

1.5 Notation

As can be expected, a considerable number of references have been used as sources for this work, each one with its own notation conventions. Moreover, it is well-known that there are significant differences in the symbolic notations used in the mathematics and physics literature, while both of them have contributed significantly to the references in this work. Therefore, in order to maintain consistency throughout this research, the notation used in the explanation of a specific method may differ from the one used in the original source.

The following notational conventions are used in this work:

- Vector constants, variables and functions are denoted by lowercase boldface (e.g. $\mathbf{u}, \mathbf{v}, \boldsymbol{\phi}, \boldsymbol{\psi}, ...$).
- Linear operators are denoted by uppercase letter without parenthesis in the arguments (e.g. $L(\mathbf{u}) \equiv L\mathbf{u}$).
- Multilinear and nonlinear operators are denoted by uppercase letter with parenthesis in the arguments (e.g. $NL(\mathbf{u}), M(\mathbf{u}, \mathbf{v}), N(\mathbf{u}, \mathbf{v}, \mathbf{w})$).
- Matrix constants, variables and functions are denoted by uppercase boldface (e.g. $\mathbf{A}, \mathbf{Q}, ...$).
- Bilinear and trilinear forms are denoted in uppercase boldface with their arguments in parenthesis (e.g. $\mathbf{M}(\mathbf{u}, \mathbf{v}), \mathbf{N}(\mathbf{u}, \mathbf{v}, \mathbf{w}), ...$)
- $|\mathbf{v}|$ is the Hilbert norm of the vector $\mathbf{v}$.
- $|a|$ is the modulus of the scalar a.
- $\overline{a}$ is the complex conjugate of $a \in \mathbb{C}$.
- $\Re(a)$ denotes the real part of $a \in \mathbb{C}$.
- $\Im(a)$ denotes the imaginary part of $a \in \mathbb{C}$.
- $\langle , \rangle$ denotes the scalar product in a Hilbert space.
- L^* is the adjoint of the linear operator L.
- $N(L)$ is the null space and $R(L)$ the range of the linear operator L.

- $M^{\perp}$ is the orthogonal of M.
- $\nabla \mathbf{u}$ is the gradient of $\mathbf{u}$.
- $\Delta \mathbf{u}$ is the Laplacian of $\mathbf{u}$.
- $\mathbb{J}_{\mathbf{v}}\mathbf{f}$ is the Jacobian of a function $\mathbf{f}$ with $D(\mathbf{f}) \subset \mathbb{C}^m$ with respect to the vector $\mathbf{v} \in \mathbb{R}^n$.
- $\text{spec}(T)$ is the spectrum of operator T.
- $\frac{\partial^*}{\partial^* u}$ denotes the Wirtinger derivative with respect to $u \in \mathbb{C}$.
- $\mathbb{W}\mathbb{J}_{\mathbf{u}}\mathbf{f}$ denotes the "Wirtinger Jacobian" of a function $\mathbf{f}$ with $D(f) \subset \mathbb{C}^m$ with respect to the vector $\mathbf{u} \in \mathbb{C}^n$, defined in Section 2.1.4.

We will use the following convention for the variables:

- t will be the standard time.
- x will denote, in general settings, an independent variable, and in PDE contexts the uni-dimensional space independent variable.
- y will denote, in general settings, a dependent variable, and in PDE contexts the spatial position dependent variable (for instance, the position of a vehicle).
- ω will denote the angular frequency in periodic functions.
- T will denote the period in periodic functions.
- r will denote the delay (reaction time) in delay equations, and will follow the convention:
  - r_μ for the limiting delay at microscopic scale,
  - r_m for the limiting delay at mesoscopic scale,
  - r_M for the limiting delay at macroscopic scale,
- λ will denote eigenvalues in characteristic functions.
- κ will denote the wavenumber in spatially unidimensional waves.
- ε will denote the expansion parameter in asymptotic expansions.
- $\mu = (p - p_0)$ will denote the deviation from the bifurcation value of parameter p in a Hopf bifurcation induced by this parameter variation.
- τ, depending on the context, will denote:
  - a time variable alternative to t, or
  - a scaled time (normally slower than t).
- ξ, depending on the context, will denote:
  - a space variable alternative to x, or
  - a scaled space (normally larger than x).
- Δ will denote the difference between two variables in a sequence e.g. $\Delta y_n = y_{n+1} - y_n$.

Other symbols will be defined in the text when needed.

Chapter 2

Background

This chapter contains a brief overview of the most relevant models and analytical techniques that are being used at this moment in the study of vehicular traffic and its interaction with communication technologies. The activity in this field has been intense since the early 1950's, and therefore the body of knowledge is substantial, thus in this chapter only the most salient characteristics of each model or technique are mentioned, referring the reader to the included references for further details.

We start by providing a brief introduction to the mathematical concepts that will be used in subsequent chapters, followed by a summary of the state of the art in vehicular traffic models and communication traffic models. We finish with an application scenario that relates several of the concepts introduced as a motivational example to illustrate the aim and scope of this thesis.

2.1 Mathematical techniques relevant to this research

In this section we include basic material and references to the fundamental mathematical concepts and techniques that are used in the following chapters. Only the most salient features of each area are mentioned, and we refer to the included references for further details.

2.1.1 Perturbation methods for nonlinear equations

As we will see, the equations describing the dynamics of vehicular traffic are most frequently nonlinear differential equations, which are, in general, not solvable analytically. Therefore methods to calculate approximate solutions to nonlinear equations are necessary for our analysis. Most important among these methods are the perturbation (also known as asymptotic) methods, in which the approximate solution is obtained as the first few terms of an asymptotic expansion of the exact solution. These expansions are obtained in terms of an expansion parameter, that may be present naturally in the original equation, or is introduced externally (for instance, as a deviation from an equilibrium value) to obtain the expansion. In the following we are going to follow the books by Nayfeh et al. ([51], [52]). For simplicity we focus in this summary on scalar functions, but this can be easily generalize for vector

functions.

General procedure

A general physical problem for which we search a solution of a scalar function $u(x, \varepsilon)$ can frequently be described by a nonlinear differential equation $\frac{du}{dx} = F(u, x, \varepsilon)$. This equation is in general not solvable, but if there is an equilibrium solution (typically a fixed point) for an $\varepsilon = \varepsilon_0$ (that we can always scale to $\varepsilon_0 = 0$), we search for solutions in powers of ε in the form:

$$u(x; \varepsilon) = u_0(x) + \varepsilon u_1(x) + \varepsilon^2 u_2(x) + ... \tag{2.1}$$

The perturbation methods consist of introducing this type of expansion in the original equation (and the boundary conditions) and expanding for small ε. Given that this equation must hold for all values of ε, each coefficient for each power of ε must vanish independently because sequences of ε^k are linearly independent. This generates a set of equations that are solved up to a given order to obtain the desired approximation.

Asymptotic series

A series $\sum_{k=0}^{\infty}(a_k/x^k)$ with the a_m independent of x, is an asymptotic series for y, written

$$y \sim \sum_{k=0}^{\infty} \frac{a_k}{x^k} \quad as \quad |x| \to \infty, \tag{2.2}$$

if and only if

$$y = \sum_{k=0}^{n} \frac{a_k}{x^k} + o(|x|^{-n}) \quad as \quad |x| \to \infty. \tag{2.3}$$

Even when this series is divergent, its usefulness resides in that for a given n, the first n terms of the series can represent y with an error that can be made as small as necessary by taking $|x|$ large enough. This is why asymptotic series are so extensively used in perturbation analysis, using $\varepsilon = 1/x$ in (2.2) and looking for approximate solutions for small ε.

The concept pf asymptotic series is generalized in the asymptotic *expansions* [51], in which the expansion, instead of powers of ε, is made on a generalized sequence $\delta_k(\varepsilon)$, but we will exclusively use asymptotic series expansions in this work.

Uniformity, straightforward expansion and secular terms

We can express the expansion in (2.1) as:

$$u(x; \varepsilon) = \sum_{k=0}^{N} a_k(x)\varepsilon^k + R_N(x; \varepsilon), \tag{2.4}$$

where $R_N(x; \varepsilon)$ is the approximation error for order N. We say that the expansion is *uniformly valid* if

$$R_N(x; \varepsilon) = O(\varepsilon^N) \quad \forall x. \tag{2.5}$$

When this condition is not met, the expansion is *nonuniformly vald* and we say that it is a *singular perturbation* expansion. Nonuniformity of series expansion manifests usually through the appearance of terms $a_k(x)$ in (2.4) such that $a_k(x)/a_{k-1}(x)$ is unbounded when x tends to infinity. We can illustrate this with a simple example. Let us consider the initial value problem for the *Duffing oscillator*:

$$\begin{aligned} \frac{d^2y}{dt^2} + y + \varepsilon y^3 = 0, \\ y(0) = A, \quad \frac{dy}{dt}(0) = 0, \end{aligned} \tag{2.6}$$

where ε is a small parameter that is going to be used as expansion parameter. We can try the straightforward expansion:

$$y(t) = y_0(t) + \varepsilon y_1(t) + \varepsilon^2 y_2(t) + ... \tag{2.7}$$

Substituting in (2.6) and equating the terms of the same order of ε:

1. Order ε^0:

$$\frac{d^2y_0}{dt^2} + y_0 = 0, \tag{2.8}$$

with solution:

$$y_0(t) = A\cos(t). \tag{2.9}$$

2. Order ε^1:

$$\frac{d^2y_1}{dt^2} + y_1 = -y_0^3 = -A^3\cos^3(t). \tag{2.10}$$

This nonhomogeneous equation can be integrated using standard methods to get:

$$y_1(t) = -\frac{A^3}{32}\cos(t) - \frac{3A^3}{8}t\sin(t) + \frac{A^3}{32}\cos(3t). \tag{2.11}$$

The second term of (2.11) is a secular term that is unbounded when $t \to \infty$. It is then clear that these secular terms must not be allowed in the approximate solutions if we want them to be uniformly valid. Quoting from [51]: *The appearance of secular terms is characteristic of nonlinear oscillation problems, hence one should not expect to obtain a uniformly valid straightforward expansion in these cases.*

To adress this problem different techniques have been proposed in the literature, like the methods of strained coordinates/parameters, multiple scales, harmonic balance and averaging [52]. We will briefly introduce the two first methods, that are going to be used in later chapters.

Method of strained coordinates/parameters

In the case of linear oscillators, the oscillations are produced always at a fixed frequency, with an amplitude that is dependent on the initial conditions of the physical system. In contrast, a feature of nonlinear oscillations is that there exists an *amplitude-frequency interaction*, usually produced by a parameter in the governing equation whose variation determines the amplitude and frequency of the solution. A prototypical example of this situation is the *Hopf bifurcation*, in which a variation in a parameter in an ODE changes the solution of the equation form a fixed-point stable solution to an oscillatory behaviour [46]. This phenomenon is also observed in DDEs [29], and is the object of research of this work in chapter 4.

To manage this amplitude-frequency interaction, is is usually employed a scaling of either the independent variables of the problem (strained coordinates) or a specific parameter (strained parameter) such that this interaction can be accounted for in the series expansion. Most important among these methods is the *Poincaré-Lindstedt method* that expands the frequency in powers of the parameter ε [71]. To illustrate the method we go back to the example equation (2.6). We let the frequency be an asymptotic series expansion on ε.

$$\omega = 1 + \varepsilon\omega_1 + \varepsilon^2\omega_2 + ..., \tag{2.12}$$

and define an scaled time variable $\tau = \omega t$. We then express (2.6) as:

$$\frac{d^2y}{d\tau^2} + y + \varepsilon y^3 = 0. \tag{2.13}$$

Expanding

$$y(\tau) = y_0(\tau) + \varepsilon y_1(\tau) + \varepsilon^2 y_2(\tau) + ... \tag{2.14}$$

we get:

1. Order ε^0:

$$\frac{d^2y_0}{d\tau^2} + y_0 = 0 \quad \Longrightarrow \quad y_0(\tau) = A\cos(\tau). \tag{2.15}$$

2. Order ε^1:

$$\frac{d^2y_1}{d\tau^2} + y_1 = -y_0^3 + 2\omega_1\frac{d^2y_0}{d\tau^2} = -A^3\cos^3(\tau) - 2\omega_1 A\cos(\tau) = \\ -\frac{3A^3}{4}\cos(\tau) - \frac{A^3}{4}\cos(3\tau) - 2\omega_1 A\cos(\tau). \tag{2.16}$$

To eliminate the secular terms we need that

$$\frac{3A^3}{4} - 2\omega_1 A = 0 \quad \Longrightarrow \omega_1 = -\frac{3A^2}{8}, \tag{2.17}$$

so equation (2.16) becomes:

$$\frac{d^2y_1}{d\tau^2} + y_1 = -\frac{A^3}{4}\cos(3\tau), \tag{2.18}$$

with solution

$$y_1(\tau) = \frac{A^3}{32}\cos(3\tau). \tag{2.19}$$

Then the approximation to order 1 is:

$$y(t) = A\cos(\omega t) + \varepsilon\frac{A^3}{32}\cos(3\omega t) + O(\varepsilon^2),$$
$$\omega = 1 - \frac{3}{8}\varepsilon A^2. \tag{2.20}$$

This procedure could be employed to obtain the subsequent approximation orders. A complete algorithm to apply this method to vector DDEs is the object of chapter 4.

Method of multiple scales

Another view of the stretching of time in equation (2.20) is to consider that y of two time variables, namely t and εt. The idea behind the method of multiple scales is to consider the expansion to be a function of multiple independent variables, instead of one. This idea, in PDEs can be either applied to space or time variables. For instance, to use different scales in time one defines:

$$\tau_n = t\varepsilon^n \quad n = 0, 1, 2, ... \tag{2.21}$$

Then the derivatives in t become partial derivatives in the scaled times, i.e.:

$$\frac{d}{dt} = \frac{d\tau_0}{dt}\frac{\partial}{\partial\tau_0} + \frac{d\tau_1}{dt}\frac{\partial}{\partial\tau_1} + ... = D_0 + \varepsilon D_1 + ..., \tag{2.22}$$
$$\frac{d^2}{dt^2} = D_0^2 + 2\varepsilon D_0 D_1 + \varepsilon^2(D_1^2 + 2D_0 D_2) + ... \tag{2.23}$$

Then the solution is represented by the expansion:

$$x(t;\varepsilon) = \varepsilon x_1(\tau_0, \tau_1, \tau_2, ...) + \varepsilon^2 x_2(\tau_0, \tau_1, \tau_2, ...) + ..., \tag{2.24}$$

and, as usual, introducing this solution in the original equation and equating the coefficients for the different orders of ε we get a system of equation that provides the conditions that each x_k has to comply so that there are not secular terms.

This method is used in this thesis in chapter 5, in conjunction with the method of Poincaré-Lidstedt, to obtain a solution for the mesoscopic scale in the form of the Complex Ginzburg Landau Equation (introduced in section 2.1.3).

2.1.2 Delay Differential Equations

We have already mentioned in the introduction the importance of an adequate modelling of the reaction times in the mobility equations of vehicular traffic. This section gives a brief introduction to the *Delay Differentil Equations* (DDEs) based on the references [29] and [30] for the most formal aspects, and also on [66] and [16] for a more application oriented approach.

Formal definition

From [30]: If $r \geq 0$ is a real number and $C([a,b],\mathbb{R}^n)$ is the space of continuous functions mapping the interval $[a,b]$ into $\mathbb{R}^n$ with the topology of uniform convergence, we define $C = C([-r,0],\mathbb{R}^n)$. If

$$\sigma \in \mathbb{R}, \quad \text{and} \quad \mathbf{u} \in C([-\sigma - r, \sigma + A],\mathbb{R}^n), \tag{2.25}$$

then for any $t \in [\sigma, \sigma + A]$ we let $\mathbf{u}_t \in C$ be defined by $\mathbf{u}_t(\theta) = \mathbf{u}(t+\theta)$, $-r \leq \theta \leq 0$. If D is a subset of $\mathbb{R} \times C, \mathbf{f} : D \to \mathbb{R}^n$ is a given function and " $\cdot$ " denotes the right hand side derivative, we say that the relation

$$\dot{\mathbf{u}} = \mathbf{f}(t, \mathbf{u}_t) \tag{2.26}$$

is a *retarded functional differential equation* on D and will denote this equation by RFDE.

For a given $\sigma \in \mathbb{R}, \phi \in C$ we say that $\mathbf{u}(\sigma, \boldsymbol{\phi}, \mathbf{f})$ is a solution of equation (2.26) with initial value $\boldsymbol{\phi}$ at σ or simply a solution through $(\sigma, \boldsymbol{\phi})$ if there is an $A > 0$ such that $\mathbf{u}(\sigma, \boldsymbol{\phi}, \mathbf{f})$ is a solution of equation (2.26) on $[\sigma - r, \sigma + A]$ and $\mathbf{u}_\sigma(\sigma, \boldsymbol{\phi}, \mathbf{f}) = \boldsymbol{\phi}$.

This is a very general definition that includes ODEs ($r = 0$) and discrete delay differential difference equations like

$$\dot{\mathbf{u}} = \mathbf{f}(t, \mathbf{u}(t), \mathbf{u}(t - \tau_1(t)), \mathbf{u}(t - \tau_2(t)), ..., \mathbf{u}(t - \tau_p(t))). \tag{2.27}$$

In this thesis we will be interested in the case of a single, constant delay r like:

$$\dot{\mathbf{u}} = (t, \mathbf{u}(t), \mathbf{u}(t - r)), \tag{2.28}$$

which will be generically referred to as a *Delay Differential Equation* (DDE). Reference [30] contains the formal characterization of RFDEs and the conditions for existence, uniqueness and continuity of their solutions. We will provide in the following just a simple example and some comments on the Hopf bifurcation phenomenon.

A simple scalar example

Consider the following typical example of scalar DDE (as appears in [66]):

$$\frac{du}{dt} = -\alpha u(t - r), \tag{2.29}$$

where $\alpha, u \in \mathbb{R}$, which, depending on the sign of α is a positively or negatively delayed system. First we can scale the equation taking $\tau = rt$ and $\beta = \alpha r$ to get the equation

$$\frac{du}{d\tau} = -\beta u(\tau - 1). \tag{2.30}$$

This equation is linear, so, using the same method as for linear ODEs, to determine the stability of the trivial solution ($u(\tau) = 0$) we look for solutions in the form $u(\tau) = e^{\lambda\tau}$ with $\lambda \in \mathbb{C}$. Defining the linear operator L as:

$$L(u) = \frac{du}{d\tau} + \beta u(\tau - 1). \tag{2.31}$$

Then $L(e^{\lambda\tau}) = 0$ if and only if λ is a root of the *characteristic equation*

$$h(\lambda) \equiv \lambda + \beta e^{-\lambda} = 0. \tag{2.32}$$

In contrast with the linear ODEs, where there is a finite number of solutions (determining the eigenvalues and stability of the system), in this characteristic equation we have an infinite number of solutions, and therefore a much richer solution set. In fact, an analysis of the equation (2.32) reveals different behaviour depending on the value of the parameter β:

- For $\beta <= \frac{1}{e} \approx 0.37$ the solution $u(\tau)$ does not exhibit oscillations and decays exponentially to the equilibrium.
- For $\frac{1}{e} < \beta < \frac{\pi}{2}$, $u(\tau)$ is oscillatory with exponential damping towards the equilibrium.
- For $\beta = \frac{\pi}{2}$, $u(\tau)$ is oscillatory with constant amplitude.
- For $\beta > \frac{\pi}{2}$, $u(\tau)$ is oscillatory with increasing amplitude (unstable).

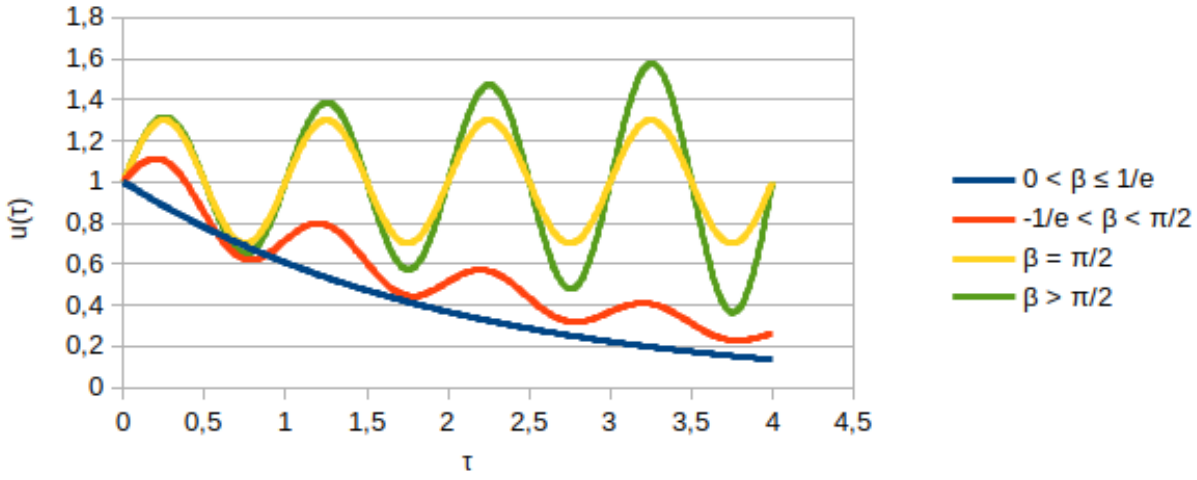


Figure 2.1: Solutions for $u(\tau)$ in the simple DDE example with initial condition $u(0) = 1$.

Figure 2.1 shows the different solutions depending on the parameter β. This simple example illustrate how the DDEs, even being linear, present significantly more challenges than their non-retarded counterparts.

The Hopf Bifurcation

The Hopf bifurcation is a phenomenon well established in the theory of ODEs, and explains the transition from equilibrium to oscillation in nonlinear ODEs when a parameter in the equation reaches a specific threshold [46]. It happens that this type of bifurcation is also observed in nonlinear DDEs. Given the relevance of the Hopf bifurcation for the results of this thesis we present in this section the Hopf Bifurcation Theorem for DDEs as outlined in [66].

We consider the one-parameter family of autonomous delay equations:

$$\mathbf{u}'(t) = \mathbf{f}(\mathbf{u}_t, r), \tag{2.33}$$

where $\mathbf{f} : C \times \mathbb{R} \to \mathbb{R}^n$ is twice continuously differentiable and $\mathbf{u} = \mathbf{0}$ is an equilibrium state for all values of r:

$$\mathbf{f}(\mathbf{0}, r) \equiv \mathbf{0}. \tag{2.34}$$

Linearizing $\mathbf{f}$ around $\mathbf{u} = 0$ yields:

$$\mathbf{f}(\mathbf{u}, r) = L(r)\mathbf{u} + \mathbf{h}(\mathbf{u}, r), \tag{2.35}$$

where $L(r) : C \to \mathbb{R}^n$ is a bounded linear operator and $\mathbf{h}$ is higher order:

$$\lim_{\mathbf{u}\to\mathbf{0}} \frac{|\mathbf{h}(\mathbf{u}, r)|}{\|\mathbf{u}\|} = 0. \tag{2.36}$$

The characteristic equation of the linear operator L is then:

$$\begin{aligned} \det(\lambda\mathbf{I} - \mathbf{A}(r, \lambda)) &= 0, \\ \mathbf{A}_{ij}(r) &= L(r)_i(\mathbf{e}_\lambda \mathbf{e}_j), \end{aligned} \tag{2.37}$$

where $\mathbf{e}_i$ is the standard basis for $\mathbb{C}^n$ and $\mathbf{e}_\lambda$ is the eigenvector of eigenvalue λ. We make the following assumptions on the eigenvalues of (2.37):

Assumption 2.1. The linear system $L(r)$ has a non-constant periodic solution for $r = r_0$, which is determined by a pair of simple imaginary roots $\pm j\omega_0$, with $\omega_0 \neq 0$, while no other root is an integer multiple of $j\omega_0$.

Assumption 2.2. By the differentiability of $\mathbf{f}$ and the implicit function theorem, there exist a continuously differentiable family of roots $\lambda(r)$ for small deviations of r_0 for which $Re(\lambda'(r)) \neq 0$, implying that the roots $\lambda(r)$ cross the imaginary axis as r varies.

The Hopf Bifurcation Theorem is formulated thus:

Theorem 2.1 (Hopf Bifurcation Theorem [66])**.** *Let assumptions 2.1 and 2.2 hold. Then there exist $\varepsilon_0 > 0$, real-valued even functions $r(\varepsilon)$ and $T(\varepsilon) > 0$ satisfying $r(0) = r_0$ and $T(0) = 2\pi/\omega_0$, and a non constant $T(\varepsilon)$-periodic function $\mathbf{p}(t, \varepsilon)$, with all functions being continuously differentiable in ε for $|\varepsilon| < \varepsilon_0$, such that $\mathbf{p}(t, \varepsilon)$ is a solution of (2.33) and $\mathbf{p}(t, \varepsilon) = \varepsilon\mathbf{q}(t, \varepsilon)$ where $\mathbf{q}(t, 0)$ is a $2\pi/\omega_0$-periodic solution of $\mathbf{q}' = L(0)\mathbf{q}$.*

Moreover, there exist $\mu_0, \beta_0, \delta > 0$ such that if (2.33) has a nonconstant periodic solution $\mathbf{u}(t)$ of period P for some r satisfying $|r - r_0| < \mu_0$ with $\max_t |\mathbf{u}(t)| < \beta_0$ and $|P - 2\pi/\omega_0| < \delta$, then $r = r(\varepsilon)$ and $\mathbf{u}(t) = \mathbf{p}(t + \theta, \varepsilon)$ for some $|\varepsilon| < \varepsilon_0$ and some θ.

If $\mathbf{f}$ is five times continuously differentiable then:

$$r(\varepsilon) = r_0 + r_1\varepsilon^2 + O(\varepsilon^4), \tag{2.38}$$

$$T(\varepsilon) = \frac{2\pi}{\omega_0}\left(1 + T_1\varepsilon^2 + O(\varepsilon^4)\right). \tag{2.39}$$

If all other eigenvalues for $\varepsilon = 0$ have strictly negative real parts except for $\pm j\omega_0$ then $\mathbf{p}(t, \varepsilon)$ is asymptotically stable if $r_1 > 0$ and unstable if $r_1 < 0$.

2.1.3 The Complex Ginzburg-Landau equation (CGLE)

The CGLE formalism is framed in the more general theory of modulation equations, which search for solutions to PDEs as modulations in space and time of a basic periodic pattern when a specific parameter surpasses a certain threshold. This theory was initially developed in the 1960s-70s to explain large scale patterns in hydrodynamic problems. From then on it has been widely used and further developed in areas as superconductivity, optics and reaction-diffusion chemical systems. The subject is also generally referred to as *pattern formation* systems, and, as such, a first comprehensive account of different theories has been provided in [10]. Useful introductions to the CGLE specifically has been given in [62], [11], [3] and [22].

The CGLE formalism search for approximate solutions near a Hopf bifurcation in nonlinear PDEs of the form:

$$\mathbf{u}_t = \mathbf{f}(\mu, \mathbf{u}, \mathbf{u}_\mathbf{x}, \mathbf{u}_\mathbf{xx}, ...), \tag{2.40}$$

where $\mathbf{u}(\mathbf{x}, t) \in \mathbb{R}^n$ is a real vector function depending on time and space, $\mathbf{f}$ is a nonlinear function, $\mathbf{x}$ is the space variable, μ is a real parameter and the subscripts denote partial derivatives. In the following we assume the space to be 1 dimensional ($\mathbf{x} = x$). It is also assumed that the equilibrium solution $\mathbf{u}(x, t) \equiv 0$ is asymptotically stable for $\mu < 0$ and the instability manifests when $\mu > 0$. The theory searches for approximate solutions that are the result of a slow time-varying scalar amplitude modulating a basic waveform periodic pattern $\mathbf{p}(x, t) = e^{j(\omega_0 t + \kappa_0 x)}\boldsymbol{\phi}_{0,\kappa_0}$:

$$\mathbf{u}(x, t, \tau) = A(\tau)e^{j(\omega_0 t + \kappa_0 x)}\boldsymbol{\phi}_{0,\kappa_0} + \overline{A}(\tau)e^{-j(\omega_0 t + \kappa_0 x)}\overline{\boldsymbol{\phi}}_{0,\kappa_0}. \tag{2.41}$$

where A is a complex scalar function of a slow time τ ($\tau << t$) that modulates the basic periodic pattern, which is the fundamental solution to the linear problem of (2.40). The CGLE formalism establishes that $A(\tau)$ is the solution to the scalar PDE:

$$\partial_\tau A = C_1 \Delta_\xi A + C_2 A + C_3 \left|A\right|^2 A, \tag{2.42}$$

where ξ is a scaled space and the C_i are complex constant determined as the result of certain solvability conditions imposed in (2.41) by equation (2.40). It is also frequent to find a rescaled version of the equation in a standard form by scaling the time and space variables:

$$\partial_\tau A = A + (1 + jb)\Delta_\xi A - (1 + jc)\left|A\right|^2 A. \tag{2.43}$$

Generally speaking, one has to see this equation as the simplest nonlinear approximation of the nonlinear equation (2.40), including just a single cubic term. Even though the CGLE is widely used and still a focus of extensive research and numerous publications, there are comparatively few sources that methodologically describe how the CGLE equation is obtained from the original PDE system. In the following we offer an outline of the general methodology to derive the CGLE based on [39], which contains a simple and easy to follow example for a reaction-diffusion system, and [47], which provides a more detailed and mathematical approach to the method. We use a notation partially based on these sources, adapting it when necessary to our notation, and closely follow the structure in [47].

Spectral assumptions

We consider the transformation of problem (2.40) separating the linear and nonlinear parts:

$$\mathbf{u}_t = L(\mu, \partial_x)\mathbf{u} + NL(\mu, \partial_x, \mathbf{u}), \tag{2.44}$$

where L is a linear differential operator in the space variable x and NL are the nonlinear terms satisfying $NL(\mu, \partial_x, \varepsilon\mathbf{u}) = O(\varepsilon^2)$. Inserting the exponential solution $\mathbf{v}(x,t) = e^{j\kappa x + \lambda t}\boldsymbol{\phi}$ in the linear part of (2.44) we obtain the spectral problem:

$$\lambda\boldsymbol{\phi} = \mathbf{L}(\mu, \kappa)\boldsymbol{\phi}, \tag{2.45}$$

with λ the eigenvalues, $\mathbf{L}(\mu,\kappa)$ the matrix and $\boldsymbol{\phi}$ the eigenvectors associated to the linear operator $L(\mu, \partial_x)$. The general situation leading to the CGLE can be characterized as follows:

There exist $\delta, \gamma > 0$, $\kappa_0 \in \mathbb{R}$ and eigenvalues $\lambda : (-\delta, \delta) \times (\kappa_0 - \delta, \kappa_0 + \delta) \to \mathbb{C}$ such that for all $\mu \in (-\delta, \delta)$ the spectrum of $\mathbf{L}(\mu,\kappa)$ satisfies the following:

1. *For $\kappa \notin (-\kappa_0 - \delta, -\kappa_0 + \delta) \cup (\kappa_0 - \delta, \kappa_0 + \delta)$ we have $\mathrm{spec}(\mathbf{L}(\mu,\kappa)) \subset \{\Re(\sigma) \leq \gamma\}$.*
2. *For $\kappa \in (\kappa_0 - \delta, \kappa_0 + \delta)$ we have $\mathrm{spec}(\mathbf{L}(\mu,\kappa)) = \{\lambda(\mu,\kappa)\} \cup S_s(\mu,\kappa)$ with $S_s(\mu,\kappa) \subset \{\Re(\sigma) \leq \gamma\}$ and $\lambda(\mu,\kappa)$ is an algebraically simple eigenvalue with the expansion*

$$\lambda(\mu,\kappa) = \lambda_0(\mu) + \lambda_1(\mu)(\kappa - \kappa_0) + \Lambda(\mu)(\kappa - \kappa_0)^2 + ... \tag{2.46}$$

3. *We have $\Re(\lambda_0(0) = 0)$, $d/d\mu\Re(\lambda_0)(0) = 0$, $\Re(\lambda_1(0)) = 0$ and $\Re(\Lambda(0)) > 0$.*

$S_s(\mu,\kappa)$ is the stable part of the spectrum of $\mathbf{L}(\mu,\kappa)$. These conditions guarantee that $\Re(\lambda(0,\kappa) \leq 0)$ with equality only for κ_0. We also will use the symbols:

$$\lambda_{0,1} = \frac{d}{d\mu}\lambda_0(0) \in \mathbb{C}, \quad c_g = -j\lambda_1(0) \in \mathbb{R} \quad \text{and} \quad \Lambda_0 = \Lambda(0). \tag{2.47}$$

The parameter c_g is the group velocity of the basic pattern $\mathbf{p}(x,t)$. The general situation for which we will calculate the CGLE is $\kappa_0 \neq 0$ and $\lambda(0,\kappa_0) = j\omega_0$ with $\omega_0 > 0$, which correspond to traveling waves solutions.

The linear part (dispersion)

The linear part of the CGLE corresponds to the dispersion term in (2.42) and is calculated considering the solution to the linear problem $\mathbf{v}(x,t) = e^{j\kappa x + \lambda(\mu,\kappa)t}\boldsymbol{\phi}_{\mu,\kappa}$, which verifies:

$$\partial_t\mathbf{v} = L(\mu, \partial_x)\mathbf{v} = \lambda(\mu,\kappa)\mathbf{v}. \tag{2.48}$$

When we are close to the bifurcation $(\mu,\kappa) \approx (0,\kappa_0)$, we use the parameter scaling:

$$\mu = \varepsilon^2 \quad \text{and} \quad \kappa = \kappa_0 + \varepsilon\nu \quad \text{with} \quad 0 < \varepsilon \ll 1, \tag{2.49}$$

which, using (2.46), leads to

$$\lambda(\varepsilon^2, \kappa_0 + \varepsilon\nu) = j\omega_0 + \varepsilon^2\lambda_{0,1} - \varepsilon j c_g\nu - \varepsilon^2\Lambda_0\nu^2 + O(\varepsilon^3). \tag{2.50}$$

Then the solution $\mathbf{v}$ in (2.48) can be written

$$\mathbf{v}(x,t) = e^{\left(\lambda_{0,1}-\Lambda_0\nu^2\right)\varepsilon^2 t + j\varepsilon(x-c_g t)\nu + O(\varepsilon^3)} e^{j(\omega_0 t+\kappa_0 x)} \boldsymbol{\phi}_{\varepsilon^2,\kappa_0+\varepsilon\nu}. \tag{2.51}$$

The second factor in the right-hand-side of this equation is approximately the basic periodic pattern $\mathbf{p}(x,t) = e^{j(\omega_0 t+\kappa_0 x)}\boldsymbol{\phi}_{0,\kappa_0}$, while the first factor depens only on the slow time variable and the large space variable:

$$\tau = \varepsilon^2 t, \quad \xi = \varepsilon(x - c_g t). \tag{2.52}$$

Notice that the large space scaling is done with respect to the frame of reference relative to the group velocity c_g. If we define the parabolic equation:

$$\partial_\tau B = \Lambda_0 \Delta_\xi B + \lambda_{0,1} B, \tag{2.53}$$

with $B(\xi,\tau) \in \mathbb{C}$, we find that it has the general solution

$$B(\xi,\tau) = \int_{\nu\in\mathbb{R}} e^{j\nu\xi} e^{(\lambda_{0,1}-\Lambda_0\nu^2)\tau} f(\nu) dm(\nu), \tag{2.54}$$

where m is a complex-valued Radon measure on $\mathbb{R}$. Thus,we expect that the modulation ansatz

$$\mathbf{v}(x,t) = B(\varepsilon(x-c_g t), \varepsilon^2 t)\mathbf{p}(x,t) + \overline{B}(\varepsilon(x-c_g t), \varepsilon^2 t)\overline{\mathbf{p}}(x,t). \tag{2.55}$$

approximates solutions to (2.48) whenever B satisfies (2.53).

The nonlinear part (modulation)

To determine the nonlinear part of equation (2.42) the perturbation methods introduced in section 2.1.1 are used. We start from an approximation of the periodic solution to equation (2.44) in the form given by the strained coordinates method:

$$\mathbf{u}(x,t) = \varepsilon\mathbf{u}_1(x,t) + \varepsilon^2\mathbf{u}_2(x,t) + \varepsilon^3\mathbf{u}_3(x,t) + ... \tag{2.56}$$

We will assume that the expansion is based on a basic periodic pattern $\mathbf{p}(x,t) = e^{j(\omega_0 t+\kappa_0 x)}\boldsymbol{\phi}_{0,\kappa_0}$. We will denote $E(x,t) = e^{j(\omega_0 t+\kappa_0 x)}$ and therefore $\mathbf{p}(x,t) = E(x,t)\boldsymbol{\phi}_{0,\kappa_0}$. In the proximity of the bifurcation we expect that the basic pattern predominates and is modulated by the slow-time amplitude, so $\mathbf{u}_1(x,t) = A(\tau)\mathbf{p}(x,t) + c.c.$, where *c.c.* stands for *complex conjugate*. We also expect that the nonlinearities will generate higher harmonics of the basic pattern in the form $\varepsilon^l E^m$. This way, we create the ansatz:

$$\begin{aligned}\mathbf{u}(x,t) =& \varepsilon(A(\tau)E(x,t)\boldsymbol{\phi}_{0,\kappa_0} + c.c.) + \varepsilon^2 \sum_{l=-1}^{1} E^{2l}\boldsymbol{\psi}_{2l}(\tau) \\ &+ \varepsilon^3 \sum_{l=-2}^{1} E^{2l+1}\boldsymbol{\psi}_{2l+1}(\tau) + O(\varepsilon^4).\end{aligned} \tag{2.57}$$

with the only dependence in x occurring in $E(x,t)$, while the amplitude A and the vectors $\boldsymbol{\psi}_m$ depend only on the slow time τ. We now need to introduce this ansatz in both sides of

equation (2.44) and equate the terms with the same expansion order $\varepsilon^l E^m$, so we need to expand the linear and nonlinear parts in the following way:

$$\begin{aligned} L(\varepsilon^2, \partial_x) E^m \boldsymbol{\psi} &= E^m \mathbf{L}(\varepsilon^2, m\kappa_0)\boldsymbol{\psi} \\ NL(0, \partial_x, \varepsilon \sum_{-J}^{J} E^m \boldsymbol{\psi}_m) &= \varepsilon^2 \sum_{l,m=-J}^{J} E^{l+m} \mathbf{M}_{l,m}(\boldsymbol{\psi}_l, \boldsymbol{\psi}_m) + \\ &\quad \varepsilon^3 \sum_{l,m,n=-J}^{J} E^{l+m+n} \mathbf{N}_{l,m,n}(\boldsymbol{\psi}_l, \boldsymbol{\psi}_m, \boldsymbol{\psi}_n) + O(\varepsilon^4), \end{aligned} \tag{2.58}$$

where $\mathbf{M}_{l,m}$ and $\mathbf{N}_{l,m,n}$ are the bilinear and trilinear forms (symmetric with respect to the order of arguments and indices) that stem from the series expansion of the nonlinear part of (2.44), NL.

Then, introducing (2.57) in (2.44), and using the expressions in (2.58) we obtain an equation for each expansion order $\varepsilon^l E^m$. We include here the equations for $m \geq 0$ since the equation for $m < 0$ are just the complex conjugate of the positive one:

- $\varepsilon^1 E^1$:

$$j\omega_0 A \boldsymbol{\phi}_{0,\kappa_0} = j\omega_0 A \boldsymbol{\phi}_{0,\kappa_0}. \tag{2.59}$$

  This is just the verification that the basic pattern $\mathbf{p}(x,t)$ is the solution to the linear equation (2.48) for $\mu = 0$.

- $\varepsilon^2 E^0$:

$$0\boldsymbol{\psi}_0 = \mathbf{L}(0,0)\boldsymbol{\psi}_0 + |A|^2 \, 2\mathbf{M}_{1,-1}(\boldsymbol{\phi}_{0,\kappa_0}, \overline{\boldsymbol{\phi}}_{0,\kappa_0}). \tag{2.60}$$

  This equation yields the component $\boldsymbol{\psi}_0$ as:

$$\boldsymbol{\psi}_0(\tau) = |A(\tau)|^2 \, \mathbf{w}_0, \tag{2.61}$$

$$\mathbf{w}_0 = 2\mathbf{L}(0,0)^{-1}\mathbf{M}_{1,-1}(\boldsymbol{\phi}_{0,\kappa_0}, \overline{\boldsymbol{\phi}}_{0,\kappa_0}). \tag{2.62}$$

  Notice that this component may introduce a constant "drift" of the average of the periodic solution $\mathbf{u}(x,t)$ from the equilibrium solution $\mathbf{u} \equiv 0$ when $\mu > 0$. We will see in later chapters that this drift may have an important impact in the stability of the traffic process.

- $\varepsilon^2 E^2$:

$$2j\omega_0 \boldsymbol{\psi}_2 = \mathbf{L}(0, 2\kappa_0)\boldsymbol{\psi}_2 + A^2 \mathbf{M}_{1,1}(\boldsymbol{\phi}_{0,\kappa_0}, \boldsymbol{\phi}_{0,\kappa_0}). \tag{2.63}$$

  This equation yields the first harmonic component $\boldsymbol{\psi}_2$ as:

$$\boldsymbol{\psi}_2(\tau) = A^2(\tau)\mathbf{w}_2, \tag{2.64}$$

$$\mathbf{w}_2 = (2j\omega_0 \mathbf{I} - \mathbf{L}(0, 2\kappa_0))^{-1} \mathbf{M}_{1,1}(\boldsymbol{\phi}_{0,\kappa_0}, \boldsymbol{\phi}_{0,\kappa_0}), \tag{2.65}$$

  where $\mathbf{I}$ is the identity matrix.

- $\varepsilon^3 E^1$:

$$\begin{aligned}\partial_\tau A\boldsymbol{\phi}_{0,\kappa_0} + j\omega_0\boldsymbol{\psi}_1 =&\lambda_{0,1}A\boldsymbol{\phi}_{0,\kappa_0} + \mathbf{L}(0,\kappa_0)\boldsymbol{\psi}_1 \\ &+ A2\mathbf{M}_{1,0}(\boldsymbol{\phi}_{0,\kappa_0},\boldsymbol{\psi}_0) + \overline{A}2\mathbf{M}_{2,-1}(\boldsymbol{\psi}_2,\overline{\boldsymbol{\phi}}_{0,\kappa_0}) \\ &+ |A|^2 A3\mathbf{N}_{1,1,-1}(\boldsymbol{\phi}_{0,\kappa_0},\boldsymbol{\phi}_{0,\kappa_0},\overline{\boldsymbol{\phi}}_{0,\kappa_0}).\end{aligned} \tag{2.66}$$

  Finally this is the equation that will deliver the CGLE. Reordering the equation as:

$$(\mathbf{L}(0,\kappa_0) - j\omega_0)\boldsymbol{\psi}_1 =(\partial_\tau A - \lambda_{0,1}A)\boldsymbol{\phi}_{0,\kappa_0} - |A|^2 A\boldsymbol{\psi}_*, \tag{2.67}$$

  with

$$\boldsymbol{\psi}_* = 2\mathbf{M}_{1,0}(\boldsymbol{\phi}_{0,\kappa_0},\mathbf{w}_0) + 2\mathbf{M}_{2,-1}(\mathbf{w}_2,\overline{\boldsymbol{\phi}}_{0,\kappa_0}) + 3\mathbf{N}_{1,1,-1}(\boldsymbol{\phi}_{0,\kappa_0},\boldsymbol{\phi}_{0,\kappa_0},\overline{\boldsymbol{\phi}}_{0,\kappa_0}), \tag{2.68}$$

  we must notice that, given that $j\omega_0$ is an algebraically simple eigenvalue of $\mathbf{L}(0,\kappa_0)$, equation (2.66) will be solvable if and only if its right hand side is orthogonal to the eigenvector $\boldsymbol{\phi}^*_{0,\kappa_0}$ of the adjoint of $\mathbf{L}(0,\kappa_0)$. This is normally referred to as the *solvability condition*.

  If we select $\boldsymbol{\phi}^*_{0,\kappa_0}$ so that $\left\langle \boldsymbol{\phi}_{0,\kappa_0}, \boldsymbol{\phi}^*_{0,\kappa_0} \right\rangle = 1$, then the solvability condition can be expressed as:

$$\partial_\tau A - \lambda_{0,1}A - \eta |A|^2 A = 0, \tag{2.69}$$

  with $\eta = \left\langle \boldsymbol{\psi}_*, \boldsymbol{\phi}^*_{0,\kappa_0} \right\rangle$. This is the expression of the nonlinear part of the CGLE.

.

Complete CGLE and scaling

Joining the linear part (2.53) and the nonlinear part (2.69), we get the non scaled version of the CGLE:

$$\partial_\tau A = \Lambda_0\Delta_\xi A + \lambda_{0,1}A + \eta |A|^2 A.$$

In the literature it is customary to call $\gamma = -\eta$ to get the more usual form:

$$\partial_\tau A = \Lambda_0\Delta_\xi A + \lambda_{0,1}A - \gamma |A|^2 A. \tag{2.70}$$

To obtain the most standard form of the equation, the following scaling is usually employed:

$$\begin{aligned}\tilde{\tau} &= \Re(\lambda_{0,1})\tau, \\ \tilde{\xi} &= \sqrt{\frac{\Re(\lambda_{0,1})}{\Re(\Lambda_0)}}\xi, \\ \tilde{A} &= \sqrt{\frac{|\Re(\gamma)|}{\Re(\lambda_{0,1})}}e^{j\Im(\lambda_{0,1})\tau}A.\end{aligned}$$

Dropping the tildes in the variable names, and assuming $\Re(\gamma) > 0$, this yields the standard equation:

$$\partial_\tau A = A + (1+jb)\Delta_\xi A - (1+jc)|A|^2 A, \tag{2.71}$$

with $b = \Im(\Lambda_0)/\Re(\Lambda_0)$ and $c = \Im(\gamma)/\Re(\gamma)$.

Linear stability of the CGLE

First, we have to note that the criticality of the Hopf bifurcation is determined by the coefficient of the nonlinear term γ in (2.70):

- If $\Re(\gamma) \geq 0$ then the bifurcation is *supercritical* and the solution is stable. This yields the form of the CGLE in (2.71).
- If $\Re(\gamma) < 0$ then the bifurcation is *subcritical* and the solution is unstable. In this case, the sign of the coefficient of the nonlinear term must be changed, i.e.:

$$\partial_\tau A = A + (1 + jb)\Delta_\xi A + (1 + jc)\left|A\right|^2 A. \tag{2.72}$$

In the case of the supercritical bifurcation, traveling waves of the modulating amplitude A are specific solutions of the equation (2.71). We reproduce here a simple account of the plane waves solutions in uni-dimensional space included in [39]. For stability in higher dimensional spaces one can find results in [3] and [33].

Equation (2.71) has solutions of the form:

$$A_Q = a_Q e^{j(\omega_Q + Q\xi)\tau}, \tag{2.73}$$

with

$$|a_Q| = 1 - Q^2, \tag{2.74}$$
$$\omega_Q = -c + (c - b)Q^2, \tag{2.75}$$

where Q is the wavenumber (in the scaled space ξ). This can be checked inserting (2.73) in (2.71).

The stability of these waves is also studied in [22]:

- There will be instability (i.e. sustained plane waves) if

$$1 + bc < 0. \tag{2.76}$$

  The line $1 + bc = 0$ is denominated the *Benjamin-Feir* instability line.

- The range of wavenumbers of these oscillations is:

$$0 < |Q| < \left(\frac{1 + bc}{3 + bc + 2c^2}\right)^{\frac{1}{2}}. \tag{2.77}$$

2.1.4 The Wirtinger derivative

Given that in Chapter 5 we will need to manage a real valued functions as the sum of a complex valued one plus its conjugate, we introduce here the Wirtinger derivative formalism, which, although extensively used in some engineering fields, is rarely explicitly stated or justified. We will follow in this brief introduction the references [18, 34, 38].

We consider a function $f : \mathbb{C} \ni z = a + jb \mapsto f(z) = u(a, b) \in \mathbb{R}$. This function $f(z)$ will be, in general, not holomorphic, since Cauchy-Riemann requires in this case that $\partial u/\partial a = \partial u/\partial b = 0$, and that only holds for a real constant. One could, in principle, manage the function as a real multivariate function, applying its partial derivatives $\partial u/\partial a$ and $\partial u/\partial b$ when necessary, but, in case that f is a nontrivial function that involves intricate operations with z and $\bar{z}$ in the complex domain, this becomes increasingly cumbersome. To manage this efficiently Wilhelm Wirtinger introduced in 1927 a special partial differential operators on $f(z, \bar{z})$ that behaves in a very similar way to ordinary derivatives respect to real variables.

The Wirtinger derivatives (here denoted by ∂_w) of a complex function $f(z, \bar{z})$ with respect to the complex variables z and $\bar{z}$ are defined as follows:

$$\frac{\partial_w f(z,\bar{z})}{\partial_w z} = \frac{1}{2}\left(\frac{\partial f}{\partial \Re(z)} - j\frac{\partial f}{\partial \Im(z)}\right),$$
$$\frac{\partial_w f(z,\bar{z})}{\partial_w \bar{z}} = \frac{1}{2}\left(\frac{\partial f}{\partial \Re(z)} + j\frac{\partial f}{\partial \Im(z)}\right).$$

It is usual to encounter this operators in the literature in the same notation as the complex partial derivatives (i.e $\partial/\partial z$), but we remark with the subindex the special character of the operator.

The great advantage of using this formalism is that we can treat z and $\bar{z}$ as independent variables when using these derivatives applying the rules of real calculus, in particular:

$$\frac{df(z(t),\bar{z}(t))}{dt} = \frac{\partial_w f}{\partial_w z}\frac{dz}{dt} + \frac{\partial_w f}{\partial_w \bar{z}}\frac{d\bar{z}}{dt}.$$

Moreover, when $f(z)$ is complex analytic at a point, its Wirtinger derivative ($\partial_w f/\partial_w z$) agrees with its complex derivative df/dz. Additionally, Wirtinger derivatives have the following properties:

- Linearity:

$$\frac{\partial_w}{\partial_w z}(\alpha f + \beta g) = \alpha\frac{\partial_w f}{\partial_w z} + \beta\frac{\partial_w g}{\partial_w z},$$
$$\frac{\partial_w}{\partial_w \bar{z}}(\alpha f + \beta g) = \alpha\frac{\partial_w f}{\partial_w \bar{z}} + \beta\frac{\partial_w g}{\partial_w \bar{z}}.$$

- Product rule:

$$\frac{\partial_w}{\partial_w z}(f \cdot g) = \frac{\partial_w f}{\partial_w z}g + \frac{\partial_w g}{\partial_w z}f,$$
$$\frac{\partial_w}{\partial_w \bar{z}}(f \cdot g) = \frac{\partial_w f}{\partial_w \bar{z}}g + \frac{\partial_w g}{\partial_w \bar{z}}f.$$

- Chain rule:

$$\frac{\partial_w f(g(z,\bar{z}),\bar{g}(z,\bar{z}))}{\partial_w z} = \frac{\partial_w f}{\partial_w g}\frac{\partial_w g}{\partial_w z} + \frac{\partial_w f}{\partial_w \bar{g}}\frac{\partial_w \bar{g}}{\partial_w z},$$
$$\frac{\partial_w f(g(z,\bar{z}),\bar{g}(z,\bar{z}))}{\partial_w \bar{z}} = \frac{\partial_w f}{\partial_w g}\frac{\partial_w g}{\partial_w \bar{z}} + \frac{\partial_w f}{\partial_w \bar{g}}\frac{\partial_w \bar{g}}{\partial_w \bar{z}}. \tag{2.78}$$

This formalism can be extended to vector functions. In the case of a vector function $\mathbf{f}(\mathbf{z}) \in \mathbb{C}^m$, with $\mathbf{z} = (z_1, z_2, ..z_n) \in \mathbb{C}^n$ we define a "Wirtinger Jacobian" as:

$$\mathbb{WJ}_{\mathbf{z}}\mathbf{f} = \begin{pmatrix} \frac{\partial_w f_1}{\partial_w z_1} & \dots & \frac{\partial_w f_1}{\partial_w z_n} \\ \dots & & \\ \frac{\partial_w f_m}{\partial_w z_1} & \dots & \frac{\partial_w f_m}{\partial_w z_n} \end{pmatrix}. \tag{2.79}$$

This formalism will be extremely useful in the calculations of stability at the mesoscopic scale in Chapter 5.

2.2 Models for vehicular traffic dynamics

Since the early 20th century, when automotive traffic gained importance as one of the cornerstones of modern economies, there has been increasing interest in the mathematics and physics community to study and characterize the traffic process as a physical system obeying predictable laws. Vehicular traffic was seen either as a multi-particle system or as a continuous flow whose features resemble well known physical systems, and were therefore amenable to be studied using existing mathematical techniques employed in modern physics [48].

Many road traffic studies are focused on the determination of the conditions that generate congestion and traffic jams, for which it is usually used the so-called *fundamental diagram*, which related the vehicle density ρ with the density current (flow) q, as shown in Figure 2.2 from [48]. The traffic transition from *free traffic* at low densities to *congested traffic* at high densities.

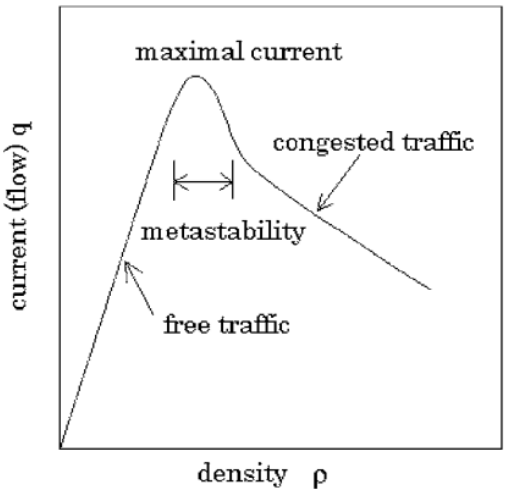


Figure 2.2: Fundamental diagram relating the vehicle density ρ with the density current (flow) q (source: [48]).

Three main techniques are usually used to perform these analysis: *microscopic models*, where traffic is seen as individual interacting particles, *macroscopic models*, where traffic is seen as a

compressible fluid, and *cellular automata* models, which simplifies the microscopic approach by discretizing the time and space dimensions and representing the vehicle interactions with simple rules. We will focus on continuous time models, so the relevant models for us will be the microscopic and macroscopic models. The cellular automata model is a discrete time approximation and will be briefly covered for completeness.

2.2.1 General overview of microscopic car-following models

In road traffic studies the microscopic models regard the traffic process as a dynamical system governed by the interaction of individual particles (i.e., the vehicles). All microscopic models rely on determining the reaction of a specific vehicle (normally, the acceleration) as a function of some variables that describe the surrounding conditions (normally, the dynamics of the surrounding vehicles). In general terms, the driver responds to a given stimulus as:

$$\text{Response} = \alpha \cdot \text{Stimulus} \quad , \tag{2.80}$$

where α is a proportionality factor to respond to the stimulus. The stimulus function can be based on many factors: distance, speed, relative speed, etc. As we have seen in section 1, the factor α usually consider some kind of reaction time of the following driver. In the existing models this is the usual way to consider the reaction times, instead of doing it in terms of Retarded Functional Differential Equation (RFDE) [29], which we will do in the following chapters.

The most important class of microscopic models are the $car - following$ models (sometimes referred too as *follow-the-leader* models), where the acceleration of a vehicle depends on the dynamics of the preceding vehicle. These models started to appear in the 1950's, and were developed by Herman et al. at the General Motors (GM) Research Laboratories. These models evolved significantly in the following decades, and [61] provides a good summary of the historical evolution. A summary of the main features for the most important ones follows.

Linear model

The simplest approach proposed by the GM team in 1958 [9] was to consider as the stimulus the difference in speed of the two vehicles, assessed by the driver of vehicle n after some reaction time r_n. If we denote by y_n the position of vehicle n, the difference between its position and that of the preceding vehicle $n+1$ is $(y_{n+1} - y_n)$ and the difference between their respective velocities is $(y'_{n+1} - y'_n)$. Then, the change in acceleration of the follower after the reaction time would be:

$$y''_n(t + r_n) = \alpha(y'_{n+1}(t) - y'_n(t)) \quad , \tag{2.81}$$

where we can see this as a simple RFDE.

This initial model was used to perform a first stability analysis. If we rescale the time variable as $t^* = \frac{t}{r_n}$, (2.81) simplifies to:

$$y''_n(t^* + 1) = C(y'_{n+1}(t^*) - y'_n(t^*)) \quad , \tag{2.82}$$

where $C = \alpha r_n$. Introducing a moving coordinate system for both vehicles such that $s(t) = y_{n+1}(t) - y_n(t)$, and considering the leader velocity as v_0, we can transform (2.82):

$$s''(t^*) = Cs'(t^* - 1) \quad . \tag{2.83}$$

This equation is the same as the one introduced in the simple example of DDE in section 2.1.2, in which we introduced characteristic equation:

$$\lambda - Ce^{-\lambda} = 0 \quad . \tag{2.84}$$

We reproduce the stability limiting values introduced in section 2.1.2 in terms of the parameter $\alpha = \dfrac{C}{r_n}$ (see also [16]):

- For $\alpha <= \frac{1}{e \cdot r_n} \approx \frac{0.37}{r_n}$ the follower does not exhibit oscillations in $s'(t)$.
- For $\frac{1}{e \cdot r_n} < \alpha < \dfrac{\pi}{2}$, $s'(t)$ is oscillatory with exponential damping.
- For $\alpha = \dfrac{\pi}{2}$, $s'(t)$ is oscillatory with constant amplitude.
- For $\alpha > \dfrac{\pi}{2}$, $s'(t)$ is oscillatory with increasing amplitude (unstable).

While this model has been useful to set the path for following models and provide some insights regarding stability, it still fell short of explaining the traffic process as a steady state flow. The linear nature of the relationship does not explain the more complex relationship between density (ρ) and flow ($q = v \cdot \rho$) in figure 2.2 [61]. Thus, more sophisticated, nonlinear models have been proposed as an evolution of the linear model.

General Motors (GM) model

Subsequent proposals from the GM Research Group considered a non constant reactivity parameter α so that the microscopic equations could explain the nonlinear dependence of the density ρ and the flow q (the *fundamental diagram* in figure 2.2).

In [23] an improvement is proposed, such that the dependence of the acceleration is modulated by considering the reactivity as inversely proportional to the separation of the vehicles. i.e.:

$$y_n''(t + r_n) = \alpha \frac{(y_{n+1}'(t) - y_n'(t))}{(y_{n+1}(t) - y_n(t))} \quad , \tag{2.85}$$

which yields the relationship between the density ρ and the velocity v:

$$v = \alpha \cdot \log(\frac{\rho_{max}}{\rho}) \quad , \tag{2.86}$$

where ρ_{max} is the maximum vehicle density (bumper-to-bumper concentration).

This approach, though explains in a better way the nonlinearity of flow and density relation, still provides unrealistic values in certain conditions: in the case of very low concentration of vehicles, the velocity in (2.86) can reach arbitrarily high values.

As a solution, a general nonlinear car-following model was proposed in [24], where an additional dependency on the velocity of the follower vehicle:

$$y_n''(t+r_n) = \alpha \frac{y_n'(t)^m}{(y_{n+1}(t) - y_n(t))^l}(y_{n+1}'(t) - y_n'(t)) \quad . \tag{2.87}$$

This formula can model different degrees of influence of the variables by means of the exponents m and l, and extensive work in search of the optimal combination has been done in the past (see for instance a summary in [56]). In Figure 2.3 a comparison between the fundamental diagram generated by different values of the exponent l is reproduced from the original sourde. The general relationship between the velocity v and the density ρ is [31] :

$$v = v_f \left(1 - \left(\frac{\rho}{\rho_{max}}\right)^{l-1}\right)^{\frac{1}{1-m}} \quad , \tag{2.88}$$

where v_f is the *free traffic* velocity (maximum velocity when $\rho \to 0$).

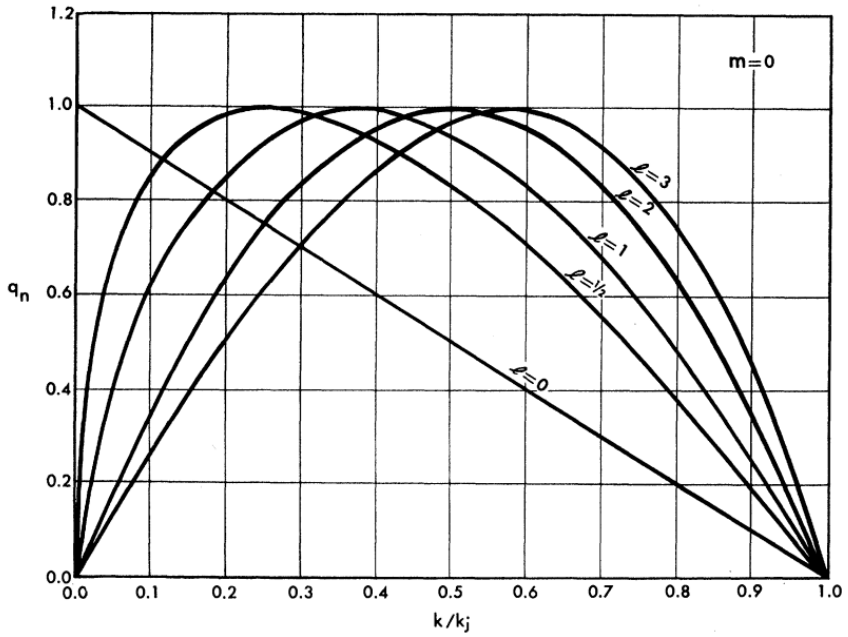


Figure 2.3: Relationship of flow (in graph q_n) and density (in graph $\frac{k}{k_j} \equiv \frac{\rho}{\rho_{max}}$) for $m = 0$ and different values of l (Source: [24])

In any case, these models, despite accurately represent real world situations and explain some important traffic dynamics, allow the vehicles to be arbitrarily close when both have the same velocity, which is unrealistic when such velocity is high.

The Optimal Velocity Model (OVM)

An alternative approach called the Optimal Velocity Model (OVM) was introduced in [53] to model a behaviour in which the follower adjust its velocity according to an optimal velocity, which is a function V of the distance between the vehicles, i.e.:

$$y'_n(t + r_n) = V(y_{n+1}(t) - y_n(t)) = V(\Delta y_n(t)) \quad , \tag{2.89}$$

where V is nonlinear and has to be monotonically increasing and has to have a maximum value. In this way:

$$y''_n(t + r_n) = V'(\Delta y_n(t))(y'_{n+1}(t) - y'_n(t)) \quad . \tag{2.90}$$

This approach does modulate the velocity depending on the distance, and presents the advantage of being easily tractable analytically. With this model, Newell integrated in a single theory the results from previous linear car-following models and the nonlinear phenomena observed in macroscopic continuous models, including the formation of shock waves.

A proposal for the optimal velocity that has been widely used in the literature is introduced in [4]:

$$V(\Delta y_n(t)) = \frac{v_{max}}{2}(\tanh(\Delta y_n(t) - d_c) - \tanh(d_c)) \quad , \tag{2.91}$$

where v_{max} is the maximum velocity achievable by the vehicles, and d_c is the equilibrium (safety) distance. Generally, a sigmoidal function that provides the inflection point at d_c is suitable to be used in this model. It is important to have this inflection point to obtain robust density waves that represent traffic jam with this model [48].

In [4] it was also introduced a simple approximation of the acceleration function to remove the implicit dependency on the delay, by means of Taylor series expansion:

$$y'_n(t + r_n) = y'_n(t) + r_n \cdot y''_n(t) + O(t^2) \quad . \tag{2.92}$$

So, using equation (2.89):

$$V(\Delta y_n(t)) = y'_n(t) + r_n \cdot y''_n(t) + O(t^2) \quad , \tag{2.93}$$

and finally:

$$y''_n(t) \approx \frac{1}{r_n}(V(\Delta y_n(t)) - y'_n(t)) \quad . \tag{2.94}$$

Nevertheless, the assumption behind equation (2.90) is that the vehicle always can change the velocity to the optimal one in time r_n, regardless of the present value of the velocity $y'_n(t)$. This allow for extremely high values for the acceleration function in certain circumstances, which is rather unrealistic.

The stability analysis of this model is provided in [48]. Applying linear stability analysis to a uniform traffic flow, it is determined that the stability condition of the system is:

$$r_n < \frac{1}{2V'(d_c)} \quad . \tag{2.95}$$

It is important to note that this stability condition, that refers to a multi-vehicle situation, is applicable to the mesoscopic scale introduced in Section 1.2.

The Intelligent Driver Model (IDM)

The Intelligent Driver Model (IDM) is a car-following model introduced in 1999 by Treiber et al. [69, 68, 36, 70] that adressed some of the shortcomings of the previously proposed microscopic models. The model uses an acceleration function that is dependent on the distance s, the speed of the vehicle v, and the relative velocity with respect to the preceeding vehicle $s' = v_l - v$, and it complies with a set of *first principles* that any complete model must fulfill:

- The acceleration is a strictly decreasing function of speed v.
- The acceleration is an increasing function of the distance s.
- The acceleration is an increasing function of the speed of the leading vehicle v_l.
- There is a minimum gap s_{min} (bumper-to-bumper distance).

In addition, the IDM has this specific characteristics:

- The equilibrium distance is not less than a safe distance $s_{min} + vT$, where T is the time gap to the leading vehicle.
- An intelligent braking strategy is implemented:
  - Te deceleration is "soft", such that it increases gradually to a comfortable value b and decreases smoothly to 0 when reaching a steady state.
  - In a critical situation, the value b may be exceeded until the danger is averted.
- The transition between driving states must be smooth, so the derivative of the acceleration function is finite at all times.

Different versions of the model have been introduced in the recent years, to finally reach the most recent version of the IDM acceleration equation in [70]:

$$v'(s, s', v) = a \left[1 - \left(\frac{v}{v_d} \right)^{\delta} - \left(\frac{s_{min} + \max\left(0, vT + \frac{vs'}{2\sqrt{ab}}\right)}{s} \right)^2 \right]. \tag{2.96}$$

The second term inside the brackets implements the convergence to a desired velocity v_d, and the third term implements the convergence to the desired distance $s_{min} + vT$ and the intelligent braking strategy with the term $\frac{vs'}{2\sqrt{ab}}$.

The IDM has demonstrated to reproduce realistic situations and explains very well the fundamental diagram in single lane traffic scenarios. It has been evaluated extensively in the cited references, mostly by means of simulation techniques, and at the moment of writing is extensively used in vehicular traffic research.

In steady state homogeneous traffic (all vehicles behaving according to the same IDM), the vehicles will stay in an equilibrium distance

$$s_{eq} = s_{min} + T v_d, \tag{2.97}$$

and equation (2.96) determines an equilibrium velocity v_0 that is the solution to the equation

$$s_{eq} = \frac{s_{min} + T v_0}{\sqrt{1 - \left(\frac{v_0}{v_d}\right)^{\delta}}}. \tag{2.98}$$

resulting in a value $v_0 < v_d$.

Notice that equation (2.96) is a non retarded equation. In [70] it is mentioned that this model describes more closely the characteristics of semi-automated driving y adaptive cruise control, but to capture human aspects and reaction time it is necessary to model with DDEs, that are more unstable. Some numerical examples are given on the impact of reaction times, but not analytical results are given. In next chapters we will apply the analytical techniques introduced in this thesis to the IDM.

The new DDE model (nDDE)

As a way to overcome the limitations of existing models referred above, a more recent car-following model has been proposed in ([1, 56]). This model complies with the main requirements used in the previous models (dependence on the distance and the relative velocity, compliance with the first principles detailed in the Section on the IDM, realistic values for the physical magnitudes) but, most importantly, it includes in the model the delay due to reaction time due to the driver, the vehicle or any other cause.

The model similarly focuses on the case of two vehicles (denoted now as 0 for the leading car and -1 for the following car). We also consider that the leading car has a constant velocity $y_0'(t) = v_0$, and we define the new variables $s(t)$ for the distance between the cars and $s'(t)$ for the relative velocity:

$$s(t) = (y_0(t) - y_{-1}(t)) \quad , \tag{2.99}$$

$$s'(t) = (v_0 - y_{-1}'(t)) \quad . \tag{2.100}$$

We then have:

$$s''(t) = (-y_{-1}''(t)) \quad . \tag{2.101}$$

So, we can express the retarded dependence of the acceleration function (like in equations (2.87) and (2.90)) in a general way as:

$$-s''(t+\tau) = y_{-1}''(t+r) = g(s(t), s'(t)) \quad , \tag{2.102}$$

where g is some function that has to fulfill the following requirements:

i.) We must avoid $y_0(t) - y_{-1}(t) = 0$, so for any v_0 it is defined an m, minimum distance between cars. In equilibrium, the two cars will be at a distance m, cruising at the same speed, and the acceleration $y''_{-1}(t) = 0$.

ii.) There is a maximum acceleration $a > 0$ and a maximim deceleration $b < 0$, in such a way that $b < g(s(t), s'(t)) < a$.

iii.) If the two cars have the same velocity but are not at the equilibrium distance M, the following car will try to reach this equilibrium distance, i.e.:

$$y''_{-1}(t) = g(s,0) \begin{cases} > 0 \text{ if } s > M & , \\ = 0 \text{ if } s = M & , \\ < 0 \text{ if } s < M & . \end{cases} \tag{2.103}$$

iv.) The function g is increasing with respect to s.

The model ([1, 56]) is built on the following sigmoidal function, that meets the previous requirements:

$$g(s, s') = a - \frac{(a+b)}{1 + \frac{b}{a} e^{d(s - M + Ks')}}, \forall (s, s') \in \mathbb{R}^2 \quad . \tag{2.104}$$

where d is a parameter to model the intensity of the response of the car-driver ensemble, and K is a parameter to model the driver's response according to the safe distance and the perceived relative velocity (see [56] for further details).

This model offer more realistic behaviour than the previous models since:

- The acceleration is now bounded to a range of values, which are chosen to represent real vehicle values.
- The equilibrium distance is an increasing function of the vehicle velocity.

This is the nDDE model (new car-following traffic model), and in [56] it is provided an analysis of the dynamical characteristics and the change from stability to oscillatory solutions in equilibrium depending on the value of the delay term (Hopf bifurcation). The reference also characterizes the nDDE equation as a Retarded Functional Differential Equation (RFDE) [29], and study the structure of the solutions produced by this bifurcation and its impact on the traffic process. Some validation results on this model will be provided in Section 3.2.3, and it will be the main example of application of the the results included in chapter 4.

2.2.2 General overview of macroscopic models

In previous sections we have made some references to the macroscopic behaviour of traffic, and to the fundamental diagram that relates its macroscopic magnitudes. At the macro level, traffic is modelled as a compressible fluid, and is described in terms of the spatial vehicle density in the road $\rho(x,t)$ and the average velocity $v(x,t)$ as functions of space x and time t. A related function is the traffic flow (vehicles passing per time unit) which is

$q(x,t) = \rho(x,t) \cdot v(x,t)$. This is normally expressed by two equations: the continuity equation that describes the conservation law for the traffic , and the momentum equation that describes the dependence of the velocity v, and hence the flow q, on the rest of variables and parameters.

The advantages of this approach with respect to the microscopic view are [31]:

i.) Good agreement with empirical data.

ii.) Convenience for analytical investigations.

iii.) Simple treatment of inflows from ramps.

iv.) Possibility of analysis of traffic in several lanes.

Next sections introduce some notes on the historical evolution of these models.

Lighthill-Whitman model

All macroscopic models are some kind of derivation of the original one, proposed by Lighthill and Whitman in 1955 [42]. The model is a fluid-dynamic model based on the fact that the traffic away from entering and exiting points must comply with a conservation law, provided by the continuity equation for fluids:

$$\frac{\partial \rho}{\partial t} + \frac{\partial q}{\partial x} = 0 \quad , \tag{2.105}$$

where, as stated earlier, $q(x,t) = \rho(x,t) \cdot v(x,t)$. This equation is the fundamental part of all macroscopic traffic models. The difficulty then is to determine the traffic flow $q(x,t)$. In [42], a simple dependence between the flow and density is used, assuming that the velocity in the road is a function of the density:

$$q(x,t) = q(\rho(x,t)) = \rho \cdot v(\rho(x,t)) \quad . \tag{2.106}$$

A linear velocity dependence widely used in analytical studies is:

$$v(\rho) = v_{max}\left(1 - \frac{\rho}{\rho_{max}}\right) \quad , \tag{2.107}$$

where ρ_{max} is the maximum density (bumper-to-bumper). Following [31], we introduce (2.107) in (2.105):

$$\frac{\partial \rho}{\partial t} + \frac{\partial q}{\partial x} = \frac{\partial \rho}{\partial t} + \frac{\partial \rho \cdot v}{\partial x} = \frac{\partial \rho}{\partial t} + C(\rho)\frac{\partial \rho}{\partial x} = 0 \quad , \tag{2.108}$$

where

$$C(\rho) = \frac{\partial q}{\partial x} = v(\rho) + \rho\frac{\partial v}{\partial \rho} \quad . \tag{2.109}$$

Equation (2.108) is a nonlinear wave equation, that explains the propagation of kinematic waves in backwards direction. Also, $C(\rho)$) is the speed of the characteristic lines, which are then dependent on the density. This causes that, in contrast to linear waves, the characteristic lines of points with different densities can intersect because the speed in congested areas is lower. This ultimately create density discontinuities and shock waves.

A good analysis of the conditions for the formation of shock waves is provided in [40].

Burgers equation

We follow in this section the reference [31], where additional details can be found.

To avoid the creation of shock waves, it is necessary to add some diffussion term to the Lighthill-Whitman model:

$$\frac{\partial \rho}{\partial t} + C(\rho)\frac{\partial \rho}{\partial x} = \frac{\partial}{\partial x}\left(D\frac{\partial \rho}{\partial x}\right) \quad . \tag{2.110}$$

If the linear dependence of the velocity with the density of (2.107) is considered, we get:

$$C(\rho) = v_{max}(1 - 2\frac{\rho}{\rho_{max}}) \quad , \tag{2.111}$$

and finally the *Burgers equation*:

$$\frac{\partial C}{\partial t} + C\frac{\partial C}{\partial x} = D\frac{\partial^2 \rho}{\partial x^2} \quad . \tag{2.112}$$

which is the simplest equation containing nonlinear propagation and diffusion. This equation solves the problem of shock waves, but do not explain the formation of density waves and traffic jams.

Modern macroscopic models

Other macroscopic models have been proposed that complement the continuity equation and explain the generation of density waves, like [57] that introduces a dynamic velocity equation derived from the microscopic OVM, or [59] that introduces a gas-kinetic model using the *Boltzman* equation.

One of the most widely used macroscopic models now was introduced in the 1990s by Kerner and Kornhauser [35], which uses a velocity equation analog to the Navier-Stokes model for compressible fluids, by introducing a viscosity term of the form $\mu\frac{\partial v^2}{\partial x^2}$:

$$\rho\frac{\partial v}{\partial t} + \rho v\frac{\partial v}{\partial x} = \frac{\rho}{\tau}[V(\rho) - v] - c_0^2\frac{\partial \rho}{\partial x} + \mu\frac{\partial^2 v}{\partial x^2} \quad , \tag{2.113}$$

where V is the optimal velocity (dependent on the vehicle density) and c_0, τ and μ are constants to be determined by real measurements. This model, while convenient from the analytical point of view, is sensible to the parameters choice and the dependence of the velocity with the density [31]. This is because, in the same way as the OVM, the velocity does not depend on the relative velocity between cars. In fact, as we shall see in next section, the two models can be linked by explicit relations between their respective parameters.

Microscopic to macroscopic link for the OVM

Equation (2.91) from the OVM provides an explicit, not retarded dependence of the acceleration on the distance, the velocity and the reaction time, and makes this model very convenient for establishing a relationship between the micro and the macro models. In [41]), Lee et al provided a practical method to derive the momentum equation for the macroscopic model from the OVM microscopic equation (2.91) and the fluid continuity equation (2.105).

In what follows, this section follows [48] to derive the micro-macro link. This is the basic method on which we base the development of a general macroscopic model that we describe in chapter 6.

The method starts by defining two microscopic field variables:

$$\begin{aligned} \hat{\rho}(x,t) &= \sum_j \delta(y_n(t) - x) \quad , \\ \hat{q}(x,t) &= \sum_j \dot{y}_n(t)\delta(y_n(t) - x) \quad , \end{aligned} \tag{2.114}$$

where $y_n(t)$ is the coordinate of vehicle n at time t, the dot $\dot{\square}$ denotes differentiation with respect to time t and $\delta()$ is Dirac's delta generalized function.

We then define a coarse-grained functions for the density ρ and flow q by convolving in time and space:

$$\begin{aligned} \rho(x,t) &\equiv \int_{\mathbb{R}}\int_{\mathbb{R}} \Phi(x-\xi, t-\tau)\hat{\rho}(\xi,\tau)d\xi dt\tau \quad , \\ q(x,t) &\equiv \int_{\mathbb{R}}\int_{\mathbb{R}} \Phi(x-\xi, t-\tau)\hat{q}(\xi,\tau)d\xi d\tau \quad , \end{aligned} \tag{2.115}$$

where $\Phi(x,t)$ is a nonnegative and normalized mollifier function. By integration by parts, the continuity equation (2.105) is obtained, and from it the dynamic equation for q:

$$\frac{\partial q}{\partial t} + \rho \left\langle \ddot{y}_n(\tau) \right\rangle_{(x,t)} - \frac{\partial}{\partial x}\left[\rho \left\langle \dot{y}_n(\tau)^2 \right\rangle_{(x,t)}\right] \quad , \tag{2.116}$$

where we use the bracketed average defined as:

$$\left\langle \ddot{y}_n(\tau) \right\rangle_{(x,t)} \equiv \frac{1}{\rho}\int_{\mathbb{R}}\int_{\mathbb{R}} \Phi(x-\xi, t-\tau)\sum_j \ddot{y}_n(\tau)\delta(y_n(\tau)-\xi)d\xi d\tau \quad . \tag{2.117}$$

The velocity is calculated as:

$$v(x,t) = \frac{q(x,t)}{\rho(x,t)} = \left\langle \dot{y}_n(\xi,\tau) \right\rangle_{(x,t)} \quad . \tag{2.118}$$

Then equation (2.116) is rewritten as:

$$\rho\left(\frac{\partial v}{\partial t} + v\frac{\partial v}{\partial x}\right) = \rho \left\langle \ddot{y}_n(\tau) \right\rangle_{(x,t)} - \frac{\partial \rho\theta}{\partial x} \quad , \tag{2.119}$$

where $\theta(x,t) = \langle \ddot{y}_n(\xi,\tau)\rangle_{(x,t)} - v(x,t)^2$.

The bracketed average is calculated from the OVM (2.94):

$$\langle \ddot{y}_n(\tau)\rangle_{(x,t)} = \frac{1}{r}\left(\langle V(\Delta y_n)\rangle - v\right) \quad . \tag{2.120}$$

The series expansion of the coarse grained OVM velocity is:

$$\langle V(\Delta y_n)\rangle = V\left(\Delta y_n + \sum_{m=2}^{\infty}\frac{1}{m!}V^{(m)}(\langle \Delta y_n\rangle)\left\langle(\Delta y_n - \langle \Delta y_n\rangle)^m\right\rangle\right) \quad , \tag{2.121}$$

and the coarse-grained headway:

$$\langle \Delta y_n\rangle = \rho^{-1} + \frac{1}{2\rho}\frac{\partial \rho^{-1}}{\partial x} + \frac{1}{6\rho^2}\frac{\partial^2 \rho^{-1}}{\partial x^2} \quad . \tag{2.122}$$

Using the leading term of (2.121):

$$V(\Delta y_n) = V(\rho^{-1}) + \frac{V'(\rho^{-1})}{2\rho}\frac{\partial \rho^{-1}}{\partial x} + \frac{1}{6\rho^2}\frac{\partial^2 v}{\partial x^2} \quad , \tag{2.123}$$

we finally obtain the momentum equation:

$$\frac{\partial v}{\partial t} + v\frac{\partial v}{\partial x} = \frac{1}{r}[V(\rho^{-1}) - v] - \frac{V'(\rho^{-1})}{2r\rho^3}\frac{\partial \rho}{\partial x} + \frac{1}{6r\rho^2}\frac{\partial^2 v}{\partial x^2} \quad . \tag{2.124}$$

Normally, the OVM velocity is expressed as a function of the distance, that is why (2.122) - (2.124) are expressed in terms of ρ^{-1}.

Notice the similarity of (2.124) and (2.113). Indeed, the phenomenological constants in (2.113) can be expressed in terms of the OVM parameters:

$$\begin{aligned} c_0^2 &= \frac{V'(\rho_0^{-1})}{2r\rho_0^2} \quad , \\ \mu &= \frac{1}{6r\rho_0} \quad , \end{aligned} \tag{2.125}$$

where ρ_0 is the density value in equilibrium.

Reference [48] also provides a linear stability analysis of the PDE equation (2.124). The stability condition derived is in this case:

$$r < \frac{1}{2V'(\rho_0^{-1})} \quad , \tag{2.126}$$

which is totally consistent with (2.95).

2.2.3 Cellular automata model

Cellular automata (CA) models [72] have been proposed to account for complex system behaviour generated by simple interactions between its components. [44] provides a good introduction of the application of CA models to road traffic.

For instance, one can consider the dynamics of the movement on a one-dimensional lattice following the rule (CA 184 [72]):

$$y_n(t+1) = y_n(t) + min[1, y_{j+1}(t) - y_n(t) - 1] \quad , \tag{2.127}$$

where y_n is the (discrete) space position of vehicle j, and t is now discrete time.

In this way, a vehicle moves ahead one space if the following space is free, and otherwise it remains in the same spot.

The model (2.127) considers then a (step) velocity of 1 or 0, but it has been extended to consider variable (integer) velocity v_{max}:

$$\begin{aligned} y_n(t+1) = y_n(t) + \min[v_{max}, y_{j+1}(t) - y_n(t) - 1] = \\ y_n(t) + \min[v_{max}, \Delta y_n(t) - 1] \quad . \end{aligned} \tag{2.128}$$

This can be rewritten as:

$$\begin{aligned} y_n(t+1) - 2y_n(t) + y_n(t-1) = \\ \min[v_{max}, \Delta y_n(t) - 1] - [y_n(t) - y_n(t-1)] \quad , \end{aligned} \tag{2.129}$$

that, when converting t to continuous and taking $\Delta t \to 0$ yields:

$$\frac{\mathrm{d}^2 y_n(t)}{\mathrm{d}t^2} = \min[v_{max}, \Delta y_n(t) - 1] - \frac{\mathrm{d}y_n(t)}{\mathrm{d}t} \quad , \tag{2.130}$$

which is equivalent to the optimal velocity model (2.94) with delay time $\tau = 1$

This framework has been used to derive different traffic models, incorporating increasing complexity [44]:

- Deterministic models, as the previous one, only dependent on initial conditions.
- Stochastic models, incorporating stochastic terms to account for real-life changing conditions.
- Slow-to-start models, which accounts for the different reaction times before and after the jam.

2.3 Communications traffic modeling

2.3.1 Performance evaluation in network design and management

Telecommunication network engineering has faced from its origin the classical resource allocation problem: normally, the demand is not deterministic, and the resources are limited.

This means that we need to deploy the minimal amount of resources to cope with the expected demand, so that a minimum quality level is offered. A classical problem is to determine how many telephone circuits are needed to serve a number of users generating calls with a specific pattern.

The quality objectives are determined by the minimum service level expected by the users , normally in terms of availability and communications quality. This is usually described in probabilistic terms, e.g., probability of connection, probability of interruption or probability of lost information.

Performance evaluation seeks the mathematical rules and methods that govern the tradeoff between demand, quality and resources. This has been historically developed by Teletraffic theory, and this section provides a very brief introduction to the subject.

2.3.2 Evolution of network technologies and usage patterns

Communications technologies have been evolving from the origins of telephone networks, steadily introducing improvements in transmission technology, network structure and services provided. Some landmark technological shifts were:

- Telephone networks deployment in 1920s, initially local service and later international service.
- Automatic switching from 1940s to 1970s.
- Digitalization of telephone service in the 1980s.
- Internet in 1990s.
- Mobile networks in 2000s.
- Access technologies (fiber) multiplying access speeds by x1000 in 2010s.

The evolution has been especially disruptive in the last 30 years, when Internet and mobile network technologies have completely changed the way communications are done in modern societies. In this period we have passed from using only fixed voice service to high quality data and video transmission in mobility through radio links.

This trend is only continuing at this moment through the introduction of new communication capabilities in the next generation of mobile networks (5G) [50]. These technologies will allow the provision of ever more demanding quality services, including management of high mobility scenarios (Section 2.3.4).

2.3.3 Mobile network standards evolution

Mobile network technology evolves through roughly one decade cycles, over which a new technology is introduced while the previous one is commercially exploited. In terms of the service capabilities, the different mobile generations have evolved from analog to high speed digital services:

- 1980's **1G**: analog, low quality voice.

- 1990's **2G**: 1st digital tech, standard voice + 10's kbps data.
- 2000's **3G**: standard voice + 100's kbps data, 100s ms latency.
- 2010's **4G**: HQ voice (IP) + 10's Mbps data, 10s ms latency.
- 2020's **5G**: 100's Mbps - Gbps data, very low-latency.

We are now in a situation where data services over mobile connections are already offering **speeds comparable to fixed networks**. In fact, streaming and remote work services are perfectly supported by 4G (where available), but delays still in the order of 10s ms, with significant variation (*"jitter"*), which causes that Delay-critical services still only provided by fixed connections.

5G standards are now capable for the first time to offer very low latencies, which will enable the support of delay critical services over mobile connections for the first time.

2.3.4 New network paradigms in the 2020s

In addition to low latencies, 5G provides mechanisms that will enable even more sophisticated services and strong self-management capabilities.

Small cells and densification The higher frequencies used in 5G and the increasing capacity necessary to cope with the increasing traffic will require the deployment of many more access points. This will impose a new demand of wired connections to feed these access points, which will change the basic network structure.

This will also create new problems in the assignation and management of user connectivity in scenarios of multiple access choice and high mobility.

M2M and IoT Non human traffic sources will become increasingly important in terms of number of connections and traffic generated [15]. The scale and patterns of these traffic sources will introduce higher variability in the traffic generation process.

Even when the traffic volume may not be very high, some applications may require very stringent latency requirements.

Network slicing New control plane will allow to partition the network resources to assign dedicated capacity to different subnetworks. This poses new problems as to how perform this partitioning in the mos efficient way both from the point of view of the service provider (minimize cost) as from the point of view of the users (simplicity), therefore simple models for capacity management of these subnetworks are needed.

V2V services Vehicle-to-vehicle (V2V) and vehicle-to-infastructure (V2I) communications will be new services offered by 5G, due to the lower latencies allowed by the new standard. This is an important enabler for safely deploying self-autonomous driving systems.

Paramount for the successful adoption of these services is (i) to have a deep understanding of the traffic requirements and models for these communications, which are quite different

to the traditional internet connections, and (ii) understand the challenges and risks derived of the mobility scenarios, i.e., understand the interplay between these new network traffic models and the mobility (road traffic) models over which they will work.

This may be especially critical for applications highly dependent on strict timing, which would be affected by both network traffic and road traffic conditions.

2.3.5 Communication models for V2X technologies

V2X technologies have seen an strong development as a result of the advances on the mobile communications technologies in the last two decades, up to the point to be considered a reliable support of communications between vehicles to coordinate driving functions. The application of these technologies are focused mostly in safety applications and autonomous driving (also referred to as ITS, Intelligent Transportation Systems), which inherently require a very low packet loss probability and communications delay. The required level of performance has only started to be achieved with the fourth generation of mobile networks in the decade 2010-2020, though the range of applications and the amount of real applications have been somewhat limited as of today [21, 49]. The standards are being developed along 2 main tracks:

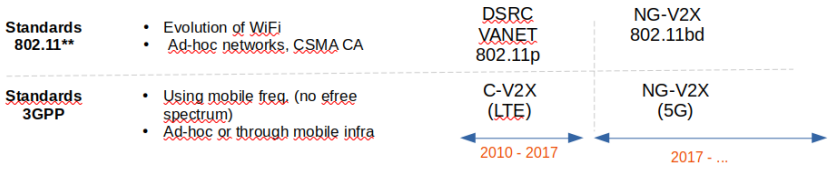


Figure 2.4: V2X standards evolution

IEEE standards (802.11), a set of technologies branched from WiFi standards and oriented to vehicle to vehicle communications, and 3GPP (3rd Generation Partnership Project) standards, derived from the technologies that support public mobile communications. In Figure 2.4 a summary of the evolution of these standards is provided. The most important standars in the first wave for each of these standardization bodies have been: ´

- **Dedicated Short Range Communications (DSRC)**, also known as the **802.11p** standard from IEEE, consisting on the setting up of an ah-hoc network among close vehicles to exchange status updates.
- **Cellular Vehicle-to-Everyting (V2X)**, from 3GPP, using dedicated capacity of the public mobile infrastructure to support communications between vehicles, either using the nodes of the mobile networks (called mode 3) or by direct messages between the vehicles (called mode 4).

These technologies are considered as capable of supporting safety applications requiring minimum delays greater than 100 ms in situation of low load, but they are unsuitable for the most demanding applications of V2X applications, as autonomous driving or platoon management. For instance [49], DSRC performance deteriorates due to packet collisions and the "hidden node" problem, as we shall see in the example in Section 2.4.

It is now with the introduction of the latest generation of mobile communications when the application of these technologies to the most advanced V2X applications are being seriously proposed. The evolution of the former standards that are now being developed are:

- **802.11bd**, the evolution of 802.11p that, besides being backwards compatible with DSRC, includes newer medium access protocols developed in recent WiFi versions, and provides much higher speed and communication range.
- **New Radio V2X (NR-V2X)**, which are being introduced in the Releases 16 and 17 of 3GPP standards, introducing performance improvements and adaptation to the 5G radio technologies.

We use now a simplified model of the DSRC protocol as a first approach to test the performance of the car-following model under study, taking into account the additional source of complexity which is the influence of the communications process on the variability of the delay of the system.

2.4 Motivational example: V2V network supporting traffic coordination

For the first model evaluation we will consider a multi-vehicle system in which each vehicle broadcasts the information about its state (position-speed) to the rest of vehicles using DSRC messages, and each vehicle adapts its own dynamics by adjusting the acceleration according to some algorithm that model the driver behaviour (like the microscopic models seen in Section 2.2.1).

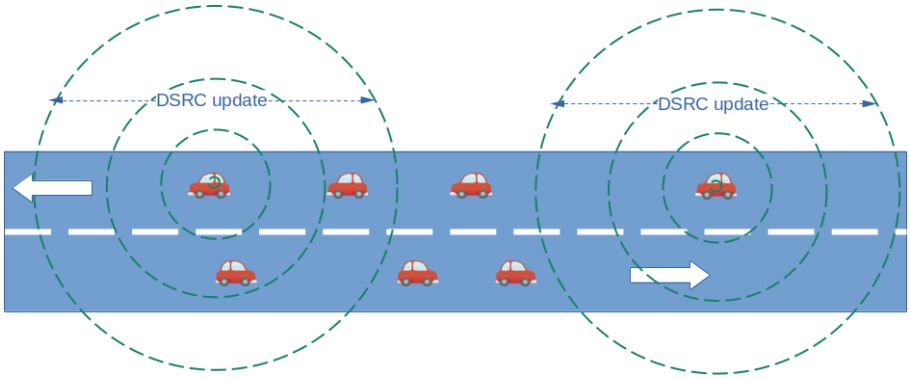


Figure 2.5: DSRC scheme

A simplified scheme of the DSRC relationship is provided in Figure 2.5. Each vehicle send its status messages accessing the shared channel, and the message is received by the vehicles in its area of coverage (defined by a radius R). The messages are sent by each vehicle periodically but asynchronously, in such a way that there are two sources of *"collision"* (two vehicles transmitting at the same time and thus mutually interfering their transmission), which translates to a corresponding delay by the need of retransmitting the message after a random waiting time [27, 28]:

1. **C1**: Collision due to **simultaneous transmission inside the coverage area**. The usage of the channel is governed by the Medium Access Control (MAC) function through the protocol CSMA-CA (Carrier Sense Multiple Access - Congestion Avoidance) by which each node detects other transmissions in the channel, and only tries to send a message when the channel is free. Nevertheless, a small probability exist that two nodes initiate the transmission unbeknownst to each other in the same time slot, which produces a collision and the need for a retransmission. The theory to calculate the impact of this event has been studied for instance in [27, 28], where the process is modelled as a Markov Stochastic Process, and is governed by the equations of the probability of transmission in a randomly selected slot P_E and the probability of collision P_C:

$$P_E = \frac{2(1-P_C)^2}{2 + P_C \cdot W - 3P_C}(TS \cdot \alpha) \quad , \tag{2.131}$$

$$P_C = 1 - e^{2\rho D P_E} \quad , \tag{2.132}$$

where α is the message generation rate of each vehicle, TS is the length of a timeslot (basic digital transmission time), W is the average waiting time after a collision, R is the radius of the coverage area of the vehicle, D is the distance for which a collision is detected ($D > R$), and ρ is the vehicle density.

These coupled equations are numerically solved, and the result is used to calculate the delay by collision in the MAC function τ_{MAC}

$$r_{\text{MAC}} = \frac{P_C \cdot T_t(W-1)}{2} + T_t \quad , \tag{2.133}$$

where T_t is the packet transmission time (= message size / channel speed).

2. **C2**: Collision due to the **"hidden node" problem** [37, 67]. Due to the limited reach of the transmission of a given vehicle, it is possible that two vehicles are so far away that they do not detect each other's transmissions, but some vehicles in between are able to receive both of them, so, if they are simultaneous, neither message is received correctly by this intermediate vehicle. This is further aggravated by the fact that neither of the transmitting vehicles is able to detect each other's simultaneous transmission, so they do not abort, thus wasting channel time for a longer time than in the CSMA-CA collision. This situation is illustrated in Figure 2.6.

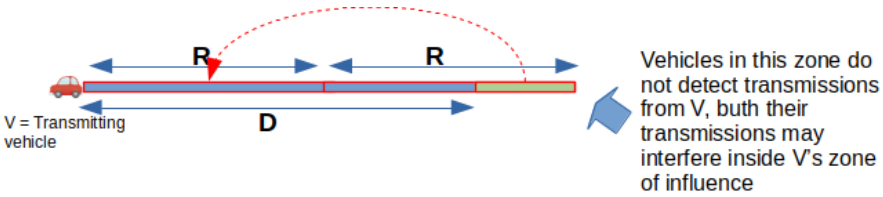


Figure 2.6: Interference as the source of main delay

For this situation the probability of a successful transmission can be calculated using the classical unslotted ALOHA model [2]:

$$P_A = e^{-2\cdot\rho\cdot(D+\frac{T_t}{TS}(2R-D))P_E} \quad . \tag{2.134}$$

On average a receiving vehicle will get the information correctly after an average number of trials of the transmitter (using the geometric distribution $\overline{N} = \frac{1}{P_A}$), so the average delay for the hidden node problem is:

$$r_{\text{HN}} = \frac{1}{\alpha \cdot P_A} \quad . \tag{2.135}$$

In general, with the small amount of communications traffic generated in V2X scenarios, the effect of $C1$ collisions is much less important than the effect of $C2$ collisions, so:

$$r_{\text{HN}} >> r_{\text{MAC}} \quad , \tag{2.136}$$

and thus in our modelling we will model the communications delay as τ_{HN}. We can expect that variations in this delay will instability problems if this communication channel is used for vehicle traffic management purposes. This is in fact what is numerically evaluated in the continuation of this example in section 3.2.5.

Chapter 3

Simulation platform

3.1 Development of simulation model on *ns-3* platform

ns-3 (Network Simulator version 3 [55]) is an open source platform for discrete-event (i.e. Monte-Carlo) simulation for communication systems. It is based on C++ and Python, with an extensive model library for Internet and mobile communications systems. It is presently used by the telecommunications research community to build realistic scenarios to model complex communication systems, and is a key tool for many projects in current network research activity.

The interesting aspect of using *ns-3* for our analysis is three-fold: first, it provides a library of mobility models (e.g., constant/variable velocity and acceleration, ...) that has been extended to model the dynamics of the nDDE models; secondly, it offers models to simulate all modern communication systems, thus allowing a seamless integration of the simulation of the mobility and communications dynamics; finally, it allows us to simulate micro (i.e., two vehicles) and macro (many vehicles) scenarios using the same code base.

The contents of this chapter are mostly related to the technical characteristics and validation of the software platform that has been built to support the mathematical results of this thesis. In this sense, it is not strictly needed to read this chapter to understand the contents of the following chapters, though it provides insights on how to interpret the simulated results presented to validate the mathematical models.

3.1.1 *ns-3* platform characteristics

The main components of *ns-3* are summarized below [54]:

- **Node**: the basic computing device abstraction is called the node. The C++ Node class provides methods for managing the representations of computing devices in simulations.
- **Application**: the basic abstraction for a user program that generates some activity to be simulated is the application. The C++ Application class provides methods for managing the representations of our version of user-level applications in simulations.

- **Channel**: in the simulated world of *ns-3*, one connects a Node to an object representing a communication channel. Here the basic communication subnetwork abstraction is called the channel and is represented in C++ by the class Channel.
- **Net device**: in *ns-3* the net device abstraction covers both the software driver and the simulated hardware. A net device is "installed" in a Node in order to enable the Node to communicate with other Nodes in the simulation via Channels.

These are the basic components to simulate the communications components of the system, but, in addition, *ns-3* provides some basic mobility models to simulate communication scenarios in situations where the nodes are mobile. The most useful mobility models for road traffic simulations provided by *ns-3* are:

- **Constant position**: Mobility model in which the current position does not change once it has been set and until it is set again explicitly to a new value.
- **Constant velocity**: Mobility model in which the current speed does not change once it has been set and until it is set again explicitly to a new value. The position of the object is updated in simulated time according to this velocity.
- **Constant acceleration**: Mobility model in which the current acceleration does not change once it has been set and until it is set again explicitly to a new value. The position and velocity of the object is updated in simulated time according to this acceleration.
- **Random mobility**: in addition to these simple models, more sophisticated models are provided to implement random mobility scenarios:
  - Random direction.
  - Random velocity.
  - Random walk model.

Further details of these mobility models can be found in [55].

3.1.2 Enhancement of the existing mobility models

The standard mobility models described in previous section fall short to provide the microscopic behaviour of the car-following models of Section 2.2.1. Therefore, additional development over the standard *ns-3* distribution had to be done to implement the driver behaviour over these simple models. The implementation of the car-following models required the following actions:

- Building the structure to model the road and vehicles system (set of *node* objects and their relationship).
- Modification of the existing *ns-3* object *constant-acceleration-mobility-model* to include information on the preceding node and to enable the delayed update of the acceleration (retarded variables).
- Introduction of the nDDE model dynamics in the simulation logic.

Road and vehicle structures New structure to simulate the single road infrastructure have been created:

- **Active nodes** structure, to account for the nodes involved in the simulation. For micro simulations this is simply a pair of mobile nodes, but for multi vehicle scenario in macro simulations a more complex structure that takes into account the initial condition of the vehicle positions and velocities, and the boundary conditions of the entering and exiting vehicles, have to be created. This structure provide the ordering of vehicles that link each vehicle with its predecessor (car-following leader) on the road.
- **Road density** to account for the influence of the vehicle density on the road on the communications delay, statistics of the vehicle distribution have to be regularly updated, for which new data structures have to be created.

Modification of the constant acceleration model To implement the car-following driver behaviour, some modifications have been introduced to the existing *ns-3* C++ class that implements the constant acceleration mobility model. This has been done by creating a new class (*car-following-mobility-model-accel*) that inherits the characteristics of the object *constant-acceleration-mobility-model*, which implements the movement of an uniformly accelerated object using a parameter for the acceleration. The car-following model is implemented by updating the value of the acceleration every unit of discretized time according to the algorithm of the model simulated. To do this, the following data structures and functions have been added to the base class *constant-acceleration-mobility-model*:

- **Data structures**
  - Vector of **previous velocity** values.
  - Vector of **previous position** values.
  - Variable for the **delay** (reaction time of the driver).
  - Variable for the local **density** of vehicles in the present position.
- **Functions**
  - Update/consult the previous position.
  - Update/consult the previous velocity.
  - Update/consult the current values of acceleration and velocity.
  - Update/consult the current value of delay (reaction time of the driver).
  - Update/consult the current value of density.

Position and update engine The standard mobility models provided by *ns-3* recalculate the position of the mobile object every time that the logic of the simulation needs to look at that position, based on the position and some constant values of acceleration and velocity for the mobile object. But in the car-following models, the position *and* the velocity or acceleration of the object are changing continuously. Therefore, to simulate this continuous

update a discrete approximation of the continuous evolution had to be implemented. This calculation engine, which updates the values at a fixed discretizing time quantum, is very much like a time integration algorithm in a finite elements integration algorithm. The method implemented at this moment is the simplest one, with a fixed time quantum q_τ determined at the beginning of the simulation (as 1/100th of the delay r for the reaction time).

This update engine is also in charge of recalculating the values of the vehicle density in each position, so that it can be used when the delay is dependent on the density on the road.

Models implemented in the simulator The following car-following models have been introduces in the simulator:

- Linear and nonlinear GM models.
- Optimal Velocity model (OVM).
- nDDE model.
- Improved nDDE model (nDDEa) (see Section 3.2.4).
- Intelligent Driver Model (IDM) introduced in [69].

The implementation of additional car-following models is straightforward provided that the basic information used in the retarded acceleration calculation is always the relative position s, the relative velocity s' and the velocity of the vehicle v.

Main features of the program Figure 3.1 shows a high level view of the simulator execution. The key features of the inner workings of the program are:

1. **Initial and Boundary Conditions**: vehicles are created with configurable initial positions and velocities, and new vehicles can enter the simulation at the road boundary (x=0) according to specified density/time profiles.
2. **Car-Following Models**: the different models for vehicle acceleration and velocity adjustment are implemented, selectable via a command-line parameter. These include:
   - Linear model
   - Optimal Velocity Model (OVM)
   - Padial/Casal (PC) and improved variants
   - Intelligent Driver Model (IDM)
3. **Delay and Noise**: the reaction time (delay) and random noise can be configured to simulate more realistic driver behavior.
4. **Density Calculation**: the program computes local traffic density, which can affect vehicle behavior and communication delay.
5. **Output**: the simulation writes time series data (positions, velocities, accelerations, etc.) for all vehicles to output files for later analysis.

6. **Parameterization**: all key parameters (densities, velocities, road lengths, time intervals, etc.) are configurable via command-line arguments

For more details, Annex A contains the object-oriented programming structures (C++) that support this logic.

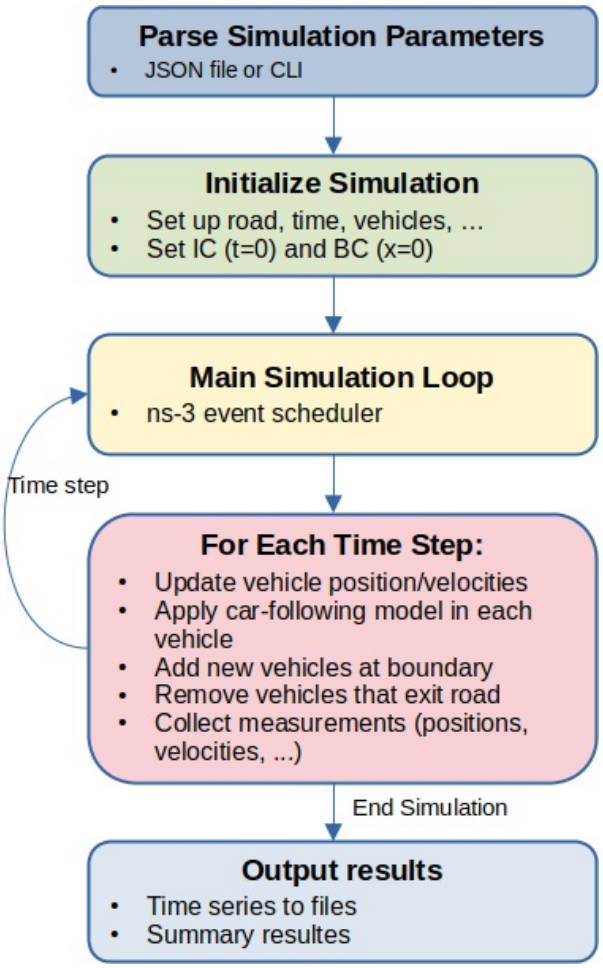


Figure 3.1: Flow diagram of the simulator

3.1.3 Communication models

The *ns-3* platform has a huge library of up-to-date models for the latest communication technologies, that simulate the innermost details of the protocols used in the standards. The simulator is even able to be integrated with real communication software using a framework called Direct Code Execution (DCE). A sample list of existing models in *ns-3* is:

- WiFi (IEEE 802.11.*).
- Internet protocols (TCP / IP, IPv4, IPv6).
- LTE (3GPP).
- Radio propagation models.

The main idea of this work is to eventually integrate the road traffic dynamics with these communication models, so that to study the dynamics of the coupled system vehicles - network. For the time being, the interaction of the communication layer with the road traffic simulation has been done through direct implementation of the performance evaluation formulas (e.g. (2.134) and (2.135) for DSRC) to calculate the delay experienced by the communication process.

3.2 Validation of existing traffic models

The first step after building the simulator has been to check its validity by comparing its results with analytical models or previously published results. We have checked the validity of the results for the GM, OVM and nDDE models in section 2.2.1 by comparing the simulator results with the results in references [61], [48] and [56] respectively. In addition to these initial work, additional results have been produced using the simulation platform for two investigation activities:

- Introduction of a improvement in the acceleration function used in the nDDE model, to account for real vehicle characteristics.
- First evaluation of the vehicle + communication dynamics coupling using the nDDE model and the DSRC communication protocol.

The results of these two latter activities were the main contributions for a communication for the Congress of Differential Equation an Applications (CEDYA 2022), presented in July 2022 [19].

3.2.1 General Motors (GM) model validation

A first result have been the reproduction of the simple GM linear model published in [61]. These results, despite being rather basic, have been important to ensure the validity and the accuracy of the simulation program.

The results tested correspond to the scenario of two vehicles in which the follower behaves like the GM linear model, described by equation (2.81). In [61] the following evolution is provided for a scenario in which the leader changes its velocity with uniform deceleration during 2 seconds to uniformly accelerate to its original velocity during the next 2 seconds. The scenario tested is for a value delay $r = 1.5s$ and a reactivity $\alpha = 1/(r \cdot e)$ which determine the limiting stability value $C = \alpha r = e^{-1}$.

The Figure 3.2 provides the reaction of the follower in terms of acceleration, velocity, relative velocity and distance. In the two first graphs, the solid line is for the leader and the dotted line is for the follower. Figure 3.3 contains similar results generated with the simulator. It can be checked that the results are virtually identical.

Results for other values for the factor C for the same acceleration pattern for the leader are equally reproduced, as shown in figures 3.4 and 3.5.. The figures show the different instability patterns depending on C, as has been described in Section 2.2.1 (linear model).

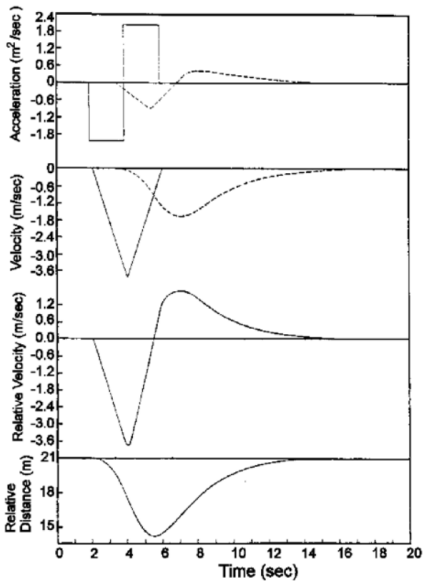


Figure 3.2: Evolution of 2 vehicles dynamic for linear GM model in [61] for $C = e^{-1}$ (Figure 4.2 in the original).

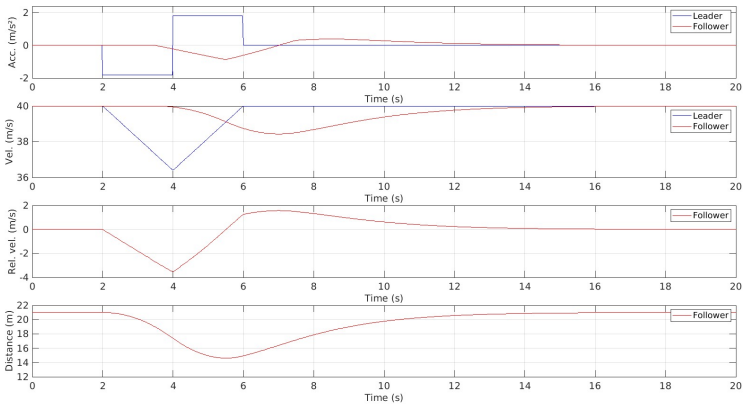


Figure 3.3: Evolution of 2 vehicles dynamic for linear GM model calculated with *ns-3* simulator.

Given that these results are easily reproduced using a simple numerical integration tool, the interest of this validation has been mostly on checking the validity of the implementation of the simulator, whose algorithms are much more convoluted than a numerical integration. The simulator have been put at test for more complex behaviors with the Optimal Velocity Model (OVM).

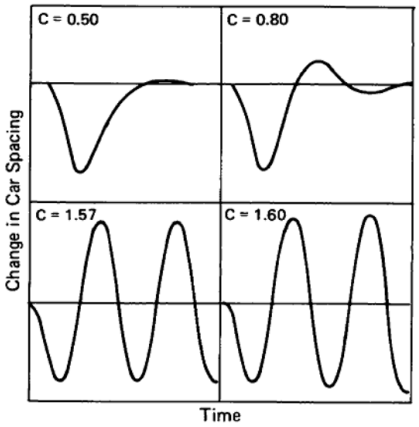


Figure 3.4: Evolution of the follower vehicle for linear GM model in [61] for several values of C (Figure 4.3 in the original).

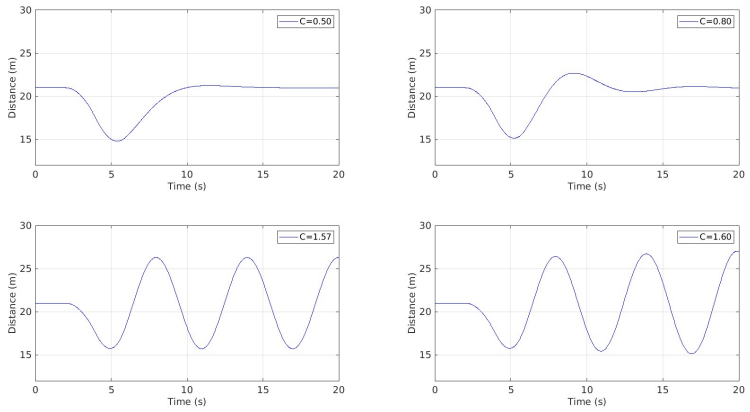


Figure 3.5: Evolution of the follower vehicle for linear GM model and for several values of C, calculated with *ns-3* simulator.

3.2.2 Optimal Velocity Model (OVM) validation

In this case, validations have been done comparing the simulator output for macroscopic scenarios to results presented in [48].

First, the accuracy to reproduce the stability limit for the OVM model was done for a basic macroscopic scenario with $v_{max} = 2$ and $d_c = 5$ in (2.91). In this case, using (2.95), the stability limit is :

$$r_n < \frac{1}{2V'(\rho_0^{-1})} = 0.5 \text{ s} \quad . \tag{3.1}$$

Figure 3.6 shows the evolution for three time instants ($t = 0$, $t = 50s$ and $t = 100s$) of the distance and velocity for 100 vehicles in the macroscopic simulation, for a delay value $r_n = 0.4s$. The stable traffic pattern is initially modified with a noise pattern, that is progressively damped down because the value of the delay is under the stability limit ($0.5s$).

On the contrary, if the delay values is over the limit, it can be expected that instability arises.

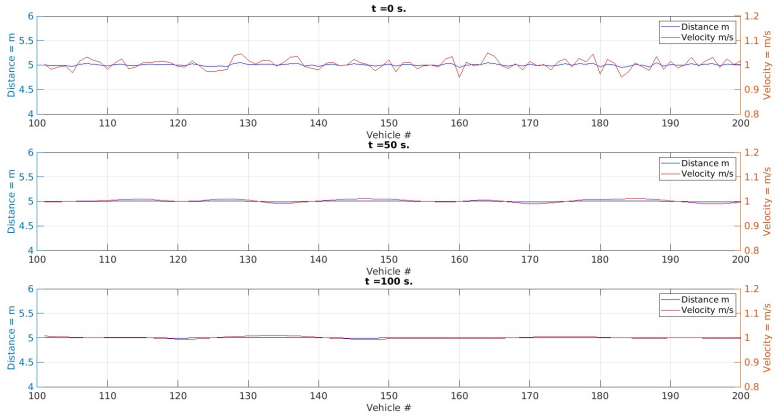


Figure 3.6: Evolution of macroscopic scenario with delay under the stability limit ($\tau = 0.4s$).

This is the case for the scenario with $r_n = 0.7s$, shown in Figure 3.7. In this case, the noise is not damped and density waves are developed, as predicted by the theory.

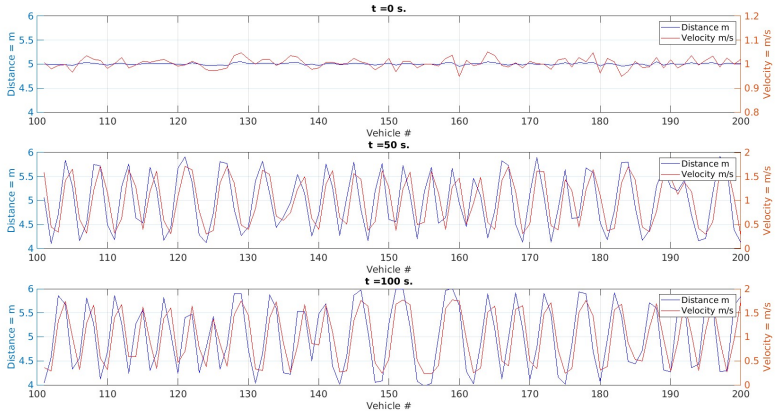


Figure 3.7: Evolution of macroscopic scenario with delay over the stability limit ($\tau = 0.7s$).

An additional validation has been performed for this model, for which some more simulated results are provided in [48]. In this reference, a discrete difference equation approximation of the differential equation (2.94) is provided:

$$y_n(t + 2r_n) = y_n(t + r_n) + rV(\Delta y_n(t)) \quad . \tag{3.2}$$

This approximation has an stability limit [48]:

$$r_n < \frac{1}{3V'(\rho_0^{-1})} = 0.333 \text{ s} \quad . \tag{3.3}$$

Figure 3.8 shows a Monte-Carlo simulation presented in [48] using this approximated difference equation model, with the same fundamental parameters in the OVM model and a delay $\tau = 0.5s$. In this case, given the lower stability limit for the approximation, the traffic evolves to an inhomogeneous flow with density waves, with values for the inter-vehicle distance between $4m$ and $6m$ approximately.

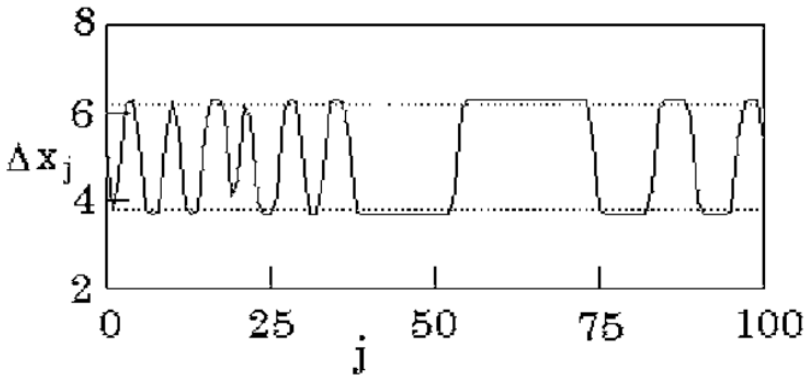


Figure 3.8: Macroscopic simulation of the difference equation (3.2) with $\tau = 0.5s$ [48]

Figure 3.9 shows the same scenario simulated with our *ns-3*-based simulator. In this case, the simulation time step has been set equal to the delay r_n, so that to simulate the discrete difference equation (3.2) instead of the continuous differential equation (2.94).

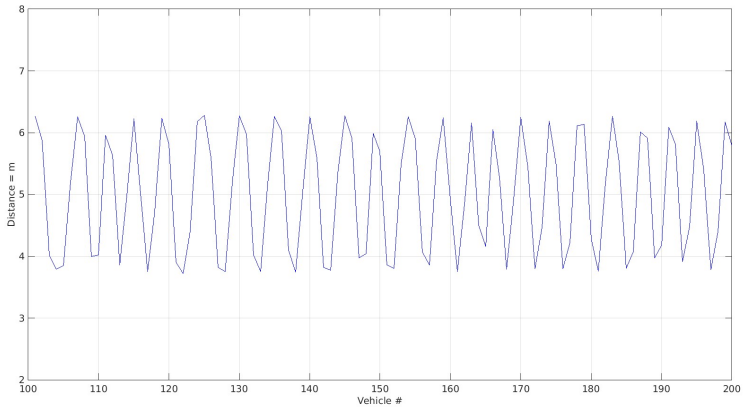


Figure 3.9: Macroscopic simulation of the difference equation (3.2) with $\tau = 0.5s$ [48]

The results show the similitude of the simulation with the original results, and the capabilities of the *ns-3*-based simulator developed to also manage coarse time resolution, which may be convenient in case that simulation times are prohibitive for continuous time simulations.

3.2.3 nDDE model validation

A final validation work has been done to reproduce the existing results on nDDE model that has been published. To perform the validation we have used the same scenarios as in [56], whose parameters are summarized in table 3.1.

Param	Description	Value
a	Maximum acceleration in nDDE	$2.0576 m/s^2$
$a(0)$	Acceleration at $v = 0$ in nDDEa	$6.6666 m/s^2$
b	Maximum deceleration	$1.5677 m/s^2$
v_0	Leader velocity	$22.2222 m/s$
M	Safe distance for v_0	$44.4444 m$
d	Car + driver response intensity	0.1124
K	Driver sensitivity to s'	$11.3890 s$

Table 3.1: nDDE parameters used in the simulations.

Reference [56] includes a detailed characterization of the original nDDE model, in which numerical simulations of the solutions in the Hopf bifurcation for different delay parameters τ are provided. We follow the same structure to present the results, in which each graphic has three parts: (a) is the graphic of the s, s' and s'' with respect to time; (b) show the 2D-curve (s, s'); and (c) the 3D-curve (s, s', s'').

Figure 3.10 provides the original results in [56] for a delay $r = 1.2s$. This has been generated using the code dde23 of Matlab to solve the DDE. Figure 3.11 shows the results produced by the simulator. We can see that the simulation reproduces with a high degree of accuracy the results produced by the numerical integration of the equations.

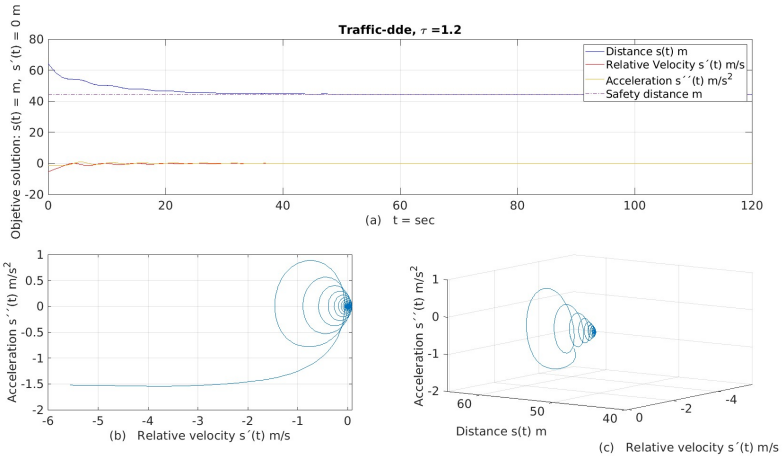


Figure 3.10: Oscillatory and stable solution for $\tau = 1.2s$ in nDDE in [56].

It is also interesting to check for higher delay values, since for very high values the instability of the system lead to the crash of the vehicles (distance < 0). This can be seen in Figure 3.12, where after a short time, the solution contains negative values for the inter-vehicle distance.

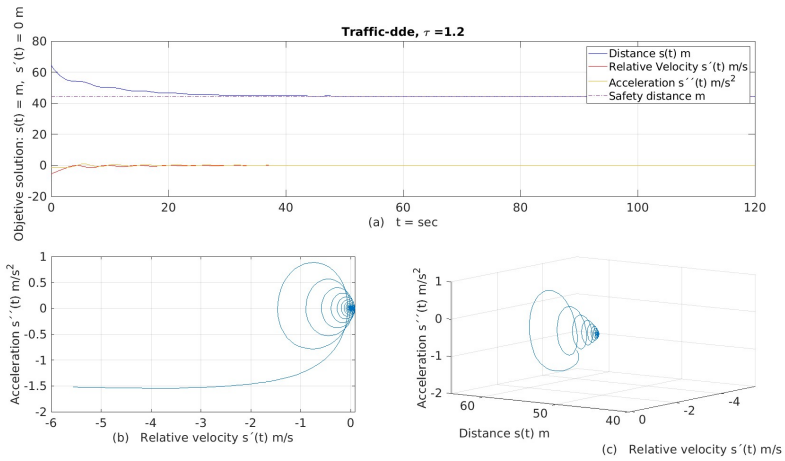


Figure 3.11: Oscillatory and stable solution for $\tau = 1.2s$ in nDDE using the *ns-3* simulation.

But this is explicitly avoided in the simulation, as can be seen in Figure 3.13. This allow us to use the simulation program to study situations with complex interactions beyond the analysis of the Hopf bifurcation, which is specially important to evaluate the behaviour of the nDDE acceleration model in multi vehicle (macro) scenarios.

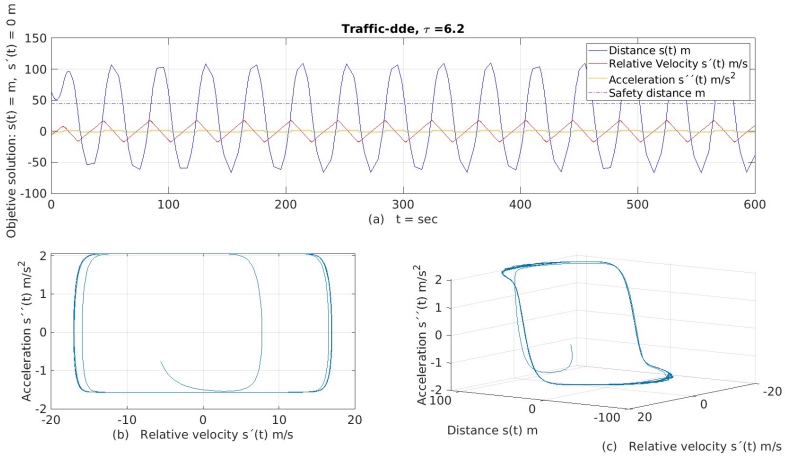


Figure 3.12: Oscillatory and unstable solution for $\tau = 6.2s$ in nDDE in [56].

3.2.4 nDDEa model development and evaluation

The nDDE model introduced in [56] considers a dependence of the acceleration function $g(s, s')$ with respect to the distance s and relative speed s' with a smooth variation of the acceleration $(g(s, s') > 0)$ and deceleration $(g(s, s') < 0)$ values near the equilibrium line $(g(s, s') = 0)$, as shown in Figure 3.14 Nevertheless, once the deviation on s or s' is significant, the acceleration and deceleration values easily reach the maximum values. For the model to be more realistic, it should be expected that the acceleration and deceleration processes would be somewhat more progressive.

For the deceleration action one can expect great variations in the values, if needed (by

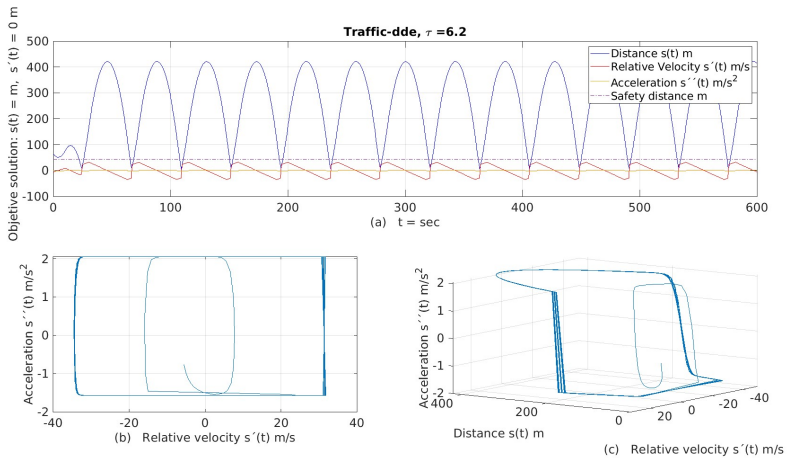


Figure 3.13: Oscillatory and unstable solution for $\tau = 6.2s$ in nDDE using the *ns-3* simulation.

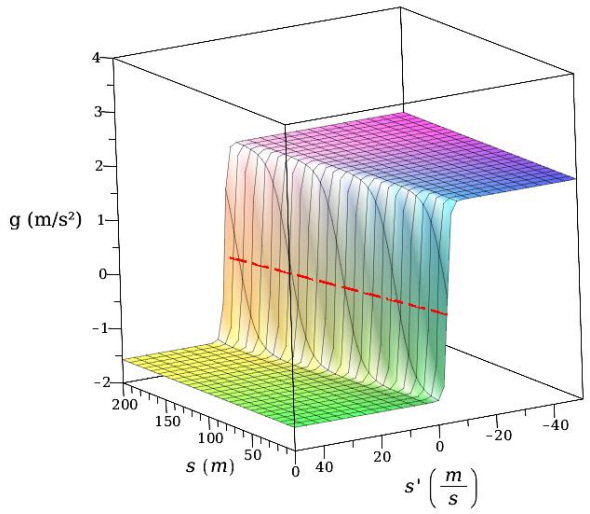


Figure 3.14: A typical nDDE function (the equilibrium line $g(s, s') = 0$ in dashed red line).

the action of variably pressing the brakes), but for the acceleration process it is physically impossible to accelerate over the limits imposed by the engine-gear mechanism. Indeed, the maximum acceleration achievable is dependent not only on a given engine power output, but also on the vehicle speed and the gear engaged. This is measured in the typical acceleration diagrams provided by car manufacturers, as shown in Figure 3.15

So it is expected that the real acceleration process is smoother than the one in the original nDDE model, with the maximum acceleration a dependent on the velocity. For the purpose of this analysis, we consider a simple function to model the acceleration process:

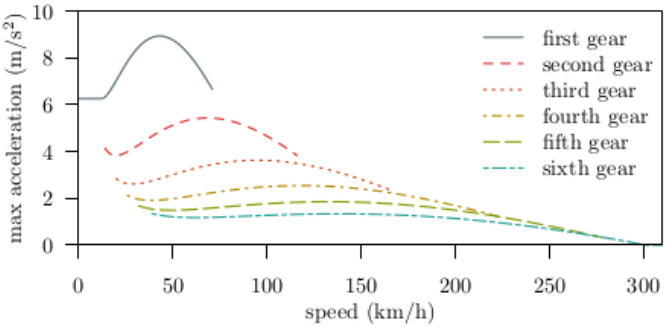


Figure 3.15: Example of acceleration diagram (from [63])

$$a(s') = \frac{2}{3} e^{0.25 - \frac{((v_0 - s') + 10)^2}{400}} ((v_0 - s') + 10) \quad , \tag{3.4}$$

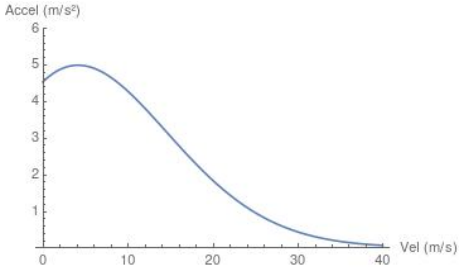


Figure 3.16: Maximum acceleration function

where we have used the relationship between the absolute and relative velocities $v = v_0 - s'$. This function emulates the progressive decrease of the maximum acceleration when the vehicle gains speed, until it is not capable of accelerating near a maximum speed (in this case, 40 m/s).In this way, the nDDE model is transformed on account of this maximum acceleration:

$$-s''(t+r) = g(s, s') = a(s') - \frac{(a(s') + b)}{1 + \frac{b}{a(s')} e^{d(s - M + Ks')}}, \forall (s, s') \in \mathbb{R}^2 \quad . \tag{3.5}$$

Figure 3.17 shows how the shape of the dependency changes for positive values of acceleration. It is worth noting that the equilibrium line ($g(s, s') = 0$) is the same both in figures 3.14 and 3.17. Therefore, it can be expected that the dynamics of the system near the equilibrium state will be similar in both versions of the nDDE model. It is the acceleration behaviour far from the equilibrium that is changed, which has an effect of improving the model behaviour from a macroscopic point of view.

For the sake of clarity, in the rest of the thesis we will refer to the original nDDE model in ([56]) as nDDE, and to the second one including the maximum acceleration limit as nDDEa.

Figure 3.18 shows the simulation of the evolution in $t = 100s$ and $t = 120s$ of a traffic flow of the OVM model that initially is stable with an equilibrium distance $s_{init} = 50m$ and an

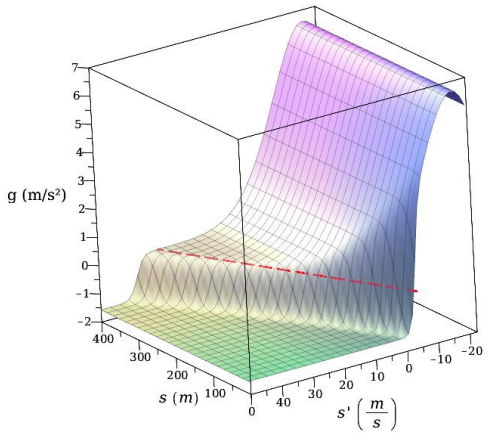


Figure 3.17: nDDE model with maximum acceleration dependent on velocity (the equilibrium line $g(s, s') = 0$ in dashed red line).

initial velocity $v_{init} = 22.2222m/s$, when the delay is $r = 0.45s > r_{lim}$. The evolution for 50 vehicles in the simulation (index 251 to 300) is shown. The propagating density waves are manifested in groups of vehicles with similar velocities and distances (stop and go traffic), groupings that are backwards propagated in the road to the following vehicles.

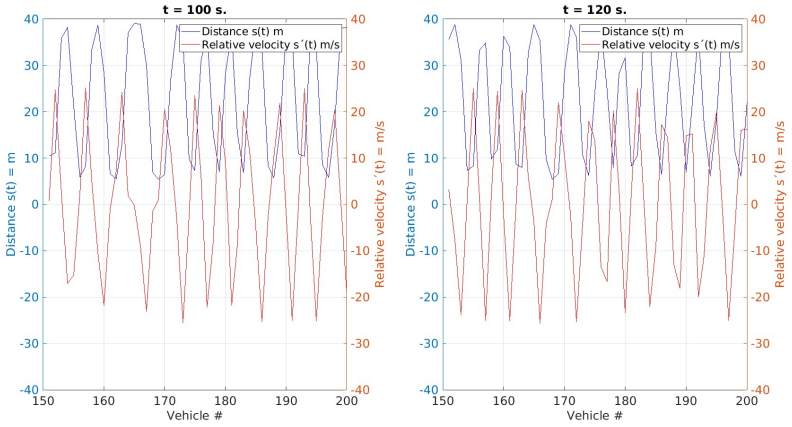


Figure 3.18: Distance and velocity evolution for OVM simulation. $\tau = 0.5s$, $t = 100s, 120s$.

It can be seen that the changes of velocity of the OVM model are rather sudden due to the high values for the acceleration and deceleration characteristic of this model. Therefore, vehicles switch between maximum to minimum velocity quite suddenly, which is not very realistic.

To check the adequacy of the nDDE model to study macroscopic traffic evolution, similar scenarios have been simulated with nDDE and nDDEa acceleration models. Figure 3.19 represents the evolution for nDDE model. This model shows a higher stability, due to the inclusion in the acceleration calculation of the relative velocity, instead of just the distance

like in the OVM model. In this instance instability sets in for higher values of the delay (we used $r = 3s$), but the shape of the density waves is similar due to the similar values of acceleration inherent to both models, if only in the nDDE case, as opposed to the OVM model, the acceleration and deceleration curves are not symmetric with respect to the variable s.

In Figure 3.20 the same evolution for the nDDEa model is presented. In this case we observe a smoother transition from the stop situation to the higher speeds as a result of the application of the maximum acceleration dependence on the velocity. This also produces groups with a higher number of vehicles, which seems more in agreement with reality. So, these preliminary

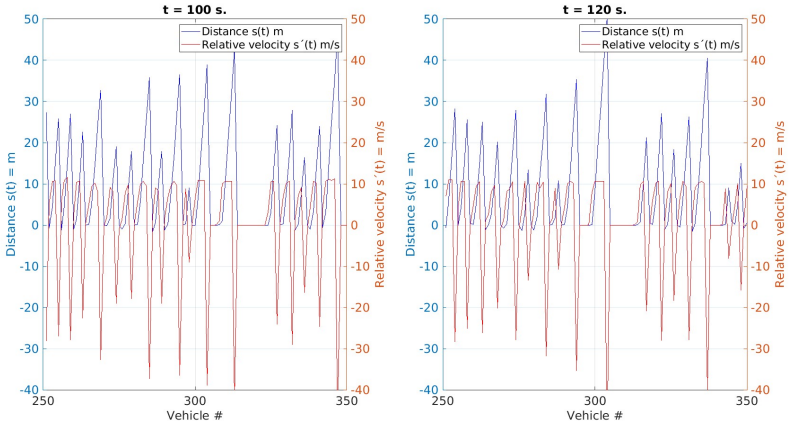


Figure 3.19: Distance and velocity evolution for nDDE model simulation. $\tau = 3s$, $t = 100s, 120s$.

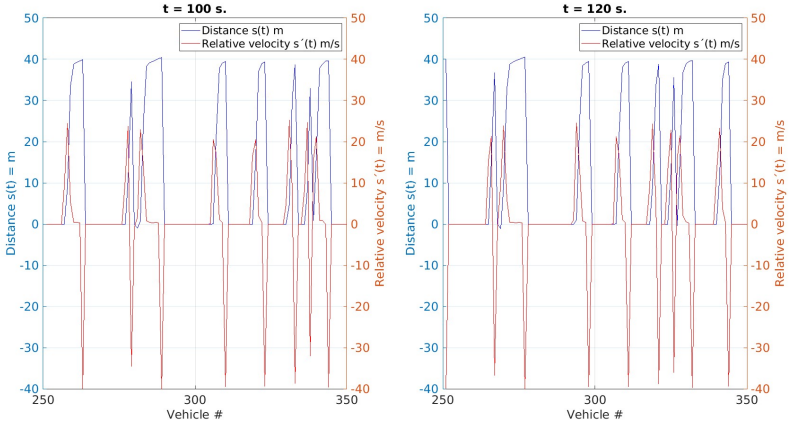


Figure 3.20: Distance and velocity evolution for nDDEa model simulation. $\tau = 3s$, $t = 100s, 120s$.

results indicate that the nDDE models reproduce the behaviour expected at the macroscopic scale (wave formation and propagation), and, when a realistic function for the acceleration process is used in nDDEa, it provides a more realistic traffic representation.

3.2.5 First evaluation of the coupled system vehicles - network

The effect of introducing a variable delay in the nDDEa model as an effect of communications congestion has been simulated. First we focus on the impact on the microscopic modelling, and later we provide some comments on the macroscopic modelling.

Microscopic behaviour of nDDE model with variable delay

The consideration of the dependence of the delay on the traffic density introduces and additional degree of complexity if we want to consider that the changes in density could influence the velocity of all the vehicles, including the leader. In such a model, equations (2.99) to (2.101) become (for a general vehicle n inside the traffic flow):

$$s_n(t) = (y_{n+1}(t) - y_n(t)) \quad , \tag{3.6}$$

$$s'_n(t) = (y'_{n+1}(t) - y'_n(t)) \quad , \tag{3.7}$$

$$s''_n(t) = (y''_{n+1}(t) - y''_n(t)) \quad . \tag{3.8}$$

So, given that now the velocity of the leader is not constant, the reaction of the follower would be:

$$s''_n(t+r) = g(s(t), s'(t), y'_{n+1}(t)) + y''_{n+1}(t) \tag{3.9}$$

where now we consider $y'_{n+1}(t)$ instead of a constant velocity v_0, and the effect on the acceleration of the leader.

In a traffic system with N vehicles, this provides the basis for a system of N second order differential equations which is not autonomous. This complicates the analysis considerably, and do not allow the same study of the structure of the solutions at the Hopf bifurcation point as in [56]. We will see in Chapter 5 how to address this in the case of constant delay.

Nevertheless, we can now test the influence of the variable delay on the microscopic behaviour by considering an intermediate case, in which a simpler two-vehicle system is part of an autonomously driven platoon (with the leader maintaining constant velocity) which travel along a road with light load, but with the road in opposite direction having variable density, which would induce changes in the experienced delays (in both directions of the road).

In such a case, gathering equations (3.5), (2.134) and (2.135), we now have the following system of equations governing the dynamics of the two-vehicle system:

$$\begin{cases} s''(t + r(\rho)) = -g(s, s') = -a(s') + \frac{(a(s')+b)}{1+\frac{b}{a(s')}e^{d(s-M+Ks')}} & , \\ r(\rho) = \frac{1}{\alpha}e^{2\cdot\rho\cdot\alpha(D\cdot TS+2T_t(2R-D))} & , \end{cases} \tag{3.10}$$

where ρ is the density of the road in opposite direction, and we have considered the probability of collision of the MAC function in equation (2.131) as $P_C = 0$.

As an example of the impact, we first provide the results for the case in which the platoon traverses a road sector with significantly more density in the opposite road. Figures 3.21 and 3.22 show the evolution of the dynamics of the follower vehicle when the density it encounters

in the opposite road changes from 0.0225 veh./m (inter-vehicle distance of 44.44 m) to values of 0.04275 veh./m (distance 21.85 m) and 0.04725 veh./m (distance 21.16 m) respectively.

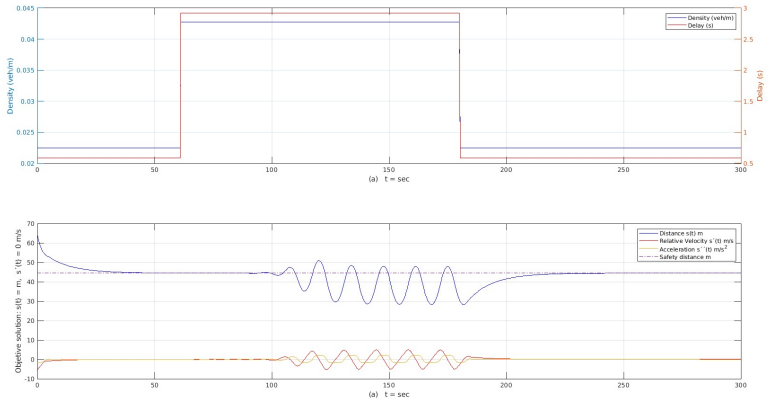


Figure 3.21: Micro evolution for delay depending on vehicle density. Density change from 0.0225 veh./m to 0.04275 veh./m.

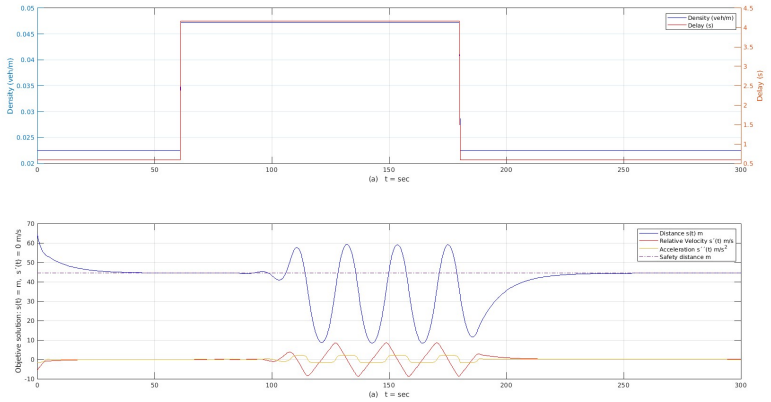


Figure 3.22: Micro evolution for delay depending on vehicle density. Density change from 0.0225 veh./m to 0.04725 veh./m.

It can be appreciated that:

- Small variations of vehicle density produce remarkably different instability oscillations (the highest density value differs only 10% in the two examples).
- The instability takes some time to set in after the density changes, and it takes a much shorter time to recover once the density and the delay have returned to lower values.

The complexity that can be produced by more complex patterns in the distribution of the density in the opposite road is illustrated in Figure 3.23.

Despite the complexity introduced by the variable delay, this scenario is relatively simple, since the delay variation is not influenced by the action of the two vehicles of the car-following model.

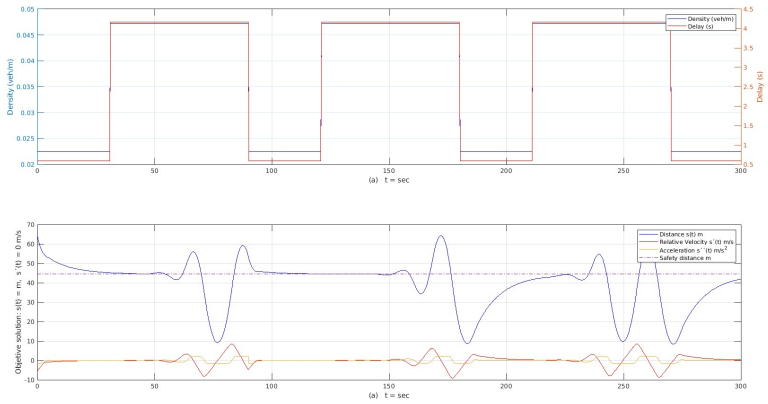


Figure 3.23: Micro evolution for delay depending on vehicle density. Density change repeatedly from 0.0225 veh./m to 0.04725 veh./m.

Nevertheless, from the point of view of the global traffic process (beyond the car-following two-car system), it is also interesting to analyze the complete coupling of the vehicles and communication system, including the feedback process that the change of the velocity of the vehicles introduce on the density of vehicles, which in turn modify the delay and therefore again the velocity.

Given the complexity associated with the system defined by equation (3.9) to analyze a multi-vehicle system following the nDDE model, to study the global behaviour of the system requires the usage of the paradigm of the macro model. We will provide some ideas about this in next section.

Macroscopic behaviour of nDDE model with variable delay

According to the classical analysis of traffic modelling (see e.g. [48] and [31]), to properly analyze the macroscopic behaviour of the nDDE model, in addition to the *continuity* equation that relates the vehicle density and the vehicle flow (2.105), it is necessary to obtain the *momentum* equation, which determines how the velocity of the traffic flow varies as a function of the density and the velocity of the neighboring vehicles. For instance, the *momentum* equation for the OVM has been provided in equation (2.124).

To derive an equivalent equation for the nDDE model would require, according to the methodology described in [41], to get some approximation of the acceleration equation that relate *explicitly* the distance, the velocity *and* the delay involved (as was done for the OVM model in equation (2.94)), i.e.:

$$-s''(t) \approx f(s(t), s'(t), r) \quad . \tag{3.11}$$

Using this equation it is feasible to derive an approximation for the *momentum* equation near the equilibrium. This characterization is part of the methods introduced in Chapter 6 of this thesis, but, taking advantage of the simulation platform developed, we will test now

the influence of the delay on the macroscopic behaviour of the nDDEa model, before having analytic results.

We have tested an scenario that is initially stable as shown in Figure 3.24, where the system is composed by 600 vehicles cruising at a velocity $v = 15,6m/s$ and an inter-vehicle distance of $s = 33.33m$, each one behaving according to the nDDEa model with constant delay $r = 0.5s$. As expected, for such low values for the delay, the traffic remains in equilibrium, maintaining the initial conditions (time $t = 100$ and $t = 150s$ are shown).

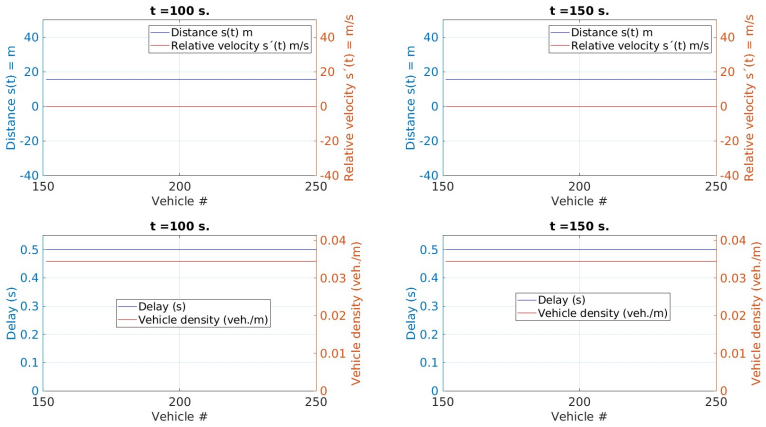


Figure 3.24: Macro evolution with density 0.03 veh./m and constant delay $\tau = 0.5s$.

The same scenario considering a variable delay induced by the changes in density is shown in figures 3.25 and 3.26. In this case, the value of density at each point x is calculated as the average of the vehicle density $\langle\rho(x)\rangle$ at the surrounding area $[x - R, x + R](R = 300m)$. The delay experienced in x is then a function of the density $r(\langle\rho(x)\rangle)$ following equation (3.10).

We show in figures 3.25 and 3.26 the evolution for several points in time, namely 20 s, 50 s, 100 s and 150 s. For practical considerations, we have limited the maximum delay in the function $r(\langle\rho(x)\rangle)$ to $r_{max} = 5s$.

- After 20 s ($t = 20s$) the system is still near the equilibrium state, with values of density and delay starting to change, which introduce variation in the distance and relative velocity.
- In $t = 50s$ the delay fluctuates heavily, and the different delays produce density waves.
- In $t = 100s$ and $t = 150s$ the density waves grow in size, and the delay fluctuates between the maximum and minimum values depending on the accumulation of vehicles.

These results show that due to the exponential dependence of the delay on the density in equation (3.10), small density variations may produce significant excursions in the delay, which in turn cause the formation of density waves that reinforce the density variations.

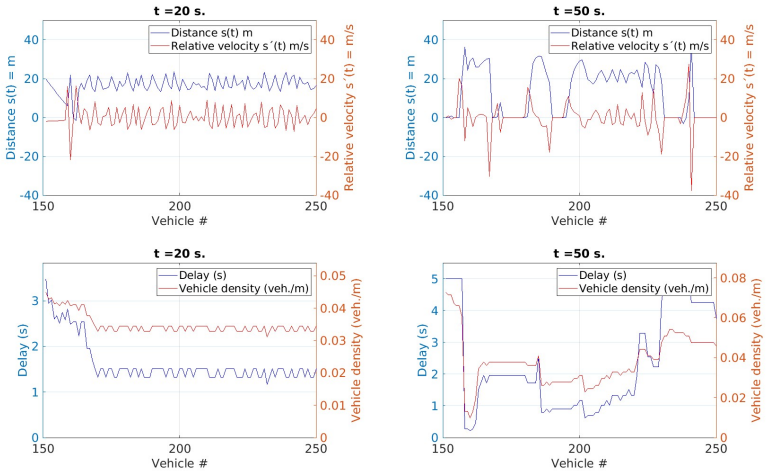


Figure 3.25: Macro evolution with density 0.03 veh./m and and variable delay dependent on the density.

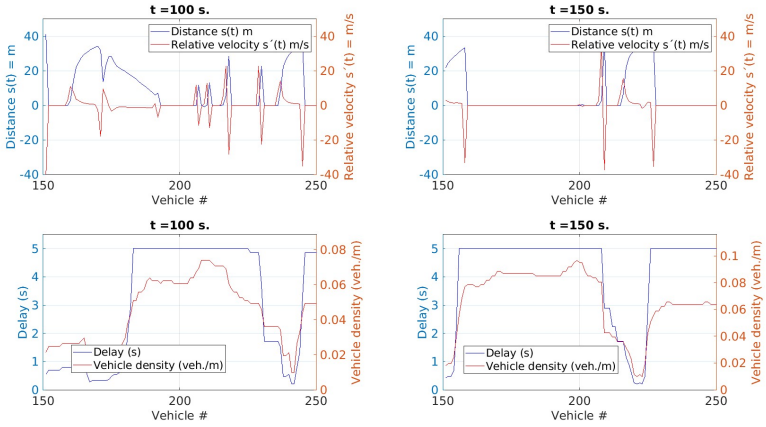


Figure 3.26: Macro evolution with density 0.03 veh./m and and variable delay dependent on the density.

3.3 Final comments

This chapter has introduced the software simulation platform built to validate the mathematical results of this thesis. The software has been validated by comparing its results with previously published simulations and to the expected behaviour of analytical models, when available. The results indicate a high degree of accuracy and the capacity of the platform to simulate different scales (micro and macro) and complex environments and interactions of the mobility and communications planes.

In this regard, it is worth noting that the platform can perform efficiently in a standard computer platform (x64, 16 GB RAM), for instance:

- Microscopic simulations of 500 seconds of simulated time in less than 30 s.

- Macroscopic scenario with > 100 nodes implementing the nDDE model during 2000 seconds of simulated time in less than 1 hour.

Chapter 4

The Hopf bifurcation in the microscopic modelling

Section 2.2.1 has given a brief historical perspective of the evolution of microscopic models. These models have been steadily improving, incorporating ever more realistic characteristics, to evolve from linear models to quite sophisticated ones, like nDDE and IDM. In spite of this, there are still aspects of microscopic modelling that have not been addressed in the literature, in particular:

1. It is needed a better characterization of the solutions of the dynamics in the interaction of a single vehicle far from the bifurcation point.
2. We lack of a clear view of how the microscopic characteristics induces the behaviour of the traffic process of many vehicles. In the existing literature, only the simplest microscopic models are linked to macroscopic equations [41].

While the second point will be the object of Chapters 5 and 6, this chapter addresses the first point by introducing a new methodology to derive explicit power series approximations for the limit cycle periodic solutions of the Hopf bifurcation in autonomous delayed difference equations (DDEs). The method extends the methodology introduced in [8] by providing a detailed algorithm that allows the automation of the iterative calculations up to any desired order of approximation, ensuring a specific error tolerance for any nonlinear DDE presenting a Hopf bifurcation. The application of the methodology is demonstrated for three relevant delay-differential models: first and foremost, the car-following model (nDDE model) introduced in previous chapters, whose oscillations are regarded as a plausible explanation of the origin of density waves and congestion in road traffic; secondly, additional illustrative examples from other relevant fields: a SIR epidemic model for propagation of diseases with temporary immunity and a macroeconomic model that takes into account the delays of the impact of aconomic policies.

The contents of this chapter have been published in the article *"Calculation of explicit expressions for the Hopf bifurcation limit cycles in delay-differential equations"* in the journal *Opuscula Mathematica*. [20]. The notation, though, will vary with respect to the published paper due to some adaptations needed to make the notation in this chapter consistent with

the rest of the thesis.

4.1 Problem statement

We consider the autonomous nonlinear delay differential equation for the vector function $\mathbf{u} \in \mathbb{R}^n$, $n \geq 1$:

$$\mathbf{u}'(t) = \mathbf{g}\left(r, \mathbf{u}(t), \mathbf{u}(t-r)\right), \tag{4.1}$$

where $t \in \mathbb{R}^+$, and $r \in \mathbb{R}^+$ is some parameter. We also consider $\mathbf{g} \in C^k(\mathbb{R}^+ \times \mathbb{R}^n \times \mathbb{R}^n; \mathbb{R}^n)$ with $k \geq 3$, and, without loss of generality, the equilibrium point of the system to be $\mathbf{u}(t) = \mathbf{0}$, at which $\mathbf{g}(r, \mathbf{0}, \mathbf{0}) = \mathbf{0} \quad \forall r \geq 0$.

This equation is a particular case of the *Retarded Functional Differential Equation (RFDE)* class defined in [29], where, in this instance, $\mathbf{g}$ presents a single, constant delay r. These equations are also known as constant discrete delay equations [66], and will be subsequently referred to as DDE. In [29] conditions for existence, uniqueness, continuity, differentiability and continuation of the equation solutions are provided. The solutions to this type of equations can undergo the Hopf bifurcation phenomenon when the parameter r is varied, such that starting from a specific threshold r_0 the solution changes from a constant equilibrium to a nonzero periodic solution. In this paper we provide a method to systematically derive explicit expressions for the oscillatory solutions of the Hopf bifurcation of equations of type (4.1) up to any desired approximation order, based on the original method introduced in [8].

In order to assess the stability of the system, the linearized approximation of (4.1) is used:

$$\boldsymbol{\eta}'(t) = \mathbf{P}(r)\boldsymbol{\eta}(t) + \mathbf{Q}(r)\boldsymbol{\eta}(t-r), \tag{4.2}$$

where $\mathbf{P}(r) = \mathbb{J}_{\mathbf{u}}\mathbf{g}(r, \mathbf{u}, \mathbf{v}) \mid_{\mathbf{u}=\mathbf{v}=\mathbf{0}}$ and $\mathbf{Q}(r) = \mathbb{J}_{\mathbf{v}}\mathbf{g}(r, \mathbf{u}, \mathbf{v}) \mid_{\mathbf{u}=\mathbf{v}=\mathbf{0}}$, and $\mathbb{J}_*$ is the Jacobian matrix with respect to variable $*$. Based on [29, 66], the following assumptions are considered:

Assumption 4.1. The linear system (4.2) has a non-constant periodic solution for some $r = r_0$, which is determined by a pair of purely imaginary roots $\{\lambda_0 = j\omega_0, \overline{\lambda}_0 = -j\omega_0\}$, $\omega_0 > 0$, in the characteristic equation of (4.2), while the other roots of the characteristic equation $\lambda_i \neq \lambda_0, \overline{\lambda}_0$ satisfy $\lambda_i \neq m\lambda_0$ for any integer m.

Assumption 4.2. By the differentiability of $\mathbf{g}$ and the implicit function theorem, there exist a continuously differentiable family of roots $\lambda(r)$ for small deviations of r for which $Re(\lambda'(r)) \neq 0$, implying that the roots $\lambda(r)$ cross the imaginary axis as r varies.

These assumptions imply that for small deviations of r_0 there exist non-constant periodic solutions for the nonlinear equation (4.1) with period close to $2\pi/\omega_0$, as stated by the *Hopf Bifurcation Theorem* (see *Theorem 1.1* in ch. 11 of [29], or *Theorem 6.1* in [66], and section 2.1.2).

Methods to derive numerical solutions for this type of bifurcations have been widely used for a long time. It is well known that regular asymptotic expansions based on a straightforward parameter variation are usually not uniformly valid due to the presence of secular terms in the expansion. To overcome this problem, techniques known as singular perturbation methods

have been introduced to find approximate solutions to ODEs bifurcations, among which the most salient are multiple scales, harmonic balance and Poincaré-Lindstedt methods [52, 71]. More recently they have also been adapted to be applied to other type of equations, like DDEs and fractional calculus equations [7, 26, 60, 73, 74]. Due to the complexity of the calculation of the higher order terms in these methods, the majority of applications have been restricted to systems of equations derived from an scalar differential equation (comparatively easier to manipulate), and the validity of the solution has been only limited to small deviations from the limit value of the bifurcation parameter.

The reference [8] established a new framework to generically tackle DDE bifurcations by extending the Poincaré-Lindstedt method for ODEs to any nonlinear autonomous DDE equation that complies with specific solvability conditions. The paper provides an existence theorem for uniformly valid asymptotic series expansions of the solution, alongside a detailed recursive algorithm for the calculation of such expansions. However, no methodical approach to solve the DDE that arise in each iteration step was provided, thus limiting the applicability of the method to lower order systems up to few orders of approximation, where these calculations are manageable. This paper extends that methodology with an algorithm to systematically perform the calculations of these intermediate DDEs, thus yielding approximate periodic solutions for equations like (4.1) up to any desired expansion order, allowing the calculation of accurate approximations even for delays significantly greater than the bifurcation delay r_0.

To illustrate the complete procedure enabled by this extended methodology, we present explicit expressions for the approximate periodic solutions for three relevant problems in the area of delayed systems. First, the original analysis of the nDDE model in [56] is expanded by providing explicit expressions for its periodic equilibrium solutions. Secondly, to illustrate applicability to other fields we provide two additional examples. One is the application to an epidemic disease transmission model (SIR model), in which temporary immunity induces oscillations and subsequent epidemic waves, and for which an explicit relationship between the immunity period and the frequency and strength of these waves can be derived. The other is the application to a financial model that combines the interaction between inflation, interest rate and investment level as an explanation of the apparition of macroeconomic cycles.

4.2 Poincaré-Lindstedt method applied to DDEs

4.2.1 General overview of the method

The Poncaré-Lindstedt method for DDEs requires a number of sequential transformations to the original equation so that any DDE problem is expressed in a general standard form. Therefore, in order to ease the understanding of the notation during the whole calculation process, we first provide in Table 4.1 a general outline of the different steps taken to build the solution, structured by the paper section where they are explained.

Section 4.2.2 details the successive changes of independent and dependent variables made to the initial equation in order to get an standard set of equations to which apply the systematic calculations. The objective is to reduce the original problem in the form (4.1) for an arbitrary value of λ, which we have denoted as DDE_t, to an standard form in which the solution is 2π

periodic, which we call DDE_z.

Section 4.2.3 introduces the method used to derive a series expansion for the solutions to this system, based on iteratively equating the terms of the same order in the differentiated series expansion and in DDE_z. The validity of the solution thus calculated is ensured by the solvability conditions and an existence theorem. The final solution is obtained by solving the nonhomogeneous linear DDE that arises in each iteration, that we have called DDE_{z_j}.

Section 4.3 will subsequently introduce a general procedure to calculate the solutions of the different DDE_{z_j} thus allowing the application of this method up to any desired series expansion order.

Section 4.2.2

$\boldsymbol{DDE_t}$ (4.1) $\xrightarrow{\substack{\hat{t}=\omega_0 t \\ \mathbf{u}(t)\to\mathbf{u}(\hat{t})}}$ $\boldsymbol{DDE_{\hat{t}}}$ (4.3) $\xrightarrow{\substack{\mathbf{u}=\varepsilon\mathbf{v} \\ \mathbf{u}\to\mathbf{v}}}$ $\boldsymbol{DDE_v}$ (4.9) $\xrightarrow{\substack{\tau=\frac{2\pi}{T(\varepsilon)}\hat{t} \\ \mathbf{v}\to\mathbf{z}}}$

$\mathbf{u}'(t) = \mathbf{g}(r, \mathbf{u}(t), \mathbf{u}(t-r)) \Longrightarrow \mathbf{u}'(\hat{t}) = \mathbf{f}(\hat{r}, \mathbf{u}(\hat{t}), \mathbf{u}(\hat{t}-\hat{r})) \Longrightarrow \mathbf{v}'(\hat{t}) = \dfrac{\mathbf{f}\left(\hat{r}, \varepsilon\mathbf{v}(\hat{t}), \varepsilon\mathbf{v}(\hat{t}-\hat{r})\right)}{\varepsilon} \Longrightarrow$

$\Downarrow$ $\Downarrow$ $\Downarrow$

$\mathbf{u}(t)$
Periodic $\frac{2\pi}{\omega_0}$ for $r = r_0$
Periodic $T > \frac{2\pi}{\omega_0}$ for $r > r_0$

$\mathbf{u}(\hat{t})$
2π periodic for $\hat{r} = \hat{r}_0 = r_0\omega_0$
$\hat{T} > 2\pi$ periodic for $\hat{r} > \hat{r}_0$
$\frac{1}{\hat{T}}\|\mathbf{u}\|_{L^2} = \kappa(\varepsilon)\varepsilon^2$

$\mathbf{v}(\hat{t})$
2π periodic for $\hat{r} = \hat{r}_0 = r_0\omega_0$
$\hat{T}(\varepsilon) > 2\pi$ periodic for $\hat{r} > \hat{r}_0$
$\frac{1}{\hat{T}(\varepsilon)}\|\mathbf{v}\|_{L^2} = \kappa(\varepsilon)$

Section 4.2.2 (contd.) ***Section 4.2.3***

$\boldsymbol{DDE_z}$ (4.10)

$\tau = \frac{2\pi}{\hat{T}(\varepsilon)}\hat{t}$, $\mathbf{v}\to\mathbf{z}$ $\Longrightarrow \mathbf{z}'(\tau,\varepsilon) = \dfrac{\hat{T}(\varepsilon)}{2\pi}\dfrac{\mathbf{f}\left(\hat{r}(\varepsilon), \varepsilon\mathbf{z}(\tau,\varepsilon), \varepsilon\mathbf{z}\left(\tau - \frac{2\pi}{\hat{T}(\varepsilon)}\hat{r}(\varepsilon), \varepsilon\right)\right)}{\varepsilon}$

Series solution
$\mathbf{z}(\tau,\varepsilon) = \sum_{j=0}^{m}\mathbf{z}_j(\tau)\varepsilon^j + O(\varepsilon^{m+1})$,
$\hat{r}(\varepsilon) = \sum_{j=0}^{m}\hat{r}_j\varepsilon^j + O(\varepsilon^{m+1})$,
$\hat{T}(\varepsilon) = \sum_{j=0}^{m}\hat{T}_j\varepsilon^j + O(\varepsilon^{m+1})$,

$\Downarrow$ $\Longrightarrow$

$\mathbf{z}(\tau,\varepsilon)$
2π periodic for all ε
$\frac{1}{2\pi}\|\mathbf{z}\|_{L^2} = \kappa(\varepsilon)$

Theorem 4.1 (Existence of solution).
$\boldsymbol{DDE_{z_j}}$ (4.20)

$$\boxed{\mathbf{z}_j'(\tau) = \mathbf{A}(\hat{r}_0)\mathbf{z}_j(\tau) + \mathbf{B}(\hat{r}_0)\mathbf{z}_j(\tau-\hat{r}_0) + \mathbf{h}_j(\tau)}$$

Table 4.1: General overview of Chapter 4 notation.

4.2.2 System of equations transformation

The Poincaré-Lindstedt method for DDEs requires a number of sequential transformations to the original equation so that any DDE problem is expressed in a general standard form. First we transform equations (4.1) and (4.2) by means of a re-scaling of the time variable, $\hat{t} = t\omega_0$, where ω_0 is the fundamental frequency of the Hopf bifurcation (see Assumption 4.1). Thus we get the $DDE_{\hat{t}}$ form of the problem:

$$\mathbf{u}'(\hat{t}) = \frac{\mathbf{g}(\hat{r}, \mathbf{u}(\hat{t}), \mathbf{u}(\hat{t}-\hat{r}))}{\omega_0} = \mathbf{f}(\hat{r}, \mathbf{u}(\hat{t}), \mathbf{u}(\hat{t}-\hat{r})), \tag{4.3}$$

$$\boldsymbol{\eta}'(\hat{t}) = \mathbf{A}(\hat{r})\boldsymbol{\eta}(\hat{t}) + \mathbf{B}(\hat{r})\boldsymbol{\eta}(\hat{t}-\hat{r}), \tag{4.4}$$

where $\hat{r} = r\omega_0$, with $\mathbf{A}(\hat{r}) = \mathbf{P}(r)/\omega_0$ and $\mathbf{B}(\hat{r}) = \mathbf{Q}(r)/\omega_0$. The particularization of (4.4) for $\hat{r} = \hat{r_0} = r_0\omega_0$ has periodic solutions with period 2π, among which we will consider a solution $\mathbf{v}_0(\hat{t})$ that verifies:

$$\frac{1}{2\pi}\int_0^{2\pi} |\mathbf{v}_0(\hat{t})|^2 d\hat{t} = 1. \tag{4.5}$$

Additionally, we denote by L the constant coefficient differential delay operator derived from (4.4) for $\hat{r} = \hat{r}_0$, that will be used in the iterative calculations in later steps of the process:

$$L\boldsymbol{\eta} = \boldsymbol{\eta}'(\hat{t}) - \mathbf{A}(\hat{r}_0)\boldsymbol{\eta}(\hat{t}) - \mathbf{B}(\hat{r}_0)\boldsymbol{\eta}(\hat{t} - \hat{r}_0), \tag{4.6}$$

and we denote the null space of the operator L as $N(L) \subset \mathbb{P}^\infty$, ($\mathbb{P}^\infty$ being the subspace of C^∞ of 2π periodic vector functions). In the specific case of the Hopf bifurcation, the single pair of eigenvalues assumed in Assumption 4.1 determines a dimension $l = 2$, so we will consider a fixed orthonormal basis $\{\boldsymbol{\phi}_1(\hat{t}), \boldsymbol{\phi}_2(\hat{t})\}$ for the space $N(L)$.

It will also be necessary to consider the formal adjoint operator L^*:

$$L^*\boldsymbol{\eta} = \boldsymbol{\eta}'(\hat{t}) + \mathbf{A}^T(\hat{r}_0)\boldsymbol{\eta}(\hat{t}) + \mathbf{B}^T(\hat{r}_0)\boldsymbol{\eta}(\hat{t} + \hat{r}_0), \tag{4.7}$$

with $\dim(N(L^*)) = \dim(N(L)) = 2$ and a fixed orthonormal basis of the space $N(L^*)$ $\{\boldsymbol{\phi}_1^*(\hat{t}), \boldsymbol{\phi}_2^*(\hat{t})\}$, $\mathbf{A}^T$ and $\mathbf{B}^T$ being the transposes of $\mathbf{A}$ and $\mathbf{B}$ respectively.

The Poincaré-Lindstedt method for DDEs is based on the search of the periodic solutions of (4.3) by means of an expansion parameter ε, defined, for convenience, as:

$$\frac{1}{\hat{T}}\int_{\hat{T}} |\mathbf{u}(\hat{t})|^2 d\hat{t} = \kappa(\varepsilon)\cdot\varepsilon^2, \tag{4.8}$$

where $\mathbf{u}(\hat{t})$ is the periodic solution with period $\hat{T}$ that arise in the Hopf bifurcation for the delay $\hat{r}$, and $\kappa(\varepsilon)$ is a scaling factor that will be determined during the solution construction (see Remark 1). In this way, for any $\varepsilon > 0$ we can change the dependent variable $\mathbf{u}(\hat{t}) = \varepsilon\mathbf{v}(\hat{t})$, so that (4.3) and (4.8) are transformed into the DDE_v form of the problem :

$$\mathbf{v}'(\hat{t}) = \begin{cases} \dfrac{\mathbf{f}\left(\hat{r}, \varepsilon\mathbf{v}(\hat{t}), \varepsilon\mathbf{v}(\hat{t} - \hat{r})\right)}{\varepsilon} & \text{for } \varepsilon \neq 0, \\ \mathbf{A}(\hat{r})\mathbf{v}(\hat{t}) + \mathbf{B}(\hat{r})\mathbf{v}(\hat{t} - \hat{r}) & \text{for } \varepsilon = 0, \end{cases} \tag{4.9}$$

$$\frac{1}{\hat{T}(\varepsilon)}\int_0^{\hat{T}(\varepsilon)} |\mathbf{v}(\hat{t})|^2 d\hat{t} = \kappa(\varepsilon),$$

where the implicit dependence of the period $\hat{T}$ on ε is noted.

Finally, the time variable is again re-scaled as $\tau = (2\pi/\hat{T}(\varepsilon))\cdot\hat{t}$, so that the solution is periodic 2π in τ for any $\hat{r}(\varepsilon) > \hat{r}_0$, noting now the implicit dependence of $\hat{r}$ on ε. We then define:

$$\mathbf{z}(\tau, \varepsilon) = \mathbf{v}\left(\frac{\hat{T}(\varepsilon)}{2\pi}\tau\right),$$

so, $\mathbf{z}(\tau,\varepsilon) \in \mathbb{P}$ (space of with 2π periodic vector functions). Moreover, we get the expression for the DDE_z form of the problem:

$$\mathbf{z}'(\tau,\varepsilon) = \begin{cases} \dfrac{\hat{T}(\varepsilon)}{2\pi} \dfrac{\mathbf{f}\left(\hat{r}(\varepsilon), \varepsilon\mathbf{z}(\tau,\varepsilon), \varepsilon\mathbf{z}\left(\tau - \frac{2\pi}{\hat{T}(\varepsilon)}\hat{r}(\varepsilon), \varepsilon\right)\right)}{\varepsilon} & \text{for } \varepsilon \neq 0, \\ \mathbf{A}(\hat{r}_0)\mathbf{z}(\tau,0) + \mathbf{B}(\hat{r}_0)\mathbf{z}(\tau - \hat{r}_0, 0) & \text{for } \varepsilon = 0, \end{cases} \tag{4.10}$$

$$\frac{1}{2\pi}\int_0^{2\pi} |\mathbf{z}(\tau,\varepsilon)|^2 d\tau = \kappa(\varepsilon). \tag{4.11}$$

Notice that for $\varepsilon = 0$ we have $\mathbf{z}(\tau,0) = \mathbf{v}_0(\tau)$, and

$$\frac{1}{2\pi}\int_0^{2\pi} |\mathbf{z}(\tau,0)|^2 d\tau = \frac{1}{2\pi}\int_0^{2\pi} |\mathbf{v}_0(\tau)|^2 d\tau = 1 = \kappa(0).$$

We finally select any linear functional $\Phi : \mathbb{P} \longrightarrow \mathbb{R}$ that verifies:

$$\Phi\mathbf{v}_0 = 0,$$

which allows us to define the additional equation:

$$\Phi\mathbf{z} = 0. \tag{4.12}$$

The role of this functional is to set a specific time reference for the solution, given that we will build a periodic solution lacking any particular initial condition. This completes the system of equations (4.10), (4.11) and (4.12), which is verified for $\varepsilon = 0$ by $\mathbf{v}_0(\tau)$.

4.2.3 Solutions as series expansion

Having set the original equations in terms of the new variables, we express the solutions of $\mathbf{z}(\tau,\varepsilon), \hat{r}(\varepsilon)$ and $\hat{T}(\varepsilon)$ as asymptotic power series expansions on ε:

$$\mathbf{z}(\tau,\varepsilon) = \sum_{j=0}^{m} \mathbf{z}_j(\tau)\varepsilon^j + O(\varepsilon^{m+1}), \tag{4.13}$$

$$\hat{r}(\varepsilon) = \sum_{j=0}^{m} \hat{r}_j\varepsilon^j + O(\varepsilon^{m+1}), \tag{4.14}$$

$$\hat{T}(\varepsilon) = \sum_{j=0}^{m} \hat{T}_j\varepsilon^j + O(\varepsilon^{m+1}), \tag{4.15}$$

where $\mathbf{z}_j : \mathbb{R}^+ \to \mathbb{R}^n$ and $\mathbf{z}_j(\tau) \in \mathbb{P}$. The values $\hat{r}_0 = r_0 \cdot \omega_0$ and $\hat{T}_0 = 2\pi$ are known. In addition we define the linear functional Φ in (4.12) as the one that zeroes the first component of the solution vector $\mathbf{z}$ in $\tau = 0$:

$$\Phi\mathbf{z} = \Phi\mathbf{z}(\cdot,\varepsilon) = \mathbf{z}^1(0,\varepsilon) = 0, \tag{4.16}$$

where the superscript $[]^1$ denotes the first component of a vector. The calculation starts by determining $\mathbf{z}_0(\tau) = \mathbf{v}_0(\tau)$ from the basis $\{\boldsymbol{\phi}_1, \boldsymbol{\phi}_2\}$ such that it verifies (4.16) :

$$\mathbf{z}_0^1(0) = 0. \tag{4.17}$$

In the following we summarize the methodology of iterative calculations introduced in [8].

Equation for order j of ε

In order to set the notation, we first note the general expression of the Taylor expansion of $\mathbf{f}(\hat{r}, \mathbf{x}, \mathbf{y})$ around the equilibrium point $(\mathbf{x}_0, \mathbf{y}_0) = (\mathbf{0}, \mathbf{0})$ as:

$$\mathbf{f}(\hat{r}, \mathbf{x}, \mathbf{y}) = \mathbf{A}(\hat{r})\mathbf{x} + \mathbf{B}(\hat{r})\mathbf{y} + \mathbf{C}(\hat{r}, \mathbf{x}, \mathbf{x}) + \mathbf{D}(\hat{r}, \mathbf{x}, \mathbf{y}) + \mathbf{E}(\hat{r}, \mathbf{y}, \mathbf{y}) + \Phi(\hat{r}, \mathbf{x}, \mathbf{y}), \tag{4.18}$$

with $\mathbf{C}, \mathbf{D}$ and $\mathbf{E}$ representing the quadratic terms of the expansion (bilinear forms), while Φ represents the remaining higher order terms.

The solution of the system is found by first introducing the series expansion of the variables ((4.13) - (4.15)) in the DDE_z equation (4.10), and equating the terms for the same powers of ε. Then we get for $j \geq 1$:

$$\mathbf{z}_j'(\tau) = \varepsilon^j \text{ term of Series} \left(\frac{\hat{T}(\varepsilon)}{2\pi} \frac{\mathbf{f}\left(\hat{r}(\varepsilon), \varepsilon\mathbf{z}(\tau, \varepsilon), \varepsilon\mathbf{z}\left(\tau - \frac{2\pi}{\hat{T}(\varepsilon)}\hat{r}(\varepsilon), \varepsilon\right)\right)}{\varepsilon} \right), \tag{4.19}$$

which, inserting in (4.19) the expression of $\mathbf{f}$ in (4.18), can be expressed for any j as the following nonhomogeneous linear DDE, that we will call DDE_{z_j}:

$$\mathbf{z}_j'(\tau) = \mathbf{A}(\hat{r}_0)\mathbf{z}_j(\tau) + \mathbf{B}(\hat{r}_0)\mathbf{z}_j(\tau - \hat{r}_0) + \mathbf{h}_j(\tau), \tag{4.20}$$

where $\mathbf{h}_j(\tau)$ depends on the terms $\mathbf{z}_k(\tau), k < j$, and verifies, by (4.6):

$$\mathbf{h}_j(\tau) = L\mathbf{z}_j \, .$$

In order to express the structure of $\mathbf{h}_j(\tau)$, we also define the linear operators $M, N : \mathbf{w} \in \mathbb{R}^n \to \mathbb{R}^n$:

$$M\mathbf{w} = \mathbf{C}(\hat{r}_0, \mathbf{z}_0(\tau), \mathbf{w}) + \frac{\mathbf{D}(\hat{r}_0, \mathbf{w}, \mathbf{z}_0(\tau - \hat{r}_0))}{2}, \tag{4.21}$$

$$N\mathbf{w} = \frac{\mathbf{D}(\hat{r}_0, \mathbf{z}_0(\tau), \mathbf{w})}{2} + \mathbf{E}(\hat{r}_0, \mathbf{z}_0(\tau - \hat{r}_0), \mathbf{w}). \tag{4.22}$$

In terms of the defined notation, the following relationship arises:

$$\mathbf{h}_j(\tau) = L\mathbf{z}_j(\tau) = \hat{T}_j\boldsymbol{\theta}(\tau) + \hat{r}_j\boldsymbol{\sigma}(\tau) + M\mathbf{z}_{j-1}(\tau) + N\mathbf{z}_{j-1}(\tau - \hat{r}_0) + \mathbf{p}_j(\tau), \tag{4.23}$$

with:

$$\boldsymbol{\theta}(\tau) = \frac{1}{2\pi}\left(\mathbf{z}_0'(\tau) + \hat{r}_0\mathbf{B}(\hat{r}_0)\mathbf{z}_0'(\tau - \hat{r}_0)\right), \tag{4.24}$$

$$\boldsymbol{\sigma}(\tau) = \mathbf{A}'(\hat{r}_0)\mathbf{z}_0(\tau) + \mathbf{B}'(\hat{r}_0)\mathbf{z}_0(\tau - \hat{r}_0) - \mathbf{B}(\hat{r}_0)\mathbf{z}_0'(\tau - \hat{r}_0), \tag{4.25}$$

where $\mathbf{A}'(\hat{r}) = \frac{\partial \mathbf{A}(\hat{r})}{\partial \hat{r}}$, $\mathbf{B}'(\hat{r}) = \frac{\partial \mathbf{B}(\hat{r})}{\partial \hat{r}}$, and $\mathbf{p}_j(\tau)$ is a 2π periodic function depending on the following variables:

$$\mathbf{p}_j(\tau) \equiv \mathbf{p}_j(\mathbf{z}_0(\tau), ..., \mathbf{z}_{j-1}(\tau), \hat{r}_0, ..., \hat{r}_{j-1}, \hat{T}_0, ..., \hat{T}_{j-1}),$$

with $\mathbf{p}_1 = \mathbf{0}$. So we get from (4.23) a different DDE for each order of ε, which expresses $\mathbf{z}_j$ in terms of $\hat{r}_k$, $\hat{T}_k$, and $\mathbf{z}_k(\tau), k = 0..j-1$.

To calculate $\mathbf{z}_j(\tau)$ we use two additional equations. From (4.16):

$$\mathbf{z}_j^1(0) = 0, \tag{4.26}$$

and, from (4.11), we define a new equation for $\mathbf{z}_j(\tau)$ by taking an arbitrary real number q_j such that:

$$\int_0^{2\pi} \langle \mathbf{z}_0(\tau), \mathbf{z}_j(\tau) \rangle \, d\tau = q_j. \tag{4.27}$$

Remark 1. The choice of the q_j is not critical for the final solution construction. Choosing different $\{q_j\}$ sets will produce different $\{\mathbf{z}_j(\tau)\}$, $\{\hat{r}_j\}$ and $\{\hat{T}_j\}$ solution sets, but all of them will eventually converge to the same solution with a different value of ε. This is the reason for introducing the scaling factor $\kappa(\varepsilon)$ in (4.8) in the solution construction: different $\{q_j\}$ sets produce different $\kappa(\varepsilon)$, but the quantity $\kappa(\varepsilon) \cdot \varepsilon^2$ in (4.8) remains constant. Nevertheless, it must also be noted that a sensible choice of the set $\{q_j\}$ will have impact on the speed of the convergence of the series to the final solution. In our numerical experience, assuming the proximity of the final solution to the initial solution $\mathbf{z}_0(\tau)$, lower values of $\{q_j\}$ produce a quicker convergence, so we use $q_j = 0 \, \forall j$ in the included examples.

Now we introduce the conditions for the system solvability.

Definition 4.1. System solvability: The system (4.10), (4.11) and (4.12) is formally solvable when the following conditions are met :

i) There exist unique $\hat{r}_1$ and $\hat{T}_1$ such that:

$$\int_0^{2\pi} \left\langle \hat{T}_1 \boldsymbol{\theta}(\tau) + \hat{r}_1 \boldsymbol{\sigma}(\tau) + M\mathbf{z}_0(\tau) + N\mathbf{z}_0(\tau - \hat{r}_0), \boldsymbol{\phi}_i^*(\tau) \right\rangle d\tau = 0 \quad i = 1, 2.$$

ii) It is verified that:

$$\int_0^{2\pi} \left\langle \hat{T}\boldsymbol{\theta}(\tau) + \hat{r}\boldsymbol{\sigma}(\tau), \boldsymbol{\phi}_i^*(\tau) \right\rangle d\tau = 0 \;\; i = 1, 2 \Longrightarrow \hat{r} = 0, \hat{T} = 0, \tag{4.28}$$

where $\{\boldsymbol{\phi}_1^*(\hat{t}), \boldsymbol{\phi}_2^*(\hat{t})\}$ is the orthonormal basis of the null space of the adjoint operator $N(L^*)$.

Remark 2. The two conditions given in Definition 4.1 are sufficient for the system (4.23), (4.26) and (4.27) to have a unique solution $\mathbf{z}_j(\tau)$ for any q_j and $\mathbf{p}_j$. Indeed, condition (4.28) means that $span(\{\boldsymbol{\theta}(\tau), \boldsymbol{\sigma}(\tau)\}) \subset N(L^*)$, so, considering the orthogonality condition of $R(L)$ with respect to the null space of the adjoint operator (i.e. $R(L) = N(L^*)^\perp$), we have:

- For any $\left\{\hat{T}_j, \hat{r}_j\right\} \subset \mathbb{R}$ such that

$$\int_0^{2\pi} \left\langle \hat{T}_j \boldsymbol{\theta}(\tau) + \hat{r}_j \boldsymbol{\sigma}(\tau), \boldsymbol{\phi}_i^*(\tau) \right\rangle d\tau = k_i,\ i = 1, 2,$$

  there exists a unique $\mathbf{o}_j(\tau) \in N(L^*)$, $\mathbf{o}_j(\tau) = -\hat{T}_j \boldsymbol{\theta}(\tau) - \hat{r}_j \boldsymbol{\sigma}(\tau)$ such that

$$\int_0^{2\pi} \langle \mathbf{o}_j, \boldsymbol{\phi}_i^*(\tau) \rangle \, d\tau = -k_i,\ i = 1, 2.$$

  Taking $\mathbf{p}_j(\tau) = \mathbf{o}_j(\tau) - M\mathbf{z}_{j-1}(\tau) - N\mathbf{z}_{j-1}(\tau - \hat{r}_0)$ ensures the verification of the orthogonality condition.

- Conversely, for any $\mathbf{p}_j(\tau) \in \mathbb{P}$ such that

$$\int_0^{2\pi} \langle \mathbf{p}_j + M\mathbf{z}_{j-1}(\tau) + N\mathbf{z}_{j-1}(\tau - \hat{r}_0), \boldsymbol{\phi}_i^*(\tau) \rangle \, d\tau = k_i,\ i = 1, 2,$$

  there exist unique $\left\{\hat{T}_j, \hat{r}_j\right\} \subset \mathbb{R}$ such that

$$\int_0^{2\pi} \left\langle \hat{T}_j \boldsymbol{\theta}(\tau) + \hat{r}_j \boldsymbol{\sigma}(\tau), \boldsymbol{\phi}_i^*(\tau) \right\rangle d\tau = -k_i,\ i = 1, 2,$$

  verifying the orthogonality condition.

This, together with equations (4.26) and (4.27) (for any q_j), ensure the uniqueness of $\mathbf{z}_j(\tau)$, which hence iteratively determine a unique solution for the system (4.10), (4.11) and (4.12).

To determine $\mathbf{h}_j(\tau)$ in equation (4.20), we first must determine the unknown values for $\hat{r}_j$ and $\hat{T}_j$. Using once again the orthogonality condition $R(L) = N(L^*)^\perp$, we get:

$$\int_0^{2\pi} \langle L\mathbf{z}_j(\tau), \boldsymbol{\phi}_i^*(\tau) \rangle \, d\tau = \int_0^{2\pi} \langle \mathbf{h}_j(\tau), \boldsymbol{\phi}_i^*(\tau) \rangle \, d\tau = 0 \qquad \text{for } i = 1, 2. \tag{4.29}$$

The system (4.29) generates two equations with the unknowns $\hat{r}_j$ and $\hat{T}_j$, which provides the desired scalar values.

Asymptotic validity of the solution

The asymptotic validity of the solution calculated with the previous algorithm is ensured by the following theorem, whose proof can be found in the original reference.

Theorem 4.1 (Casal, Freedman [8])**.** *Under Assumptions 4.1 and 4.2, for an ε small enough, a sufficient condition for the system of equations* (4.10)*,* (4.11) *and* (4.12) *to possess a unique and smooth solution $\left(\hat{r}(\varepsilon), \hat{T}(\varepsilon), \mathbf{z}(\tau, \varepsilon)\right)$, with $\mathbf{z}(\cdot, \varepsilon)$ periodic 2π, $\hat{r}(0) = \hat{r}_0$, $\hat{T}(0) = 2\pi$ and $\mathbf{z}(\tau, 0) = \mathbf{v}_0(\tau)$, is that the system is* formally solvable *in the sense of Definition 4.1.*

Under these conditions the solution $\hat{r}(\varepsilon), \hat{T}(\varepsilon), \mathbf{z}(\tau, \varepsilon)$ will possess asymptotic expansions of the form (4.13)*,* (4.14) *and* (4.15) *with the latter holding uniformly validly in τ with $\mathbf{z}_j(\tau)$ $2\pi-$periodic.*

In these expressions, the $\left(\hat{r}_j, \hat{T}_j, \mathbf{z}_j(\tau)\right)$, are recursively the solutions of (4.23)*,* (4.26) *and* (4.27)*, whose existence is guaranteed by the conditions of* formal solvability*.*

4.3 Procedure to obtain a explicit solution of a desired order

4.3.1 General expression for the solution of order j

Equation DDE_{z_j} (4.20) is the cornerstone to calculate the complete solution by an iterative process starting from $\mathbf{v}_0(\tau)$ in (4.13). In the example included in [8] the solution for these equations for orders 1 and 2 are directly presented, and there is not indication on how this is accomplished. Moreover, it is clear that for higher orders the DDE_{z_j} can become highly complex. This problem is addressed in this section, where we provide a systematic approach to derive the solution up to the desired order of expansion for systems of any differential order, which can be efficiently implemented with standard computer tools.

For each order j, after the calculation of $\hat{T}_j$ and $\hat{r}_j$, and with $\mathbf{z}_k(\tau)$ known $\forall k < j$, we look for solutions of (4.23) that are periodic 2π. Equation (4.20) generates an nonhomogeneous DDE whose homogeneous version is coincident with the particularization of (4.6) for $\hat{r} = \hat{r}_0$, i.e:

$$\begin{aligned} L\mathbf{z}_j(\tau) = \mathbf{h}_j(\tau) &= \mathbf{z}_j'(t) - \mathbf{A}(\hat{r}_0)\mathbf{z}_j(\tau) - \mathbf{B}(\hat{r}_0)\mathbf{z}_j(\tau - \hat{r}_0) \\ &= \hat{T}_j\boldsymbol{\theta}(\tau) + r_j\boldsymbol{\sigma}(\tau) + M\mathbf{z}_{j-1}(\tau) + N\mathbf{z}_{j-1}(\tau - \hat{r}_0) + \mathbf{p}_j(\tau), \end{aligned} \tag{4.30}$$

so the nonhomogeneous term $\mathbf{h}_j(\tau) \in \mathbb{P}$, and is dependent on the following variables:

$$\mathbf{h}_j(\tau) \equiv \mathbf{h}_j(\mathbf{z}_0(\tau), ..., \mathbf{z}_{j-1}(\tau), \hat{r}_0, ..., \hat{r}_j, \hat{T}_0, ..., \hat{T}_j). \tag{4.31}$$

To look for the periodic solutions $\mathbf{z}_j(\tau)$ we rely on the expression of the solution of a general linear DDE initial value problem:

$$\mathbf{u}(t) = \boldsymbol{A}\mathbf{u}(t) + \boldsymbol{B}\mathbf{u}(t - r) + \boldsymbol{\gamma}(t), \quad t \geq 0, \quad \mathbf{u}_0 = \boldsymbol{\phi},$$

where $\boldsymbol{A}, \boldsymbol{B} \in \mathbb{R}^n \times \mathbb{R}^n$, $\mathbf{u}_0$ is a continuous function $\boldsymbol{\phi}(t) : [-r, 0) \longrightarrow \mathbb{R}^n$ representing the initial condition, and $\boldsymbol{\gamma}(t) : \mathbb{R}^+ \to \mathbb{R}^n$ is the nonhomogeneous term. The solution of this linear equation can be expressed in terms of the solution for the homogeneous problem and a particular solution for the nonhomogeneous problem with null initial condition (see [29] and [66]):

$$\mathbf{u}(t) = \mathbf{u}(t, \boldsymbol{\phi}, \boldsymbol{\gamma}) = \mathbf{u}(t, \boldsymbol{\phi}, \mathbf{0}) + \mathbf{u}(t, \mathbf{0}, \boldsymbol{\gamma}).$$

Applying this principle to equation DDE_{z_j} (4.20), we will calculate the periodic solutions of this equation as:

$$\mathbf{z}_j(\tau) = \widetilde{\mathbf{z}}_j(\tau) + \widehat{\mathbf{z}}_j(\tau), \tag{4.32}$$

where $\widetilde{\mathbf{z}}_j(\tau)$ is the general homogeneous solution and $\widehat{\mathbf{z}}_j(\tau)$ the particular solution for (4.20).

Regarding $\widetilde{\mathbf{z}}_j(\tau)$, it is easily calculated from the basis of 2π periodic vectors $\boldsymbol{\phi}_i$ for the null space of the operator L given in (4.6):

$$\widetilde{\mathbf{z}}_j(\tau) = \sum_{i=1}^{2} \widetilde{c}_{ji}\boldsymbol{\phi}_i(\tau) = \widetilde{\mathbf{a}}_j \cos(\tau) + \widetilde{\mathbf{b}}_j \sin(\tau), \tag{4.33}$$

where $\widetilde{c}_{ji} \in \mathbb{R}$ and $\widetilde{\mathbf{a}}_j, \widetilde{\mathbf{b}}_j \in \mathbb{R}^n$.

The calculation of the particular solution $\widehat{\mathbf{z}}_j(\tau)$ is more involved. We start by noting the structure of the nonhomogeneous term $\mathbf{h}_j(\tau)$ in (4.31) by the following proposition.

Proposition 1.

The function $\mathbf{h}_j(\tau)$ can be expressed as a truncated Fourier series up to the index $j+1$, that is:

$$\mathbf{h}_j(\tau) = \boldsymbol{\alpha}_{j0} + \sum_{k=1}^{j+1}(\boldsymbol{\alpha}_{jk}\cos(k\tau) + \boldsymbol{\beta}_{jk}\sin(k\tau)), \tag{4.34}$$

where $\boldsymbol{\alpha}_{jk}, \boldsymbol{\beta}_{jk} \in \mathbb{R}^n$.

Proof. A solution $\mathbf{z}_0(\tau)$ to the homogeneous equation:

$$\mathbf{z}_0'(\tau) = \mathbf{A}(\hat{r}_0)\mathbf{z}_0(\tau) + \mathbf{B}(\hat{r}_0)\mathbf{z}_0(\tau - \hat{r}_0)$$

can be built from the base $\boldsymbol{\phi}_i(\tau)$:

$$\mathbf{z}_0(\tau) = \sum_{i=1}^{2} C_{0i}\boldsymbol{\phi}_i(\tau), \tag{4.35}$$

with $C_{0i} \in \mathbb{R}$.

From Assumption 4.1, the linear equation (4.2) presents a pair of pure imaginary roots $\pm j\omega_0$, so a basis $\{\boldsymbol{\psi}_i(t)\}, i = 1..2$ for the periodic solutions of equation (4.2) can have the form:

$$\boldsymbol{\psi}_i(t) = \boldsymbol{\alpha}_i\cos(\omega_0 t) + \boldsymbol{\beta}_i\sin(\omega_0 t),$$

where $\boldsymbol{\alpha}_i, \boldsymbol{\beta}_i \in \mathbb{R}^n$ can be chosen so that the basis $\{\boldsymbol{\psi}_i(t)\}$ is orthonormal. Then an orthonormal basis for the solutions of equation (4.4) can have the form:

$$\boldsymbol{\phi}_i(\hat{t}) = \boldsymbol{\psi}_i\left(\frac{\hat{t}}{\omega_0}\right) = \boldsymbol{\alpha}_i\cos(\hat{t}) + \boldsymbol{\beta}_i\sin(\hat{t}). \tag{4.36}$$

So, (4.35) and (4.36) yield that $\mathbf{z}_0$ is a first order trigonometric polynomial, that is:

$$\mathbf{z}_0(\tau) = \sum_{i=1}^{2} C_{0i}\boldsymbol{\phi}_i(\tau) = \sum_{i=1}^{2} C_{0i}(\boldsymbol{\alpha}_i\cos(\tau) + \boldsymbol{\beta}_i\sin(\tau)). \tag{4.37}$$

Recalling (4.30), the function $\mathbf{h}_j(\tau)$ has the following form in each step:

$$\mathbf{h}_j(\tau) = \hat{T}_j\boldsymbol{\theta}(\tau) + \hat{r}_j\boldsymbol{\sigma}(\tau) + M\mathbf{z}_{j-1}(\tau) + N\mathbf{z}_{j-1}(\tau - \hat{r}_0) + \mathbf{p}_j(\tau). \tag{4.38}$$

We note, for each component of $\mathbf{h}_j(\tau)$ in (4.38), the following properties:

(a) The two first terms are a linear operator on $\mathbf{z}_0(\tau)$, $\mathbf{z}_0(\tau - \hat{r}_0)$ and their first derivatives (equations (4.24) and (4.25)), thus yielding a first order trigonometric polynomial.

(b) The third and fourth terms of (4.38) increase the trigonometric order of $\mathbf{z}_{j-1}(\tau)$ in 1 by means of the bilinear forms M (4.21) and N (4.22) applied to $\mathbf{z}_{j-1}(\tau)$ and $\mathbf{z}_{j-1}(\tau - \hat{r}_0)$ respectively.

(c) $\mathbf{p}_j(\tau)$ is a trigonometric polynomial of order $j+1$ by virtue of cross products of $\mathbf{z}_k, k < j$ and their derivatives, plus the expansion term of order j of (4.18).

Finally, taking into account that the order 0 solution $\mathbf{z}_0(\tau)$ has by (4.37) a trigonometric order 1, the preceding properties $((a)-(c))$ ensure that equation (4.34) is verified for all orders of j, thus proving the proposition. □

The next Corollary enable us to calculate $\widehat{\mathbf{z}}_j(\tau)$:

Corollary 1. *The particular solution of* (4.20) $\widehat{\mathbf{z}}_j(\tau)$ *is a trigonometric polynomial of degree* $j+1$*, which can be expressed as:*

$$\widehat{\mathbf{z}}_j(\tau) = \widehat{\mathbf{a}}_{j0} + \sum_{k=1}^{j+1} (\widehat{\mathbf{a}}_{jk}\cos(k\tau) + \widehat{\mathbf{b}}_{jk}\sin(k\tau)), \tag{4.39}$$

where $\widehat{\mathbf{a}}_{jk}, \widehat{\mathbf{b}}_{jk} \in \mathbb{R}^n$.

Moreover:

$$\widehat{\mathbf{z}}'_j(\tau) = \sum_{k=1}^{j+1} (-\widehat{\mathbf{a}}_{jk}k\sin(k\tau) + \widehat{\mathbf{b}}_{jk}k\cos(k\tau)). \tag{4.40}$$

Then the particular solution can be calculated by solving the system obtained by introducing the expressions (4.39) *for* $\mathbf{z}_j(\tau)$ *and* (4.40) *for* $\mathbf{z}'_j(\tau)$ *in the identity* DDE_{z_j} (4.20)*. Equating the coefficients of the same trigonometric term in each of the* n *components produces a linear system of order* $n(2j+3)$ *which provides the desired solution for the coefficients* $\widehat{\mathbf{a}}_{jk}$ *and* $\widehat{\mathbf{b}}_{jk}$*.*

Proof. $\widehat{\mathbf{z}}_j(\tau)$ and $\widehat{\mathbf{z}}'_j(\tau)$ must have the same trigonometric degree, so by (4.20) and Proposition 1 that degree must be $j+1$. The rest is a consequence of this fact. □

4.3.2 Solution $\mathbf{z}_j(\tau)$ of DDE_{z_j}

To determine $\mathbf{z}_j(\tau)$ by (4.32) we need to have $\widetilde{\mathbf{z}}_j(\tau)$ and $\widehat{\mathbf{z}}_j(\tau)$. The particular solution $\widehat{\mathbf{z}}_j(\tau)$ has been already obtained by Corollary 1, so to uniquely determine the solution to the homogeneous equation $\widetilde{\mathbf{z}}_j(\tau)$, we get the coefficients $\widetilde{c}_{ji}$ in (4.33) for every iteration by applying the supplementary conditions for orthogonality and phase with respect to the order 0 solution $\mathbf{z}_0$.

To get $\mathbf{z}^1_j(0) = 0$ (see (4.26)), we use the expressions (4.33) and (4.39), such that:

$$0 = \mathbf{z}^1_j(0) = \widehat{\mathbf{z}}^1_j(0) + \widetilde{\mathbf{z}}^1_j(0) = \widehat{\mathbf{a}}^1_{j0} + \sum_{k=1}^{j+1} \widehat{\mathbf{a}}^1_{jk} + \widetilde{c}_{j1}\boldsymbol{\phi}^1_1(0) + \widetilde{c}_{j2}\boldsymbol{\phi}^1_2(0). \tag{4.41}$$

From (4.27), we choose $q_j = 0$ for $j \geq 1$:

$$0 = \int_0^{2\pi} \langle \mathbf{z}_j(\tau), \mathbf{z}_0(\tau)\rangle \, d\tau = \int_0^{2\pi} \langle \widehat{\mathbf{z}}_j(\tau) + \widetilde{\mathbf{z}}_j(\tau), \mathbf{z}_0(\tau)\rangle \, d\tau. \tag{4.42}$$

The system (4.41) - (4.42) provides the solution for $\widetilde{c}_{ji}, i = 1, 2$ that uniquely determine $\widetilde{\mathbf{z}}_j(\tau)$. This finishes the calculation of $\mathbf{z}_j(\tau)$.

4.3.3 Complete solution

Following this procedure, for the final solution $\mathbf{z}(\tau, \varepsilon)$ two series expansions are carried out simultaneously, one asymptotic in powers of ε, and the other Fourier-type in periods multiple of 2π.

$$\mathbf{z}(\tau, \varepsilon) = \sum_{j=0}^{N} \mathbf{z}_j(\tau)\varepsilon^j, \tag{4.43}$$

$$\mathbf{z}_j(\tau) = \mathbf{a}_{j0} + \sum_{k=1}^{j+1}(\mathbf{a}_{jk}\cos(k\tau) + \mathbf{b}_{jk}\sin(k\tau)), \tag{4.44}$$

that, together with (4.32), (4.33) and (4.39) yield:

$$\begin{aligned}
&\mathbf{a}_{j0} = \widehat{\mathbf{a}}_{j0}, && && \text{for } k = 0,\\
&\mathbf{a}_{j1} = \widehat{\mathbf{a}}_{j1} + \widetilde{\mathbf{a}}_j, && \mathbf{b}_{j1} = \widehat{\mathbf{b}}_{j1} + \widetilde{\mathbf{b}}_j, && \text{for } k = 1,\\
&\mathbf{a}_{jk} = \widehat{\mathbf{a}}_{jk}, && \mathbf{b}_{jk} = \widehat{\mathbf{b}}_{jk}, && \text{for } k > 1.
\end{aligned}$$

At last, the explicit solution to the original equation up to order N is recovered as:

$$\mathbf{u}_N(t) = \tilde{\varepsilon}\left(\mathbf{z}_0\left(\frac{2\pi}{\hat{T}(\tilde{\varepsilon})}\omega_0 t\right) + \sum_{j=1}^{N}\mathbf{z}_j\left(\frac{2\pi}{\hat{T}(\tilde{\varepsilon})}\omega_0 t\right)\tilde{\varepsilon}^j\right), \tag{4.45}$$

where $\tilde{\varepsilon}$ is the solution to the equation:

$$r = \frac{1}{\omega_0}\sum_{j=0}^{N}\hat{r}_j\tilde{\varepsilon}^j. \tag{4.46}$$

4.3.4 Error estimation

Strict error bounds for approximate solutions in systems of differential equations are difficult to calculate. For ODEs and PDEs the bounds are usually based on specific characteristics of the differential equation, and no general methodology exist. If we denote the differential problem as $\mathbf{u}' = \mathbf{f}(t, \mathbf{u})$ and $\mathbf{u}_N$ as the approximation of order N, it is usually searched a relationship of the error function calculated in some norm $\|\mathbf{u} - \mathbf{u}_N\|$, with the *residual* function $\mathbf{R}_N$ that measures how well $\mathbf{u}_N$ satisfies the differential equation:

$$\mathbf{R}_N(t) = \mathbf{u}_N'(t) - \mathbf{f}(t, \mathbf{u}_N(t)).$$

If the problem is well-posed, then it is considered that the residual represents a good measure of the deviation of the approximation from the real solution (see, for instance, [17]).

In the specific case of RFDEs of discrete type, the difficulty of the problem is compounded by the delay terms. There exist recent works that allow to calculate an error bound for

approximate periodic solutions in differential delay equations by the estimation of a set of parameters and the verification of three inequalities [25]. Nevertheless, these calculations require a significant amount of computing effort, that may be beyond the effort to calculate the approximation itself. Therefore, given this difficulty and considering the regularity of the problem we are addressing, we use in this paper for the measure of the relative error the supremum norm of the residual in $[0, \hat{T}_N]$, where $\hat{T}_N$ is the period of the approximate solution, i.e.:

$$e_{r1} = \frac{\|\mathbf{R}_N(t)\|_\infty}{\|\mathbf{u}'_N(t)\|_\infty} = \frac{\sup\left\{|\mathbf{u}'_N(t) - \mathbf{f}(t, \mathbf{u}_N(t), \mathbf{u}_N(t-r))| : t \in [0, \hat{T}_N]\right\}}{\sup\left\{|\mathbf{u}'_N(t)| : t \in [0, \hat{T}_N]\right\}}. \tag{4.47}$$

In addition to this measure of residual error, in the examples in next section we will also compare the approximate solutions with numerical integrations obtained with the solver routine for DDEs of Maple 2023 (dsolve). This numerical solution, denoted $\tilde{\mathbf{u}}(t)$, becomes quasi-periodic with a period $\tilde{T}$ after a long enough initial time t_0. In addition to numerically verify quasi-periodicity, the precise value of t_0 is further determined by the conditions $\tilde{\mathbf{u}}^1(t_0) = \mathbf{u}_N^1(0) = 0$ and $\operatorname{sgn}\left(d\tilde{\mathbf{u}}^1/dt(t_0)\right) = \operatorname{sgn}\left(d\mathbf{u}_N^1/dt(0)\right)$. Our estimation for the relative error of the calculated solution $\mathbf{u}_N(t)$ with respect to the numerical solution $\tilde{\mathbf{u}}(t)$ is thus based on this time reference:

$$e_{r2} = \frac{\|\tilde{\mathbf{u}}(t_0+t) - \mathbf{u}_N(t)\|_\infty}{\|\tilde{\mathbf{u}}(t_0+t)\|_\infty} = \frac{\sup\left\{|\tilde{\mathbf{u}}(t_0+t) - \mathbf{u}_N(t)| : t \in [0, \tilde{T}]\right\}}{\sup\left\{|\tilde{\mathbf{u}}(t_0+t)| : t \in [0, \tilde{T}]\right\}}. \tag{4.48}$$

The advantage of this approach is that in the case that the numerical method is error controlled, in the sense that $\|\mathbf{u}(t_0+t) - \tilde{\mathbf{u}}(t_0+t)\|_\infty \leq \delta$, it provides a hard bound for the absolute error of the calculated approximation $\mathbf{u}_N(t)$, that is, $\|\mathbf{u}(t_0+t) - \mathbf{u}_N(t)\|_\infty \leq \|\mathbf{u}(t_0+t) - \tilde{\mathbf{u}}(t_0+t)\|_\infty + \|\tilde{\mathbf{u}}(t_0+t) - \mathbf{u}_N(t)\|_\infty = \delta + \|\tilde{\mathbf{u}}(t_0+t) - \mathbf{u}_N(t)\|_\infty$. In this way we can determine with the aid of the numerical solution $\tilde{\mathbf{u}}(t)$ the minimum expansion order N that provides a maximum error in a specific scenario.

4.4 Numerical examples

4.4.1 nDDE car-following model

In road traffic modelling a typical micro model is the *follow-the-leader* or *car-following* model, where the driver's actions in a vehicle n are induced by the relative motion of the vehicle $n+1$ ahead. As we have seen in Section 2.2.1, these models are those that consider the influence of the inter-vehicle distance $(y_{n+1}(t) - y_n(t))$ and the difference between their respective velocities $(y'_{n+1}(t) - y'_n(t))$ [23, 24, 14, 53, 4]. We will focus on the nDDE model [56] that, as has been noted in Section 2.2.1, presents advantages from the point of view of the phenomenological explanation, and for which, conveniently, a complete analysis of the Hopf bifurcation that it presents is also provided in the original reference.

This new model represents the situation of two vehicles in a single lane (denoted as 0 for the leading car and -1 for the following car). It considers that the leading car has a constant

velocity $y_0'(t) = v_0$, and the following variables for the distance between the cars ($s(t)$) and the relative velocity ($s'(t)$):

$$s(t) = (y_0(t) - y_{-1}(t)), \qquad s'(t) = (v_0 - y'_{-1}(t)).$$

We then have $s''(t) = -y''_{-1}(t)$. We recall that the nDDE model expresses the retarded dependence of the acceleration as a function of $s(t)$ and $s'(t)$. In this way we have the system (nDDE):

$$-s''(t+r) = y''_{-1}(t+r) = g(s(t), s'(t)), \tag{4.49}$$

where g is the following sigmoid function:

$$g(s, s') = a - \frac{(a+b)}{1 + \frac{b}{a}e^{d(s-M+Ks')}}, \forall (s, s') \in \mathbb{R}^2. \tag{4.50}$$

In (4.49) and (4.50) r is the delay or reaction time, M is the equilibrium distance, d is a parameter to model the intensity of the response of the car-driver ensemble, and K is a parameter to model the driver's response according to the safe distance and the perceived relative velocity.

Reference [56] provides an analysis of the dynamical characteristics of the Hopf bifurcation, showing the change from stability to oscillatory solutions in equilibrium depending on the value of the delay term. It also characterizes the nDDE equation as a Retarded Functional Differential Equation (RFDE) [29], and studies the structure of the solutions produced by this bifurcation and its impact on the traffic process. As an application of the methodology introduced in this paper, next we use it to calculate the explicit expression for the periodic solutions arising near the bifurcation point for this model.

System of equations and equilibrium solution

We start by redefining the variables so that the equilibrium point is $\mathbf{0}$, defining $u_1 = s - M$ and $u_2 = s'$, and transforming equation (4.49) into a system of first order DDEs:

$$\begin{aligned} u_1'(t) &= u_2(t), \\ u_2'(t) &= -a + \frac{(a+b)}{1 + \frac{b}{a}e^{d(u_1(t-r)+Ku_2(t-r))}}. \end{aligned} \tag{4.51}$$

Next, we consider the linearized system:

$$\begin{aligned} u_1'(t) &= u_2(t), \\ u_2'(t) &= -D\left(u_1(t-r) + Ku_2(t-r)\right), \end{aligned} \tag{4.52}$$

where $D = d\frac{ab}{a+b}$. This system is characterized by the following matrices (as in equation (4.2)):

$$\mathbf{P} = \begin{pmatrix} 0 & 1 \\ 0 & 0 \end{pmatrix}, \qquad \mathbf{Q} = \begin{pmatrix} 0 & 0 \\ -D & -DK \end{pmatrix}.$$

In order to calculate the critical delay r_0 that produces the periodic solution of period ω_0 corresponding to the Hopf bifurcation, we proceed in the usual way to derive the characteristic equation by trying an exponential function as the eigenfunction of the system. Introducing a general solution of the form $\boldsymbol{\alpha}e^{j\omega_0 t}$, with $\boldsymbol{\alpha} \in \mathbb{R}^2$ constant, we get the characteristic equation:

$$\omega_0^2 = D(1 + jK\omega_0)e^{j\omega_0 r_0},$$

which, in turn, generates the following equations corresponding to the real and imaginary parts:

$$K = \frac{\tan(\omega_0 r_0)}{\omega_0}, \qquad D = \omega_0^2 \cos(\omega_0 r_0). \tag{4.53}$$

These two transcendental equations define the bifurcation point (ω_0, r_0).

Solution bases We get the following solution basis in terms of the scaled time $\hat{t} = \omega_0 t$:

$$\boldsymbol{\phi}_1(\hat{t}) = \frac{1}{\sqrt{\pi(1+\omega_0^2)}}(\cos(\hat{t}), -\omega_0 \sin(\hat{t})), \qquad \boldsymbol{\phi}_2(\hat{t}) = \frac{1}{\sqrt{\pi(1+\omega_0^2)}}(\sin(\hat{t}), \omega_0 \cos(\hat{t})).$$

For the adjoint system, we get the following basis in $\hat{t}$:

$$\boldsymbol{\phi}_1^*(\hat{t}) = \frac{\cos(\omega_0 r_0)}{\sqrt{\pi(1+\omega_0^2\cos^2(\omega_0 r_0))}}(\omega_0 \cos(\hat{t}), \tan(\omega_0 r_0)\cos(\hat{t}) - \sin(\hat{t})),$$
$$\boldsymbol{\phi}_2^*(\hat{t}) = \frac{\cos(\omega_0 r_0)}{\sqrt{\pi(1+\omega_0^2\cos^2(\omega_0 r_0))}}(\omega_0 \sin(\hat{t}), \cos(\hat{t}) + \tan(\omega_0 r_0)\sin(\hat{t})).$$

Explicit expression of periodic solutions

From now on we will focus on a particular case of system (4.51), using the same physical parameters as in [56], summarized in Table 4.2.

Param	Description	Value
a	Maximum acceleration in $nDDE$	2.0576 m/s^2
b	Maximum deceleration	1.5677 m/s^2
v_0	Leader velocity	22.2222 m/s
M	Safe distance for v_0	44.4444 m
d	Car + driver response intensity	0.1124
K	Driver sensitivity to s'	11.3890 s

Table 4.2: nDDE parameters for the evaluated scenario [56].

Under these conditions, the bifurcation point can be calculated numerically from (4.53):

$$\omega_0 = 1.1424, \qquad r_\mu = r_0 = 1.3079, \tag{4.54}$$

denoting the limiting delay as r_μ to remark that this limit refers to the microscopic scale of traffic. We obtain the following orthonormal base for the solutions of the linearized system (4.52):

$$\boldsymbol{\phi}_1(\hat{t}) = (0.3716\cos(\hat{t}), -0.4245\sin(\hat{t})), \qquad \boldsymbol{\phi}_2(\hat{t}) = (0.3716\sin(\hat{t}), 0.4245\cos(\hat{t})),$$

and the base for the adjoint system:

$$\boldsymbol{\phi}_1^*(\hat{t}) = (0.0492\cos(\hat{t}), -0.0431\sin(\hat{t}) + 0.5604\cos(\hat{t})),$$
$$\boldsymbol{\phi}_2^*(\hat{t}) = (-0.0492\sin(\hat{t}), -0.0431\cos(\hat{t}) - 0.5604\sin(\hat{t})).$$

We then use these values to derive the approximations to the solutions of $\mathbf{z}(\tau,\varepsilon), \hat{r}(\varepsilon)$ and $\hat{T}(\varepsilon)$ by iteratively calculating the terms $\mathbf{z}_j(\tau)$, $\hat{r}_j$ and $\hat{T}_j$ as described in Sections 4.2 and 4.3. We have performed the automation of the symbolic and numerical calculations by means of a program developed on the Maple 2023 platform.

First, using the basis of the linear system $\{\boldsymbol{\phi}_1, \boldsymbol{\phi}_2\}$, we start by selecting the fundamental solution $\mathbf{z}_0(\tau)$ so that it is compatible with the phase condition (4.17). This leads us to the choice $\mathbf{z}_0(\tau) = \sqrt{2\pi}\cdot\boldsymbol{\phi}_2(\tau)$. Using this as our first solution, we iteratively calculate the subsequent orders following the described methodology. The results are presented (up to order 5) in different tables. Table 4.3 contains the coefficients for the series expansion of $\hat{r}$ and $\hat{T}$,

Coef.	o0	o1	o2	o3	o4	o5
$\hat{r}_j$	1.4940	0.0000	0.1666	0.0000	0.0387	0.0013
$\hat{T}_j$	2π	0.0000	0.7465	0.0000	0.1814	0.0056

Table 4.3: Coefficients for series expansion of $\hat{r}$ and $\hat{T}$.

	u_1					
Trig. order	o0	o1	o2	o3	o4	o5
Const	0.0	-5.6e-01	0	-1.6e-01	-4.2e-03	-5.6e-02
$\cos(\tau)$	9.3e-01	0.0	6.3e-02	0.0	1.2e-02	4.7e-04
$\sin(\tau)$	0.0	5.7e-01	5.8e-03	1.6e-01	5.5e-03	5.4e-02
$\cos(2\tau)$		-4.7e-03	1.1e-02	1.9e-03	3.7e-03	9.2e-04
$\sin(2\tau)$		-8.9e-03	-5.7e-03	2.2e-03	-1.1e-03	1.6e-03
$\cos(3\tau)$		0.0	2.9e-03	6.8e-06	-3.7e-03	-1.3e-04
$\sin(3\tau)$			-3.7e-06	5.4e-03	9.1e-05	-3.0e-04
$\cos(4\tau)$				-1.0e-04	3.0e-04	2.5e-04
$\sin(4\tau)$				-1.2e-04	-2.6e-04	2.7e-04
$\cos(5\tau)$					3.1e-05	-2.9e-06
$\sin(5\tau)$					9.6e-07	9.4e-05
$\cos(6\tau)$						-2.3e-06
$\sin(6\tau)$						-2.3e-06

Table 4.4: Coefficients for space u_1.

up to order 5. Tables 4.4 and 4.5 contain the coefficients for each trigonometric order for the space $u_1(t)$ and the relative velocity $u_2(t)$ series expansions. Notice that Table 4.3 for the delay and period is provided in terms of the scaled time $\hat{t} = \omega_0 t$, while Tables 4.4 and 4.5 for the

u_2

Trig. order	o0	o1	o2	o3	o4	o5
Const	0.0	0.0	0.0	0.0	0.0	0.0
$\cos(\tau)$	0.0	-6.5E-01	-6.6E-03	-1.0E-01	-5.5E-03	-3.1E-02
$\sin(\tau)$	1.1	0.0	-5.5E-02	-1.0E-13	-1.1E-02	-4.1E-04
$\cos(2\tau)$		2.0E-02	1.3E-02	-7.4E-03	9.5E-04	-3.3E-03
$\sin(2\tau)$		-1.1E-02	2.5E-02	5.6E-03	5.4E-03	1.7E-03
$\cos(3\tau)$			1.3E-05	-1.8E-02	-3.1E-04	3.2E-03
$\sin(3\tau)$			1.0E-02	2.3E-05	-1.4E-02	-4.3E-04
$\cos(4\tau)$				5.5E-04	1.2E-03	-1.3E-03
$\sin(4\tau)$				-4.8E-04	1.4E-03	1.2E-03
$\cos(5\tau)$					-5.5E-06	-5.4E-04
$\sin(5\tau)$					1.8E-04	-1.7E-05
$\cos(6\tau)$						1.5E-05
$\sin(6\tau)$						-1.6E-05

Table 4.5: Coefficients for relative velocity u_2.

periodic solutions are provided in terms of the scaled time $\tau = (2\pi/\hat{T}(\varepsilon)) \cdot \hat{t} = (2\pi/\hat{T}(\varepsilon)) \cdot \omega_0 t$. It is worth noting that even when we get null values for the parameters $\hat{u}_i$ and $\hat{T}_i$, as is the case for order 1 and 3, there are still nonzero terms for those orders in the series expansion of the solution.

At this point we are already able to generate valuable insights based on these coefficients. We can, for instance, draw the bifurcation diagram for the different components of the solution by representing the maximum and minimum of the oscillations for each value of the delay. This is shown in Figure 4.1 below. Notice that this diagram is generated almost instantly from the series expansion obtained, with no need to perform numerical integrations for each value of r, as is customary when no explicit expression for the solution exists.

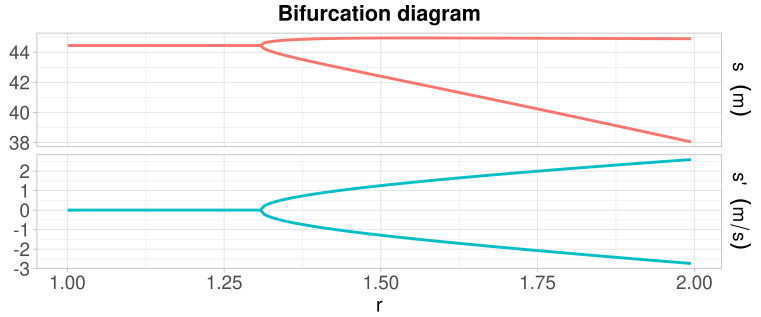
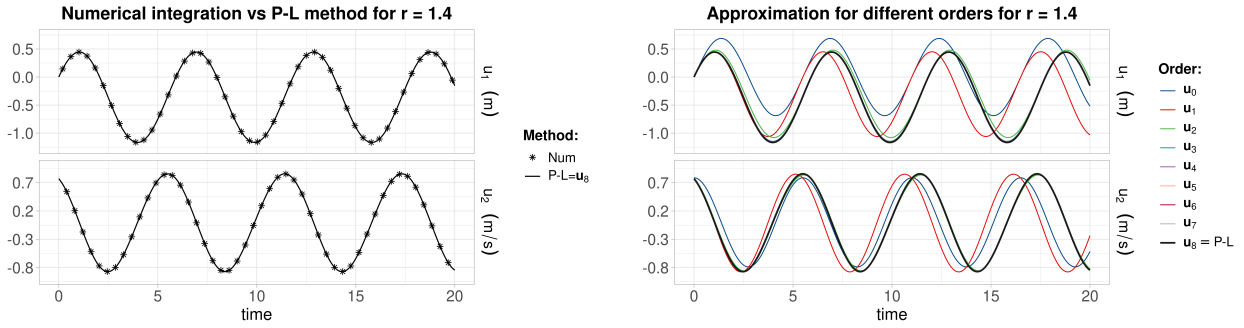


Figure 4.1: Bifurcation diagram of s and s' in the nDDE model (4.50).

More detailed results for specific values of delay follow. Given that the periodic solution for values of delay that are very close to the bifurcation value $r_\mu = 1.3079$ have very small amplitude, we test delay values sensibly greater to get oscillations with significant amplitudes. The results compare the approximation obtained with the Poincaré-Lindstedt method up to order 8 (referred to as *P-L* or $\mathbf{u}_8$ in the graphs) to the solution calculated by the numerical integration (referred to as *Num*). The Maple routine used is dsolve. In this case, using the

algorithm rkf45 with parameters abserr = relerr = 10^{-9} (for details of this solver, see [45]). The numerical integration results are calculated with an initial condition $u_1(0) = 20\ m$ and $u_2(0) = 17.22\ m/s$, taking the steady state after a sufficiently large initial time $t_0 > 1000s$, while the explicit calculation by Poincaré-Lindstedt method is directly calculated up to the order 8.

Figure 4.2a presents the comparison of the solutions of system (4.51) for a delay $r = 1.4s$. Note that in the numerical solution graph the time value is relative to t_0. As expected, the closeness of both calculations is remarkable. Figure 4.2b shows the approximate solutions for each series expansion order. In this case, the order expansions beyond order 2 have a marginal contribution to the final approximation. To get these comparable graphs we have used the same estimation for the expansion parameter $\tilde{\varepsilon} = 0.7385$.



(a) Numerical solution $\tilde{\mathbf{u}}(t_0 + t)$ and P-L calculation $\mathbf{u}_8(t)$.

(b) Approximation for each series expansion order. $\tilde{\varepsilon} = 0.7385$.

Figure 4.2: Asymptotic stable solution of u_1 and u_2 for $r = 1.4s$ in nDDE (4.51).

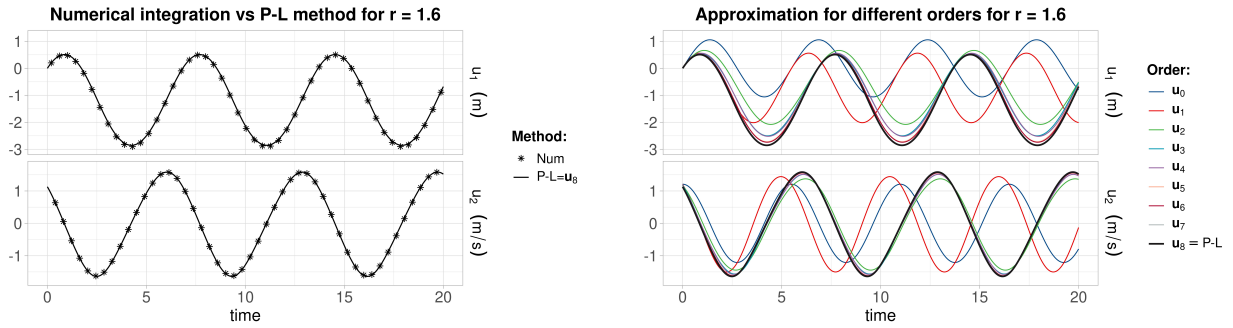
Figures 4.3a and 4.3b show the same graphs for a higher delay value of $r = 1.6s$. It can be seen that for this higher delay the shape of the solution starts to deviate from the sinusoidal shape characteristic of $\mathbf{z}_0(t)$. The approximation is remarkable close to the numerical integration, but in this case more expansion orders are needed in order to get a suitable approximation. Finally, we provide in figures 4.4a and 4.4b the same graphs for a delay $r = 1.8s$. Now the series expansions are still not sufficient even for an expansion of order 8, nevertheless more terms in the calculation would eventually provide the desired accuracy.

Error estimation

Table 4.6 contains the values for the residual e_{r1} and the relative error e_{r2} from equations (4.47) and (4.48), for the three values of delay.

The error for order 1 is not included because no estimation for the expansion parameter $\tilde{\varepsilon}$ is computable with (4.46) when only one term of the expansions is available.

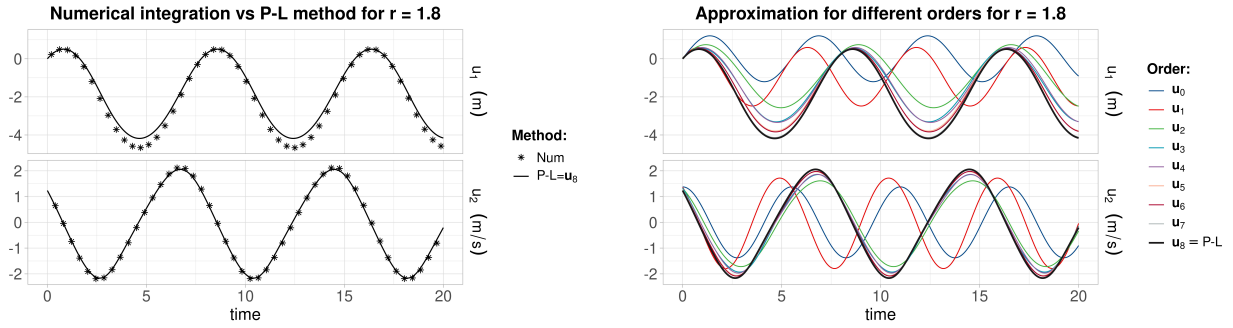
The values confirm that the residual e_{r1} is a good indicator of the level of error committed in the calculated solution $\mathbf{u}_N(t)$. Also, these values clearly show how more orders of integration are needed when the value of the delay becomes higher. In any case, calculations up to order



(a) Numerical solution $\tilde{\mathbf{u}}(t_0+t)$ and P-L calculation $\mathbf{u}_8(t)$.

(b) Approximation for each series expansion order. $\tilde{\varepsilon} = 1.1303$.

Figure 4.3: Asymptotic stable solution of $u_1(t)$ and $u_2(t)$ for $r = 1.6s$ in nDDE (4.51).



(a) Numerical solution $\tilde{\mathbf{u}}(t_0+t)$ and P-L calculation $\mathbf{u}_8(t)$.

(b) Approximation for each series expansion order. $\tilde{\varepsilon} = 1.3111$.

Figure 4.4: Asymptotic stable solution of $u_1(t)$ and $u_2(t)$ for $r = 1.8s$ in nDDE (4.51).

	$Error(\%)$	$\mathbf{u}_2$	$\mathbf{u}_3$	$\mathbf{u}_4$	$\mathbf{u}_5$	$\mathbf{u}_6$	$\mathbf{u}_7$	$\mathbf{u}_8$
$r = 1.4s$	e_{r1}	5.35	4.10	0.71	0.50	0.15	0.09	0.03
	e_{r2}	6.84	11.30	1.27	1.66	0.28	0.33	0.07
$r = 1.6s$	e_{r1}	22.29	29.03	6.68	8.84	3.05	3.93	1.57
	e_{r2}	17.30	42.04	6.35	11.32	2.76	4.49	1.37
$r = 1.8s$	e_{r1}	35.90	51.42	15.52	22.20	8.68	7.75	7.42
	e_{r2}	22.38	74.05	9.50	23.51	4.96	11.43	3.56

Table 4.6: Relative errors for the different values of r.

20 have been performed that produce relative errors below 1% for the highest delay $r = 1.8s$.

4.4.2 SIR Epidemic model

Models for infectious diseases are frequently based on the so-called compartmental models, where the population is divided in separated groups according to a person's situation with respect to the disease, typically in groups like Susceptible (S), Infected (I), Exposed (E), Recovered (R) and Asymptomatic (A). The flow of population from one group to the other

groups are modeled by a set of nonlinear differential equations that take into account the disease characteristics and the possible actions, like vaccination campaigns (see for instance [32], [13] and [6]). Specially relevant are the models with temporary immunity, in which some time after the recovery (typically some months after the natural infection or the vaccination), a recovered person in group R loses immunity and returns to the susceptible group S. Some studies in this line, using the DDE and Hopf bifurcation framework have been recently published (for instance [5], [64], [65], [58] and [43]). We provide in the following section an example of application of the method to explicitly calculate the Hopf bifurcation solutions to a SIR model with temporary immunity.

System of equations and equilibrium solution

We base the analysis on a model proposed in [6] (Ch. 10), that considers three population groups: Susceptible (S), Infected (I) and Recovered (R) (the SIR model), and a total population $P = I + S + R$. The model includes births and deaths (both related and not related to the disease), and therefore have a total population P that is variable, which makes the model somewhat more complicated. Thus, the system we will consider is the following:

$$\begin{aligned} I'(t) &= \beta S(t)I(t) - \mu I(t) - \alpha I(t), \\ S'(t) &= \Lambda(P) - \beta S(t)I(t) - \mu S(t) + f\alpha(1-\mu r)I(t-r), \\ R'(t) &= -\mu R(t) + f\alpha I(t) - f\alpha(1-\mu r)I(t-r), \end{aligned} \tag{4.55}$$

where:

- β is the contagion rate, proportional to the product of the susceptible and the infected,
- α is the output rate from the infected state, considering both the deaths and the recovered from the disease,
- f is the fraction of α that recovers, passing from the group I to the group R,
- r is the immunity period, after which the recovered pass to be susceptible again, passing from the R group to the S group,
- $\Lambda(P)$ is the birth rate and μ is the natural death rate (not related to the disease). The conditions $\Lambda(P_{max}) = \mu P_{max}$ and $\Lambda'(P_{max}) < \mu$, where P_{max} is the maximum population achievable, are necessary to ensure the asymptotic stability (see [6]), so the function that we will use is the following:

$$\Lambda(P) = \Lambda(I+S+R) = \frac{\mu(1+P_{max})P}{1+P}.$$

To evaluate the possible equilibria of the system, it is usually calculated the *basic reproduction number* ϱ_0, defined as the *expected number of secondary cases produced, in a completely susceptible population, by a typical infective individual* [12]. In the case that $\varrho_0 < 1$ then the only asymptotically stable solution is the *disease-free equilibrium* (DFE) ($I_\infty = 0, S_\infty > 0, R_\infty = 0$), i.e., all the population is susceptible and there is no disease because there are not infected individuals. If, on the other hand, $\varrho_0 \geq 1$ then there exists a state called the

endemic equilibrium (EE), with $(I_\infty > 0, S_\infty > 0, R_\infty > 0)$. Reference [13] provides the method to calculate this number for a general compartmental model based on the so called *next generation matrix*, that we have used to calculate:

$$\varrho_0 = \frac{\beta P_{max}}{\mu + \alpha} \ . \tag{4.56}$$

To calculate the equilibrium points, we solve the steady state equations for (4.55):

$$\begin{aligned} &\beta S_\infty I_\infty - (\mu + \alpha) I_\infty = 0, \\ &\Lambda(I_\infty + S_\infty + R_\infty) - \beta S_\infty I_\infty - \mu S_\infty + f\alpha(1 - \mu r) I_\infty = 0, \\ &- \mu R_\infty + f\alpha\mu r I_\infty = 0. \end{aligned} \tag{4.57}$$

Note that the endemic equilibrium solution $(I_\infty, S_\infty, R_\infty)$ in (4.57) is dependent on λ. Given that the equilibrium solution must be subtracted from the original variables (I, S, R) so that to transform the system (4.55) into a system with equilibrium $\mathbf{0}$, this considerably complicates the expressions of the matrices $\mathbf{P}(r)$ and $\mathbf{Q}(r)$ in (4.2), and therefore the calculation of the bifurcation point (r_μ, ω_0), so computer calculus tools are necessary to derive these expressions.

Explicit expression of periodic solutions

We will study an scenario based on the values of table 4.7.

Param	Description	Value
α	Output rate of infected state	0.1 (/infected/day)
β	Contagion rate	0.01 (/infected/susceptible)
μ	Death rate	10^{-4} (/pop/day)
f	Fraction of recovered	0.98
P_{max}	Maximum population	30 ($\times 10^6$)

Table 4.7: Parameters used in the study of the SIR model (4.55).

Using these values we first check the value of the basic reproduction number using (4.56), to get $\varrho_0 = 2.997 > 1$. The endemic equilibrium in this system for these values is calculated using equations (4.57):

$$\begin{aligned} I_\infty &= \frac{1.8 \cdot 10^4 r - 3.8 \cdot 10^6 + 3.6 \cdot 10^2 \sqrt{2.2 \cdot 10^2 r^2 + 3.3 \cdot 10^6 r + 1.5 \cdot 10^8}}{3.4 \cdot 10^2 r^2 + 7.7 \cdot 10^4 r + 7.5 \cdot 10^5}, \\ R_\infty &= 0.098 r \cdot I_\infty, \\ S_\infty &= 10.01. \end{aligned}$$

Taking this equilibrium point we calculate $\mathbf{P}(r)$, $\mathbf{Q}(r)$ and the characteristic equation, whose expressions are highly nontrivial and therefore are omitted here. Under these conditions, the bifurcation point is numerically calculated, yielding:

$$\omega_0 = 0.03440, \qquad r_0 = 102.0308.$$

Considering these values, we obtain the following orthonormal basis for the solutions of the linearized system in the scaled time $\hat{t} = \omega_0 t$:

$$\boldsymbol{\phi}_1(\hat{t}) = (0.0712\cos(\hat{t}), -0.3946\sin(\hat{t}), -0.0712\cos(\hat{t}) + 0.3905\sin(\hat{t})),$$
$$\boldsymbol{\phi}_2(\hat{t}) = (0.0712\sin(\hat{t}), 0.3946\cos(\hat{t}), -0.0172\sin(\hat{t}) - 0.3905\cos(\hat{t})),$$

and the basis for the adjoint system:

$$\boldsymbol{\phi}_1^*(\hat{t}) = (-0.5555\sin(\hat{t}), -0.0970\cos(\hat{t}) - 0.0178\sin(\hat{t}), -5.1\cdot 10^{-6}\cos(\hat{t}) + 2.7\cdot 10^{-5}\sin(\hat{t})),$$
$$\boldsymbol{\phi}_2^*(\hat{t}) = (0.5555\cos(\hat{t}), -0.0970\sin(\hat{t}) + 0.0178\cos(\hat{t}), -5.1\cdot 10^{-6}\sin(\hat{t}) - 2.7\cdot 10^{-5}\cos(\hat{t})).$$

We now use these bases to derive the approximations to the solutions of $\mathbf{z}(\tau,\varepsilon), \hat{r}(\varepsilon)$ and $\hat{T}(\varepsilon)$ using the script developed. Again, we choose as the fundamental solution $\mathbf{z}_0(\tau) = \sqrt{2\pi}\cdot\boldsymbol{\phi}_2(\tau)$ so that it is compatible with the phase condition (4.17). Using this as our first solution, we iteratively calculate the subsequent orders following the described methodology. In this instance we just reproduce the results for the coefficients for the series expansion of $\hat{r}$ and $\hat{T}$, up to order 5 (in terms of the scaled time $\hat{t} = \omega_0 t$):

Coef.	o0	o1	o2	o3	o4	o5
$\hat{r}i$	3.510	0	0.0239	0	$3.3\cdot 10^{-4}$	$-4\cdot 10^{-6}$
$\hat{T}_i$	2π	0	0.0398	0	$5.1\cdot 10^{-4}$	$-6\cdot 10^{-6}$

Table 4.8: Coefficients for series expansion of r and $\hat{T}$.

I

Trig. order	o0	o1	o2	o3	o4	o5
Const	0.0	0.0	0.0	0.0	0.0	0.0
$\cos(\tau)$	1.8e-01	0.0	-1.1e-03	-1.7e-05	-6.8e-06	-1.1e-07
$\sin(\tau)$	0.0	1.3e-02	3.6e-05	2.8e-05	-2.1e-06	4.5e-07
$\cos(2\tau)$		2.4e-03	1.9e-03	-3.3e-05	1.1e-05	-7.5e-07
$\sin(2\tau)$		-1.3e-02	3.4e-04	9.2e-05	1.9e-06	1.3e-06
$\cos(3\tau)$			-6.8e-04	8.2e-05	7.7e-06	3.2e-07
$\sin(3\tau)$			-3.8e-04	-1.5e-04	7.6e-06	-1.5e-06
$\cos(4\tau)$				-3.3e-05	-7.6e-06	9.9e-07
$\sin(4\tau)$				2.6e-05	-9.5e-06	-4.6e-07
$\cos(5\tau)$					5.5e-07	-7.8e-07
$\sin(5\tau)$					2.2e-06	2.0e-07
$\cos(6\tau)$						1.1e-07
$\sin(6\tau)$						2.3e-08

Table 4.9: Coefficients for Infected variable I.

Figure 4.5 shows the bifurcation diagram in this model. Note the non-constant endemic equilibrium solution for delays smaller than the bifurcation value $r_0 = 102.03$ days. Computations for these graphs with a resolution of 200 points took less than 30 seconds with a solution expansion of order 14 using the Maple 2023 platform. The results for the approximation obtained with the Poincaré-Lindstedt method compared to the solution calculated by numerical integration are presented next. The numerical integration results are calculated with the

S

Trig. order	o0	o1	o2	o3	o4	o5
Const	0.0	0.0	0.0	0.0	0.0	0.0
$\cos(\tau)$	0.0	-7.1e-02	1.7e-03	-5.9e-04	3.3e-05	-9.1e-06
$\sin(\tau)$	9.9e-01	0.0	2.5e-05	4.1e-05	-6.8e-07	6.0e-07
$\cos(2\tau)$		6.8e-04	-3.8e-03	7.9e-05	-4.2e-05	1.9e-06
$\sin(2\tau)$		2.6e-02	9.8e-05	-5.8e-05	8.6e-06	-1.5e-06
$\cos(3\tau)$			6.3e-04	1.9e-04	-1.5e-05	3.3e-06
$\sin(3\tau)$			-8.8e-04	1.4e-04	3.6e-06	-1.8e-08
$\cos(4\tau)$				3.9e-05	1.9e-05	-1.5e-06
$\sin(4\tau)$				-6.7e-05	1.1e-05	1.0e-06
$\cos(5\tau)$					-1.2e-06	2.7e-07
$\sin(5\tau)$					-7.5e-07	-4.2e-07
$\cos(6\tau)$						-1.7e-07
$\sin(6\tau)$						5.4e-08

Table 4.10: Coefficients for Susceptible variable S.

R

Trig. order	o0	o1	o2	o3	o4	o5
Const	0.0	0.0	0.0	0.0	0.0	0.0
$\cos(\tau)$	-1.8e-01	7.1e-02	-6.1e-04	6.0e-04	-2.6e-05	9.1e-06
$\sin(\tau)$	-9.8e-01	-1.3e-02	-5.8e-05	-7.0e-05	2.8e-06	-1.1e-06
$\cos(2\tau)$		-2.7e-03	1.9e-03	-4.6e-05	3.1e-05	-1.2e-06
$\sin(2\tau)$		-1.3e-02	-3.8e-04	-3.5e-05	-9.7e-06	1.8e-07
$\cos(3\tau)$			5.1e-05	-2.7e-04	7.2e-06	-3.5e-06
$\sin(3\tau)$			1.2e-03	1.1e-05	-1.1e-05	1.5e-06
$\cos(4\tau)$				-6.1e-06	-1.1e-05	4.7e-07
$\sin(4\tau)$				4.0e-05	-1.8e-06	-5.5e-07
$\cos(5\tau)$					6.0e-07	5.0e-07
$\sin(5\tau)$					-1.4e-06	2.2e-07
$\cos(6\tau)$						6.0e-08
$\sin(6\tau)$						-7.6e-08

Table 4.11: Coefficients for Recovered variable R.

initial condition of $I_0 - I_\infty = 10^{-5}$, $S_0 - S_\infty = -10^{-5}$ and $R_0 - R_\infty = 0$, taking the steady state after a sufficiently large initial time, while the explicit calculation by Poincaré-Lindstedt method is directly calculated up to the order 8.

Figure 4.6 presents the comparison of the solutions of system (4.55) for a delay $r = 120$ days, greater than the Hopf bifurcation threshold $r_0 = 102.03$ days. The solutions in the graphs represent the deviation with respect to the endemic equilibrium point ($I_\infty = 0.5896,\ S_\infty = 10.01,\ R_\infty = 6.9344$). As expected, the closeness of both calculations is remarkable. Figure 4.6b shows the approximate solution up to a certain series expansion order, using the estimation for the expansion parameter $\tilde{\varepsilon} = 1.7403$. In this case, the order expansions beyond order 4 have a marginal contribution to the final approximation.

For the sake of comparison we also provide the results up to order 8 for a delay $r = 140$ days in Figure 4.7. The endemic equilibrium point is now ($I_\infty = 0.5581,\ S_\infty = 10.01,\ R_\infty = 7.6573$). Notice that the total population in the endemic equilibrium (18.22) is different with respect

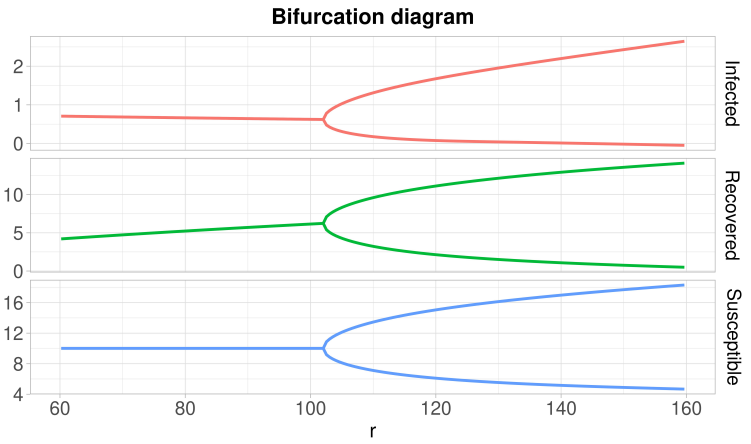
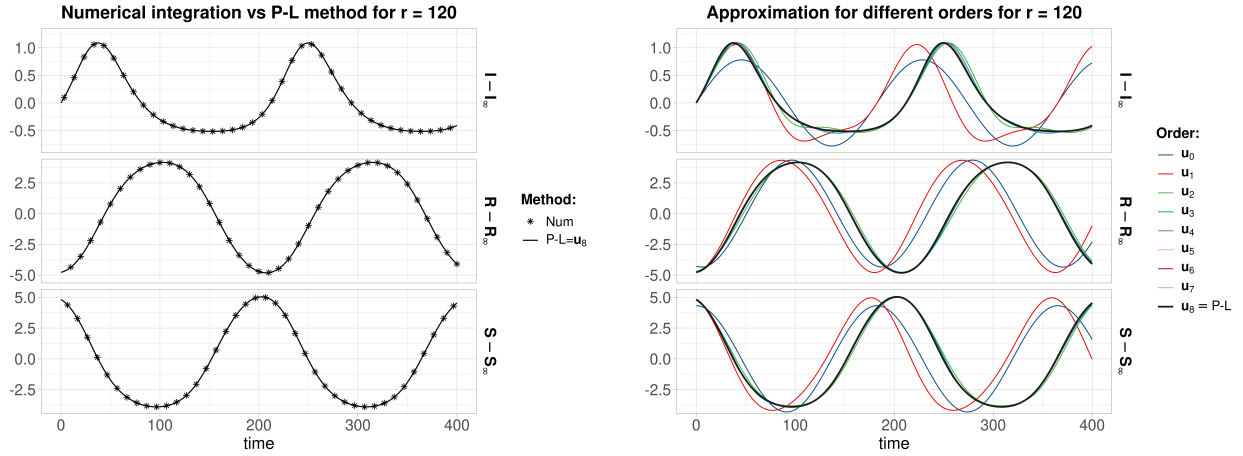


Figure 4.5: Bifurcation diagram of I, R and S in the SIR model (4.55).



(a) Numerical solution $\tilde{\mathbf{u}}(t_0+t)$ and P-L calculation $\mathbf{u}_8(t)$.

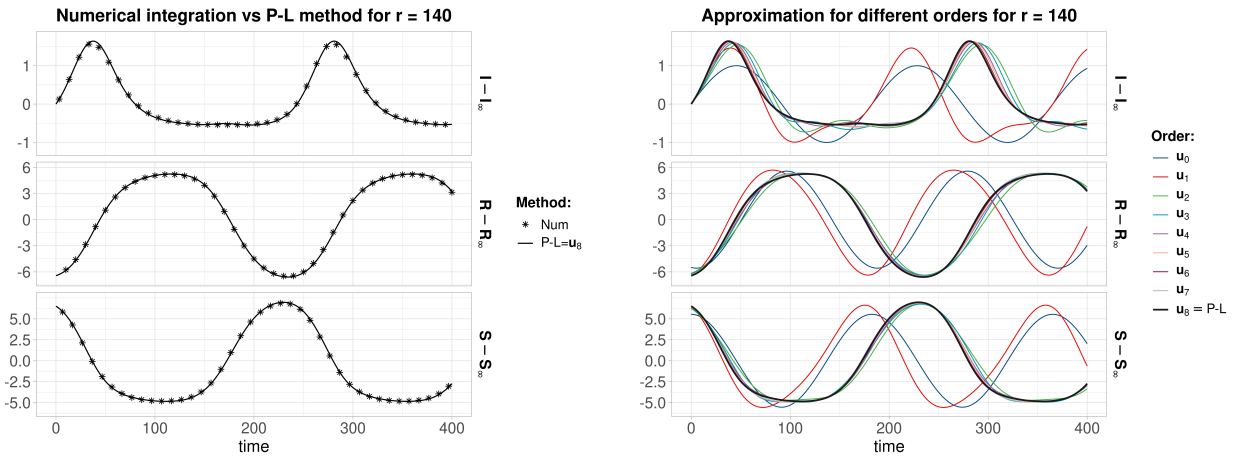
(b) Approximation for each series expansion order. $\tilde{\varepsilon} = 1.7403$.

Figure 4.6: Asymptotic stable solution of I, R and S for $r = 120$ days in model in eq. (4.55).

to the previous example (17.53). It can be appreciated that more expansion terms are needed to get an adequate accuracy for a higher delay.

Table 4.12 show the residual e_{r1} and the relative error with respect to the numerical solution e_{r2} for these scenarios. In this instance, calculations up to order 8 ensure a relative error below 1% for the lower delay $r = 120$ days, and comparable error measures using the residual instead of the approximate solution error. To get relative errors below 1% in the case $r = 140$ days we need to calculate at least the expansions up to order 12.

These results show the generality of the developed methodology to solve problems in different areas, and the applicability of the method to obtain explicit solutions in complex delayed problems, including DDEs of order greater than 2, or systems of DDEs of higher dimension.



(a) Numerical solution $\tilde{\mathbf{u}}(t_0+t)$ and P-L calculation $\mathbf{u}_8(t)$.

(b) Approximation for each series expansion order. $\tilde{\varepsilon} = 2.2063$.

Figure 4.7: Asymptotic stable solution of I, R and S for $r = 140$ days in model in eq. (4.55).

	$Error(\%)$	$\mathbf{u}_2$	$\mathbf{u}_3$	$\mathbf{u}_4$	$\mathbf{u}_5$	$\mathbf{u}_6$	$\mathbf{u}_7$	$\mathbf{u}_8$
$r = 120$ days	e_{r1}	10.47	5.17	1.88	1.34	0.62	0.47	0.16
	e_{r2}	16.42	23.28	3.06	5.06	0.72	1.60	0.33
$r = 140$ days	e_{r1}	29.87	16.03	8.51	5.91	4.39	3.11	2.14
	e_{r2}	37.33	74.45	8.64	21.43	3.40	9.58	2.94

Table 4.12: Relative errors (%) for the SIR model scenario.

4.4.3 Macroeconomic model

Finally, to further illustrate the practicality of the method, we apply it to a model frequently studied in finance analysis, which relates time series for different macroeconomic variables, namely interest rate, price index and investment demand, to study the formation of monetary cycles.

System of equations and equilibrium solution

We follow the reference [75], where an analysis of the asymptotic stability and the Hopf bifurcation characterization is offered for the following delayed macroeconomic system:

$$\begin{aligned} R'(t) &= (I(t) - \alpha)R(t) + P(t-r), \\ I'(t) &= 1 - \beta I(t) - R(t)^2, \\ P'(t) &= -R(t) - \gamma P(t), \end{aligned} \tag{4.58}$$

where $R(t)$ is the interest rate, $I(t)$ is the investment demand, $P(t)$ is the price index, $\alpha > 0$ is the saving amount, $\beta > 0$ is the cost of the investment and $\gamma > 0$ is the elasticity of demand of commercial markets. In this model it is considered that the price change does not

immediately affect the interest rate, for which there is a delay r. The original reference [75] provides a detailed analysis of the system (4.58), of which the main results follow.

We consider the equilibrium solution when $t \to \infty$ ($R(\infty) = 0, I(\infty) = \frac{1}{\beta}, P(\infty) = 0$). The linearized system around this equilibrium point is the following:

$$\begin{aligned} R'(t) &= \frac{-\alpha\beta + 1}{\beta} + P(t-r), \\ I'(t) &= -\beta I(t), \\ P'(t) &= -R(t) - \gamma P(t). \end{aligned} \tag{4.59}$$

This system is characterized by the matrices:

$$\mathbf{P} = \begin{pmatrix} \frac{-\alpha\beta+1}{\beta} & 0 & 0 \\ 0 & -\beta & 0 \\ -1 & 0 & -\gamma \end{pmatrix}, \qquad \mathbf{Q} = \begin{pmatrix} 0 & 0 & 1 \\ 0 & 0 & 0 \\ 0 & 0 & 0 \end{pmatrix}.$$

We again calculate the critical delay λ_0 and the critical periodic solution of period ω_0 corresponding to the Hopf bifurcation by means of the characteristic equation in terms of the complex variable λ:

$$(\lambda + \beta)(\lambda^2 + (\alpha + \gamma - \frac{1}{\beta})\lambda + (\alpha - \frac{1}{\beta})\gamma + e^{-zr}) = 0.$$

Apart from the obvious root $\lambda = -\beta$, we search for solutions of the form $\lambda = j\omega_0$ for a given delay r_0. It can be proved that if the condition $\alpha\beta\gamma - \gamma - \beta < 0$ holds, there exist a unique positive solution for ω_0 (see [75]):

$$\omega_0 = \sqrt{\frac{-(\alpha - \frac{1}{\beta})^2 - \gamma^2 + \sqrt{((\alpha - \frac{1}{\beta})^2 - \gamma^2)^2 + 4}}{2}}, \tag{4.60}$$

determined by the delay values:

$$r_0^i = \frac{1}{\omega_0}(\arccos(\omega_0^2 - (\alpha - \frac{1}{\beta})\gamma) + 2\pi i).$$

In [75] it is proved that these parameters determine a Hopf bifurcation asymptotically stable. We will be interested in the lowest value for the delay r_0^i:

$$r_0^0 = r_0 = \frac{1}{\omega_0}(\arccos(\omega_0^2 - (\alpha - \frac{1}{\beta})\gamma)). \tag{4.61}$$

Explicit expression of periodic solutions

We will consider the parameters for system (4.58) included in Table 4.13 (as in the original reference we use here dimensionless parameters).

Param	Description	Value
α	Savings amount	0.5
β	Cost of investment	0.8
γ	Elasticity of demand	0.8

Table 4.13: Parameters used in the study of the financial model (4.58)

Under these conditions, the equilibrium point can be calculated using (4.60) and (4.61):

$$\omega_0 = 0.6321, \qquad r_0 = 0.05.$$

Taking these values, we obtain the following orthonormal basis for the solutions of the linearized system (4.59) in the scaled time $\tau = \omega_0 t$:

$$\begin{aligned} \boldsymbol{\phi}_1(\tau) &= (0.4028\cos(\tau), 0, -0.3100\cos(\tau) - 0.2450\sin(\tau)), \\ \boldsymbol{\phi}_2(\tau) &= (0.4028\sin(\tau), 0, -0.3100\sin(\tau) + 0.2450\cos(\tau)), \end{aligned} \tag{4.62}$$

and the basis for the adjoint system:

$$\begin{aligned} \boldsymbol{\phi}_1^*(\tau) &= (-0.4028\sin(\tau), 0, -0.2546\cos(\tau) - 0.3021\sin(\tau)), \\ \boldsymbol{\phi}_2^*(\tau) &= (0.4028\cos(\tau), 0, -0.2546\sin(\tau) + 0.3021\cos(\tau)). \end{aligned}$$

Notice that in this case the function for the second component of the two bases is 0. This does not mean that the second component of the periodic solution will be null, but rather that it will be composed of terms with frequencies $n\omega_0$ with $n > 1$, as we will see.

We now use these values to derive the approximations to the solutions of $\mathbf{z}(\tau, \epsilon), \hat{r}(\epsilon)$ and $T(\epsilon)$. We have made the necessary modifications to the Maple script to perform the described calculations. e recall that he fundamental solution $\mathbf{z}_0(\tau)$ has to be compatible with the phase condition (4.17), therefore $\mathbf{z}_0(\tau) = \sqrt{2\pi} \cdot \boldsymbol{\phi}_2(\tau)$. Using this as our first solution, we iteratively calculate the subsequent orders following the described methodology. The results for the expansion of the delay and the period are presented (up to order 5) in Table 4.14.

Coef.	o0	o1	o2	o3	o4	o5
$\hat{r}_i$	0.031608	0	0.34529	0	0.18990	0
T_i	2π	0	-5.20429	0	5.55556	0

Table 4.14: Coefficients for series expansion of λ and T

Tables 4.15 , 4.16 and 4.17 contain the coefficients for each trigonometric order for the interest rate, investment and price index series expansions, respectively. Again, Table 4.14 is provided in terms of the scaled time $\hat{t} = \omega_0 t$, and Tables 4.15 , 4.16 and 4.17 are provided in terms of the scaled time $\tau = \frac{2\pi}{T(\epsilon)}\hat{t} = \frac{2\pi}{T(\epsilon)}\omega_0 t$. It is worth noting that even when the parameters $\hat{r}_i$ and T_i are null, as is the case for order 1, 3 and 5, there are still nonzero terms for those orders for the variable I. Also note that the variables R and P have null coefficients for the even trigonometric orders, while variable I has null coefficients for the odd ones. This is why the corresponding component of the fundamental solution of the linearized system (4.59) is

R

Trig. order	o0	o1	o2	o3	o4	o5
Const	0.0	0.0	0.0	0.0	0.0	0.0
$\cos(\tau)$	1.0	0.0	1.6e-01	0.0	1.4e-02	0.0
$\sin(\tau)$	0.0	0.0	1.8e-02	0.0	-1.3e-02	0.0
$\cos(2\tau)$		0.0	0.0	0.0	0.0	0.0
$\sin(2\tau)$		0.0	0.0	0.0	0.0	0.0
$\cos(3\tau)$			-1.1e-01	0.0	9.0e-02	0.0
$\sin(3\tau)$			-1.8e-02	0.0	8.7e-03	0.0
$\cos(4\tau)$				0.0	0.0	0.0
$\sin(4\tau)$				0.0	0.0	0.0
$\cos(5\tau)$					1.3e-02	0.0
$\sin(5\tau)$					4.6e-03	0.0
$\cos(6\tau)$						0.0
$\sin(6\tau)$						0.0

Table 4.15: Coefficients for Interest Rate variable R.

I

Trig. order	o0	o1	o2	o3	o4	o5
Const	0.0	-6.4e-01	0.0	-2.0e-01	0.0	-4.0e-02
$\cos(\tau)$	0.0	0.0	0.0	0.0	0.0	0.0
$\sin(\tau)$	0.0	0.0	0.0	0.0	0.0	0.0
$\cos(2\tau)$		2.9e-01	0.0	3.7e-02	0.0	-5.5e-02
$\sin(2\tau)$		1.8e-01	0.0	-9.9e-02	0.0	6.9e-02
$\cos(3\tau)$			0.0	0.0	0.0	0.0
$\sin(3\tau)$			0.0	0.0	0.0	0.0
$\cos(4\tau)$				-3.8e-02	0.0	4.6e-02
$\sin(4\tau)$				-1.9e-02	0.0	3.0e-02
$\cos(5\tau)$					0.0	0.0
$\sin(5\tau)$					0.0	0.0
$\cos(6\tau)$						4.4e-03
$\sin(6\tau)$						2.7e-03

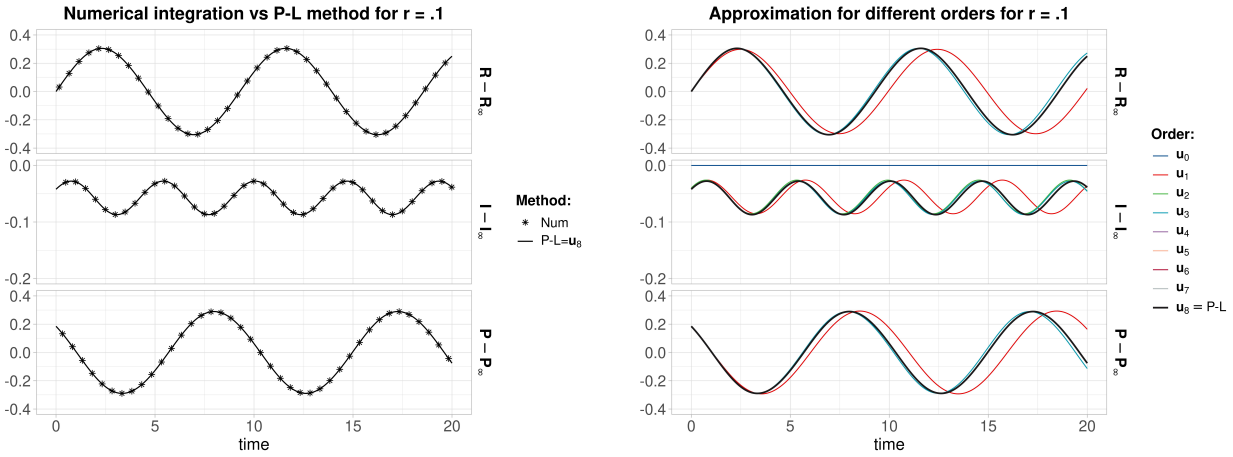
Table 4.16: Coefficients for Investment variable I.

null, as has been pointed out before. The results for the approximation obtained with the Poincaré-Lindstedt method compared to the solution calculated by numerical integration are presented below. The numerical integration results are calculated with the initial condition of $R_0 = 0.3$, $I_0 = -0.3$ and $P_0 = 0$, taking the steady state after a sufficiently large initial time, while the explicit calculation by Poincaré-Lindstedt method is directly calculated up to the order 8, (thus including the values of tables 4.14, 4.15, 4.16 and 4.17, plus values for order 6 to 8, not included in the tables). Figure 4.8a presents the comparison of the solutions of system (4.58) for a delay $r = 0.1s$, higher than the Hopf bifurcation delay $r_0 = 0.05s$. As expected, the closeness of both calculation is remarkable. Figure 4.8b shows the approximate solution up to a certain series expansion order. In this case, the order expansions beyond order 4 have a marginal contribution to the final approximation.

P

Trig. order	o0	o1	o2	o3	o4	o5
Const	0.0	0.0	0.0	0.0	0.0	0.0
$\cos(\tau)$	-7.8e-01	0.0	3.6e-01	0.0	-1.6e-01	0.0
$\sin(\tau)$	6.1e-01	0.0	2.0e-01	0.0	-2.2e-01	0.0
$\cos(2\tau)$		0.0	0.0	0.0	0.0	0.0
$\sin(2\tau)$		0.0	0.0	0.0	0.0	0.0
$\cos(3\tau)$			2.9e-02	0.0	-5.5e-02	0.0
$\sin(3\tau)$			-4.5e-02	0.0	6.2e-02	0.0
$\cos(4\tau)$				0.0	0.0	0.0
$\sin(4\tau)$				0.0	0.0	0.0
$\cos(5\tau)$					-2.3e-03	0.0
$\sin(5\tau)$					3.4e-03	0.0
$\cos(6\tau)$						0.0
$\sin(6\tau)$						0.0

Table 4.17: Coefficients for Price Index variable P.

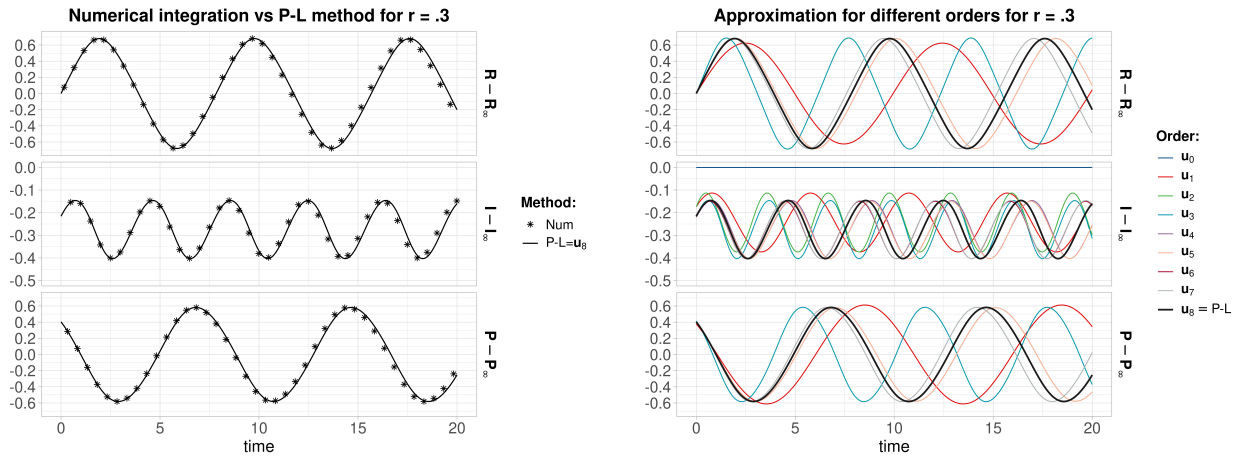


(a) Numerical solution $\tilde{\mathbf{u}}(t_0 + t)$ and P-L calculation $\mathbf{u}_8(t)$.

(b) Approximation for each series expansion order. $\tilde{\varepsilon} = 0.2956$.

Figure 4.8: Asymptotic stable solution of $R(t)$, $I(t)$ and $P(t)$ for $r = 0.1s$ in model in eq. (4.58).

Figures 4.9a and 4.9b show the same graphs for a much higher delay value of $r = 0.3s$. It can be seen again that for this higher delay value the approximation is remarkably close to the numerical integration, but in this case it is needed to calculate more expansion orders in order to get a suitable approximation.



(a) Numerical solution $\tilde{\mathbf{u}}(t_0+t)$ and P-L calculation $\mathbf{u}_8(t)$.

(b) Approximation for each series expansion order. $\tilde{\varepsilon} = 0.6173$.

Figure 4.9: Asymptotic stable solution of $R(t)$, $I(t)$ and $P(t)$ for $r = 0.3s$ in model in eq. (4.58).

Finally, the bifurcation diagram is included in figure 4.10 and the relative error in table 4.18.

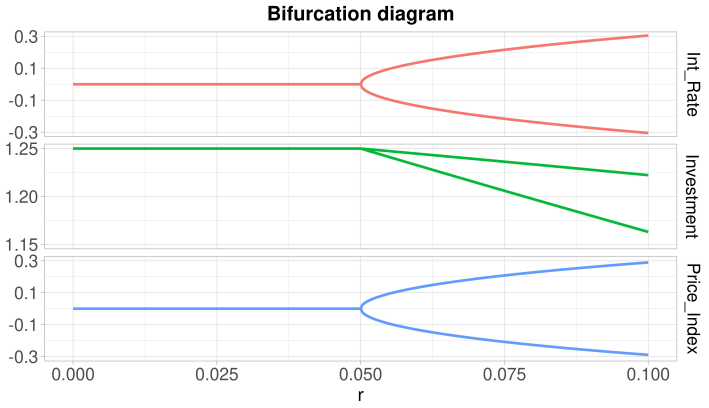


Figure 4.10: Bifurcation diagram for the macroeconomic model (4.58).

	$Error(\%)$	$\mathbf{x}_2$	$\mathbf{x}_3$	$\mathbf{x}_4$	$\mathbf{x}_5$	$\mathbf{x}_6$	$\mathbf{x}_7$	$\mathbf{x}_8$
$\lambda = 0.1$	r_r	1.2	0.52	0.10	0.06	0.01	< 0.01	< 0.01
	e_r	4.74	4.77	0.22	0.21	0.02	< 0.01	< 0.01
$\lambda = 0.3$	r_r	18.41	14.85	5.01	4.52	2.28	1.91	1.0
	e_r	78.46	79.00	13.70	13.44	7.21	7.05	3.42

Table 4.18: Relative errors (%) for the macroeconomic model scenario.

These results show the adequacy of the developed methodology to face quite different problems, and the applicability to higher dimensional problems than second order DDEs as is the nDDE case. We further illustrate this feature with an additional example in next section.

4.5 Final comments

This chapter has introduced a complete methodology and technical result for the calculation of precise series expansions for the periodic solutions that stem in the vicinity of the Hopf bifurcations in DDEs. The methodology extends the general methodology provided in [8], allowing the implementation of the iterative calculations using any modern symbolic and numerical computation system, and enabling to carry on the calculations up to the desired order expansion, with the only possible limitation of the numerical precision and memory capacity of the computing platform.

This methodology offers clear advantages over existing numerical integration methods when calculating precise periodic solutions for Hopf bifurcations in DDEs: on the one hand, numerical integration methods require additional checks to ensure that the solution has reached the periodic phase after the initial transient phase, which may be time consuming, specially in systems in which the frequency and amplitude of the solution converge very slowly in time; on the other hand, this method allows for precise calculations of the frequency and amplitude of the steady-state solution instantly, taking advantage of pre-computed coefficients for the series expansions of the solution.

The results presented show remarkable accuracy, with the only requirement of using ever more terms in the series expansion the higher the value of the delay we are studying. It is worth mentioning that in the examples presented we managed to get relative errors below 1% for values of delay 35% greater than the bifurcation value. This can be efficiently managed if the coefficients are pre-computed up to a sufficiently high order. Moreover, this allows the calculation of high precision bifurcation diagrams almost instantly. In our numerical experiments we have managed to calculate the coefficients up to order 20 before we reach the limits of the machine capacity in a standard installation.

It has been also verified that the error management based on the residual of the DDE can provide sufficient accuracy to implement efficient error control schemes that do not depend on the availability of error bounds from numerical integration.

In summary, the method is general enough to be applied to a wide spectrum of problems of considerable complexity for which there were not available procedures for deriving accurate explicit solutions before. Areas of study in which a closed expression for the solution of a DDE is necessary can benefit from the application of this methodology, specially for scenarios far from the bifurcation point.

Chapter 5

Stability and the Complex Ginzburg-Landau Equation (CGLE) in mesoscopic modelling

5.1 Problem statement

As explained previous chapters, microscopic modelling is perhaps the modelling area in which more results have been produced. Since the 1950's, these models became increasingly sophisticated depending on additional parameters beyond the distance and relative velocity. But regarding the link between the microscopic and macroscopic behaviour, the efforts have been only partially successful. At this point in time the relationship between the micro and macro scales has been only established in approximate equations, that are just valid for the large space scales (long wavelength approximation) and only applicable to the simplest microscopic models like the Optimal velocity Model (OVM).

In addition, there is not a known method to calculate precisely the bifurcation point at which the macroscopic traffic loses stability, and, again, only approximate calculations for the simpler models like the OVM exist. This is of extraordinary importance to determine the stability of the traffic process as a whole, since, as we will see, the delay threshold at which the solution to the equations is unstable is in general different in the micro and the macro scales.

Therefore a significant part of the research for this thesis has been focused on getting more precise calculations for both the bifurcation point of the multi-vehicle scenario, and on obtaining accurate expressions for the traffic behaviour not only at the long wavelength scale, but also at the scale relevant to the onset of instability. We will call this scale near the bifurcation point in scenarios with multiple vehicles, in between the micro and the macro scales, the *mesoscale*.

In this regard, it is important to note that it is intended to make these mathematical methods general enough to be used with any microscopic model based on the variables usually considered in standard models (namely distance, velocity and acceleration of the

vehicles). This generalized acceleration model could eventually be enriched with additional dependencies at the expense of modifying the mathematical procedures to consider these additional dependencies, but the spirit of the method would remain the same.

5.2 Linear stability: calculation of the bifurcation point

The problem that we will consider is the analysis of a many-vehicle traffic process in a single lane, in which each vehicle is governed by the same microscopic model. We will assume this model to be general in the dependence on the vehicle dynamics, and start from a retarded acceleration expression of the microscopic model, expressed in form of a DDE:

$$a(t+r) = a(s(t), s'(t), v(t), ...). \tag{5.1}$$

where $s(t)$ is the distance with respect to the preceding vehicle, $s'(t)$ its time derivative and $v(t)$ the vehicle velocity, though we allow for possible dependence on other variables. In the following we consider the function $a(s(t), s'(t), v(t))$, but this method can be easily generalized to other type of dependence.

On the other hand, we will consider the traffic flow in a single lane in terms of the position of the vehicle n, denoted by $y_n(t)$, and the distance of the vehicle n with respect to the preceding vehicle $n+1$ as $\Delta y_n(t)$. These variables are represented in figure 6.1.

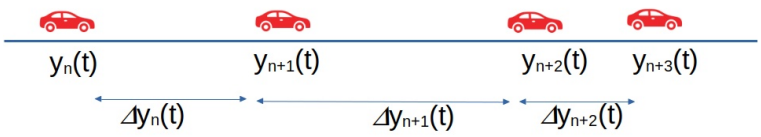


Figure 5.1: Position and distance of the vehicles in the microscopic view of traffic.

In the equilibrium $(s, v) = (\Delta y'_n(t), y'_n(t)) = (s_0, v_0)\ \forall n$, and we can describe the absolute position of the vehicle n as:

$$y_n(t) = s_0 n + v_0 t \tag{5.2}$$

We expect that in the linear stability limit, where the equilibrium is lost, the solution of the instability will have the wave form:

$$\begin{aligned} y_n(t) = s_0 n + v_0 t + \delta y \left(e^{j\kappa x + \lambda t} + e^{-j\kappa x + \bar{\lambda} t} \right) = \\ s_0 n + v_0 t + \delta y \left(e^{j\kappa s_0 n + \lambda t} + e^{-j\kappa s_0 n + \bar{\lambda} t} \right) \end{aligned} \tag{5.3}$$

where κ is the spatial wavenumber, λ the temporal eigenvalue of the wave and δy is the amplitude of the exponential perturbation. We then have that for the preceding vehicle $n+1$:

$$y_{n+1}(t) = s_0(n+1) + v_0 t + \delta y \left(e^{j\kappa s_0 (n+1) + \lambda t} + e^{-j\kappa s_0 (n+1) + \bar{\lambda} t} \right), \tag{5.4}$$

and we can express the distance as:

$$\Delta y_n(t) = s_0 + \delta y \left(\left(e^{j\kappa s_0} - 1 \right) e^{j\kappa s_0 n + \lambda t} + \left(e^{-j\kappa s_0} - 1 \right) e^{-j\kappa s_0 n + \bar{\lambda} t} \right). \tag{5.5}$$

We now define:

$$\varphi_n(t) = \delta y \left(e^{j\kappa s_0 n + \lambda t} \right) = \varphi_R(t) + j\varphi_I(t), \tag{5.6}$$

$$\overline{\varphi}_n(t) = \delta y \left(e^{-j\kappa s_0 n + \bar{\lambda} t} \right) = \varphi_R(t) - j\varphi_I(t). \tag{5.7}$$

Dropping the subscript n we now express the distance and relative velocity as:

$$\begin{aligned} s(t) = \Delta y_n(t) =& s_0 + \left(e^{j\kappa s_0} - 1 \right) (\varphi_R(t) + j\varphi_I(t)) + \\ & \left(e^{-j\kappa s_0} - 1 \right) (\varphi_R(t) - j\varphi_I(t)), \end{aligned} \tag{5.8}$$

$$\begin{aligned} s'(t) = \Delta y_n'(t) =& \left(e^{j\kappa s_0} - 1 \right) (\varphi_R'(t) + j\varphi_I'(t)) + \\ & \left(e^{-j\kappa s_0} - 1 \right) (\varphi_R'(t) - j\varphi_I'(t)), \end{aligned} \tag{5.9}$$

From (5.3), (5.6) and (5.7) the vehicle velocity and acceleration are:

$$v(t) = y_n'(t) = v_0 + 2\varphi_R'(t) \tag{5.10}$$

$$a(t) = y_n''(t) = 2\varphi_R''(t). \tag{5.11}$$

Since the perturbation must be verified regardless of any shift in phase, we get additional equations for its imaginary part:

$$\varphi_n^*(t) = \varphi_n(t) e^{-j\frac{\Pi}{2}} = -j \left(\varphi_R(t) + j\varphi_I(t) \right) = \varphi_I(t) - j\varphi_R(t), \tag{5.12}$$

$$y_n^*(t) = \varphi_n(t) + \varphi_n^*(t) = 2\varphi_I(t), \tag{5.13}$$

and we have the alternative equations:

$$\begin{aligned} s^*(t) = \Delta y_n^* =& s_0 + \left(e^{j\kappa s_0} - 1 \right) (\varphi_I(t) - j\varphi_R(t)) + \\ & \left(e^{-j\kappa s_0} - 1 \right) (\varphi_I(t) + j\varphi_R(t)), \end{aligned} \tag{5.14}$$

$$v^*(t) = y_n^{*\prime} = v_0 + 2\varphi_I'(t) \tag{5.15}$$

$$a^*(t) = y_n^{*\prime\prime}(t) = 2\varphi_I''(t). \tag{5.16}$$

Assuming that the acceleration function does not contain derivatives in space, we then set up the following system of DDEs:

$$\begin{cases} \varphi_R''(t) = \dfrac{a(t)}{2} = \dfrac{a(s(t-r), s'(t-r), v(t-r))}{2}, \\ \varphi_I''(t) = \dfrac{a^*(t)}{2} = \dfrac{a^*(s^*(t-r), s^{*\prime}(t-r), v^*(t-r))}{2}, \end{cases} \tag{5.17}$$

or, in the form of a first order system, by defining $\mathbf{u} = (u_1 = \varphi_R, u_2 = \varphi_I, u_3 = \varphi'_R, u_4 = \varphi'_I) \in \mathbb{R}^4$:

$$\begin{cases} u'_1(t) &= u_2(t), \\ u'_2(t) &= u_3(t), \\ u'_3(t) &= \frac{1}{2}a\left(u_1(t-r), u_2(t-r), u_3(t-r), u_4(t-r)\right), \\ u'_4(t) &= \frac{1}{2}a^*\left(u_1(t-r), u_2(t-r), u_3(t-r), u_4(t-r)\right). \end{cases} \tag{5.18}$$

And finally, considering the relationship between $a(t)$ and $a^*(t)$:

$$\begin{cases} u'_1(t) &= u_2(t), \\ u'_2(t) &= u_3(t), \\ u'_3(t) &= \frac{1}{2}a\left(u_1(t-r), u_2(t-r), u_3(t-r), u_4(t-r)\right), \\ u'_4(t) &= \frac{1}{2}a\left(u_2(t-r), -u_1(t-r), u_4(t-r), -u_3(t-r)\right), \end{cases} \tag{5.19}$$

which we will express as the vector DDE:

$$\mathbf{u}'(t) = \mathbf{f}(\mathbf{u}(t), \mathbf{u}(t-r)), \tag{5.20}$$

If $a \in C^k(\mathbb{R}^4;\mathbb{R})$ with $k \geq 2$, then $\mathbf{f} \in C^k(\mathbb{R}^4 \times \mathbb{R}^4;\mathbb{R}^4)$. We will also make use the corresponding linear problem:

$$\begin{aligned} \boldsymbol{\eta}'(t) &= \mathbf{P}\boldsymbol{\eta}(t) + \mathbf{Q}\boldsymbol{\eta}(t-r), \\ \mathbf{P} &= \mathbb{J}_{\mathbf{u}}\mathbf{f}(\mathbf{u},\mathbf{v})\,|_{\mathbf{u}=\mathbf{v}=\mathbf{0}}, \\ \mathbf{Q} &= \mathbb{J}_{\mathbf{v}}\mathbf{f}(\mathbf{u},\mathbf{v})\,|_{\mathbf{u}=\mathbf{v}=\mathbf{0}}, \end{aligned} \tag{5.21}$$

where $\mathbb{J}_*$ is the Jacobian matrix with respect to the vector $*$.

Notice that even though the function $\mathbf{f}$ is defined in the domain $\mathbb{R}^4 \times \mathbb{R}^4$, it is implemented by operating in $\mathbb{C}^4$ with complex conjugates, so the calculation of the matrices $\mathbf{P}$ and $\mathbf{Q}$ in the real domain can become very cumbersome. But, as we introduced in Section 2.1.4, this type of functions can be managed efficiently using the Wirtinger derivative formalism. In order to do so, we define the function $\mathbf{h} \in C^k(\mathbb{C}^2 \times \mathbb{C}^2;\mathbb{R}^4)$ as

$$\begin{aligned} &\mathbf{h}(\boldsymbol{\alpha},\boldsymbol{\beta}) = \mathbf{h}\left((\alpha_1,\alpha_2),(\beta_1,\beta_2)\right) = \\ &\mathbf{f}((\Re(\alpha_1),\Im(\alpha_1),\Re(\alpha_2),\Im(\alpha_2)),(\Re(\beta_1),\Im(\beta_1),\Re(\beta_2),\Im(\beta_2))), \end{aligned}$$

with $\boldsymbol{\alpha},\boldsymbol{\beta} \in \mathbb{C}^2$.

Then we look for solutions to the linear problem in the form

$$\boldsymbol{\eta}(t) = \boldsymbol{\eta}_+(t) + \boldsymbol{\eta}_-(t) = \boldsymbol{\varphi}e^{j\kappa s_0 n + \lambda t} + \bar{\boldsymbol{\varphi}}e^{-j\kappa s_0 n + \bar{\lambda} t}, \tag{5.22}$$

and, using the rules of Wirtinger calculus, express the linearized equation (5.21) as

$$\boldsymbol{\eta}'(t) = \mathbf{A}\boldsymbol{\eta}_+(t) + \bar{\mathbf{A}}\boldsymbol{\eta}_-(t) + \mathbf{B}\boldsymbol{\eta}_+(t-\lambda) + \bar{\mathbf{B}}\boldsymbol{\eta}_-(t-\lambda). \tag{5.23}$$

where:

$$\begin{aligned}\mathbf{A} &= \mathbb{W}\mathbb{J}_{\boldsymbol{\alpha}}\mathbf{h}\left(\boldsymbol{\alpha}(\mathbf{u}),\boldsymbol{\beta}(\mathbf{v})\right)\cdot\mathbb{J}_{\mathbf{u}}\boldsymbol{\alpha}(\mathbf{u})\mid_{\mathbf{u}=\mathbf{v}=\mathbf{0}},\\ \mathbf{B} &= \mathbb{W}\mathbb{J}_{\boldsymbol{\beta}}\mathbf{h}\left(\boldsymbol{\alpha}(\mathbf{u}),\boldsymbol{\beta}(\mathbf{v})\right)\cdot\mathbb{J}_{\mathbf{v}}\boldsymbol{\beta}(\mathbf{v})\mid_{\mathbf{u}=\mathbf{v}=\mathbf{0}},\end{aligned} \tag{5.24}$$

and

$$\begin{aligned}\boldsymbol{\alpha}(\mathbf{u}) &= (u_1+ju_2, u_3+ju_4),\\ \boldsymbol{\beta}(\mathbf{v}) &= (v_1+jv_2, v_3+jv_4).\end{aligned}$$

In the preceding we have used the "Wirtinger Jacobian" as defined in (2.79), the chain rule as in (2.78) and, as usual, $\mathbb{J}_*$ is the Jacobian matrix with respect to the real vector $*$. Considering (5.22), the linearized equation can be expressed as:

$$\boldsymbol{\eta}'(t) = (\mathbf{A}+\mathbf{B}e^{-\lambda r})\boldsymbol{\eta}_+(t) + (\bar{\mathbf{A}}+\bar{\mathbf{B}}e^{-\bar{\lambda} r})\boldsymbol{\eta}_-(t). \tag{5.25}$$

Notice that by linearity the solution $\boldsymbol{\eta}$ must verify that:

$$\begin{aligned}(\mathbf{A}+\mathbf{B}e^{-\lambda r})\boldsymbol{\eta}_-(t) &= 0,\\ (\bar{\mathbf{A}}+\bar{\mathbf{B}}e^{-\bar{\lambda} r})\boldsymbol{\eta}_+(t) &= 0.\end{aligned} \tag{5.26}$$

From (5.19), (5.6) and (5.7) we get:

$$\mathbf{A} = \begin{pmatrix} 0 & 0 & \frac{1}{2} & \frac{j}{2} \\ 0 & 0 & -\frac{j}{2} & \frac{1}{2} \\ 0 & 0 & 0 & 0 \\ 0 & 0 & 0 & 0 \end{pmatrix}$$

$$\mathbf{B} = \begin{pmatrix} 0 & 0 & 0 & 0 \\ 0 & 0 & 0 & 0 \\ B_1 & B_2 & B_3 & B_4 \\ -B_2 & B_1 & -B_4 & B_3 \end{pmatrix}$$

with $B_i = \dfrac{\partial a(\boldsymbol{\eta}(t))}{\partial \eta_{i+}(t)}$.

Introducing solution (5.22) in (5.23) and considering (5.26) we get the condition for the existence of the solution $\boldsymbol{\eta}(t)$ in the characteristic equation:

$$f_{ch}(r,\kappa,\lambda) = \left|\mathbf{I}\lambda - \mathbf{A} - \bar{\mathbf{A}} - \mathbf{B}e^{-\lambda r} - \overline{\mathbf{B}}e^{-\bar{\lambda} r}\right| = 0. \tag{5.27}$$

Every pair of values for the delay r and wavenumber κ will define four eigenvalues of this equation $\lambda_i(r,\kappa)$, $i = 1..4$. The critical point in the bifurcation is the minimum value of delay r_m for which there exists a purely pair of eigenvalues $\pm j\omega_0$ for a certain wave number κ_0, i.e.:

$$r_m = min(r) \quad / \quad \exists \kappa_0, \omega_0, \quad \pm j\omega_0 \in \lambda_i(r_m,\kappa_0). \tag{5.28}$$

Note that the notation of the delay limit uses the subscript m to remark that this limit referes to the mesoscopic scale, in contrast to r_μ used in Chapter 4 for the microscopic scale and r_M for the macroscopic scale that is introduced in Chapter 6. This way we define as the bifurcation point of the problem the threshold delay r_m for which waves of frequency ω_0 and wavenumber κ_0 start to appear:

$$\text{Bifurcation point} \equiv (r_m, \omega_0, \kappa_0)\,. \tag{5.29}$$

The bifurcation is usually visualized using a graphical representation of the *neutral stability line*, which is the line representing the values of (κ, r) for which we have a purely imaginary eigenvalue $\Re(\lambda) = 0$. The point at which the derivative of this line is 0 is (κ_0, r_m), where the purely imaginary eigenvalue is $j\omega_0$. An example of neutral stability line is presented in Figure 6.2.

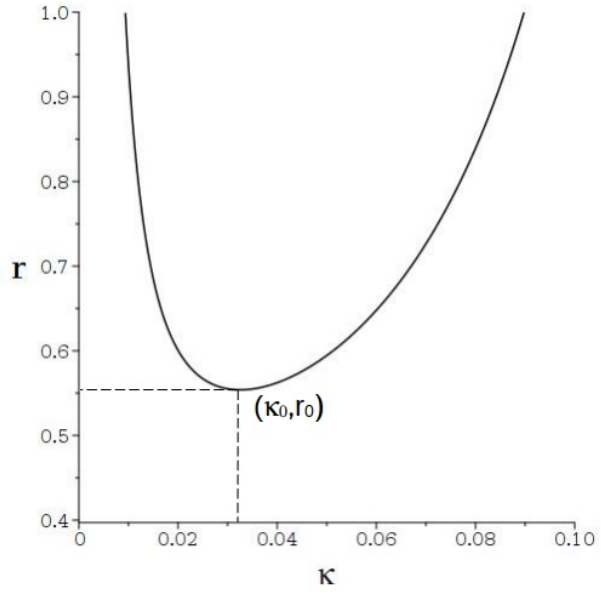


Figure 5.2: Example of neutral stability line ($\kappa(r)$ such that $\Re(\lambda(r,\kappa)) = 0$).

It is important to note that this minimum value r_m may not exist, in which case the traffic will become unstable for any delay value, but this is not to be expected in real traffic scenarios in which there must exist some tolerance in the reaction times so that the traffic process is physically possible.

Then, in accordance with the Hopf bifurcation theorem, we expect that as r deviates from r_m there will be a periodic solution to (5.20) $\mathbf{u}(r, x, t)$ with time period close to $2\pi/\omega_0$ and spatial period close to $2\pi/\kappa_0$. Moreover, in the point of bifurcation we have the fundamental periodic solution of the linear system:

$$\mathbf{v}_0(x,t) = e^{j(\omega_0 t + \kappa_0 x)}\boldsymbol{\phi}_{0,\kappa_0} + e^{-j(\omega_0 t + \kappa_0 x)}\overline{\boldsymbol{\phi}}_{0,\kappa_0}, \tag{5.30}$$

where $\boldsymbol{\phi}_{0,\kappa_0}$ is the eigenvector of the eigenvalue $j\omega_0$.

5.3 Mesoscopic model using the Complex Ginzburg-Landau equation (CGLE) formalism

The determination of a bifurcation point, if it exists, predicts the apparition of sustained oscillations in the distance and velocity of the vehicles around the equilibrium solution when the delay is greater than the critical value r_m, so the next step is to characterize the amplitude and frequency of these oscillations near this point when $r > r_m$, and $|r - r_m| / r_m << 1$. We have not found an existing methodology in the literature that addresses this calculation, with the only exception of the works from Nagatani et al [48] for the simple Optimal Velocity Model (OVM), based on techniques used in phase transition analysis. But no general method applicable to an arbitrary acceleration function exists.

As follows from the the assumptions of the problem described in the previous section, and the Hopf bifurcation theorem, we expect that for delays greater than the threshold r_m there exist solutions to (5.20) that are periodic with time period close to $2\pi/\omega_0$ and spatial period close to $2\pi/\kappa_0$. Moreover, from equation (5.20) we can see that, if we consider that the fundamental wavenumber κ_0 does not change significantly when r varies, this problem could be framed in the context of Delay Differential Equations (DDEs) that we have introduced in chapter 4. As a first approach we could use the methodology introduced in chapter 4 to calculate an approximate solution to the equation, assuming that the wave number κ of the solution is very close to κ_0.

But an alternative approach could be taken when only a second order approximation suffices. The shift in frequency of the bifurcating periodic solution can be regarded as a modulation of the fundamental frequency ω_0, which is precisely the perspective adopted in the theory of modulation equations. This theory, briefly introduced in Section 2.1.3, provides methods to calculate solutions to nonlinear PDEs near the bifurcation consisting of a slow-time varying amplitude modulating the fundamental frequency ω_0. As described in Section 2.1.3, the Complex Ginzburg-Landau Equation (CGLE) is the simplest and most frequently used approximation for finding approximate nonlinear wave solutions near bifurcation in problems subject to bifurcations of Hopf type. The advantage of this approach is that, in addition to the frequency and amplitude of the oscillations near the bifurcation point, it can offer more insights on how the envelope of the solution behaves far from the bifurcation point. The next section will delve in how the CGLE formalism is applied to the specific case of the solution of the bifurcating solutions of equation (5.20).

5.3.1 The CGLE in mesoscopic scale of traffic

Asymptotic expansion of the solution

Section 2.1.3 introduced a scheme of the general methodology to derive a CGLE from a general problem described by a nonlinear PDE that presents a Hopf bifurcation whose periodic solutions can be expressed as an asymptotic expansion. To be able to use the asymptotic expansion approximations of Chapter 4, we must assume that at the bifurcation point the solution has the form in (5.30), and, as in the CGLE formalism, the variation of the parameter (in this case, the delay), induces changes in the amplitude through modulations in time.

Then, in order to consider the space variable present in the basic pattern solution (5.30), we complete the expression of the approximate solution of order $N+1$ in a Hopf bifurcation (4.45) by including the dependence on the space variable x in this way:

$$\mathbf{u}(x,t) = \left(\varepsilon \mathbf{z}_0(t) + \sum_{j=1}^{N} \varepsilon^{j+1} \mathbf{z}_j(t)\right) e^{j\kappa_0 x} + O(\varepsilon^{N+2}), \tag{5.31}$$

with

$$\mathbf{z}_0(t) = e^{j\omega(\varepsilon)t}\boldsymbol{\phi}_{0,\kappa_0} + e^{-j\omega(\varepsilon)t}\overline{\boldsymbol{\phi}}_{0,\kappa_0}, \tag{5.32}$$

where $\omega(\varepsilon) = 2\pi\omega_0/\hat{T}(\varepsilon)$ and $\hat{T}(\varepsilon)$ is the expansion for the period, and ε is the estimated value from (4.46). In this way we obtain an asymptotic expansion as required by the CGLE methodology. Nevertheless, we must note that the expansion in the standard CGLE construction in Chapter 2 (2.57) is normally based on an expansion parameter $\varepsilon = \sqrt{\mu}$ that is explicitly related to the deviation of some parameter p, such as $\mu = \varepsilon^2 = p - p_0$, while in the case of the Poincaré-Lindstedt method for DDEs used to get (5.31) the parameter p is the delay r, and the relationship is implicit in the expansion $r(\varepsilon) = \sum_{k=0}^{\infty} \varepsilon^k r_k$. This can complicate considerably the calculation of the coefficient of the CGLE $\lambda_{0,1}$ in equation (2.70) for the following.

As stated before, the characteristic equation (5.27) determines the eigenvalues corresponding to every combination of r and κ:

$$f_{ch}(r,\kappa,\lambda) = 0 \quad \Longrightarrow \quad \lambda(r,\kappa).$$

By (2.46) and (2.47) we have that

$$\lambda_{0,1} = \frac{\partial^2}{\partial\kappa\partial\mu}\lambda(r(\mu),\kappa)\bigg|_{0,\kappa_0},$$

with $\mu = \varepsilon^2$. Then to calculate $\lambda_{0,1}$from the characteristic equation (using the implicit function theorem), we need to know in advance the expression of $r(\mu) = r(\varepsilon^2)$ to a significant degree of the expansion to calculate $\lambda_{0,1}$ accurately, which defeats the purpose of performing the calculations just to the second order approximation.

But we can circumvent this problem by noting that in the Poincaré-Listedt method for DDEs the expansion parameter ε is directly related to the amplitude of the solution. We recall that $\mathbf{z}_0(t)$ is a first trigonometric degree polynomial, and it is chosen so that:

$$\frac{1}{2\pi}\int_0^{2\pi} |\mathbf{z}_0(\tau)|^2 d\tau = \frac{\omega(\varepsilon)}{2\pi}\int_0^{2\pi/\omega(\varepsilon)} |\mathbf{z}_0(t)|^2 dt = 1.$$

So, from (5.31) and(5.32) we have

$$\mathbf{u}(x,t) = \varepsilon(e^{j(\omega(\varepsilon)t+\kappa_0 x)}\boldsymbol{\phi}_{0,\kappa_0} + c.c.) + O(\varepsilon^2),$$

if we compare (5.31) with the expression of the modulated solution in the CGLE (2.57) (substituting the basic pattern base frequency ω_0 by $\omega(\varepsilon)$):

$$\mathbf{u}(x,t) = \varepsilon(A(\xi,\tau)e^{j(\omega(\varepsilon)t+\kappa_0 x)}\boldsymbol{\phi}_{0,\kappa_0} + c.c.) + O(\varepsilon^2),$$

we must conclude by inspection that the basic solution corresponding to an $A(\xi,\tau)$ constant in time and space must be $A(\xi,\tau) = 1$, and for this solution:

$$\begin{aligned} \partial_\tau A &= \Lambda_0 \Delta_\xi A + \lambda_{0,1} A - \gamma |A|^2 A, \\ 0 &= \lambda_{0,1} A - \gamma A, \end{aligned}$$

which implies that

$$\lambda_{0,1} = \gamma.$$

So, considering (2.69) and (2.70) to costruct the CGLE approximation from the expansion obtained with the Poincaré-Lindstedt method for DDEs, it will be sufficient to calculate:

$$\gamma = -\left\langle \boldsymbol{\psi}_*, \boldsymbol{\phi}^*_{0,\kappa_0} \right\rangle, \tag{5.33}$$

with (recovering (2.68))

$$\boldsymbol{\psi}_* = 2\mathbf{M}_{1,0}(\boldsymbol{\phi}_{0,\kappa_0}, \mathbf{w}_0) + 2\mathbf{M}_{2,-1}(\mathbf{w}_2, \overline{\boldsymbol{\phi}}_{0,\kappa_0}) + 3\mathbf{N}_{1,1,-1}(\boldsymbol{\phi}_{0,\kappa_0}, \boldsymbol{\phi}_{0,\kappa_0}, \overline{\boldsymbol{\phi}}_{0,\kappa_0}), \tag{5.34}$$

and

$$\left\langle \boldsymbol{\phi}_{0,\kappa_0}, \boldsymbol{\phi}^*_{0,\kappa_0} \right\rangle = 1.$$

The dispersion term is calculated as usual (see (2.46) and (2.47)):

$$\Lambda_0 = \frac{1}{2} \frac{\partial^2 \lambda(r,\kappa)}{\partial \kappa^2}\bigg|_{r_m,\kappa_0}.$$

The (unscaled) CGLE in this problem is thus:

$$\partial_\tau A = \Lambda_0 \Delta_\xi A + \gamma \left(1 - |A|^2\right) A. \tag{5.35}$$

5.3.2 Some comments on the calculation of coefficient γ

It is convenient to remark some peculiarities of the application of the CGLE formalism to the car following traffic mesoscale.

Expressions for $\mathbf{M}_{l,m}$ and $\mathbf{N}_{l,m,n}$

The nonlinear problem $\mathbf{u}'(t) = \mathbf{f}(\mathbf{u}(t), \mathbf{u}(t-r))$ has a definite form (see (5.19)): the non-retarded part of the system is linear and present only in the two first equations:

$$\begin{cases} u_1'(t) &= u_2(t), \\ u_2'(t) &= u_3(t), \end{cases}$$

while the retarded part and the nonlinearity are present only in the two last equations:

$$\begin{cases} u_3'(t) &= \frac{1}{2}a\left(u_1(t-r), u_2(t-r), u_3(t-r), u_4(t-r)\right), \\ u_4'(t) &= \frac{1}{2}a\left(u_2(t-r), -u_1(t-r), u_4(t-r), -u_3(t-r)\right). \end{cases}$$

In addition, normally the acceleration equations do not have derivatives in the space variable x. This means that the bilinear and trilinear forms $\mathbf{M}_{l,m}$ and $\mathbf{N}_{l,m,n}$ will be easily built using the Wirtinger calculus already used in the linear part, considering only derivatives of the retarded variable $\mathbf{v}$. Omitting the dependencies of $\mathbf{h}, \boldsymbol{\alpha}$ and $\boldsymbol{\beta}$, we will have:

$$\begin{aligned} \mathbf{M}_{l,m}(\boldsymbol{\psi}_l, \boldsymbol{\psi}_m) = \frac{1}{2}\Big[& \Big(\mathbb{W}\mathbb{J}_{\boldsymbol{\beta}}\Big(\Big(\mathbb{W}\mathbb{J}_{\boldsymbol{\beta}}\mathbf{h}\cdot\mathbb{J}_{\mathbf{v}}\boldsymbol{\beta}\Big)\boldsymbol{\psi}_l\Big)\cdot\mathbb{J}_{\mathbf{v}}\boldsymbol{\beta}\Big)\boldsymbol{\psi}_m + \\ & \Big(\mathbb{W}\mathbb{J}_{\bar{\boldsymbol{\beta}}}\Big(\Big(\mathbb{W}\mathbb{J}_{\boldsymbol{\beta}}\mathbf{h}\cdot\mathbb{J}_{\mathbf{v}}\boldsymbol{\beta}\Big)\boldsymbol{\psi}_l\Big)\cdot\mathbb{J}_{\mathbf{v}}\bar{\boldsymbol{\beta}}\Big)\boldsymbol{\psi}_m + \\ & \Big(\mathbb{W}\mathbb{J}_{\boldsymbol{\beta}}\Big(\Big(\mathbb{W}\mathbb{J}_{\bar{\boldsymbol{\beta}}}\mathbf{h}\cdot\mathbb{J}_{\mathbf{v}}\bar{\boldsymbol{\beta}}\Big)\boldsymbol{\psi}_l\Big)\cdot\mathbb{J}_{\mathbf{v}}\boldsymbol{\beta}\Big)\boldsymbol{\psi}_m + \\ & \Big(\mathbb{W}\mathbb{J}_{\bar{\boldsymbol{\beta}}}\Big(\Big(\mathbb{W}\mathbb{J}_{\bar{\boldsymbol{\beta}}}\mathbf{h}\cdot\mathbb{J}_{\mathbf{v}}\bar{\boldsymbol{\beta}}\Big)\boldsymbol{\psi}_l\Big)\cdot\mathbb{J}_{\mathbf{v}}\bar{\boldsymbol{\beta}}\Big)\boldsymbol{\psi}_m\Big]\,|_{\mathbf{u}=\mathbf{v}=\mathbf{0}}, \end{aligned} \tag{5.36}$$

and

$$\begin{aligned} \mathbf{N}_{l,m,n}(\boldsymbol{\psi}_l, \boldsymbol{\psi}_m, \boldsymbol{\psi}_n) = \frac{1}{6}\Big[& \Big(\mathbb{W}\mathbb{J}_{\boldsymbol{\beta}}\Big(\Big(\mathbb{W}\mathbb{J}_{\boldsymbol{\beta}}\Big(\Big(\mathbb{W}\mathbb{J}_{\boldsymbol{\beta}}\mathbf{h}\cdot\mathbb{J}_{\mathbf{v}}\boldsymbol{\beta}\Big)\boldsymbol{\psi}_l\Big)\cdot\mathbb{J}_{\mathbf{v}}\boldsymbol{\beta}\Big)\boldsymbol{\psi}_m\Big)\cdot\mathbb{J}_{\mathbf{v}}\boldsymbol{\beta}\Big)\boldsymbol{\psi}_n + \\ & \Big(\mathbb{W}\mathbb{J}_{\boldsymbol{\beta}}\Big(\Big(\mathbb{W}\mathbb{J}_{\boldsymbol{\beta}}\Big(\Big(\mathbb{W}\mathbb{J}_{\bar{\boldsymbol{\beta}}}\mathbf{h}\cdot\mathbb{J}_{\mathbf{v}}\bar{\boldsymbol{\beta}}\Big)\boldsymbol{\psi}_l\Big)\cdot\mathbb{J}_{\mathbf{v}}\boldsymbol{\beta}\Big)\boldsymbol{\psi}_m\Big)\cdot\mathbb{J}_{\mathbf{v}}\boldsymbol{\beta}\Big)\boldsymbol{\psi}_n + \\ & \Big(\mathbb{W}\mathbb{J}_{\boldsymbol{\beta}}\Big(\Big(\mathbb{W}\mathbb{J}_{\bar{\boldsymbol{\beta}}}\Big(\Big(\mathbb{W}\mathbb{J}_{\boldsymbol{\beta}}\mathbf{h}\cdot\mathbb{J}_{\mathbf{v}}\bar{\boldsymbol{\beta}}\Big)\boldsymbol{\psi}_l\Big)\cdot\mathbb{J}_{\mathbf{v}}\boldsymbol{\beta}\Big)\boldsymbol{\psi}_m\Big)\cdot\mathbb{J}_{\mathbf{v}}\boldsymbol{\beta}\Big)\boldsymbol{\psi}_n + \\ & \Big(\mathbb{W}\mathbb{J}_{\bar{\boldsymbol{\beta}}}\Big(\Big(\mathbb{W}\mathbb{J}_{\boldsymbol{\beta}}\Big(\Big(\mathbb{W}\mathbb{J}_{\boldsymbol{\beta}}\mathbf{h}\cdot\mathbb{J}_{\mathbf{v}}\boldsymbol{\beta}\Big)\boldsymbol{\psi}_l\Big)\cdot\mathbb{J}_{\mathbf{v}}\boldsymbol{\beta}\Big)\boldsymbol{\psi}_m\Big)\cdot\mathbb{J}_{\mathbf{v}}\bar{\boldsymbol{\beta}}\Big)\boldsymbol{\psi}_n + \\ & \Big(\mathbb{W}\mathbb{J}_{\bar{\boldsymbol{\beta}}}\Big(\Big(\mathbb{W}\mathbb{J}_{\bar{\boldsymbol{\beta}}}\Big(\Big(\mathbb{W}\mathbb{J}_{\boldsymbol{\beta}}\mathbf{h}\cdot\mathbb{J}_{\mathbf{v}}\boldsymbol{\beta}\Big)\boldsymbol{\psi}_l\Big)\cdot\mathbb{J}_{\mathbf{v}}\boldsymbol{\beta}\Big)\boldsymbol{\psi}_m\Big)\cdot\mathbb{J}_{\mathbf{v}}\bar{\boldsymbol{\beta}}\Big)\boldsymbol{\psi}_n + \\ & \Big(\mathbb{W}\mathbb{J}_{\bar{\boldsymbol{\beta}}}\Big(\Big(\mathbb{W}\mathbb{J}_{\boldsymbol{\beta}}\Big(\Big(\mathbb{W}\mathbb{J}_{\bar{\boldsymbol{\beta}}}\mathbf{h}\cdot\mathbb{J}_{\mathbf{v}}\bar{\boldsymbol{\beta}}\Big)\boldsymbol{\psi}_l\Big)\cdot\mathbb{J}_{\mathbf{v}}\boldsymbol{\beta}\Big)\boldsymbol{\psi}_m\Big)\cdot\mathbb{J}_{\mathbf{v}}\bar{\boldsymbol{\beta}}\Big)\boldsymbol{\psi}_n + \\ & \Big(\mathbb{W}\mathbb{J}_{\boldsymbol{\beta}}\Big(\Big(\mathbb{W}\mathbb{J}_{\bar{\boldsymbol{\beta}}}\Big(\Big(\mathbb{W}\mathbb{J}_{\bar{\boldsymbol{\beta}}}\mathbf{h}\cdot\mathbb{J}_{\mathbf{v}}\bar{\boldsymbol{\beta}}\Big)\boldsymbol{\psi}_l\Big)\cdot\mathbb{J}_{\mathbf{v}}\boldsymbol{\beta}\Big)\boldsymbol{\psi}_m\Big)\cdot\mathbb{J}_{\mathbf{v}}\boldsymbol{\beta}\Big)\boldsymbol{\psi}_n + \\ & \Big(\mathbb{W}\mathbb{J}_{\bar{\boldsymbol{\beta}}}\Big(\Big(\mathbb{W}\mathbb{J}_{\bar{\boldsymbol{\beta}}}\Big(\Big(\mathbb{W}\mathbb{J}_{\bar{\boldsymbol{\beta}}}\mathbf{h}\cdot\mathbb{J}_{\mathbf{v}}\bar{\boldsymbol{\beta}}\Big)\boldsymbol{\psi}_l\Big)\cdot\mathbb{J}_{\mathbf{v}}\bar{\boldsymbol{\beta}}\Big)\boldsymbol{\psi}_m\Big)\cdot\mathbb{J}_{\mathbf{v}}\bar{\boldsymbol{\beta}}\Big)\boldsymbol{\psi}_n\Big]\,|_{\mathbf{u}=\mathbf{v}=\mathbf{0}}, \end{aligned} \tag{5.37}$$

with $l, m, n \in \mathbb{Z}$.

Straightforward or singular expansion

The asymptotic expansion used in the introduction of the CGLE calculation in equation (2.57) is a straightforward expansion, without considering possible dependencies of the frequency on the parameter expansion, while in the expansion obtained with the Poincaré-Lindstedt method for DDEs introduced in Chapter4, the frequency is $\omega(\varepsilon)$, as stated in equation (5.32). The reader can check Section 2.1.1 for the discussion on uniformity and singular expansion methods.

It is important to understand why the method to get the CGLE still "works" with singular expansion methods. The reason is that in uniformly valid expansions like the Poincaré-Lindstedt method, if we expand only to order 1, the simple expansion obtained has the same

frequency as the straightforward expansion. In other words, if the period of the approximation is:

$$T = \frac{2\pi}{\omega_0} + \varepsilon T_1$$

we always have that $T_1 = 0$. The reason of this can be found in the orthogonality conditions employed to calculate T_j and r_j in each iteration in (4.29):

$$\int_0^{2\pi} \langle \mathbf{h}_j(\tau), \boldsymbol{\phi}_i^*(\tau) \rangle \, d\tau = 0 \qquad \text{for } i = 1, 2.$$

We have from (4.23) (with $\mathbf{p}_1 = 0$):

$$\mathbf{h}_1(\tau) = \hat{T}_1 \boldsymbol{\theta}(\tau) + \hat{r}_1 \boldsymbol{\sigma}(\tau) + M\mathbf{z}_0(\tau) + N\mathbf{z}_0(\tau - \hat{r}_m),$$

and we can see that

a) it is verified that

$$\langle M\mathbf{z}_0(\tau) + N\mathbf{z}_0(\tau - \hat{r}_m), \boldsymbol{\phi}_i^*(\tau) \rangle = 0,$$

as $M\mathbf{z}_0(\tau) + N\mathbf{z}_0(\tau - \hat{r}_m)$ generates trigonometric terms of degrees 0 and 2, and

b) due to the solvability condition *ii*) in Definition 4.1

$$\int_0^{2\pi} \left\langle \hat{T}_1 \boldsymbol{\theta}(\tau) + \hat{r}_1 \boldsymbol{\sigma}(\tau), \boldsymbol{\phi}_i^*(\tau) \right\rangle d\tau = 0 \quad i = 1, 2 \Longrightarrow \hat{r}_1 = 0, \hat{T}_1 = 0,$$

So, $T_1 = \hat{T}_1/\omega_0 = 0$ and $r_1 = \hat{r}_1/\omega_0 = 0$ in any Poinacré-Lindstedt expansion, and until order 2 there is no change in the frequency of the approximation.

Validation of the calculation of γ

If we already have Poincaré-Lidstedt expansion calculated up to order 2, we can check the calculation of the coefficient γ in (5.33), by alternatively calculating it using the following expression, derived by inserting the expansion up to order 2 in both sides of (5.20):

$$\gamma = \left\langle \frac{j\omega_0}{2\pi} \left((2\pi r_2 - T_2 r_m) e^{j\omega_0 r_m} \mathbf{B} \cdot \boldsymbol{\phi}_{0,\kappa_0} - T_2 \boldsymbol{\phi}_{0,\kappa_0} \right), \boldsymbol{\phi}_{0,\kappa_0}^* \right\rangle, \tag{5.38}$$

where r_2 and T_2 are the second order coefficients of the expansions of r and T respectively, and $\mathbf{B}$ is (5.24). It must be noted in any case that the first term in the product (5.38) is not equal to $\boldsymbol{\psi}_*$ in (5.34), and we remark that this is useful for checking purposes, as it suffices to calculate the expansion up to order 1 to calculate (5.34).

5.3.3 Stabilty and the formation of modulating waves

Metastability and criticality of the CGLE

From the previous section we have built a solution to (5.20) in the form

$$\mathbf{u}(\varepsilon, x, t, \xi, \tau) = \varepsilon \left(A(\xi, \tau) e^{j(\omega(\varepsilon)t + \kappa_0 x)} \boldsymbol{\phi}_{0,\kappa_0} + \bar{A}(\xi, \tau) e^{-j(\omega(\varepsilon)t + \kappa_0 x)} \bar{\boldsymbol{\phi}}_{0,\kappa_0} \right) + O(\varepsilon^2), \tag{5.39}$$

as the fundamental solution when $0 < (r - r_m)/r_m \ll 1$. Consistent with Nagatani [48], who applied phase transition theory to study the different states of the traffic process, we will refer to this state of the traffic just above the critical point as *metastable*. This is because the traffic is not strictly stable in the linear sense once we have gone beyond the bifurcation point (it is oscillatory), but no qualitative change to the solution (5.39) occurs if the conditions do not change. Eventually, if the bifurcation parameter separates further from the critical point, density waves will start to form , and the traffic changes to the *congested* state.

In this regard, once we have the CGLE expression, we may ask what will happen to the envelope of the solution (5.39). As explained in Section 2.1.3, this equation has two possible behaviours:

- **CGLE supercritical**: when the equation is supercritical ($\Re(\gamma) \geq 0$) then some oscillatory solutions of the CGLE will exist. The CGLE takes the form:

$$\partial_\tau \tilde{A} = \tilde{A} + (1 + jb)\Delta_\xi \tilde{A} - (1 + jc)\left|\tilde{A}\right|^2 \tilde{A},$$

with $b = \Im(\Lambda_0)/\Re(\Lambda_0)$ and $c = \Im(\gamma)/\Re(\gamma)$, and, recalling that in our problem $\gamma = \lambda_{0,1}$:

$$\begin{aligned}
\tau &= \Re(\gamma)\varepsilon^2 t, \\
\xi &= \sqrt{\frac{\Re(\gamma)}{\Re(\Lambda_0)}}\varepsilon(x - c_g t), \\
\tilde{A} &= e^{j\Im(\gamma)\varepsilon^2 t} A.
\end{aligned}$$

Recovering (2.73) plane waves exist in the form:

$$\begin{aligned}
A_Q &= a_Q e^{j(\omega_Q + Q\xi)\tau}, \\
|a_Q| &= 1 - Q^2, \\
\omega_Q &= -c + (c - b)Q^2,
\end{aligned}$$

where Q is the wavenumber (in the scaled space ξ) and ω_Q the frequency in the scaled time τ. Plane waves will exist if

$$1 + bc < 0,$$

and the range of wavenumbers of these oscillations is:

$$0 < |Q| < \left(\frac{1 + bc}{3 + bc + 2c^2}\right)^{\frac{1}{2}}.$$

It can be expected that modulation patterns obeying this modulation in scales τ and ξ will be observed in the amplitude of the oscillations of the basic pattern (5.39). In any case, the amplitude of the modulating wave will have an amplitude $|a_Q| \leq 1$, so changes in the amplitude of the oscillations can be expected, but not beyond the oscillation limits of the basic periodic pattern.

- **CGLE subcritical**: when the equation is subcritical ($\Re(\gamma) < 0$) then no stable oscillatory solutions for (5.20) exist. Therefore it is expected that the metastable solution in this case has the simpler form:

$$\mathbf{u}(\varepsilon, x, t) = \varepsilon \left(e^{j(\omega(\varepsilon)t + \kappa_0 x)} \boldsymbol{\phi}_{0,\kappa_0} + e^{-j(\omega(\varepsilon)t + \kappa_0 x)} \bar{\boldsymbol{\phi}}_{0,\kappa_0} \right) + O(\varepsilon^2), \tag{5.40}$$

It is then clear that the sign of $\Re(\gamma)$ is of the most importance to determine the form of the metastable solution.

Impact of constant drift in metastability

Another important effect has to be considered, namely the impact of the constant term that appears due to the nonlinearities in the asymptotic expansions and the modulation equations. If we calculate an approximate solution of the form

$$\mathbf{u}(\varepsilon, x, t) = \varepsilon \mathbf{u}_0(x, t) + \varepsilon^2 \mathbf{u}_1(x, t) + \varepsilon^3 \mathbf{u}_0(x, t) + ...,$$

it is likely that the terms $\mathbf{u}_k(x, t), \quad k \geq 1$, i.e. the terms stemming from the nonlinearity, contain constant terms. This can be seen as coming from cross products of terms of pure periodic real functions with the same frequency. For instance, in the method to construct the CGLE in Section 2.1.3, the term $E^0 \boldsymbol{\psi}_0(\tau) = \boldsymbol{\psi}_0(\tau)$ in (2.57) is a constant term. Or, in Tables 4.4 and 4.16 in Chapter 4 we see constant values for some components in the Poncaré-Lindstedt approximate solutions built for orders $> o(0)$.

This in principle should not be a problem if the constant terms do not introduce a shift in the average solution of the problem. But if they do, the linear stability conditions calculated for the bifurcation point may no longer be valid. This is probably better explained through an example. If we consider the nonlinear problem

$$\mathbf{u}'(x, t) = \mathbf{f}(\mathbf{u}(x, t)), \tag{5.41}$$

we may calculate an approximate solution as

$$\mathbf{u}(\varepsilon, x, t) = \varepsilon \mathbf{p}_0(x, t) + \varepsilon^2 (\mathbf{c}_1 + \mathbf{p}_1(x, t)) + \varepsilon^3 (\mathbf{c}_2 + \mathbf{p}_2(x, t)) + ...,$$

where the $\mathbf{c}_k$ and $\mathbf{p}_k$ are constant an 0-average periodic components for each order, respectively. Then, the average (in time and space) of the solution for $r > r_m$ is no longer $\mathbf{u}_{r_m} = \mathbf{0}$, but

$$\mathbf{u}_r = \varepsilon^2 \mathbf{c}_1 + \varepsilon^3 \mathbf{c}_2 + ...$$

This can create a problem if one of the variables of the problem is limited in its macroscopic behaviour. In our problem we have the continuous variables space s and velocity v. The velocity can be adapted individually to be on the equilibrium, but the distance cannot be changed by all the vehicles at the same time. In other words, if the average of the distance in the solution is increased, this means that suddenly we would need to relocate all the N vehicles in a longer distance instantly, which is physically impossible. Therefore it can be expected that, in this specific problem, even when theoretically there exists a metastable solution for a

specific car following model, physical limitations may make that state unachievable, and then the state after the bifurcation will be the congestion instead of the metastable state.

The condition for the oscillatory solution to be stable is that either the solution $\mathbf{u}(x,t) = \mathbf{c} + \mathbf{p}(x,t)$ is physically feasible, or there exist an alternative solution $\mathbf{u}^*(x,t) = \mathbf{c}^* + \mathbf{p}(x,t)$, with a different constant term $\mathbf{c}^*$, that verifies (5.41) and is possible physically. In addition, there must exist a continuous set of solutions $\mathbf{S} = \mathbf{v}(x,t) = \mathbf{c}_v + \mathbf{p}(x,t)$ such that $\{\mathbf{u}(x,t), \mathbf{u}^*(x,t)\} \in \mathbf{S}$.

5.3.4 A simple example: the nDDE mesoscale

To illustrate the concepts introduced in this chapter, we present now the application of the mesoscopic modelling to the nDDE model for which we presented the analysis of the Hopf bifurcation in Section 4.4.1. We recall that the limiting delay at the microscopic level that considers the leader-follower ensemble, has a value $r_\mu = 1.3079$ s.

The system of equations is in this case:

$$\begin{cases} u_1'(t) &= u_2(t), \\ u_2'(t) &= u_3(t), \\ u_3'(t) &= \frac{1}{2} g\left(u_1(t-r), u_2(t-r), u_3(t-r), u_4(t-r)\right), \\ u_4'(t) &= \frac{1}{2} g\left(u_2(t-r), -u_1(t-r), u_4(t-r), -u_3(t-r)\right), \end{cases} \tag{5.42}$$

with

$$\begin{aligned} &g(v_1, v_2, v_3, v_4) = -a + \frac{(a+b)}{1 + \frac{b}{a} e^{d \cdot h(v_1, v_2, v_3, v_4)}}, \\ &h(v_1, v_2, v_3, v_4) = C_1(v_1 + j v_2) + \bar{C_1}(v_1 - j v_2) + \\ &C_2(v_3 + j v_4) + \bar{C_2}(v_3 - j v_4), \end{aligned}$$

where

$$\begin{aligned} C_1 &= e^{j\kappa} - 1, \\ C_2 &= K(e^{j\kappa} - 1) - \frac{s_0}{v_0} e^{j\kappa}. \end{aligned}$$

These equations produce the following matrices of the linear equation as in (5.25):

$$\mathbf{A} = \begin{pmatrix} 0 & 0 & \frac{1}{2} & \frac{j}{2} \\ 0 & 0 & -\frac{j}{2} & \frac{1}{2} \\ 0 & 0 & 0 & 0 \\ 0 & 0 & 0 & 0 \end{pmatrix}$$

$$\mathbf{B} = \begin{pmatrix} 0 & 0 & 0 & 0 \\ 0 & 0 & 0 & 0 \\ \frac{dab}{2(a+b)} C_1 & \frac{dab}{2(a+b)} j C_1 & \frac{dab}{2(a+b)} C_2 & \frac{dab}{2(a+b)} j C_2 \\ -\frac{dab}{2(a+b)} j C_1 & \frac{dab}{2(a+b)} C_1 & -\frac{dab}{2(a+b)} j C_2 & \frac{dab}{2(a+b)} C_2 \end{pmatrix}$$

We have omitted the dependency of C_1 and C_2 on κ in the matrix $\mathbf{B}$. Now, using the same parameters in Table 4.2, applying formula (5.27) we obtain the characteristic function and calculate the neutral stability curve, which is precisely the same that has been shown as example in Figure 6.2. The bifurcation point is then:

$$\begin{aligned} r_m &= 0.5539, \\ \kappa_0 &= 0.03255, \\ \omega_0 &= 1.3764. \end{aligned}$$

Notice that now the bifurcation delay is lower from the one we calculated in the microscopic scenario (leading and following vehicles only) $r_m < r_\mu = 1.3079$ s. We then calculate the expansion of the nonlinear part in (5.36) and (5.37). This has been automated, but as a matter of example we provide here the expression for the bilinear form $\mathbf{M}_{l,m}$ for $l, m \geq 0$:

$$\begin{aligned} \mathbf{M}_{l,m}(\mathbf{u},\mathbf{v}) = (&0, \\ &0, \\ &\frac{d^2ab(b-a)}{4(a+b)^2}((v_2j+v_1)(u_1+u_2j)C_1^2+ \\ &((v_4j+v_3)u_1+(v_3j-v_4)u_2+(v_2j+v_1)u_3+(v_1j-v_2)u_4)C_2C_1+ \\ &(v_4j+v_3)(u_3+u_4j)C_2^2), \\ &-\frac{d^2ab(b-a)}{4(a+b)^2}((v_2j+v_1)(u_1+u_2j)C_1^2+ \\ &((v_4j+v_3)u_1+(v_3j-v_4)u_2+(v_2j+v_1)u_3+(v_1j-v_2)u_4)C_2C_1+ \\ &(v_4j+v_3)(u_3+u_4j)C_2^2)\ ). \end{aligned}$$

The calculations of the straightforward expansion produce the results:

$$\begin{aligned} \boldsymbol{\phi}_{0,\kappa_0} =&(-0.2939j, -0.2939, 0.4045, -0.4045), \\ \boldsymbol{\phi}^*_{0,\kappa_0} =&(0.06764+0.0026j, 0.0026-0.06764j, 0.7038, -0.7038j), \\ \mathbf{w}_0 =&(-0.062, 1.0038, 0, 0), \\ \mathbf{w}_2 =&(3.5\cdot10^{-3}+j6.2\cdot10^{-5}, -1.1\cdot10^{-2}-j8.5\cdot10^{-5}, \\ &1.7\cdot10^{-4}+j9.7\cdot10^{-3}, 2.3\cdot10^{-4}-j3.2\cdot10^{-2}), \end{aligned}$$

Notice the real valued vector $\mathbf{w}_0$ that is not null, meaning that the average value of the solution will shift when $r > r_m$, as has been explained in Section 5.3.3.

From the characteristic function (5.27) we calculate:

$$\Lambda_0 = 499 - 1286j,$$

and from (5.33) and (5.34):

$$\gamma = -0.038 + 0.54j.$$

So, we have that $\Re(\gamma) < 0$ and therefore we do not expect modulation of the basic pattern for values of $0 < (r - r_m)/r_m \ll 1$. We can check these results in the following graphs obtained by simulation. They show the evolution of the distance and the velocity of a group of vehicles implementing the model nDDE in a single lane. Figure 5.3 shows what happens when the delay $r = 0.55$ is just below the threshold for the linear stability $r_m = 0.5539$. The figure includes five snapshots of the situation of the vehicles in terms of the velocity and distance to the leading vehicle, for time 0 s, 250 s, 500 s, 750 s and 1000 s. There we can see that, even when there is an initial disturbance, the vehicle system returns to the steady equilibrium (s_0, v_0).

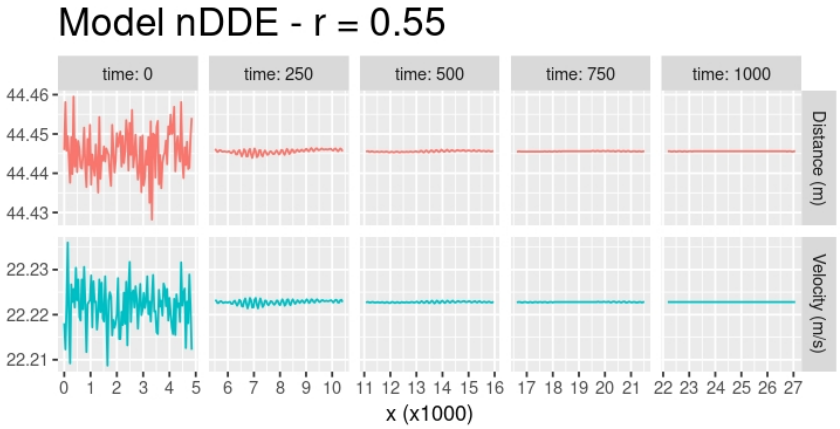


Figure 5.3: Evolution of distance and velocity of the vehicles with nDDE for $r = 0.55s$.

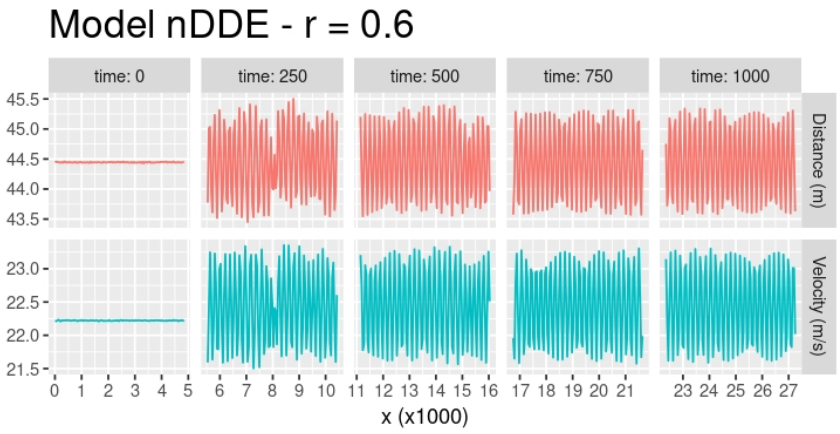


Figure 5.4: Evolution of distance and velocity of the vehicles with nDDE for $r = 0.6s$.

But when the delay goes over the limit, we can expect that oscillations start to appear. Indeed that is the case in the scenario of Figure 5.4, that shows the dynamics when the delay is $r = 0.6 > r_m$. The initial conditions are the same as in Figure 5.3. It can be observed that now oscillations in the distance and velocity of the vehicles appear, and are sustained in time. Even when the oscillations may seem haphazard in this figure, we can take a closer picture of the situation of a group of vehicles. Figure 5.5 shows a closeup of the Figure 5.4 in time

$t = 1000$. Each point in a graph of space and velocity represents the corresponding value for a specific vehicle, and the dotted lines indicate the best sinusoidal fit to those values. One can see that the vehicle dynamics is really close to a basic pattern with wavenumber of spatial period $2\pi/\kappa_0 = 193$ m.

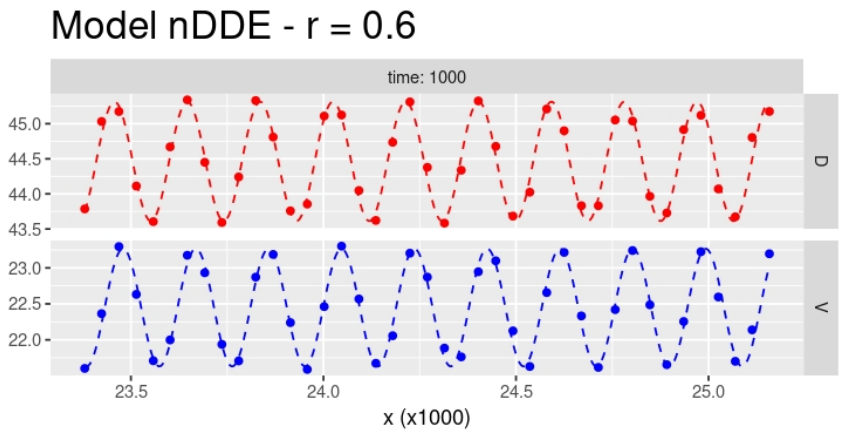


Figure 5.5: Detailed view of the evolution of the vehicles with nDDE for $r = 0.6s$.

The pattern in Figure 5.4 seems quite stable, so one may wonder what happens when the delay grows. The fact that $\Re(\gamma) < 0$ predicts that no modulations should appear in the basic pattern, so when r grows we only expect that the amplitude of the oscillations grows, but not other patterns appear in the traffic dynamics. Figures 5.6 and 5.7 confirm the expectation for a delay $r = 0.7$ s. We can be confident that, up until the macroscopic instabilities appear (which we will staudy in next chapter), stability of the metastable pattern can be expected for this nDDE model. Notice, though, that this may not be the case if the parameters of the models are changed.

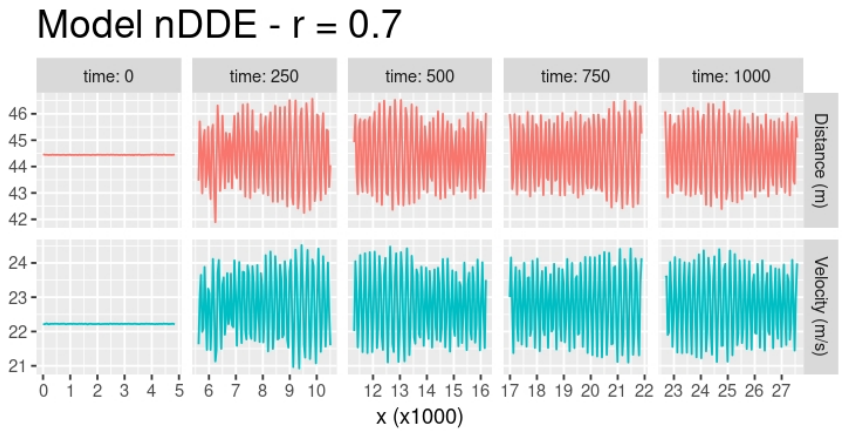


Figure 5.6: Evolution of distance and velocity of the vehicles with nDDE for $r = 0.8s$.

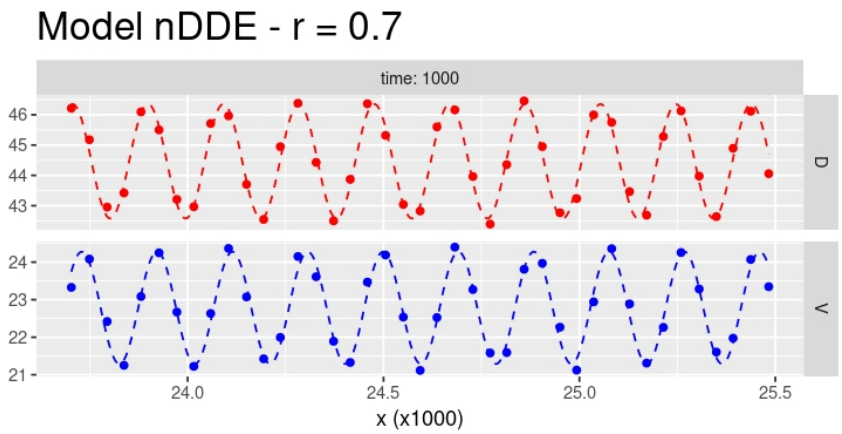


Figure 5.7: Detailed view of the evolution of the vehicles with nDDE for $r = 0.8s$.

5.4 Final comments

This chapter has introduced a novel approach to analyze situations in multi-vehicle scenarios in equilibrium near a bifurcation produced by an increase in the reaction delay of the vehicles. The method search for periodic solutions of the deviation from the equilibrium point by means of a perturbative method. This is translated to a system of retarded PDEs defined in $\mathbb{R}^4$ domain, but expressed as operations in $\mathbb{C}^4$ with complex conjugates. The difficulty of managing these functions is tackled by the use of the Wirtinger calculus techniques, which allows the calculation of the neutral stability curve and the bifurcation point (in time and space).

In addition, the Complex Ginzburg-Landau Equation formalism is used to gain more insights on the nature of the solution at the bifurcation (possibly metastable). The criteria to apply to predict a periodic or modulated pattern in the metastable state are given, and the impact of the constant terms appearing in the solution as an effect of the nonlinearities has been considered too.

The application of this methodology has been illustrated by the calculations of the same traffic model (nDDE) used in the *microscopic* analysis. More results will be provided in Chapter 7.

Chapter 6

General long-wavelength PDE for macroscopic modelling

This chapter introduces the modelling methods for the coarser view of the traffic, in which it is seen as a compressible fluid obeying equations similar to those used in fluid mechanics, that are built from the more basic laws of the microscopic view. We expand an existing methodology applicable to simple microscopic models so that it can be applied to any standard microscopic model. The final objective is to be able to predict accurately the change of the global traffic process from metastability to congestion.

6.1 Construction of the *long-wavelength* macroscopic equations

In this section we generalize the methodology used in [41] and [48] for deriving the equations that describe the macroscopic model of traffic from the dynamics of the microscopic model. In particular, the methodology included in the references derives the macroscopic fluid continuity (2.105) and momentum (2.124) equations, starting from the OVM microscopic equation, as is explained in section 2.2.2. Here we generalize this methodology to be applied to more complex microscopic models, like the nDDE model introduced in Section 2.2.1.

In this chapter we provide the full development of the calculations, in case the reader is interested in this detail. The readers interested only in the final expressions can skip to Section 6.3. Following the notation used in Section 2.2.2, we will consider a traffic flow in a single lane, in which the position of the vehicle n is denoted by $y_n(t)$. The method starts by defining two microscopic field variables in time and space for the vehicle density and for the traffic flow:

$$\begin{aligned} \hat{\rho}(x,t) &= \sum_j \delta(y_n(t) - x), \\ \hat{q}(x,t) &= \sum_j \dot{y}_n(t)\delta(y_n(t) - x), \end{aligned} \tag{6.1}$$

where $y_j(t)$ is the coordinate of vehicle j at time t, the dot $\dot{\square}$ denotes differentiation with

respect to time t and $\delta()$ is Dirac's delta generalized function. We will also denote the distance of the vehicle j with respect to the preceding vehicle $n+1$ as $\Delta y_n(t)$. These variables are represented in figure 6.1.

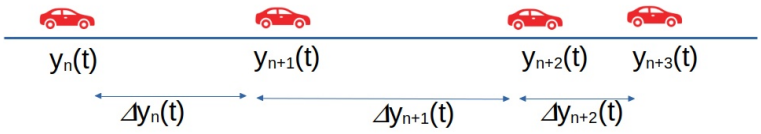


Figure 6.1: Position and distance of the vehicles in the microscopic view of traffic.

In order to get the macroscopic view, we then define coarse-graining functions for the density ρ and flow q by means of a mollifier function $\Phi(x,t)$:

$$\begin{aligned} \rho(x,t) &\equiv \int_{\mathbb{R}}\int_{\mathbb{R}} \Phi(x-\xi,t-\tau)\hat{\rho}(\xi,\tau)d\xi d\tau, \\ q(x,t) &\equiv \int_{\mathbb{R}}\int_{\mathbb{R}} \Phi(x-\xi,t-\tau)\hat{q}(\xi,\tau)d\xi d\tau, \end{aligned} \tag{6.2}$$

where $\Phi(x,t)$ is nonnegative, symmetric and peaked at $(x,t)=(0,0)$, and normalized as $\int\int_{\mathbb{R}\mathbb{R}} \Phi(x,t)dxdt = 1$. Examples of this kind of functions are shown in figure 6.2.

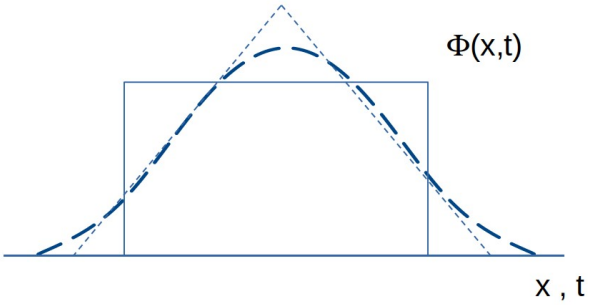


Figure 6.2: Examples of coarse-graining functions.

In the following we will lighten the notation by writing $\Phi \equiv \Phi(x-\xi,t-\tau)$, and $\iint \equiv \int_{\mathbb{R}}\int_{\mathbb{R}}$. Thus, from (6.1) and (6.2):

$$\rho(x,t) \equiv \iint \Phi \sum_i \delta(y_n(\tau)-\xi)d\xi d\tau, \tag{6.3}$$

$$q(x,t) \equiv \iint \Phi \sum_i \dot{y}_n(\tau)\delta(y_n(\tau)-\xi)d\xi d\tau. \tag{6.4}$$

We define the average in (x,t) of a quantity $O_i(\tau)$ measured in every vehicle as:

$$\langle O_i(\tau)\rangle(x,t) \equiv \frac{1}{\rho(x,t)} \iint \Phi \sum_i O_i(\tau)\delta(y_n(\tau)-\xi)d\xi d\tau \quad , \tag{6.5}$$

and in the following we will omit the time variable inside the braquets, i.e. $\langle O_i \rangle(x,t) \equiv \langle O_i(\tau) \rangle(x,t)$. This allows us to define the macroscopic velocity as:

$$v(x,t) = \langle \dot{y}_n \rangle(x,t) = \frac{q(x,t)}{\rho(x,t)} \quad . \tag{6.6}$$

6.1.1 Linearly relevant terms

It is important to note that in the construction of the macroscopic equations it is considered that the traffic is almost homogeneous, and the main objective will be to assess the linear stability of the macroscopic process. In this sense, the products of the form $\prod_{m=1}^{M} \frac{\partial^{l_m}}{\partial x^{l_m}} O_m$, where l_m are integers and O_m is an arbitrary function of ρ and v, become smaller as M increases. To analyze the linear regime, it will be sufficient to retain the elements with $M = 0$ or $M = 1$ and $l_m \leq 2$, which can be called the *linearly relevant* terms. The terms with $M \geq 2$ or $l_m > 2$ are the *linearly irrelevant* terms and will not be considered in the macroscopic equations. See [41] for more details, specifically in Appendix A it is provided an evaluation of the effect of the linearly irrelevant terms for $M = 2$.

6.1.2 Continuity equation

The continuity equation can be obtained by differentiating the density with respect to time:

$$\begin{aligned} &\frac{\partial}{\partial t}\rho(x,t) = \frac{\partial}{\partial t} \iint \Phi \sum_n \delta(y_n(\tau) - \xi) d\xi d\tau = \\ &\iint \frac{\partial}{\partial t} \left(\Phi \sum_n \delta(y_n(\tau) - \xi) \right) d\xi d\tau = \iint \Phi_t \sum_n \delta(y_n(\tau) - \xi) d\xi d\tau = \\ &- \iint \Phi_\tau \sum_n \delta(y_n(\tau) - \xi) d\xi d\tau, \end{aligned} \tag{6.7}$$

where we denote $\frac{\partial}{\partial t}\Phi \equiv \Phi_t$ and have used the fact that $\Phi_t = -\Phi_\tau$. Integrating by parts we get:

$$\frac{\partial}{\partial t}\rho(x,t) = -\int \Phi|_{\tau=-\infty}^{\tau=\infty} d\xi \sum_n \delta(y_n(\tau) - \xi) + \iint \Phi \frac{\partial}{\partial \tau} \sum_n \delta(y_n(\tau) - \xi) d\xi d\tau. \tag{6.8}$$

The first term of the right-hand side is 0, and, using now the chain rule:

$$\frac{\partial}{\partial \tau} \sum_n \delta(y_n(\tau) - \xi) = -\sum_n \dot{y}_n(\tau) \frac{\partial}{\partial \xi} \delta(y_n(\tau) - \xi), \tag{6.9}$$

we get:

$$\frac{\partial}{\partial t}\rho(x,t) = -\iint \Phi \sum_n \dot{y}_n(\tau) \frac{\partial}{\partial \xi} \delta(y_n(\tau) - \xi) d\xi d\tau. \tag{6.10}$$

Integrating by parts once again, we get:

$$\begin{aligned} &\frac{\partial}{\partial t}\rho(x,t) = -\int d\tau \ \Phi|_{\xi=-\infty}^{\xi=\infty} \sum_n \dot{y}_n(\tau) \frac{\partial}{\partial \xi} \delta(y_n(\tau) - \xi) \\ &+ \iint \Phi_\xi \sum_n \dot{y}_n(\tau) \delta(y_n(\tau) - \xi) d\xi d\tau. \end{aligned} \tag{6.11}$$

The first term is 0, thus we get (using $\Phi_x = -\Phi_\xi$):

$$\begin{aligned}\frac{\partial}{\partial t}\rho(x,t) = -\iint \Phi_x \sum_n \dot{y}_n(\tau)\delta(y_n(\tau)-\xi)d\xi d\tau = \\ -\frac{\partial}{\partial x}\iint \Phi \sum_n \dot{y}_n(\tau)\delta(y_n(\tau)-\xi)d\xi d\tau,\end{aligned} \tag{6.12}$$

that, by (6.4), finally yields:

$$\frac{\partial}{\partial t}\rho(x,t) = -\frac{\partial}{\partial x}q(x,t), \tag{6.13}$$

which is the well-known continuity equation for compressible fluids:

$$\frac{\partial}{\partial t}\rho(x,t) + \frac{\partial}{\partial x}q(x,t) = 0, \tag{6.14}$$

in subscripr form:

$$\rho_t + q_x = 0. \tag{6.15}$$

6.1.3 Momentum equation

The momentum equation is built by differentiating the flow with respect to time:

$$\begin{aligned}\frac{\partial}{\partial t}q(x,t) = \frac{\partial}{\partial t}\iint \Phi \sum_n \dot{y}_n(\tau)\delta(y_n(\tau)-\xi)d\xi d\tau = \\ \iint \frac{\partial}{\partial t}\left(\Phi \sum_n \dot{y}_n(\tau)\delta(y_n(\tau)-\xi)\right)d\xi d\tau = \iint \Phi_t \sum_n \dot{y}_n(\tau)\delta(y_n(\tau)-\xi)d\xi d\tau = \\ -\iint \Phi_\tau \sum_n \dot{y}_n(\tau)\delta(y_n(\tau)-\xi)d\xi d\tau.\end{aligned} \tag{6.16}$$

Integrating by parts:

$$\begin{aligned}\frac{\partial}{\partial t}q(x,t) = -\int \Phi|_{\tau=-\infty}^{\tau=\infty} d\xi \sum_n \dot{y}_n(\tau)\delta(y_n(\tau)-\xi) + \\ \iint \Phi \frac{\partial}{\partial \tau}\sum_n \dot{y}_n(\tau)\delta(y_n(\tau)-\xi)d\xi d\tau.\end{aligned} \tag{6.17}$$

The first term is 0, and the second term is expressed using the average defined before:

$$\begin{aligned}\frac{\partial}{\partial t}q(x,t) = \iint \Phi \sum_n \frac{\partial}{\partial \tau}\dot{y}_n(\tau)\delta(y_n(\tau)-\xi)d\xi d\tau = \\ \iint \Phi \sum_n \ddot{y}_n(\tau)\delta(y_n(\tau)-\xi)d\xi d\tau + \iint \Phi \sum_n \dot{y}_n(\tau)\frac{\partial}{\partial \tau}\delta(y_n(\tau)-\xi)d\xi d\tau = \\ \rho(x,t)\langle \ddot{y}_n\rangle(x,t) - \iint \Phi \sum_n \dot{y}_n^2(\tau)\frac{\partial}{\partial \xi}\delta(y_n(\tau)-\xi)d\xi d\tau.\end{aligned} \tag{6.18}$$

Integration of the second term of (6.18) yields:

$$\begin{aligned}
&-\iint \Phi \sum_n \dot{y}_n^2(\tau)\frac{\partial}{\partial \xi}\delta(y_n(\tau)-\xi)d\xi d\tau = \\
&-\int d\tau\ \Phi|_{\xi=-\infty}^{\xi=\infty} \sum_n \dot{y}_n^2(\tau)\delta(y_n(\tau)-\xi) + \iint \Phi_\xi \sum_n \dot{y}_n^2(\tau)\delta(y_n(\tau)-\xi)d\xi d\tau = \\
&-\iint \Phi_x \sum_n \dot{y}_n^2(\tau)\delta(y_n(\tau)-\xi)d\xi d\tau = -\frac{\partial}{\partial x}\iint \Phi \sum_n \dot{y}_n^2(\tau)\delta(y_n(\tau)-\xi)d\xi d\tau = \\
&-\frac{\partial}{\partial x}\left(\rho(x,t)\langle \dot{y}_n^2\rangle(x,t)\right).
\end{aligned} \tag{6.19}$$

From (6.18) and (6.19) we get the following expression of the original equation in term of averages:

$$\frac{\partial}{\partial t}q(x,t) = \rho(x,t)\langle \ddot{y}_n\rangle(x,t) - \frac{\partial}{\partial x}\left(\rho(x,t)\langle \dot{y}_n^2\rangle(x,t)\right). \tag{6.20}$$

To improve readability we remove the explicit mention of the independent variables when possible, so we have:

$$q_t = \rho\langle \ddot{y}_n\rangle - \frac{\partial}{\partial x}\left(\rho\langle \dot{y}_n^2\rangle\right). \tag{6.21}$$

We build the momentum equation in terms of ρ and v by using equations (6.6) and (6.15):

$$\rho_t = -v\rho_x - \rho v_x, \tag{6.22}$$

$$\begin{aligned}
&q_t = v\rho_t + \rho v_t = v(-v\rho_x - \rho v_x) + \rho v_t = -v^2\rho_x - \rho v v_x + \rho v_t = \\
&\rho(v_t + v v_x) - 2\rho v v_x - v^2\rho_x.
\end{aligned} \tag{6.23}$$

Combining (6.21) and (6.23) we get:

$$\rho(v_t + v v_x) = \rho\langle \ddot{y}_n\rangle - \frac{\partial}{\partial x}\left(\rho\langle \dot{y}_n^2\rangle\right) + 2\rho v v_x + v^2\rho_x = \rho\langle \ddot{y}_n\rangle - \frac{\partial}{\partial x}\left[\rho(\langle \dot{y}_n^2\rangle - v^2)\right]. \tag{6.24}$$

Appendix B in [41] provides the following approximation for the second term of the right-hand side of (6.24):

$$\frac{\partial}{\partial x}\left[\rho(\langle \dot{y}_n^2\rangle - v^2)\right] \approx \frac{\partial}{\partial x}\left(\rho\left(\frac{\partial v}{\partial x}\right)^2\left(\langle y_n^2\rangle - \langle y_n\rangle^2\right)\right), \tag{6.25}$$

which produces terms of differential order $M \geq 2$, therefore this term can be dropped. Thus the momentum equation can be finally expressed as:

$$v_t + v v_x = \langle \ddot{y}_n\rangle. \tag{6.26}$$

This shows the important fact that the momentum equation is the one that equates the *material derivative* of the macroscopic velocity to the average of the individual accelerations of the components of the traffic flow. Metaphorically speaking, this is where the microscopic and macroscopic scales meet. Next section provides a methodology to get such an expression from a generic car-following model.

6.2 Expression for the macroscopic acceleration

6.2.1 Managing delay in the microscopic equation

Equation (6.26) includes an expression of the acceleration $\ddot{y}_n(t)$ that is only dependent on time, and no delays are considered. Given that we will be interested in the first order linear approximations for linear stability analysis, to be able to include delayed microscopic equations we need to linearly approximate the delayed equation so that the delay appears explicitly.

We generalize the microscopic acceleration function by considering a set of m variables associated to the vehicle state represented by the vector function $\mathbf{u} : \mathbb{R}^+ \to \mathbb{R}^m$ and a function $g : \mathbb{R}^m \to \mathbb{R}$ that relates this state of the vehicle $\mathbf{u}$ with the induced acceleration. Then we can represent the microscopic acceleration as a retarded function $a : \mathbb{R}^+ \to \mathbb{R}$ such that:

$$a(t + \tau) = g\left(\mathbf{u}(t)\right), \tag{6.27}$$

and we approximate for small τ the function $a(t)$ as:

$$a(t) \approx a(t + \tau) - \tau a'(t + \tau) = g\left(\mathbf{u}(t)\right) - \tau \nabla g(\mathbf{u}) \cdot \mathbf{u}'(t), \tag{6.28}$$

where the prime symbol denotes differentiation with respect to t. It is very likely that in the right hand side of 6.28 appears the acceleration $a(t)$ as the result of the differentiation of the vehicle velocity (possibly part of the vector $\mathbf{u}(t)$). In that case, equation (6.28) must be solved for $a(t)$ in order to get an explicit, non retarded expression for the acceleration.

6.2.2 Series expansion of the acceleration function

As a general case we consider a microscopic car-following model in which the acceleration of a car $a(t)$ is dependent on the following variables:

- $\sigma(t)$: distance with respect to the preceding vehicle.
- $\sigma'(t)$: relative velocity with respect to the preceding vehicle.
- $\sigma''(t)$: relative acceleration with respect to the preceding vehicle.
- $\nu(t)$: absolute velocity of the vehicle.

Therefore we have $\mathbf{u}(t) = (\sigma(t), \sigma'(t), \sigma''(t), \nu(t))$ and, abusing the notation:

$$a(t) = a\left(\mathbf{u}(t)\right) = a\left(\sigma(t), \sigma'(t), \sigma''(t), \nu(t)\right). \tag{6.29}$$

Notice that, in this generic model:

1. the equation is not delayed, though the delay can appear explicitly in the expression of $a(t)$ as a result of the approximation procedure for delayed equations described in previous section;
2. it is not assumed that the preceding vehicle has constant velocity and therefore in general $\sigma''(t) \neq a(t)$.

We consider that every vehicle n in our sigle lane model behaves according to the previous microscopic model, and, in addition to the position of the vehicle $y_n(t)$, we will consider the inter-vehicle distance $\Delta y_n(t)$. We then have:

$$a_n(t) = \ddot{y}_n(t) = a\left(\Delta y_n(t), \Delta\dot{y}_n(t), \Delta\ddot{y}_n(t), \dot{y}_n(t)\right). \tag{6.30}$$

To use this expression in (6.26) we need to calculate:

$$\langle\ddot{y}_n\rangle = \langle a_n\rangle = \langle a\left(\Delta y_n(t), \Delta\dot{y}_n(t), \Delta\ddot{y}_n(t), \dot{y}_n(t)\right)\rangle, \tag{6.31}$$

We are interested in linear stability near the equilibrium point, where the macroscopic process must verify for all vehicles:

- Distance between vehicles: $\Delta y_n(t) = s = \rho^{-1}$.
- Relative velocity: $\Delta\dot{y}_n(t) = 0$.
- Relative acceleration: $\Delta\ddot{y}_n(t) = 0$.
- Velocity of the vehicles $= \dot{y}_n(t) = v$

We will call this macroscopic equilibrium point $(s, 0, 0, v) \equiv \mathbf{u}_M$, so we will use the following linear approximation by series expansion around this equilibrium point:

$$\ddot{y}_n(t) \approx a\left(\mathbf{u}_M\right) + \nabla_{\mathbf{u}}\, a|_{\mathbf{u}_M} \cdot \left((\,\Delta y_n(t) - s), \Delta\dot{y}_n(t)\,, \Delta\ddot{y}_n(t)\,, (\,\dot{y}_n(t) - v)\right). \tag{6.32}$$

Using this linear approximation, it is verified that:

$$\langle\ddot{y}_n\rangle \approx a((\langle\Delta y_n\rangle, \langle\Delta\dot{y}_n\rangle, \langle\Delta\ddot{y}_n\rangle, \langle\dot{y}_n\rangle), \tag{6.33}$$

and, noting that $\langle\dot{y}_n\rangle = v$, we finally get:

$$\begin{aligned}\langle\ddot{y}_n\rangle \approx a\left(\mathbf{u}_M\right) + \left(\langle\Delta y_n\rangle - s\right)\left.\frac{\partial a}{\partial\sigma}\right|_{\mathbf{u}_M} + \\ \langle\Delta\dot{y}_n\rangle\left.\frac{\partial a}{\partial\sigma'}\right|_{\mathbf{u}_M} + \langle\Delta\ddot{y}_n\rangle\left.\frac{\partial a}{\partial\sigma''}\right|_{\mathbf{u}_M}.\end{aligned} \tag{6.34}$$

Then to complete the macroscopic expression of the acceleration, we need to derive expressions for the microscopic averages inside (6.34) in terms of the macroscopic quantities ρ^{-1} and v, as is detailed in the following sections.

Relative distance $\langle\Delta y_n(t)\rangle$

We follow Annex C in [41] in this calculation. It begins by considering the definition of $\langle\Delta y_n(t)\rangle$ according to (6.5):

$$\begin{aligned}\langle\Delta y_n\rangle(x,t) = \frac{1}{\rho(x,t)}\iint\Phi\sum_n\Delta y_n(\tau)\delta(y_n(\tau)-\xi)d\xi d\tau \quad = \\ \frac{1}{\rho(x,t)}\iint\Phi\sum_n\left(y_{n+1}(\tau)-y_n(\tau)\right)\delta(y_n(\tau)-\xi)d\xi d\tau \quad .\end{aligned} \tag{6.35}$$

Omitting now the dependence on x and t we have:

$$\rho\langle \Delta y_n \rangle = \iint \Phi \sum_n \left(y_{n+1}(\tau) - y_n(\tau)\right) \delta(y_n(\tau) - \xi) d\xi d\tau \quad . \tag{6.36}$$

We define now the function $r(x,t)$ that represents the index of the vehicle in front of the position x at time t, i.e., when $y_n(t) < x < y_{n+1}(t)$ then $r(x,t) = n+1$. We will also use the following relationship:

$$\sum_n \left(y_{n+1}(t) - y_n(t)\right) \delta(y_n(t) - x) = \frac{\partial}{\partial x} y_{r(x,t)}(t) \quad . \tag{6.37}$$

Applying (6.37) to (6.36), and using the chain rule as in previous sections we have:

$$\begin{aligned} &\rho\langle \Delta y_n \rangle = \iint \Phi \frac{\partial}{\partial \xi} y_{r(\xi,\tau)}(\tau) d\xi d\tau = \\ &\int d\tau \left(\Phi y_{r(\xi,\tau)}(\tau)\right)\Big|_{\xi=-\infty}^{\xi=\infty} - \iint \Phi_\xi y_{r(\xi,\tau)}(\tau) d\xi d\tau \quad , \end{aligned} \tag{6.38}$$

where again the subindex denotes the partial derivative. The first term is 0, and the second term is transformed in this way:

$$\begin{aligned} &\rho\langle \Delta y_n \rangle = -\iint \Phi_\xi \left(\xi + y_{r(\xi,\tau)}(\tau) - \xi\right) d\xi d\tau = \\ &-\iint \Phi_\xi \xi d\xi d\tau + \iint \Phi_\xi \left(y_{r(\xi,\tau)}(\tau) - \xi\right) d\xi d\tau \quad . \end{aligned} \tag{6.39}$$

The first term of (6.39) equals 1 due to:

$$\iint \Phi_\xi \xi d\xi d\tau = \int d\tau \left(\Phi\xi\right)|_{\xi=-\infty}^{\xi=\infty} - \iint \Phi d\xi d\tau = -1 \quad , \tag{6.40}$$

and we transform the second term of (6.39) to finally obtain the expression:

$$\langle \Delta y_n \rangle = \rho^{-1} + \rho^{-1} \frac{\partial}{\partial x} \left(A1(x,t) + A_2(x,t)\right) \quad , \tag{6.41}$$

where

$$\begin{aligned} A_1(x,t) &= \iint \Phi \left(\frac{y_{r(\xi,\tau)}(\tau) - y_{r(\xi,\tau)-1}(\tau)}{2}\right) d\xi d\tau, \\ A_2(x,t) &= \iint \Phi \left(\frac{y_{r(\xi,\tau)}(\tau) + y_{r(\xi,\tau)-1}(\tau)}{2} - \xi\right) d\xi d\tau. \end{aligned} \tag{6.42}$$

We can use equation (6.41) to derive an approximation of $\langle \Delta y_n \rangle$ as a series expansion on ρ^{-1}, for which next we get the linear and the second order term.

- **Linear term**

  In the homogeneous state, we have that $y_{r(\xi,\tau)}(\tau) - y_{r(\xi,\tau)-1}(\tau) = \rho^{-1}$, and therefore $A_1(x,t) = 1/(2\rho)$. On the other hand, given that $\Phi(x,t)$ is even in x, we also have that $A_2(x,t) = 0$. So, the first order approximation is:

$$\langle \Delta y_n \rangle_{FO} = \frac{1}{\rho} + \frac{1}{2\rho} \frac{\partial \rho^{-1}}{\partial x}. \tag{6.43}$$

- **Second order term**

  To get the second order term in the approximation, we calculate $A_1 + A_2 - 1/(2\rho)$, expecting a term proportional to $\partial\rho^{-1}/\partial x$. The term A1 cannot be the source of such term since the parity in x of ρ and A_1 is even, while the parity of $\partial\rho^{-1}/\partial x$ is odd. Therefore we use:

$$A_2(x,t) = \frac{\partial}{\partial x}\left(B_1(x,t) - B_2(x,t)\right), \tag{6.44}$$

  with

$$\begin{aligned} B_1(x,t) &= \frac{1}{8}\iint \Phi\left(\frac{y_{r(\xi,\tau)}(\tau) - y_{r(\xi,\tau)-1}(\tau)}{2}\right)^2 d\xi d\tau, \\ B_2(x,t) &= \frac{1}{2}\iint \Phi\left(\frac{y_{r(\xi,\tau)}(\tau) + y_{r(\xi,\tau)-1}(\tau)}{2} - \xi\right)^2 d\xi d\tau. \end{aligned} \tag{6.45}$$

  In the homogeneous state we have $B_1 = 1/(8\rho^2)$ and $B_2 = 1/(24\rho^2)$, so we get:

$$A_2(x,t) \approx \frac{1}{12}\frac{\partial\rho^{-2}(x,t)}{\partial x} = \frac{\rho^{-1}(x,t)}{6}\frac{\partial\rho^{-1}(x,t)}{\partial x}. \tag{6.46}$$

Introducing the expression for A_2 in (6.41), the expression for $\langle \Delta y_n\rangle$ is:

$$\langle \Delta y_n\rangle = \frac{1}{\rho} + \frac{1}{2\rho}\frac{\partial\rho^{-1}}{\partial x} + \frac{1}{6\rho^2}\frac{\partial^2\rho^{-1}}{\partial x^2} + \frac{1}{6\rho}\left(\frac{\partial\rho^{-1}}{\partial x}\right)^2. \tag{6.47}$$

At last, disregarding the last term for being linearly irrelevant, we get the final approximation for the average macroscopic distance:

$$\langle \Delta y_n\rangle = \frac{1}{\rho} + \frac{1}{2\rho}\frac{\partial\rho^{-1}}{\partial x} + \frac{1}{6\rho^2}\frac{\partial^2\rho^{-1}}{\partial x^2}. \tag{6.48}$$

Relative velocity $\langle \Delta\dot{y}_n(t)\rangle$

The expression for the relative velocity is diretly included in Annex C in [41], but only some steps of the calculation are provided. We detail here the calculation for completeness. Similarly to the case of the relative distance, we start by the definition of $\langle \Delta\dot{y}_n(t)\rangle$, applying integration by parts and change of variables:

$$\begin{aligned} &\rho\langle \Delta\dot{y}_n\rangle = \iint \Phi\sum_n \left(\dot{y}_{n+1}(\tau) - \dot{y}_n(\tau)\right)\delta(y_n(\tau) - \xi)d\xi d\tau = \\ &\iint \Phi\sum_n \frac{\partial}{\partial\tau}\Delta y_n(\tau)\delta(y_n(\tau) - \xi)d\xi d\tau = \\ &\iint \Phi\frac{\partial}{\partial\tau}\sum_n \Delta y_n(\tau)\delta(y_n(\tau) - \xi)d\xi d\tau + \iint \Phi\sum_n \Delta y_n(\tau)\dot{y}_n(\tau)\frac{\partial}{\partial\xi}\delta(y_n(\tau) - \xi)d\xi d\tau \quad . \end{aligned} \tag{6.49}$$

The first term of (6.49) is calculated in this way:

$$\begin{aligned}
&\iint \Phi \frac{\partial}{\partial \tau} \sum_n \Delta y_n(\tau)\delta(y_n(\tau)-\xi)d\xi d\tau = \\
&\iint \frac{\partial}{\partial \tau}\left[\Phi \sum_n \Delta y_n(\tau)\delta(y_n(\tau)-\xi)\right] d\xi d\tau - \iint \Phi_\tau \sum_n \Delta y_n(\tau)\delta(y_n(\tau)-\xi)d\xi d\tau = \\
&\int \left[\Phi \sum_n \Delta y_n(\tau)\delta(y_n(\tau)-\xi)\right]_{\tau=-\infty}^{\tau=\infty} d\xi + \iint \Phi_t \sum_n \Delta y_n(\tau)\delta(y_n(\tau)-\xi)d\xi d\tau = \\
&\frac{\partial}{\partial t}\iint \Phi \sum_n \Delta y_n(\tau)\delta(y_n(\tau)-\xi)d\xi d\tau = \frac{\partial}{\partial t}\left[\rho\langle \Delta y_n(t)\rangle\right] \quad ,
\end{aligned} \tag{6.50}$$

while the second term of (6.49) results in:

$$\begin{aligned}
&\iint \Phi \sum_n \Delta y_n(\tau)\dot{y}_n(\tau)\frac{\partial}{\partial \xi}\delta(y_n(\tau)-\xi)d\xi d\tau = \\
&\iint \frac{\partial}{\partial \xi}\left[\Phi \sum_n \Delta y_n(\tau)\dot{y}_n(\tau)\delta(y_n(\tau)-\xi)\right] d\xi d\tau - \iint \Phi_\xi \sum_n \Delta y_n(\tau)\dot{y}_n(\tau)\delta(y_n(\tau)-\xi)d\xi d\tau = \\
&\int \left[\Phi \sum_n \Delta y_n(\tau)\dot{y}_n(\tau)\delta(y_n(\tau)-\xi)\right]_{\xi=-\infty}^{\xi=\infty} d\tau + \iint \Phi_x \sum_n \Delta y_n(\tau)\dot{y}_n(\tau)\delta(y_n(\tau)-\xi)d\xi d\tau = \\
&\frac{\partial}{\partial x}\iint \Phi \sum_n \Delta y_n(\tau)\dot{y}_n(\tau)\delta(y_n(\tau)-\xi)d\xi d\tau = \frac{\partial}{\partial x}\left[\rho\langle \Delta y_n(t)\dot{y}_n(\tau)\rangle\right] \quad ,
\end{aligned} \tag{6.51}$$

Therefore we have:

$$\rho\langle \Delta \dot{y}_n\rangle = \frac{\partial}{\partial t}\left[\rho\langle \Delta y_n(t)\rangle\right] + \frac{\partial}{\partial x}\left[\rho\langle \Delta y_n(t)\dot{y}_n(\tau)\rangle\right] \quad . \tag{6.52}$$

We will use the following approximation:

$$\langle \Delta y_n(t)\dot{y}_n(\tau)\rangle \approx v\langle \Delta y_n(t)\rangle \quad . \tag{6.53}$$

Using (6.52) and (6.53) we get:

$$\begin{aligned}
&\rho\langle \Delta \dot{y}_n\rangle = \frac{\partial}{\partial t}\left[\rho\langle \Delta y_n(t)\rangle\right] + \frac{\partial}{\partial x}\left[\rho v\langle \Delta y_n(t)\rangle\right] = \\
&\langle \Delta y_n(t)\rangle \frac{\partial \rho}{\partial t} + \rho\frac{\partial\langle \Delta y_n(t)\rangle}{\partial t} + \langle \Delta y_n(t)\rangle \rho\frac{\partial v}{\partial x} + \langle \Delta y_n(t)\rangle v\frac{\partial \rho}{\partial x} + \rho v\frac{\partial\langle \Delta y_n(t)\rangle}{\partial x} = \\
&\langle \Delta y_n(t)\rangle\left(\frac{\partial \rho}{\partial t} + \rho\frac{\partial v}{\partial x} + v\frac{\partial \rho}{\partial x}\right) + \rho\frac{\partial\langle \Delta y_n(t)\rangle}{\partial t} + \rho v\frac{\partial\langle \Delta y_n(t)\rangle}{\partial x} \quad .
\end{aligned} \tag{6.54}$$

The first term of the final expression in (6.54) is 0 by virtue of the continuity equation, so we finally get:

$$\langle \Delta \dot{y}_n\rangle = \frac{\partial\langle \Delta y_n(t)\rangle}{\partial t} + v\frac{\partial\langle \Delta y_n(t)\rangle}{\partial x} \quad , \tag{6.55}$$

which can also be expressed in terms of the *material derivative* used in fluid mechanics:

$$\langle \Delta \dot{y}_n \rangle = \left(\frac{\partial}{\partial t} + v \frac{\partial}{\partial x} \right) \langle \Delta y_n(t) \rangle \quad , \tag{6.56}$$

Now we can use the expression for the relative distance in equation (6.48), using $s = \rho^{-1}$ and the subscripts for the partial derivatives to ease the notation:

$$\langle \Delta y_n \rangle = s + \frac{s s_x}{2} + \frac{s^2 s_{xx}}{6}. \tag{6.57}$$

In this way, taking only the first two terms of this expression, which are the ones that will produce linearly relevant terms, we get:

$$\langle \Delta \dot{y}_n \rangle = \left(\frac{\partial}{\partial t} + v \frac{\partial}{\partial x} \right) \left(s + \frac{s s_x}{2} \right) = s_t + \frac{s_t s_x + s s_{xt}}{2} + v s_x + \frac{v(s s_{xx} + s_x^2)}{2} \quad . \tag{6.58}$$

Introducing the continuity equation in the form $s_t = s v_x - v s_x$:

$$\begin{aligned} \langle \Delta \dot{y}_n \rangle &= (s v_x - v s_x) + \frac{1}{2} \left((s v_x - v s_x) s_x + s \frac{\partial}{\partial x} (s v_x - v s_x) \right) + v s_x + \frac{v}{2} \left(s s_{xx} + s_x^2 \right) = \\ & s v_x - v s_x + \frac{1}{2} \left(s v_x s_x - v s_x^2 + s s_x v_x + s^2 v_{xx} - v_x s s_x - v s s_{xx} \right) + v s_x + \frac{v}{2} \left(s s_{xx} + s_x^2 \right) = \\ & s v_x + \frac{1}{2} s^2 v_{xx} + \frac{1}{2} s v_x s_x \quad . \end{aligned} \tag{6.59}$$

Finally, dropping the last term for being linearly irrelevant, and returning to the notation using $\rho = s^{-1}$ we get the approximation to the average relative velocity:

$$\langle \Delta \dot{y}_n \rangle = \frac{1}{\rho} \frac{\partial v}{\partial x} + \frac{1}{2\rho^2} \frac{\partial^2 v}{\partial x^2}. \tag{6.60}$$

Relative acceleration $\langle \Delta \ddot{y}_n(t) \rangle$

The source [41] considers just the relative distance and relative velocity as the variables that determine the acceleration. In order to build a more general model that could consider the relative acceleration, in the following we derive an expression for the average of this microscopic quantity in terms of ρ and v.

As usual we start by the definition of of $\langle \Delta \ddot{y}_n(t) \rangle$, applying integration by parts and change of variables

$$\begin{aligned} & \rho \langle \Delta \ddot{y}_n \rangle = \iint \Phi \sum_n \left(\ddot{y}_{n+1}(\tau) - \ddot{y}_n(\tau) \right) \delta(y_n(\tau) - \xi) d\xi d\tau = \\ & \iint \Phi \sum_n \frac{\partial}{\partial \tau} \Delta \dot{y}_n(\tau) \delta(y_n(\tau) - \xi) d\xi d\tau = \\ & \iint \Phi \frac{\partial}{\partial \tau} \sum_n \Delta \dot{y}_n(\tau) \delta(y_n(\tau) - \xi) d\xi d\tau + \iint \Phi \sum_n \Delta \dot{y}_n(\tau) \dot{y}_n(\tau) \frac{\partial}{\partial \xi} \delta(y_n(\tau) - \xi) d\xi d\tau \quad . \end{aligned} \tag{6.61}$$

Using the same method as in the previous section to get the *material derivative* expression:

$$\langle \Delta \ddot{y}_n \rangle = \left(\frac{\partial}{\partial t} + v \frac{\partial}{\partial x} \right) \langle \Delta \dot{y}_n(t) \rangle \quad . \tag{6.62}$$

Now using (6.60) and (6.62) we have:

$$\langle \Delta \ddot{y}_n \rangle = \left(\frac{\partial}{\partial t} + v \frac{\partial}{\partial x} \right) \left(s v_x + \frac{s^2 v_{xx}}{2} \right) \quad , \tag{6.63}$$

that, retaining only the linearly relevant terms, finally yields:

$$\langle \Delta \ddot{y}_n \rangle = \frac{1}{\rho} \left(\frac{\partial v^2}{\partial x \partial t} + v \frac{\partial^2 v}{\partial x^2} \right). \tag{6.64}$$

6.3 Final PDE system for the macroscopic process

Inserting expressions (6.48).(6.60) and (6.64) in equation (6.34) we get:

$$\begin{aligned} \langle \ddot{y}_n \rangle \approx a\left(\mathbf{u}_M\right) + \left(s \frac{\partial s}{\partial x} + \frac{s^2}{6} \frac{\partial^2 s}{\partial x^2} \right) \left. \frac{\partial a}{\partial \sigma} \right|_{\mathbf{u}_M} + \\ \left(s \frac{\partial v}{\partial x} + \frac{s^2}{2} \frac{\partial^2 v}{\partial x^2} \right) \left. \frac{\partial a}{\partial \sigma'} \right|_{\mathbf{u}_M} + s \left(\frac{\partial v^2}{\partial x \partial t} + v \frac{\partial^2 v}{\partial x^2} \right) \left. \frac{\partial a}{\partial \sigma''} \right|_{\mathbf{u}_M}, \end{aligned} \tag{6.65}$$

which, by (6.26) finally yields the following momentum equation using subscripts for partial derivatives of $s = \rho^{-1}$ and v:

$$\begin{aligned} v_t + v v_x = a\left(\mathbf{u}_M\right) + \left(s s_x + \frac{s^2}{6} s_{xx} \right) \left. \frac{\partial a}{\partial \sigma} \right|_{\mathbf{u}_M} + \\ \left(s v_x + \frac{s^2}{2} v_{xx} \right) \left. \frac{\partial a}{\partial \sigma'} \right|_{\mathbf{u}_M} + s \left(v_{xt} + v v_{xx} \right) \left. \frac{\partial a}{\partial \sigma''} \right|_{\mathbf{u}_M}. \end{aligned} \tag{6.66}$$

Now we will call:

$$\begin{aligned} C_0(\mathbf{u}) &= a\left(\mathbf{u}\right), & C_1(\mathbf{u}) &= \left. \frac{\partial a}{\partial \sigma} \right|_{\mathbf{u}}, \quad C_2(\mathbf{u}) = \left. \frac{\partial a}{\partial \sigma'} \right|_{\mathbf{u}}, \\ C_3(\mathbf{u}) &= \left. \frac{\partial a}{\partial \sigma''} \right|_{\mathbf{u}}, & C_4(\mathbf{u}) &= \left. \frac{\partial a}{\partial \nu} \right|_{\mathbf{u}}. \end{aligned} \tag{6.67}$$

In this way the macroscopic PDE system in terms of $s = \rho^{-1}$ and v becomes:

$$s_t + v s_x - s v_x = 0, \tag{6.68}$$

$$v_t + v v_x = C_0(\mathbf{u}_M) + C_1(\mathbf{u}_M)(\frac{s}{2} s_x + \frac{s^2}{6} s_{xx}) + C_2(\mathbf{u}_M)(s v_x + \frac{s^2}{2} v_{xx}) + C_3(\mathbf{u}_M)(s v_{xt} + s v v_{xx}), \tag{6.69}$$

6.4 Linear stability analysis

6.4.1 Long wavelength approximation linear equation

As stated before, the macroscopic model is constructed so that it is valid at large time and space scales. In this sense, the equations derived are only representative of the physical process in these large scales, and this is usually referred to as the model being a *long-wavelength* model.

We can use this to simplify equation (6.69) when searching for the linear stability limit in this way. We look at the (non-retarded) microscopic model of the vehicle n (in the frame of reference of vehicle n), so we have the following linear ODE:

$$\sigma_n'' = \frac{\partial a(\sigma,\sigma',\sigma'',\nu)}{\partial \sigma}\,|_{\boldsymbol{\mu}_0}\,(\sigma_n-\sigma_0) + \frac{\partial a(\sigma,\sigma',\sigma'',\nu)}{\partial \sigma'}\,|_{\boldsymbol{\mu}_0}\,\sigma_n' + \tag{6.70}$$

$$\frac{\partial a(\sigma,\sigma',\sigma'',\nu)}{\partial \sigma''}\,|_{\boldsymbol{\mu}_0}\,\sigma_n'' + \frac{\partial a(\sigma,\sigma',\sigma'',\nu)}{\partial \nu}\,|_{\boldsymbol{\mu}_0}\,(\nu_n-v_0), \tag{6.71}$$

where $\boldsymbol{\mu}_0 = (\sigma_0, 0, 0, v_0)$ is the microscopic equilibrium point. Using the notation in (6.67):

$$\sigma_n'' = C_1(\boldsymbol{\mu}_0)(\sigma_n-\sigma_0) + C_2(\boldsymbol{\mu}_0)\sigma_n' + C_3(\boldsymbol{\mu}_0)\sigma_n'' + C_4(\boldsymbol{\mu}_0)(\nu_n - v_0). \tag{6.72}$$

If we consider a perturbation similar to the one used in the mesoscopic model, i.e.

$$y_n(t) = s_0 n + v_0 t + \delta y\left(e^{j\kappa s_0 n + \lambda_m t} + e^{-j\kappa s_0 n + \bar{\lambda}_m t}\right),$$
$$y_{n+1}(t) = s_0(n+1) + v_0 t + \delta y\left(e^{j\kappa s_0 (n+1) + \lambda_m t} + e^{-j\kappa s_0 (n+1) + \bar{\lambda}_m t}\right),$$

where we have denoted the eigenvalues with the subscript m to note that they refer to the moving frame of reference of the vehicle n. For $y_n^+(t) = s_0 n + v_0 t + \delta y e^{j\kappa s_0 n + \lambda_m t}$, we get the following characteristic function:

$$\lambda_m^2 - \frac{C_4(\boldsymbol{\mu}_0) + C_2(\boldsymbol{\mu}_0)(e^{j\kappa s_0}-1)}{1 - C_3(\boldsymbol{\mu}_0)(e^{j\kappa s_0}-1)}\lambda_m - \frac{C_1(\boldsymbol{\mu}_0)(e^{j\kappa s_0}-1)}{1 - C_3(\boldsymbol{\mu}_0)(e^{j\kappa s_0}-1)} = 0.$$

We now use the *long-wavelength* approximation, that means that $0 < \kappa s_0 \ll 1$, and in this case we can approximate:

$$e^{j\kappa s_0} \approx 1 + j\kappa s_0,$$

and then the characteristic function becomes:

$$\lambda_m^2 - \frac{C_4(\boldsymbol{\mu}_0) + C_2(\boldsymbol{\mu}_0) j\kappa s_0}{1 - C_3(\boldsymbol{\mu}_0) j\kappa s_0}\lambda_m - \frac{C_1(\boldsymbol{\mu}_0) j\kappa s_0}{1 - C_3(\boldsymbol{\mu}_0) j\kappa s_0} = 0.$$

One solution to this equation is:

$$\lambda_m^- = \frac{C_4(\boldsymbol{\mu}_0) + C_2(\boldsymbol{\mu}_0) j\kappa s_0}{2(1 - C_3(\boldsymbol{\mu}_0) j\kappa s_0)}\left(1 - \sqrt{1 + \frac{4C_1(\boldsymbol{\mu}_0)(1 - C_3(\boldsymbol{\mu}_0) j\kappa s_0)}{(C_4(\boldsymbol{\mu}_0) + C_2(\boldsymbol{\mu}_0) j\kappa s_0)^2} j\kappa s_0}\right).$$

Noting now that for small x we have $\sqrt{1+x} \approx 1 + x/2$ we get:

$$\lambda_m^- \approx \frac{-C_1(\boldsymbol{\mu}_0) j\kappa s_0}{C_4(\boldsymbol{\mu}_0) + C_2(\boldsymbol{\mu}_0) j\kappa s_0} \approx \frac{-C_1(\boldsymbol{\mu}_0) j\kappa s_0}{C_4(\boldsymbol{\mu}_0)}. \tag{6.73}$$

Now we consider the macroscopic PDE equations (6.68) and (6.69), and introduce a corresponding perturbation in a wavenumber κ:

$$\begin{aligned} s(x,t) &= s_0 + \delta s e^{j\kappa x + \lambda_M t}, \\ v(x,t) &= v_0 + \delta v e^{j\kappa x + \lambda_M t}, \end{aligned} \tag{6.74}$$

now using an eigenvalue λ_M that refers to the absolute reference frame corresponding to the macroscopic process. Then, we must note that:

$$\lambda_m = \lambda_M + j\kappa v_0. \tag{6.75}$$

Introducing (6.74) in the continuity equation (6.68) we obtain:

$$\delta s = \frac{j\kappa s_0}{\lambda_M + j\kappa v_0} \delta v. \tag{6.76}$$

We have, by (6.73) and (6.75):

$$\delta s \approx -\frac{C_4(\boldsymbol{\mu}_0)}{C_1(\boldsymbol{\mu}_0)} \delta v. \tag{6.77}$$

Differentiating the continuity equation (6.68) in x:

$$s_{tx} + v s_{xx} - s v_{xx} = 0, \tag{6.78}$$

and using approximation (6.77) in the form:

$$s_{tx} \approx -\frac{C_4(\boldsymbol{\mu}_0)}{C_1(\boldsymbol{\mu}_0)} v_{tx}, \tag{6.79}$$

we finally obtain:

$$v_{tx} \approx -\frac{C_1(\boldsymbol{\mu}_0)}{C_4(\boldsymbol{\mu}_0)} (s v_{xx} - v s_{xx}) \approx \left(-\frac{C_1(\boldsymbol{\mu}_0)}{C_4(\boldsymbol{\mu}_0)} s - v \right) v_{xx}, \tag{6.80}$$

Given that we will be interested in the linear stability of the system (6.68) and (6.69), we linearize the macroscopic equations in the equilibrium point (s_0, v_0). Introducing the perturbation (6.74) in the system, using $\boldsymbol{\mu}_0 = (\sigma_0, 0, 0, \nu_0) = (s_0, 0, 0, v_0)$, and renaming $s \equiv \delta s$ and $v \equiv \delta v$ we get the linearized system:

$$s_t + v_0 s_x - s_0 v_x = 0, \tag{6.81}$$

$$\begin{aligned} v_t + v_0 v_x = {} & C_1(\boldsymbol{\mu}_0) s + C_4(\boldsymbol{\mu}_0) v + C_1(\boldsymbol{\mu}_0) \left(\frac{s_0}{2} s_x + \frac{s_0^2}{6} s_{xx} \right) + \\ & C_2(\boldsymbol{\mu}_0) \left(s_0 v_x + \frac{s_0^2}{2} v_{xx} \right) + C_3(\boldsymbol{\mu}_0)(s_0 v_{xt} + s_0 v_0 v_{xx}), \end{aligned} \tag{6.82}$$

Then if we insert the approximations (6.77) and (6.80) in (6.82), we obtain a single linear equation for v:

$$v_t + v_0 v_x = \frac{2C_2(\boldsymbol{\mu}_0) - C_4(\boldsymbol{\mu}_0)}{2} s_0 v_x + \frac{3C_2(\boldsymbol{\mu}_0) C_4(\boldsymbol{\mu}_0) - 6C_3(\boldsymbol{\mu}_0) C_1(\boldsymbol{\mu}_0) - C_4^2}{6C_4(\boldsymbol{\mu}_0)} s_0^2 v_{xx}. \tag{6.83}$$

6.4.2 Linear stability limit in the long-wavelength regime

To study the stability of the system near the equilibrium point (s_0, v_0), we introduce a perturbation of exponential type in time and space for a wavenumber κ in the form

$$v(x,t) = \delta v_\kappa e^{j\kappa x + \lambda_\kappa t}. \tag{6.84}$$

Remember that in equation (6.83) v represents the deviation with respect to the average velocity v_0. From the linearization of the long-wavelength momentum equation (6.82), and simplifying the notation $C_i \equiv C_i(\boldsymbol{\mu}_0)$ we have the linear PDE for the macroscopic velocity:

$$v_t + v_0 v_x = \frac{2C_2 - C_4}{2} s_0 v_x + \frac{3C_2C_4 - 6C_3C_1 - C_4^2}{6C_4} s_0^2 v_{xx}. \tag{6.85}$$

If we introduce the perturbation (6.84) in (6.85) we obtain the eigenvalue:

$$\lambda_\kappa = (\frac{2C_2 - C_4}{2} s_0 - v_0) j\kappa - \frac{3C_2C_4 - 6C_3C_1 - C_4^2}{6C_4} s_0^2 \kappa^2, \tag{6.86}$$

which imposes the stability condition:

$$\frac{3C_2C_4 - 6C_3C_1 - C_4^2}{6C_4} > 0, \tag{6.87}$$

6.5 Examples of macroscopic stability

For illustrative purposes we include here a couple of brief examples of application of the contents of this chapter. Nevertheless, to give aa wholistic view of the contents of the thesis, in next chapter we will detail complete examples of application to different microscopic models of all the methods introduced by this thesis, from the microscopic scale to the macroscopic one.

6.5.1 Macroscopic linear instability of the Optimal Velocity Model

We apply now the methodology to the Optimal Velocity Model (OVM) introduced in Section 2.2.1. The OVM we will use is the one introduced in [4], where the delayed velocity obeys the following sigmoidal function:

$$\nu(t+r) = V\left(\sigma(t)\right) = \frac{\nu_{max}}{2}(\tanh(\sigma(t) - s_0) - \tanh(s_0)) \quad , \tag{6.88}$$

From this equation we can get a non retarded acceleration approximation:

$$\nu(t+r) \approx \nu(t) + r a(t), \tag{6.89}$$

$$a(t) = \frac{1}{r}\left(V\left(\sigma(t)\right) - \nu(t)\right) \tag{6.90}$$

Notice that in this simpler model we have only dependence on the microscopic variables $\sigma(t)$ an $\nu(t)$, i.e. $\mathbf{u}(t) = (\sigma(t), \nu(t))$, and $a(t) = a\left(\sigma(t), \nu(t)\right)$. The coefficients for the linear expansion of the acceleration (6.67) are:

$$\begin{aligned} C_1 &= \left.\frac{\partial a}{\partial \sigma}\right|_{(s_0,v_0)} = \frac{V'(s_0)}{r}, \\ C_2 &= 0, \quad C_3 = 0, \\ C_4 &= \left.\frac{\partial a}{\partial \nu}\right|_{(s_0,v_0)} = -\frac{1}{r}, \end{aligned} \tag{6.91}$$

where we have used $\frac{\nu_{max}}{2} = V'(s_0)$.

We can apply directly the stability criteria in (6.87)

$$-C_4 = \frac{1}{r} > 0, \tag{6.92}$$

This condition is always met, so there is no macroscopic instability in the OVM. This means that once the microscopic limit is reached, no density waves are formed over the fundamental oscillations.

To illustrate this we show simulation results with a comparison of the evolution of a traffic scenario of 100 vehicles that implement the OVM model for different values of delay. The vehicles follows the optimal velocity function V in (2.91) with $v_{max} = 20$ m/s and the equilibrium distance is $d_c = 100$ m. The limiting delay at mesoscopic scale is, by (2.95)

$$r_n < \frac{1}{2V'(d_c)} = \frac{1}{v_{max}} = 0.05 \quad . \tag{6.93}$$

In Figures 6.3, 6.4 and 6.5, we can see that in all cases the delay is greater than the limiting delay, and that oscillations typical of the mesoscopic scale are formed. But we can also see that, even for values of delay far greater than this limit, like Figures 6.4 and 6.5, the mesoscopic state is not destabilized, and there is no formation of stop and go traffic, confirming the prediction of (6.92).

6.5.2 Macroscopic linear instability of the nDDE Model

Following the same methodology, we start considering the original nDDE micro equation. For clarity we rename in this context the maximum acceleration and deceleration as α and β respectively, and we use the notation for microscopic quantities introduced in (6.29):

$$a(t+r) = \alpha - \frac{(\alpha+\beta)}{1 + \frac{\beta}{\alpha} e^{d(\sigma(t) - M + K\sigma'(t))}} \tag{6.94}$$

In this micro model, we assumed before that the leader velocity is constant, with value ν_0, that induces a safety distance m, but in an scenario with multiple vehicles we need to model that this velocity will not be constant. In a general setting, it can be expected that the safety

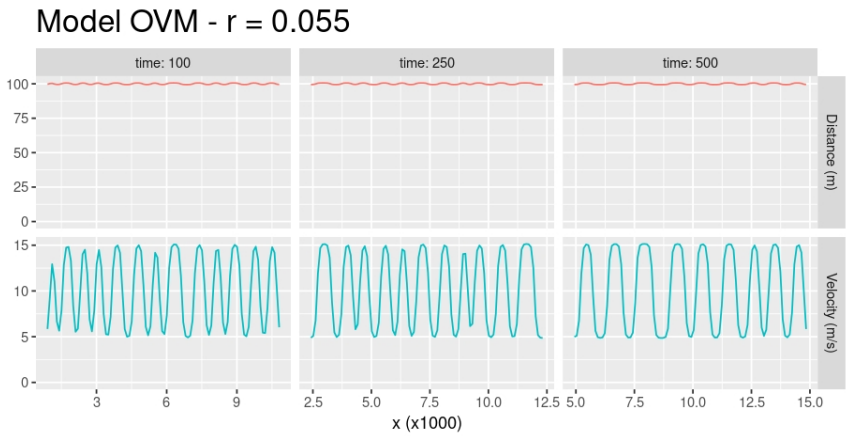


Figure 6.3: Evolution of distance and velocity of the vehicles with OVM for $r = 0.055s$.

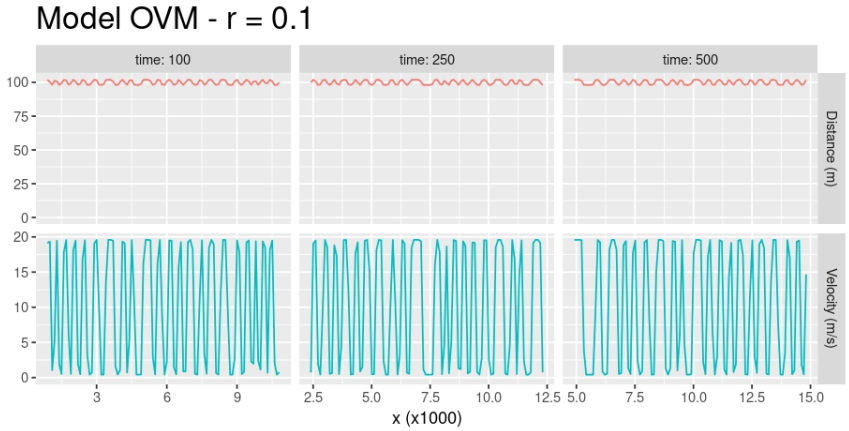


Figure 6.4: Evolution of distance and velocity of the vehicles with OVM for $r = 0.1s$.

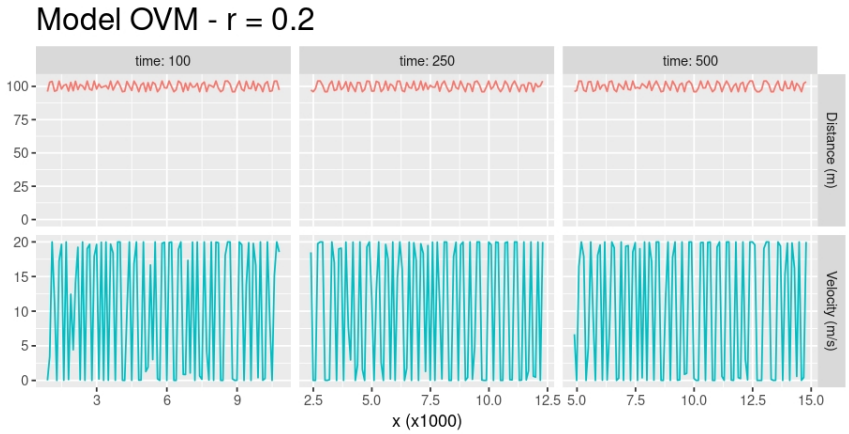


Figure 6.5: Evolution of distance and velocity of the vehicles with OVM for $r = 0.2s$.

distance is dependent on the velocity of the preceding vehicle ν_l in such a way that the greater ν_l is, the greater the safety distance m will be. For simplicity we will consider the following

linear dependence:

$$M(\nu_l) = \sigma_{min} + (\sigma_0 - \sigma_{min})\frac{\nu_l}{\nu_0}, \tag{6.95}$$

where σ_{min} is the physical limit of the inter-vehicle distance and σ_0 is the safety distance corresponding to the leader velocity ν_0 in the micro model (6.94). In this way, the equation nDDE considering the variable ν_l is:

$$\begin{aligned} a(t+r) = \alpha - \frac{(\alpha+\beta)}{1+\frac{\beta}{\alpha}e^{d(\sigma(t)-M(\nu_l(t))+K\sigma'(t))}} = \\ \alpha - \frac{(\alpha+\beta)}{1+\frac{\beta}{\alpha}e^{d(\sigma(t)-\sigma_{min}+(\sigma_0-\sigma_{min})\frac{\nu_l(t)}{\nu_0}+K\sigma'(t))}}. \end{aligned} \tag{6.96}$$

Denoting the follower velocity as $\nu(t) = \nu_l(t) - \sigma'(t)$, we get:

$$a(t+r) = \alpha - \frac{(\alpha+\beta)}{1+\frac{\beta}{\alpha}e^{d(\sigma(t)-K_0\nu(t)+K_1\sigma'(t))}}, \tag{6.97}$$

where $K_0 = \sigma_{min} + (\sigma_0 - \sigma_{min})/\nu_0$ and $K_1 = K - (\sigma_0 - \sigma_{min})/\nu_0$. For simplicity in the following we will consider $\sigma_{min} = 0$ and therefore $K_0 = \sigma_0/\nu_0$ and $K_1 = K - K_0$.

To simplify the formulas, we define the function $F : \mathbb{R}\times\mathbb{R}\times\mathbb{R} \to \mathbb{R}/F(x_1,x_2,x_3) = d(x_1 - K_0x_2 + K_1x_3)$ for the exponent in the acceleration function, so we get the retarded acceleration equation:

$$a(t+r) = \alpha - \frac{(\alpha+\beta)}{1+\frac{\beta}{\alpha}e^{F(\sigma(t),\nu(t),\sigma'(t))}}. \tag{6.98}$$

Differentiating this expression and omitting the dependence on t in the right-hand side:

$$a'(t+r) = \alpha\beta(\alpha+\beta)d\frac{e^{F(\sigma,\nu,\sigma')}}{\left(\alpha+\beta e^{F(\sigma,\nu,\sigma')}\right)^2}(\sigma' + K_1\sigma'' - K_0\nu') \tag{6.99}$$

Given that $a(t) = \nu'(t)$, and using the linearization process in (6.28) $a(t) \approx a(t+r) - ra'(t+r)$ we get:

$$a(t) = \alpha - \frac{\alpha(\alpha+\beta)}{\alpha+\beta e^{F(\sigma,\nu,\sigma')}} - r\frac{\alpha\beta(\alpha+\beta)de^{F(\sigma,\nu,\sigma')}}{\left(\alpha+\beta e^{F(\sigma,\nu,\sigma')}\right)^2}(\sigma' + K_1\sigma'' - K_0a(t)). \tag{6.100}$$

Solving for $a(t)$ and simplifying:

$$a(t) = \frac{\alpha\beta\nu_0\left[\alpha - \beta e^{2F(\sigma,\nu,\sigma')} + e^{F(\sigma,\nu,\sigma')}\left(-\alpha+\beta+(\alpha+\beta)d(\sigma'+K_1\sigma'')\tau\right)\right]}{\alpha\beta e^{F(\sigma,\nu,\sigma')}\left((\alpha+\beta)d\sigma_0 r - 2\nu_0\right) - \alpha^2\nu_0 - \beta^2\nu_0 e^{2F(\sigma,\nu,\sigma')}}. \tag{6.101}$$

In this way we get an explicit, non retarded equation of the acceleration of the form:

$$a(t) = a(\sigma(t), \sigma'(t), \sigma''(t), \nu(t)), \tag{6.102}$$

and we can apply the method to calculate the macroscopic linear stability (6.87).

The coefficients of the linear PDE near the equilibrium $(\sigma_0, \nu_0) = (s_0, v_0)$ are

$$\begin{aligned} C_1 &= -G(r)v_0, \\ C_2 &= G(r)v_0(r - K_1), \\ C_3 &= G(r)v_0 r K_1, \\ C_4 &= G(r)s_0, \end{aligned} \tag{6.103}$$

where:

$$G(r) = \frac{\alpha\beta d}{\alpha\beta d s_0 r - \alpha v_0 - \beta v_0}. \tag{6.104}$$

We can now apply the criteria of stability (6.87) to obtain:

$$r_M < \frac{s_0\left(3K_1v_0 + s_0\right)}{3v_0\left(2K_1v_0 + s_0\right)}. \tag{6.105}$$

If we use the values of the nDDE model in Table 4.2, we can determine the stability criteria:

$$r_M < 0.9679 \text{ s}, \tag{6.106}$$

We show in the following comparable results for three values of delay for the nDDE scenario that we introduced in Chapter 4 for the nDDE model, whose values are in Table 4.2, and for which we determined a limiting delay in the mesoscopic scale $r_m = 0.5539$ s. We see that the three scenarios have delays over the mesoscopic limit, and then present oscillation. The two first scenarios have $r_m < r < r_M$ and therefore present oscillation typical of mesoscopic state, but not density waves. But only in the last scenario, with $r > r_M$ after some time the macroscopic instability sets in and density waves and stop-and-go traffic manifests.



Figure 6.6: Evolution of distance and velocity of the vehicles with nDDE for $r = 0.6s$.

We will compare these results to other driving models in Chapter 7, where we provide a complete perspective of the results presented in this thesis.

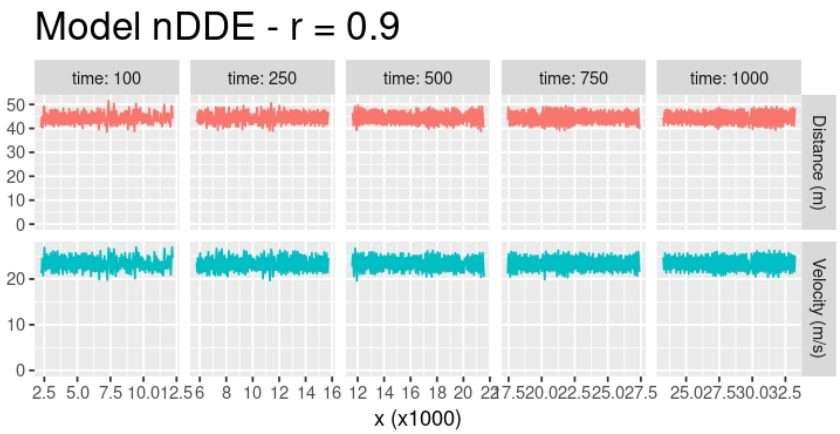


Figure 6.7: Evolution of distance and velocity of the vehicles with nDDE for $r = 0.9s$.

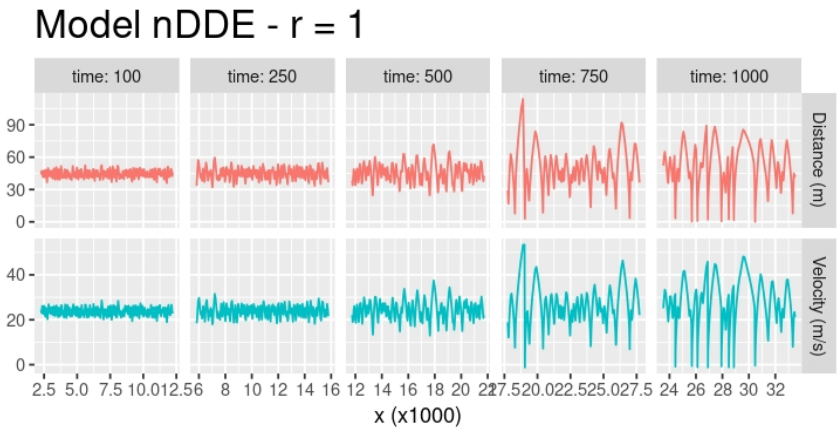


Figure 6.8: Evolution of distance and velocity of the vehicles with nDDE for $r = 1s$.

6.6 Final comments

This chapter generalized existing methodologies for deriving macroscopic PDEs equations from microscopic equation, valid for large time and space scales, such that the method can be applied to any car-following microscopic model based on standard variables (distance, velocity, relative velocity and relative acceleration). Moreover, a procedure to obtain a non-retarded acceleration expression from the (normally) retarded original equation is defined. Based on this equation, a general expression for the final PDE system for the macroscopic process is given.

In addition, we have introduced an approximation, valid for large space scales ($long - wavelength$), which considerably simplifies the obtained PDE system to a 1-dimensional PDE on the macroscopic velocity v that yields a simple stability criterion for this scale. Until now no such analysis exists in the literature that consistently addresses the conditions of the formation of density waves in different driving models.

The prescribed methods have been demonstrated for two existing traffic models (OVM and nDDE).

Chapter 7

Comparative results for existing driving models

This chapter intends to summarize all the results obtained in the research of this thesis by integrally applying the methods for the three spatial scales (micro, meso and macro) to well known, existing car-following models. Some results have been partially included in previous sections, but now they are framed in the context of a complete multiscale analysis of each model. In this way we show the general applicability of the methods while, at the same time, provide practical guidelines for their application to other traffic models, or to problems in other research fields.

Following we present the complete analysis for the car-following models introduced in Chapter 2.2.1:

- Optimal VelocityModel (OVM).
- Intelligent Driver Model (IDM).
- New DDE model (nDDE).

For the sake of clarity and readability we will reproduce the relevant equations already introduced, instead of just giving the reference to the original ones, and explicitly refer to the section describing the method applied to obtain each specific result, even at the risk of being repetitive in the exposition of the examples.

For the microscopic and mesoscopic models, we will follow the notation introduced in Section 6.2.2:

- $\sigma(t)$: distance with respect to the preceding vehicle.
- $\sigma'(t)$: relative velocity with respect to the preceding vehicle.
- $\sigma''(t)$: relative acceleration with respect to the preceding vehicle.
- $\nu(t)$: absolute velocity of the vehicle.

For the macroscopic models, we will call:

- $s(x,t) = 1/\rho(x,t)$ the inverse of the density.
- $v(x,t)$ the macroscopic velocity.

7.1 Optimal Velocity Model (OVM)

The OVM model we will analyze is described by the velocity equation (2.91):

$$\nu(t+r) = V\left(\sigma(t)\right) = \frac{\nu_{max}}{2}(\tanh(\sigma(t)-\sigma_0) + \tanh(\sigma_0)) \quad . \tag{7.1}$$

It is important to note that this model is based from the beginning on a retarded velocity equation, rather than a retarded acceleration equation. In this sense, if we consider that the leading vehicle has a constant velocity $\nu_0 = \nu_{max}/2$, the solution for the evolution of the distance $\sigma(t)$ and relative velocity $\sigma'(t)$ can be calculated using a 1-dimensional DDE of the form $\sigma'(t) = \nu(t) - \nu_0 = V(\sigma(t-r)) - \nu_0$.

Nevertheless, even if not strictly necessary, in order to use the same approach and maintain consistency in the analysis with respect to the rest of the models we will use a 2-dimensional system by introducing the retarded acceleration function:

$$a_{OVM}(t+r) = \nu'(t+r) = V'\left(\sigma(t)\right)\sigma'(t) = \frac{\nu_{max}}{2}(1-\tanh(\sigma(t)-\sigma_0)^2)\sigma'(t). \tag{7.2}$$

We will consider the following values in the analysis:

Param	Description	Value
σ_0	Equilibrium distance	100 m
ν_{max}	Maximum velocity	20 m/s
ν_0	Equilibrium (leader) velocity	10 m/s

Table 7.1: OVM parameters for the evaluated scenario.

7.1.1 OVM microscopic analysis

The DDE microscopic system to solve is:

$$\begin{aligned} u_1'(t) &= u_2(t), \\ u_2'(t) &= -\nu_0(1-\tanh(u_1(t-r)-\sigma_0)^2)u_2(t-r). \end{aligned}$$

This system is characterized by the following matrices (as in equation (4.2)):

$$\mathbf{P} = \begin{pmatrix} 0 & 1 \\ 0 & 0 \end{pmatrix}, \qquad \mathbf{Q} = \begin{pmatrix} 0 & 0 \\ 0 & -\nu_0 \end{pmatrix}.$$

Under these conditions, the bifurcation point can be calculated from the characteristic equation:

$$j\omega_0(\nu_0 e^{-j\omega_0 r_0} + j\omega_0) = 0,$$

with the solution:

$$\omega_0 = \nu_0 = 10, \qquad r_\mu = r_0 = \frac{\pi}{2\nu_0} = 0.15707,$$

denoting the limiting delay as r_μ to remark that this limit refers to the microscopic scale of traffic. As we will confirm in the mesoscopic analysis, this value is greater than the limit at mesoscopic scale, calculated for this model in [48] with value $1/(2V'(\sigma_0)) = 0.05s$.

We obtain the following orthonormal base for the solutions of the linearized system:

$$\boldsymbol{\phi}_1(t) = (0.0561\cos(\omega_0 t), -0.0561\sin(\omega_0 t)),$$
$$\boldsymbol{\phi}_2(t) = (0.0561\sin(\omega_0 t), 0.0561\cos(\omega_0 t)),$$

and the base for the adjoint system:

$$\boldsymbol{\phi}_1^*(t) = (0, -0.5641\sin(\omega_0 t)),$$
$$\boldsymbol{\phi}_2^*(t) = (0, -0.5641\cos(\omega_0 t)).$$

We then use these values to derive the approximations to the solutions of $\mathbf{z}(\tau,\varepsilon), \hat{r}(\varepsilon)$ and $\hat{T}(\varepsilon)$ by iteratively calculating the terms $\mathbf{z}_j(\tau)$, $\hat{r}_j$ and $\hat{T}_j$ as described in Sections 4.2 and 4.3. The results for the delay and period expansions are:

Coef.	o0	o1	o2	o3	o4	o5
$\hat{r}_j$	1.5707	0.0000	0.0078	0.0000	0.0001	0.0000
$\hat{T}_j$	2π	0.0000	0.0311	0.0000	0.0003	0.0000

Table 7.2: Coefficients for series expansion of $\hat{r}$ and $\hat{T}$ for the OVM scenario.

Figure 7.1 shows the bifurcation diagram drawn using the calculated coefficients.

Next graphs show the approximation calculated compared to the numerical integration and the approximation for increasing order up to order 5, for a delay value $r = 0.2\ s\ >\ r_\mu$.

7.1.2 OVM mesoscopic analysis

As has nbeen pointed out in the previous section, [48] contains a simple stability analysis for an equilibrium traffic flow composed by vehicles following this model, providing a delay limit for the stability. Nevertheless, no more insights on the nature of the solutions are provided. We will address this using the methodology of Chapter 5.

The system of equations is, using the acceleration equation (7.2):

$$\begin{cases} u_1'(t) &= u_2(t), \\ u_2'(t) &= u_3(t), \\ u_3'(t) &= \frac{1}{2} g\left(u_1(t-r), u_2(t-r), u_3(t-r), u_4(t-r)\right), \\ u_4'(t) &= \frac{1}{2} g\left(u_2(t-r), -u_1(t-r), u_4(t-r), -u_3(t-r)\right), \end{cases} \tag{7.3}$$

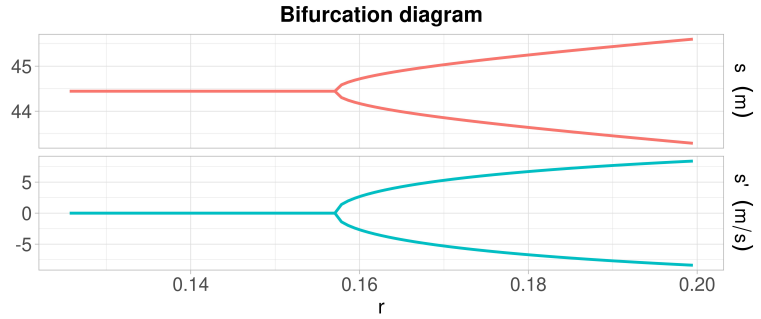
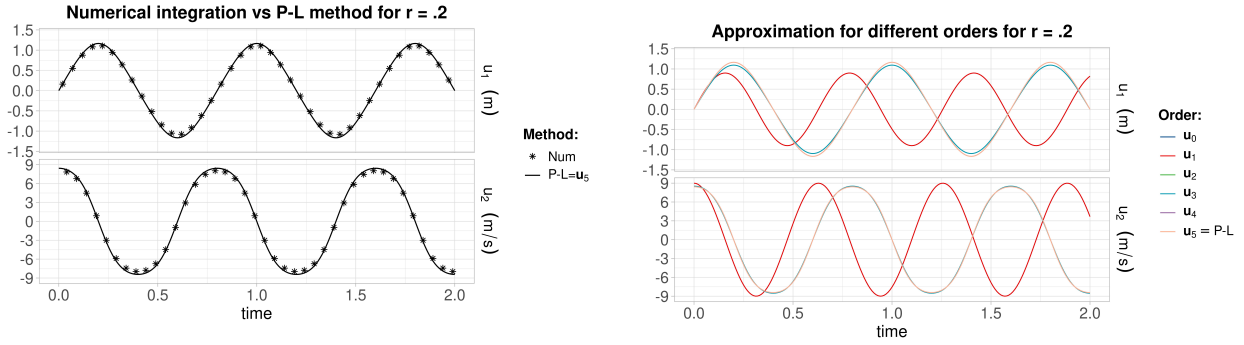


Figure 7.1: Bifurcation diagram of s and s' for the OVM model.



(a) Numerical solution $\tilde{\mathbf{u}}(t_0+t)$ and P-L calculation $\mathbf{u}_5(t)$.

(b) Approximation for each series expansion order.

Figure 7.2: Asymptotic stable solution of u_1 and u_2 for $r = 0.2s$ in OVM scenario.

with

$$g(v_1, v_2, v_3, v_4) = \Big(1 - \tanh(C(\kappa)(v_1 + jv_2) + \bar{C}(\kappa)(v_1 - jv_2))^2\Big) \cdot \Big(C(\kappa)(v_3 + jv_4) + \bar{C}(\kappa)(v_3 - jv_4)\Big),$$

where

$$C(\kappa) = e^{j\kappa} - 1.$$

These equations produce the following matrices of the linear equation as in (5.25):

$$\mathbf{A} = \begin{pmatrix} 0 & 0 & \frac{1}{2} & \frac{j}{2} \\ 0 & 0 & -\frac{j}{2} & \frac{1}{2} \\ 0 & 0 & 0 & 0 \\ 0 & 0 & 0 & 0 \end{pmatrix}$$

$$\mathbf{B} = \begin{pmatrix} 0 & 0 & 0 & 0 \\ 0 & 0 & 0 & 0 \\ 0 & 0 & \frac{C\nu_0}{2} & j\frac{C\nu_0}{2} \\ 0 & 0 & -j\frac{C\nu_0}{2} & \frac{C\nu_0}{2} \end{pmatrix} \tag{7.4}$$

We have omitted the dependency of C on κ in the matrix $\mathbf{B}$. Now, using the same parameters in Table 7.1, applying formula (5.27) we obtain the characteristic function and calculate the neutral stability curve, shown in Figure 7.3.

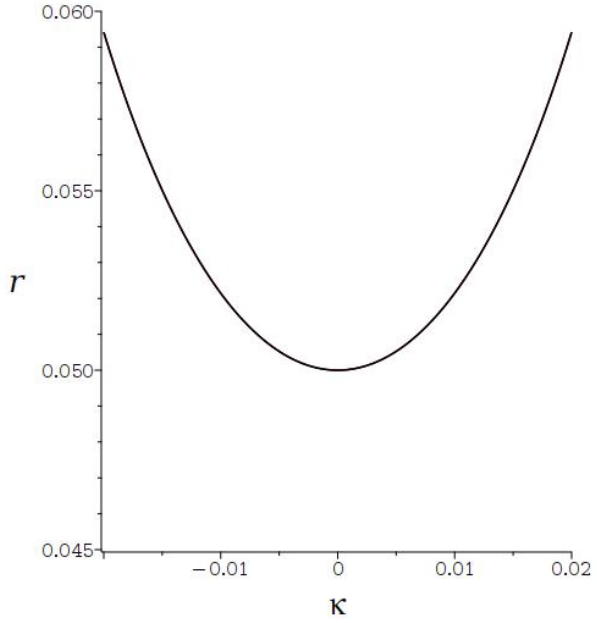


Figure 7.3: Neutral stability line ($\kappa(r)$ such that $\Re(\lambda(r,\kappa)) = 0$) in OVM scenario.

.

The bifurcation point is:

$$\begin{aligned} r_m &= 0.05, \\ \kappa_0 &= 0, \\ \omega_0 &= 0. \end{aligned}$$

This confirms the instability point given in [48] for this model. The bifurcation delay is lower from the one we calculated in the microscopic scenario (leading and following vehicles only) $r_m < r_\mu = 0.15707$ s. Nevertheless these values also reveal that the bifurcation is not of the Hopf type, which requires the existence of a simple eigenvalue $j\omega_0$ with $\omega_0 \neq 0$. Therefore we do not expect that this mesoscopic state can be modelled with the CGLE equation using the method described in Section 5.3.1.

We can, though, derive some conclusions about the solution after the bifurcation point from Figure 7.3. When the delay $r > r_m$, near the bifurcation we will have a band of wavenumbers $|\kappa| \leq \kappa_r$, with an associated eigenvalue verifying $\Re(\lambda(\kappa)) > 0$, and $\Re(\lambda(\kappa_r)) = 0$. These propagation modes will not grow until eventually saturate due to the nonlinearity, and so we can expect that for these values of delay over the bifurcation the solution will show oscillations in spatial frequencies in the range $0 \leq \kappa \leq \kappa_r$, i.e. with oscillations in the spatial wavelength range $[2\pi/\kappa_r, \infty]$.

This is confirmed by simulation analysis. Figure 7.4 shows the evolution in different time spots for the distance and velocity in a traffic flow near stability for a delay $r = 0.051$ s,

slightly higher than r_m. The corresponding maximum wavenumber is $\kappa_{0.051} = 0.688$, which corresponds to a minimum spatial wavelength $l_{0.051} = 2\pi/\kappa_{0.051} = 913\ m$. The oscillations observed in the simulation ater some initial time have an approximate wavelength $l \approx 1600\ m$, as expected in the interval $[913, \infty]$. Figure 7.5 corresponds to the delay $r = 0.055\ s$, with the corresponding maximum wavenumber $\kappa_{0.055} = 1.498$ and a minimum spatial wavelength $l_{0.055} = 419\ m$. The graph shows a oscillations with wavelength $l \approx 1000 \in [419, \infty]$.

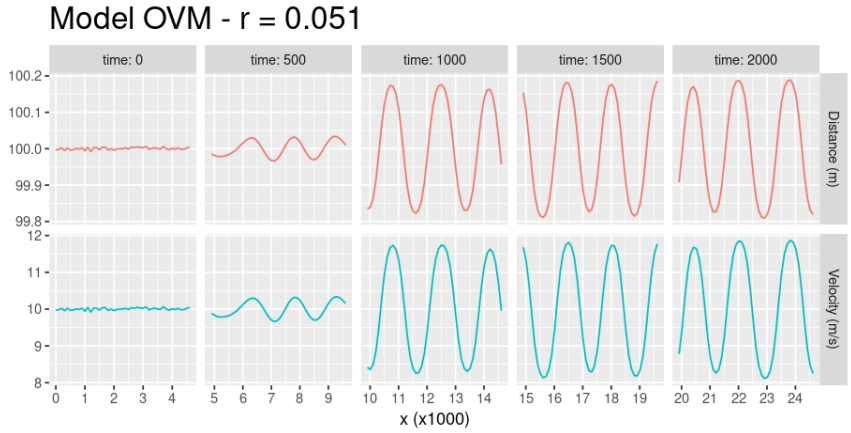


Figure 7.4: Evolution of distance and velocity of the vehicles with OVM for $r = 0.051s$.

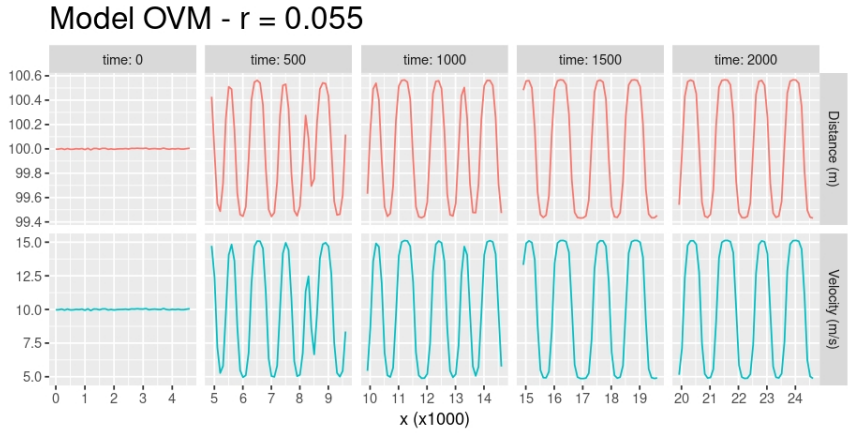


Figure 7.5: Evolution of distance and velocity of the vehicles with OVM for $r = 0.055s$.

The solutions for increasing values of the delay r will increase the spatial frequency of the oscillations and their amplitude correspondingly.

7.1.3 OVM macroscopic analysis

This analysis has already been described in Chapter 6, and is reproduced here for completeness. From the microscopic model (7.1) we get a non retarded acceleration approximation:

$$\begin{aligned}\nu(t+r) &\approx \nu(t) + ra(t),\\ a(t) &= \frac{1}{r}\left(V\left(\sigma(t)\right) - \nu(t)\right)\end{aligned}$$

Notice that in this simpler model we have only dependence on the microscopic variables $\sigma(t)$ an $\nu(t)$, i.e. $\mathbf{u}(t) = (\sigma(t), \nu(t))$, and $a(t) = a\left(\sigma(t), \nu(t)\right)$. The coefficients for the linear expansion of the acceleration (6.67) are:

$$\begin{aligned}C_1 &= \left.\frac{\partial a}{\partial \sigma}\right|_{(s_0,v_0)} = \frac{V'(s_0)}{r},\\ C_2 &= 0, \quad C_3 = 0,\\ C_4 &= \left.\frac{\partial a}{\partial \nu}\right|_{(s_0,v_0)} = -\frac{1}{r},\end{aligned} \tag{7.5}$$

where we have used $\frac{\nu_{max}}{2} = V'(s_0)$.

Applying the stability criteria in (6.87)

$$-C_4 = \frac{1}{r} > 0, \tag{7.6}$$

This condition is always met, so there is no macroscopic instability in the OVM. This means that once the microscopic limit is reached, no density waves are formed over the fundamental oscillations.

To illustrate this we show simulation results with a comparison of the evolution of a traffic scenario of 100 vehicles that implement the OVM model for different values of delay. The limiting delay at mesoscopic scale is, as we have ssen before:

$$r_m < \frac{1}{2V'(s_0)} = 0.05 \quad . \tag{7.7}$$

In Figures 7.6, 7.7 and 7.8, we can see that in all cases the delay is greater than the limiting delay, and that oscillations typical of the mesoscopic scale are formed, observing higher values of frequency and amplitude as we increase the delay value. But we can also see that, even for values of delay far greater than this limit, like Figures 7.7 and 7.8, the mesoscopic state is not destabilized, and there is no formation of stop and go traffic, confirming the prediction of (**??**).

This can be explained by the fact that equation (7.1) allows for arbitrary changes in velocity in a given time interval $[t, t+r]$. This effectively translate to unbounded acceleration and deceleration values, which, as has been pointed out in the background Chapter 2, is not realistic. This can be seen in the huge excursions in the velocity of the vehicles while they change the distance in a very small quantity.

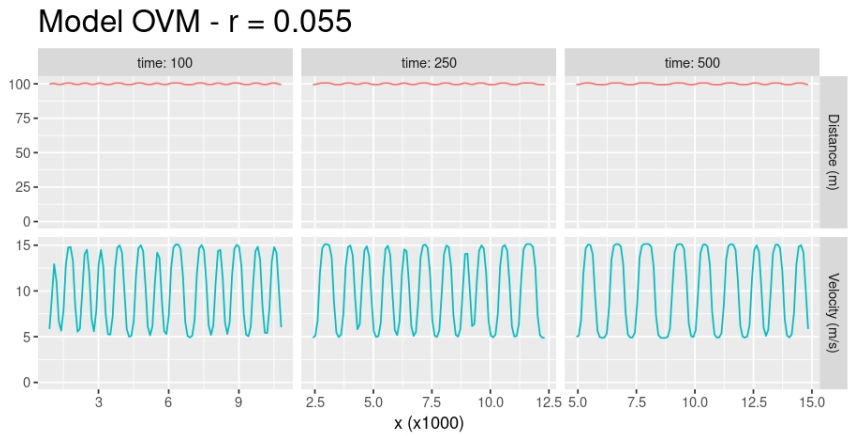


Figure 7.6: Evolution of distance and velocity of the vehicles with OVM for $r = 0.055s$.

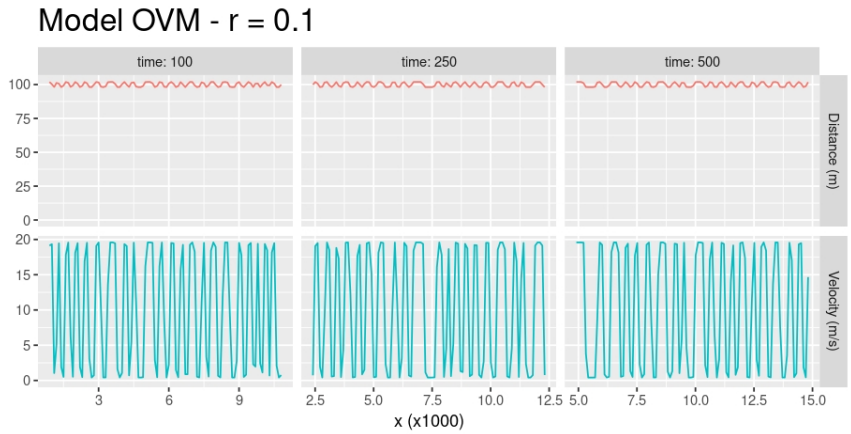


Figure 7.7: Evolution of distance and velocity of the vehicles with OVM for $r = 0.1s$.

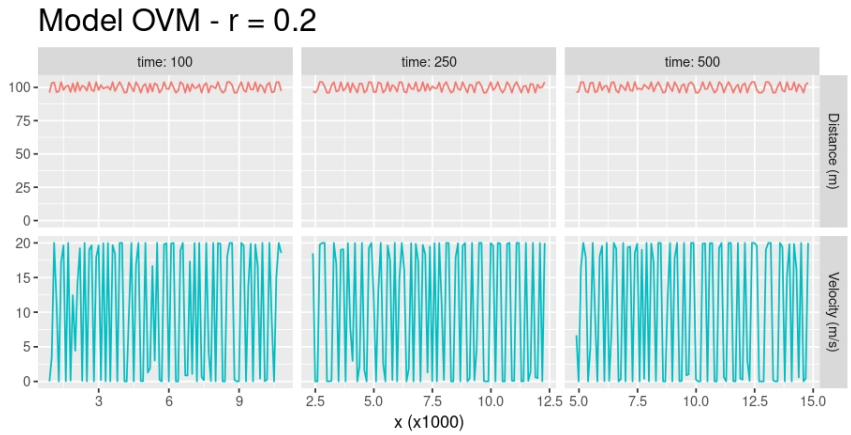


Figure 7.8: Evolution of distance and velocity of the vehicles with OVM for $r = 0.2s$.

7.2 Intelligent Driver Model (IDM)

This model, introduced in Section 2.2.1, follows the acceleration equation (2.96), updated here to the usual notation:

$$a_{IDM}(t+r) = a\left[1 - \left(\frac{\nu(t)}{\nu_d}\right)^{\delta} - \left(\frac{\sigma_{min} + \max\left(0, \nu(t)T + \frac{\nu(t)\sigma'(t)}{2\sqrt{ab}}\right)}{\sigma}\right)^2\right], \tag{7.8}$$

where ν_d is the desired velocity, σ_{min} is the minimum distance, T is a reaction time and a and b are the maximum acceleration and deceleration respectively.

In steady state homogeneous traffic (all vehicles behaving according to the same IDM), the vehicles will stay in an equilibrium distance

$$\sigma_{eq} = \sigma_{min} + T\nu_d,$$

and equation (2.96) determines an equilibrium velocity ν_0 that is the solution to the equation

$$\sigma_{eq} = \frac{\sigma_{min} + T\nu_0}{\sqrt{1 - \left(\frac{\nu_0}{\nu_d}\right)^{\delta}}}.$$

resulting in a value $\nu_0 < \nu_d$.

We will consider the following values in the analysis:

Param	Description	Value
a	Maximum acceleration	1.4 m/s^2
b	Deceleration parameter	2 m/s^2
δ	Exponent	4
T	Reaction time	0.5 s
σ_{min}	Minimum distance	2 m
ν_d	Desired velocity	22.2222 m/s
σ_0	Equilibrium distance	13.1111 m/s
ν_0	Equilibrium velocity	17.1132 m/s

Table 7.3: IDM parameters for the evaluated scenario.

7.2.1 IDM microscopic analysis

The DDE microscopic system to solve is:

$$\begin{aligned} u_1'(t) =& u_2(t), \\ u_2'(t) =& -a\left[1-\left(\frac{(\nu_0+u_2(t-r))}{\nu_d}\right)^{\delta}-\right. \\ & \left.\left(\frac{\sigma_{min}+\max\left(0,(\nu_0+u_2(t-r))T+\dfrac{(\nu_0+u_2(t-r))u_2(t-r)}{2\sqrt{ab}}\right)}{(\sigma_0+u_1(t-r))}\right)^2\right]. \end{aligned} \tag{7.9}$$

Using the values of Table 7.3, this system is characterized by the following matrices (as in equation (4.2)):

$$\mathbf{P}=\begin{pmatrix}0 & 1\\ 0 & 0\end{pmatrix}, \qquad \mathbf{Q}=\begin{pmatrix}0 & 0\\ -0.1384 & -0.6782\end{pmatrix}.$$

Under these conditions, the bifurcation point can be calculated from the characteristic equation:

$$0.6782j\omega_0 e^{-j\omega_0 r_0}-\omega_0^2+0.1384e^{-j\omega_0 r_0}=0,$$

with the solution:

$$\omega_0=0.706, \qquad r_\mu=r_0=1.8262,$$

denoting the limiting delay as r_μ to remark that this limit refers to the microscopic scale of traffic.

We obtain the following orthonormal base for the solutions of the linearized system:

$$\begin{aligned} \boldsymbol{\phi}_1(t) &= (0.4608\cos(\omega_0 t), -0.3254\sin(\omega_0 t)),\\ \boldsymbol{\phi}_2(t) &= (0.4608\sin(\omega_0 t), 0.3254\cos(\omega_0 t)), \end{aligned}$$

and the base for the adjoint system:

$$\begin{aligned} \boldsymbol{\phi}_1^*(t) &= (-0.1086\sin(\omega_0 t), -0.1538\cos(\omega_0 t)-0.5319\sin(\omega_0 t)),\\ \boldsymbol{\phi}_1^*(t) &= (0.1086\cos(\omega_0 t), -0.1538\sin(\omega_0 t)+0.5319\cos(\omega_0 t)). \end{aligned}$$

We then use these values to derive the approximations to the solutions of $\mathbf{z}(\tau,\varepsilon), \hat{r}(\varepsilon)$ and $\hat{T}(\varepsilon)$ by iteratively calculating the terms $\mathbf{z}_j(\tau)$, $\hat{r}_j$ and $\hat{T}_j$ as described in Sections 4.2 and 4.3. The results for the delay and period expansions are found in Table 7.4

Figure 7.9 shows the bifurcation diagram drawn using the calculated coefficients.

Figure 7.10 shows the approximation calculated compared to the numerical integration and the approximations for increasing order up to order 5, for a delay value $r = 1.9\ s\ >\ r_\mu$.

Coef.	o0	o1	o2	o3	o4	o5
$\hat{r}_j$	1.2893	0.0000	0.0621	0.0000	0.0004	-0.0008
$\hat{T}_j$	2π	0.0000	0.4836	0.0000	0.0319	-0.0059

Table 7.4: Coefficients for series expansion of $\hat{r}$ and $\hat{T}$ for the IDM scenario.

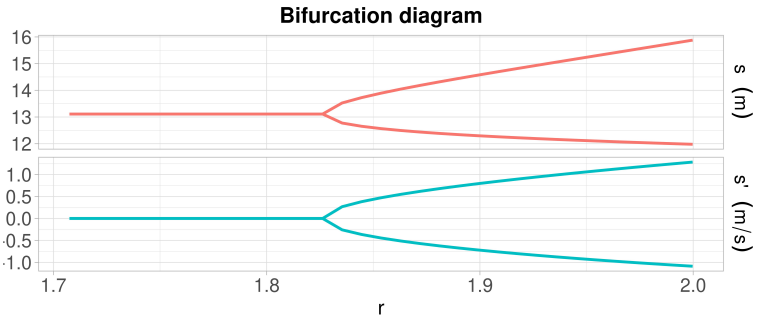
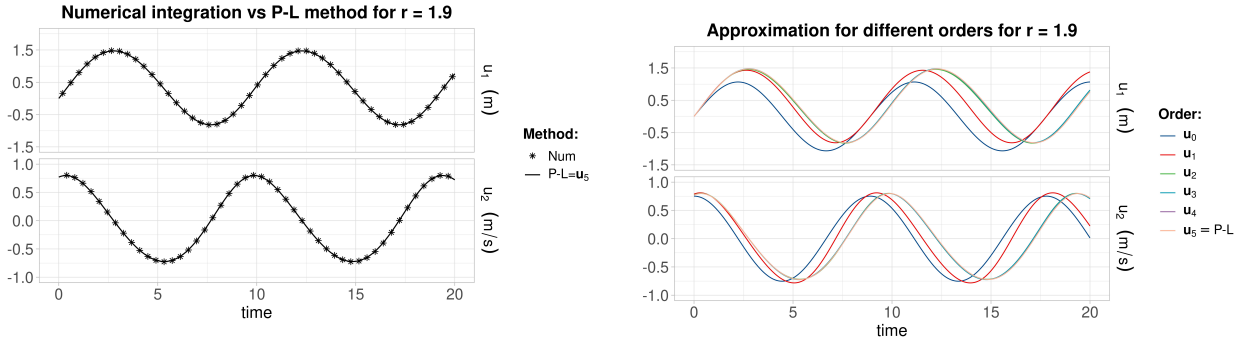


Figure 7.9: Bifurcation diagram of s and s' for the IDM model.



(a) Numerical solution $\tilde{\mathbf{u}}(t_0 + t)$ and P-L calculation $\mathbf{u}_5(t)$.

(b) Approximation for each series expansion order.

Figure 7.10: Asymptotic stable solution of u_1 and u_2 for $r = 0.2s$ in IDM scenario.

7.2.2 IDM mesoscopic analysis

The system of equations is, using the acceleration equation (7.19):

$$\begin{cases} u_1'(t) &= u_2(t), \\ u_2'(t) &= u_3(t), \\ u_3'(t) &= \frac{1}{2} g\left(u_1(t-r), u_2(t-r), u_3(t-r), u_4(t-r)\right), \\ u_4'(t) &= \frac{1}{2} g\left(u_2(t-r), -u_1(t-r), u_4(t-r), -u_3(t-r)\right), \end{cases} \tag{7.10}$$

with

$$\begin{aligned} g(v_1, v_2, v_3, v_4) =& a_{IDM}(C(\kappa)(v_1 + jv_2) + \bar{C}(\kappa)(v_1 - jv_2), \\ & C(\kappa)(v_3 + jv_4) + \bar{C}(\kappa)(v_3 - jv_4), \qquad (7.11) \\ & \nu_0 + C(\kappa)(v_3 + jv_4) + \bar{C}(\kappa)(v_3 - jv_4)), \qquad (7.12) \end{aligned}$$

where

$$C(\kappa) = e^{j\kappa} - 1.$$

These equations produce the following matrices of the linear equation as in (5.25):

$$\mathbf{A} = \begin{pmatrix} 0 & 0 & \frac{1}{2} & \frac{j}{2} \\ 0 & 0 & -\frac{j}{2} & \frac{1}{2} \\ 0 & 0 & 0 & 0 \\ 0 & 0 & 0 & 0 \end{pmatrix}$$

$$\mathbf{B} = (\mathbf{B}_1 | \mathbf{B}_2) \qquad (7.13)$$

$$\mathbf{B}_1 = \begin{pmatrix} 0 & 0 \\ 0 & 0 \\ \frac{a(Tv_0+\sigma_{min})^2 C}{\sigma_0^3} & \frac{ja(Tv_0+\sigma_{min})^2 C}{\sigma_0^3} \\ \frac{-\mathrm{I}a(Tv_0+\sigma_{min})^2 C}{\sigma_0^3} & \frac{a(Tv_0+\sigma_{min})^2 C}{\sigma_0^3} \end{pmatrix} \qquad (7.14)$$

$$\mathbf{B}_2 = \begin{pmatrix} 0 & 0 \\ 0 & 0 \\ \frac{a\left(-\left(\frac{v_0}{v0}\right)^\delta \delta\, \sigma_0^2 \sqrt{ab} + v_0(Tv_0+\sigma_{min})\left(v_0 C - 2T\sqrt{ab}\right)\right)}{2\sqrt{ab}\, v_0\, \sigma_0^2} & \frac{\frac{j}{2} a\left(-\left(\frac{v_0}{v0}\right)^\delta \delta\, \sigma_0^2 \sqrt{ab} + v_0(Tv_0+\sigma_{min})\left(v_0 C - 2T\sqrt{ab}\right)\right)}{\sqrt{ab}\, v_0\, \sigma_0^2} \\ \frac{-\frac{j}{2} a\left(-\left(\frac{v_0}{v0}\right)^\delta \delta\, \sigma_0^2 \sqrt{ab} + v_0(Tv_0+\sigma_{min})\left(v_0 C - 2T\sqrt{ab}\right)\right)}{\sqrt{ab}\, v_0\, \sigma_0^2} & \frac{a\left(-\left(\frac{v_0}{v0}\right)^\delta \delta\, \sigma_0^2 \sqrt{ab} + v_0(Tv_0+\sigma_{min})\left(v_0 C - 2T\sqrt{ab}\right)\right)}{2\sqrt{ab}\, v_0\, \sigma_0^2} \end{pmatrix} \qquad (7.15)$$

We have omitted the dependency of C on κ in the matrix $\mathbf{B}$. Now, using the same parameters in Table 7.3, applying formula (5.27) we obtain the characteristic function and calculate the neutral stability curve, shown in Figure 7.11.

The bifurcation point is:

$$\begin{aligned} r_m &= 0.5614, \\ \kappa_0 &= 0.0988, \\ \omega_0 &= 1.1828. \end{aligned}$$

Again, the bifurcation delay is lower from the one we calculated in the microscopic scenario (leading and following vehicles only) $r_m < r_\mu = 1.8262$ s. So we have a Hopf bifurcation and we can try to get an approximate solution for the amplitude at this scale with the CGLE.

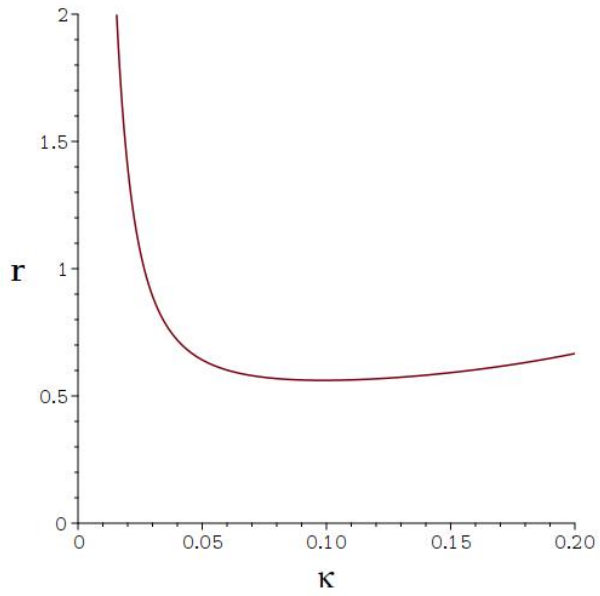


Figure 7.11: Neutral stability line ($\kappa(r)$ such that $\Re(\lambda(r,\kappa)) = 0$) in IDM scenario.

.

The calculations for to obtain the bilinear and trilinear forms in (5.36) and (5.37) are evaluated (by means of a Maple 2024 program) and produce the following straightforward expansion:

$$\begin{aligned}
\boldsymbol{\phi}_{0,\kappa_0} =& (-0.3228j, -0.3228, 0.3818, -0.3818),\\
\boldsymbol{\phi}^*_{0,\kappa_0} =& (0.098 + 0.0016j, 0.0016 - 0.098j, 0.7001j, 0.7001),\\
\mathbf{w}_0 =& (0.2678, -1.9358, 0, 0),\\
\mathbf{w}_2 =& (-9.9 \cdot 10^{-3} - j6.2 \cdot 10^{-3}, 3.6 \cdot 10^{-2} + 5.3 \cdot 10^{-3},\\
& - 1.5 \cdot 10^{-2} + j2.4 \cdot 10^{-2}, 1.3 \cdot 10^{-2} - j8.5 \cdot 10^{-2}),
\end{aligned}$$

Notice the real valued vector $\mathbf{w}_0$ that is not null, meaning that the average value of the solution will shift when $r > r_m$, as has been explained in Section 5.3.3. It is important to see what is the effect of this drift when we recover the final solution in the real domain. By equations applying equations (2.57) and (5.5), the drift in the space variable produced by the second order term for a delay $r = 0.6\ s$ is:

$$d_{\sigma_0} = \varepsilon^2 \left(\left(e^{j\kappa_0} - 1 \right) \mathbf{w}_0[1] + \left(e^{-j\kappa 0} - 1 \right) j\mathbf{w}_0[1] \right) = 0.688, \tag{7.16}$$

and the drift in the velocity variable:

$$d_{\nu_0} = 2\mathbf{w}_0[3] = 0. \tag{7.17}$$

This means that when the delay grows over the threshold r_m, the flow that was before in equilibrium as a whole requires an immediate change of the distance of all the vehicles in a quantity d_{σ_0}, which is only possible if there exist another equilibrium point (σ_0^*, ν_0^*) with $\sigma_0^* = \sigma_0 + d_{\sigma_0}$. But, due to the complicated relationship in equation (7.9) this is not the case in this model, and, as a consequence, the solution calculated using the CGLE will not be stable in any case.

This is confirmed by simulation results. Figure 7.12 shows the evolution in time of the homogeneous flow for a delay $r = 0.55\ s$, which, as expected, is stable. But in Figure 7.13, with a value $r = 0.6\ s$ just above the threshold, we do not see a metastable oscillation because the system is not able to maintain the fundamental oscillation when the equilibrium point changes. In summary, no metastable state is reached over the mesoscale threshold, and

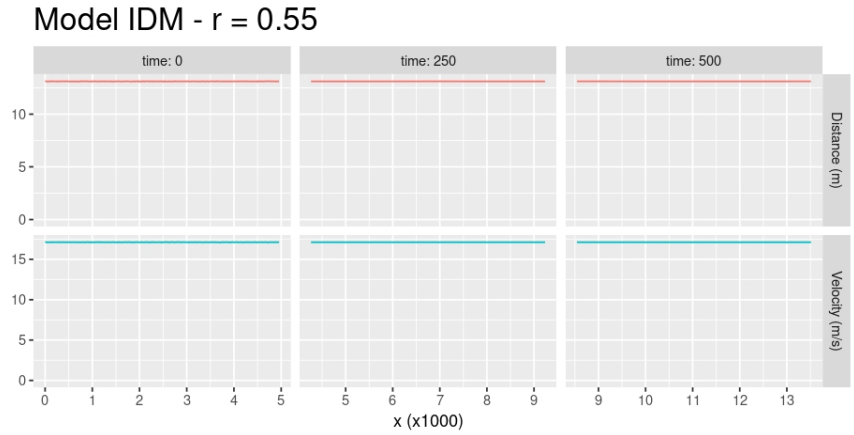


Figure 7.12: Evolution of distance and velocity of the vehicles with IDM for $r = 0.56s$.

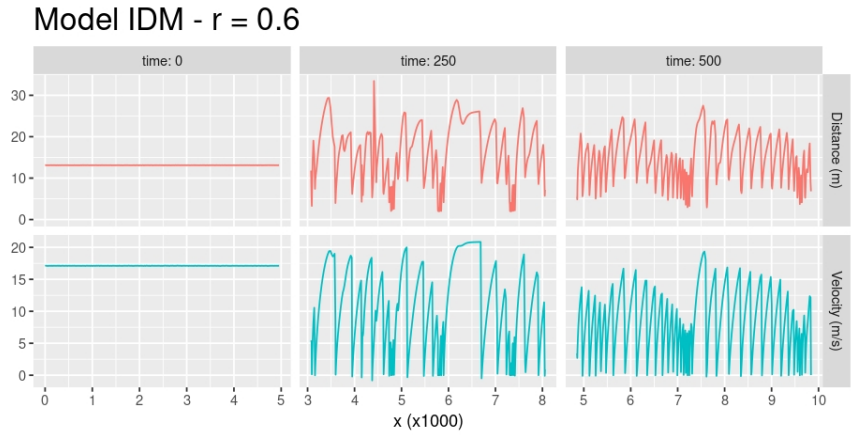


Figure 7.13: Evolution of distance and velocity of the vehicles with IDM for $r = 0.6s$.

therefore the macroscopic instability (stop and go traffic) is present in all scenarios when $r > r_\mu$.

7.2.3 IDM macroscopic analysis

The absence of metastable states in the mesoscale in this case causes that $r_M = r_m$ and any value over the mesoscale threshold shows macroscopic instability.

7.3 New DDE model (nDDE)

The nDDE model has been used as the primary example to illustrate the methods introduced in this thesis in Chapters 4, 5 and 6. Therefore this last example compiles results similar to others already presented, and is included for completeness of this summarized results chapter.

The nDDE microscopic model, using the same notation as the previous examples, is:

$$a_{nDDE}(t+r) = \alpha - \frac{(\alpha+\beta)}{1+\frac{\beta}{\alpha}e^{d(\sigma(t)-\sigma_0+K\sigma'(t))}}. \tag{7.18}$$

In order to present alternative results to those included in previous chapters, the parameters of the nDDE scenario in this section are different from those in Table 4.2, as detailed in Table 7.5.

Param	Description	Value
α	Maximum acceleration in $nDDE$	2 m/s^2
β	Maximum deceleration	1.8 m/s^2
ν_0	Leader velocity	20 m/s
σ_0	Safe distance for v_0	40 m
d	Car + driver response intensity	0.2
K	Driver sensitivity to s'	10 s

Table 7.5: nDDE parameters for the evaluated scenario [56].

7.3.1 nDDE microscopic analysis

The first order DDE system for this model is:

$$\begin{aligned} u_1'(t) &= u_2(t), \\ u_2'(t) &= -\alpha + \frac{(\alpha+\beta)}{1+\frac{\beta}{\alpha}e^{d(u_1(t-r)+Ku_2(t-r))}}. \end{aligned} \tag{7.19}$$

The linearized system is characterized by the following matrices (as in equation (7.9)):

$$\mathbf{P} = \begin{pmatrix} 0 & 1 \\ 0 & 0 \end{pmatrix}, \qquad \mathbf{Q} = \begin{pmatrix} 0 & 0 \\ -D & -DK \end{pmatrix},$$

where $D = d\frac{\alpha\beta}{\alpha+\beta}$.

The characteristic equation is:

$$\omega_0^2 = D(1+jK\omega_0)e^{j\omega_0 r_0},$$

which generates the following equations to calculate the bifurcation point (ω_0, r_0):

$$K = \frac{\tan(\omega_0 r_0)}{\omega_0}, \qquad D = \omega_0^2\cos(\omega_0 r_0). \tag{7.20}$$

Using the values of Table 7.5, the bifurcation point can be calculated numerically:

$$\omega_0 = 1.8974, \qquad r_\mu = r_0 = 0.8001,$$

and we obtain the following orthonormal base for the solutions of the linearized system:

$$\boldsymbol{\phi}_1(\hat{t}) = (0.2631\cos(\hat{t}), -0.4991\sin(\hat{t})), \qquad \boldsymbol{\phi}_2(\hat{t}) = (0.2631\sin(\hat{t}), 0.4991\cos(\hat{t})),$$

and the base for the adjoint system:

$$\boldsymbol{\phi}_1^*(\hat{t}) = (0.0560\cos(\hat{t}), -0.0295\cos(\hat{t}) + 0.5606\cos(\hat{t})),$$
$$\boldsymbol{\phi}_2^*(\hat{t}) = (-0.0560\sin(\hat{t}), -0.0295\cos(\hat{t}) - 0.5606\sin(\hat{t})).$$

We then use these values to derive the approximations as described in Sections 4.2 and 4.3. Table 7.6 contains the coefficients for the series expansion of $\hat{r}$ and $\hat{T}$, up to order 5.

Coef.	o0	o1	o2	o3	o4	o5
$\hat{r}_j$	1.5181	0.0000	0.5747	0.0000	0.0660	0.0035
$\hat{T}_j$	2π	0.0000	2.4679	0.0000	0.3280	0.0148

Table 7.6: Coefficients for series expansion of $\hat{r}$ and $\hat{T}$.

Figure 7.14 shows the bifurcation diagram, and Figure 7.15 contains the calculated solution graphs for a delay $r = 1.1$ s.

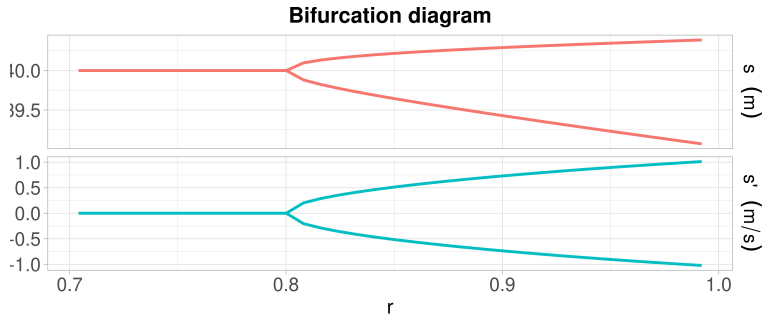


Figure 7.14: Bifurcation diagram of s and s' in the nDDE model.

Complementary results and explanations can be found in Section 4.4.1.

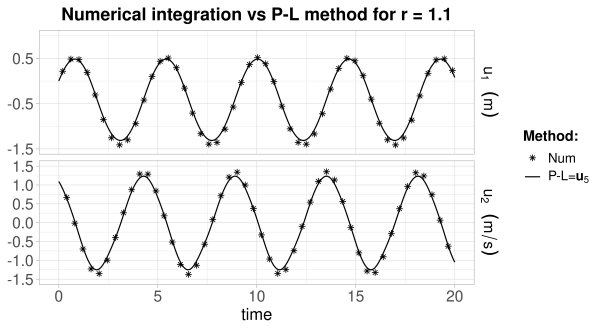
7.3.2 nDDE mesoscopic analysis

The system of equations is in this case:

$$\begin{cases} u_1'(t) &= u_2(t), \\ u_2'(t) &= u_3(t), \\ u_3'(t) &= \frac{1}{2}g\left(u_1(t-r), u_2(t-r), u_3(t-r), u_4(t-r)\right), \\ u_4'(t) &= \frac{1}{2}g\left(u_2(t-r), -u_1(t-r), u_4(t-r), -u_3(t-r)\right), \end{cases} \tag{7.21}$$



(a) Numerical solution $\tilde{\mathbf{u}}(t_0+t)$ and P-L calculation $\mathbf{u}_5(t)$.



(b) Approximation for each series expansion order.

Figure 7.15: Asymptotic stable solution of $u_1(t)$ and $u_2(t)$ for $r = 1.1s$ in nDDE.

with

$$
\begin{aligned}
g(v_1,v_2,v_3,v_4) &= -\alpha + \frac{(\alpha+\beta)}{1+\frac{\beta}{\alpha}e^{d\cdot h(v_1,v_2,v_3,v_4)}},\\
h(v_1,v_2,v_3,v_4) &= C_1(\kappa)(v_1+jv_2)+\bar{C}_1(\kappa)(v_1-jv_2)+\\
&C_2(\kappa)(v_3+jv_4)+\bar{C}_2(\kappa)(v_3-jv_4),
\end{aligned}
\tag{7.22}
$$

where

$$
\begin{aligned}
C_1(\kappa) &= e^{j\kappa}-1,\\
C_2(\kappa) &= K(e^{j\kappa}-1)-\frac{\sigma_0}{\nu_0}e^{j\kappa}.
\end{aligned}
\tag{7.23}
$$

These equations produce the following matrices of the linear equation as in (5.25):

$$
\mathbf{A} = \begin{pmatrix} 0 & 0 & \frac{1}{2} & \frac{j}{2} \\ 0 & 0 & -\frac{j}{2} & \frac{1}{2} \\ 0 & 0 & 0 & 0 \\ 0 & 0 & 0 & 0 \end{pmatrix}
$$

$$
\mathbf{B} = \begin{pmatrix} 0 & 0 & 0 & 0 \\ 0 & 0 & 0 & 0 \\ \frac{d\alpha\beta}{2(\alpha+\beta)}C_1 & \frac{d\alpha\beta}{2(\alpha+\beta)}jC_1 & \frac{d\alpha\beta}{2(\alpha+\beta)}C_2 & \frac{d\alpha\beta}{2(\alpha+\beta)}jC_2 \\ -\frac{d\alpha\beta}{2(\alpha+\beta)}jC_1 & \frac{d\alpha\beta}{2(\alpha+\beta)}C_1 & -\frac{d\alpha\beta}{2(\alpha+\beta)}jC_2 & \frac{d\alpha\beta}{2(\alpha+\beta)}C_2 \end{pmatrix}
$$

We have omitted the dependency of C_1 and C_2 on κ in the matrix $\mathbf{B}$. Now, using the same parameters in Table 4.2, applying formula (5.27) we obtain the characteristic function and calculate the neutral stability curve, shown in Figure 7.16.

The bifurcation point is then:

$$
\begin{aligned}
r_m &= 0.3518,\\
\kappa_0 &= 0.0400,\\
\omega_0 &= 2.4516.
\end{aligned}
$$

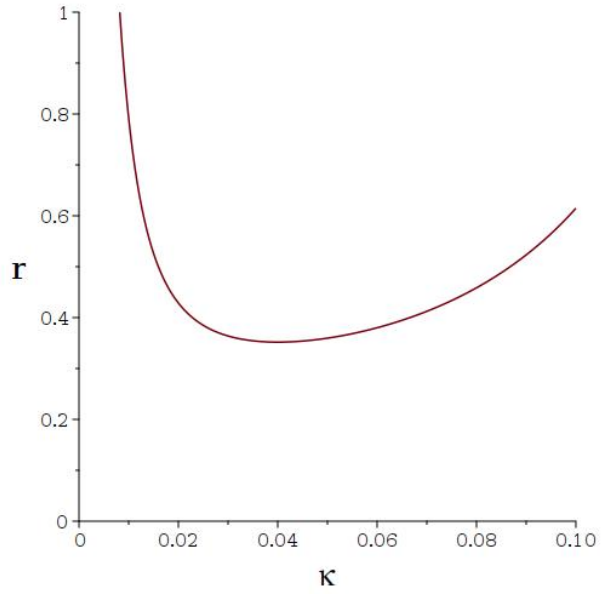


Figure 7.16: Neutral stability line ($\kappa(r)$ such that $\Re(\lambda(r,\kappa)) = 0$) for nDDE scenario.

Notice that, as in previous examples, the bifurcation delay is lower from the one we calculated in the microscopic scenario (leading and following vehicles only) $r_m < r_\mu = 1.3079$ s.

The calculations to obtain the bilinear and trilinear forms in (5.36) and (5.37) are evaluated (by means of a Maple 2024 program) and produce the following vectors from the straightforward expansion

$$\begin{aligned}
\boldsymbol{\phi}_{0,\kappa_0} =& (-0.1884j, -0.1884, 0.4629, -0.4629),\\
\boldsymbol{\phi}^*_{0,\kappa_0} =& (-0.0049 + 0.0778j, 0.0778 + 0.0049j, j0.7028, 0.7028),\\
\mathbf{w}_0 =& (0.011, 0.7445, 0, 0),\\
\mathbf{w}_2 =& (2.0 \cdot 10^{-3} - j5.8 \cdot 10^{-4}, -5.8 \cdot 10^{-3} - j5.6 \cdot 10^{-4},\\
& -2.8 \cdot 10^{-3} - j1.0 \cdot 10^{-2}, -2.7 \cdot 10^{-3} + j2.9 \cdot 10^{-2}),
\end{aligned}$$

Notice the real valued vector $\mathbf{w}_0$ that is not null, meaning that the average value of the solution will shift when $r > r_m$, as has been explained in Section 5.3.3. The drift in the space variable produced by the second order term for a delay $r = 0.6$ s is:

$$d_{\sigma_0} = \varepsilon^2 \left(\left(e^{j\kappa_0} - 1 \right) \mathbf{w}_0[1] + \left(e^{-j\kappa 0} - 1 \right) j\mathbf{w}_0[1] \right) = -0.147, \tag{7.24}$$

and the drift in the velocity variable:

$$d_{\nu_0} = 2\mathbf{w}_0[3] = 0. \tag{7.25}$$

This means that when the delay grows over the threshold r_m, the flow that was before in equilibrium as a whole requires an immediate change of the distance of all the vehicles in a quantity d_{σ_0}, which is only possible if there exist another equilibrium point (σ_0^*, ν_0^*) with $\sigma_0^* = \sigma_0 + d_{\sigma_0}$. This is indeed the case in this model, since by equations (7.21), (7.22) and

(7.23), the scenarios with the same value of σ_0/ν_0 have the same dynamics and thus produce the same oscillations around the equilibrium point. So, if the distance between the cars needs to be maintained at $\sigma_0^* = \sigma_0$, (i.e. $d_{\sigma_0^*=0}$) the shift in velocity for a delay $r = 0.6\ s$ will be:

$$d_{\nu_0^*} = \frac{\sigma_0}{\sigma_0 + d_{\sigma_0}}\nu_0 - \nu_0 = 0.073. \tag{7.26}$$

From the characteristic function (5.27) we calculate:

$$\Lambda_0 = 594 - 1349j,$$

and from (5.33) and (5.34):

$$\gamma = -0.16 + 3.52j.$$

So, we have that $\Re(\gamma) < 0$ and therefore we do not expect modulation of the basic pattern for values of $0 < (r - r_m)/r_m \ll 1$. We can check these results in the following graphs obtained by simulation. They show the evolution of the distance and the velocity of a group of vehicles implementing the model nDDE in a single lane. Figure 7.17 shows what happens when the delay $r = 0.35$ is just below the threshold for the linear stability $r_m = 0.3518$. The figure includes five snapshots of the situation of the vehicles in terms of the velocity and distance to the leading vehicle, for time 0 s, 250 s, 500 s, 750 s and 1000 s. There we can see that, even when there is an initial disturbance, the vehicle system returns to the steady equilibrium (σ_0, ν_0).

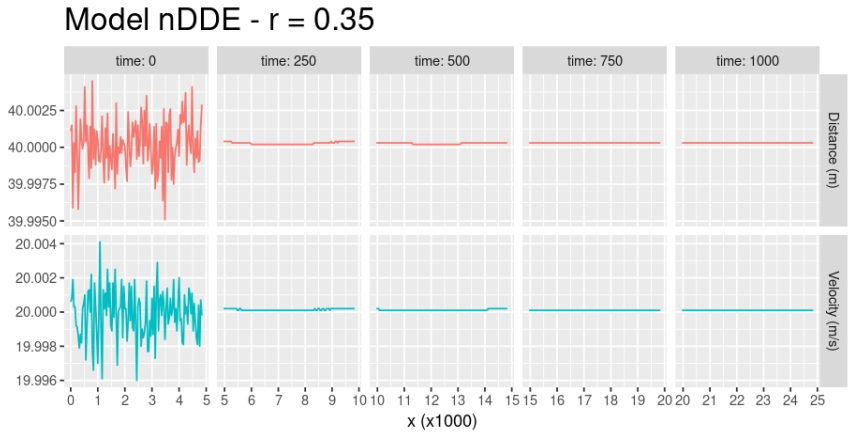


Figure 7.17: Evolution of distance and velocity of the vehicles with nDDE for $r = 0.35s$.

But when the delay goes over the limit, we can expect that oscillations start to appear. Indeed that is the case in the scenario of Figure 7.18, that shows the dynamics when the delay is $r = 0.4 > r_m$. The initial conditions are the same as in Figure 7.17. It can be observed that now oscillations in the distance and velocity of the vehicles appear, and are sustained in time. Even when the oscillations may seem haphazard in this figure, we can take a closer picture of the situation of a group of vehicles. Figure 7.19 shows a closeup of the Figure 7.18 in time $t = 1000$. Each point in a graph of space and velocity represents the corresponding value for a

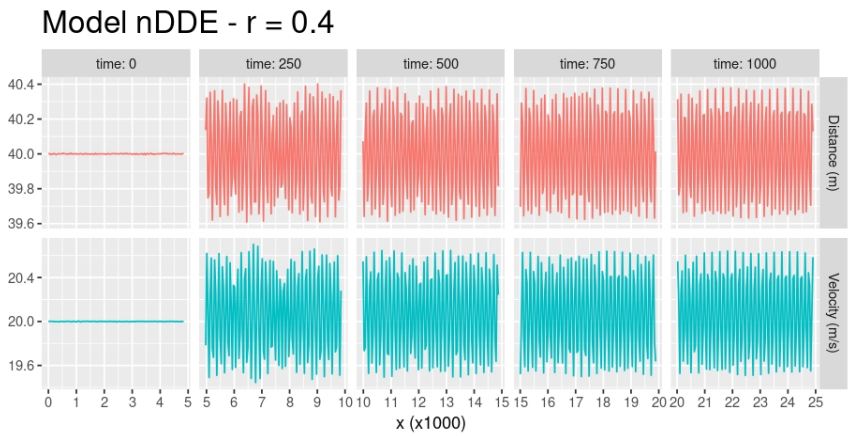


Figure 7.18: Evolution of distance and velocity of the vehicles with nDDE for $r = 0.4s$.

specific vehicle, and the dotted lines indicate the best sinusoidal fit to those values. One can see that the vehicle dynamics is really close to a basic pattern with wavenumber of spatial period $2\pi/\kappa_0 = 157$ m.

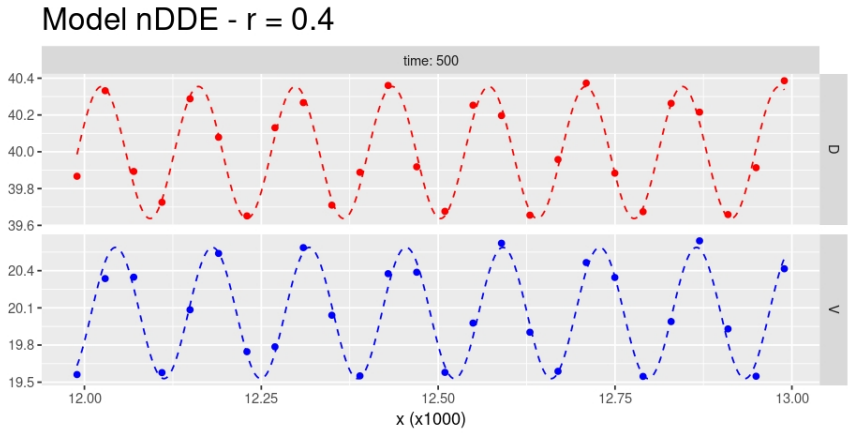


Figure 7.19: Detailed view of the evolution of the vehicles with nDDE for $r = 0.4s$.

More detailed results and explanations about the mesoscale in this model can be found in Section 5.3.4.

7.3.3 nDDE macroscopic analysis

The construction of the non-retarded acceleration function for the nDDE model has been detailed in Section 6.5.2. The equation in the form $a(t) = a(\sigma(t), \sigma'(t), \sigma''(t), \nu(t))$ is:

$$a(t) = \frac{\alpha\beta\nu_0 \left[\alpha - \beta e^{2F(\sigma,\nu,\sigma')} + e^{F(\sigma,\nu,\sigma')}\left(-\alpha + \beta + (\alpha+\beta)d(\sigma' + K_1\sigma'')\tau\right)\right]}{\alpha\beta e^{F(\sigma,\nu,\sigma')}\left((\alpha+\beta)d\sigma_0 r - 2\nu_0\right) - \alpha^2\nu_0 - \beta^2\nu_0 e^{2F(\sigma,\nu,\sigma')}}. \tag{7.27}$$

The coefficients of the linear PDE near the equilibrium $(\sigma_0, \nu_0) = (s_0, v_0)$ are, using (6.67):

$$\begin{aligned} C_1 &= -G(r)v_0, \\ C_2 &= G(r)v_0(r - K_1), \\ C_3 &= G(r)v_0 r K_1, \\ C_4 &= G(r)s_0, \end{aligned} \tag{7.28}$$

where:

$$G(r) = \frac{\alpha\beta d}{\alpha\beta d s_0 r - \alpha v_0 - \beta v_0}. \tag{7.29}$$

We can now apply the criteria of stability (6.87) to obtain:

$$r_M < \frac{s_0\left(3K_1v_0 + s_0\right)}{3v_0\left(2K_1v_0 + s_0\right)}. \tag{7.30}$$

If we use the values of the nDDE model in Table 7.5, we can determine the stability criteria:

$$r_M < 0.9629 \text{ s}, \tag{7.31}$$

We show in the following comparable results for three values of delay for the nDDE scenario that we introduced in Chapter 4 for the nDDE model, whose values are in Table 4.2, and for which we determined a limiting delay in the mesoscopic scale $r_m = 0.3518$ s. We see that the three scenarios have delays over the mesoscopic limit, and then present oscillation. The two first scenarios have $r_m < r < r_M$ and therefore present oscillation typical of mesoscopic state, but not density waves. But only in the last scenario, with $r > r_M$ after some time the macroscopic instability sets in and density waves and stop-and-go traffic manifests.

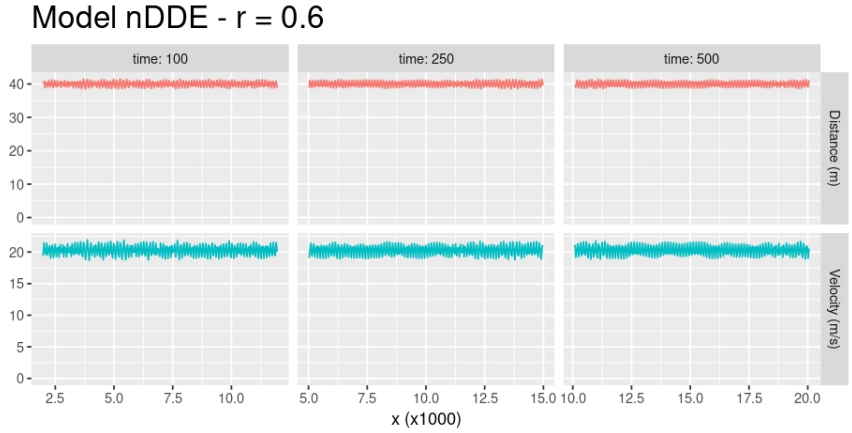


Figure 7.20: Evolution of distance and velocity of the vehicles with nDDE for $r = 0.6s$.

7.4 Final comments

In this chapter we have provided a unified view for the application of the methods introduced in this thesis by studying well known existing car-following models from a wholistic viewpoint

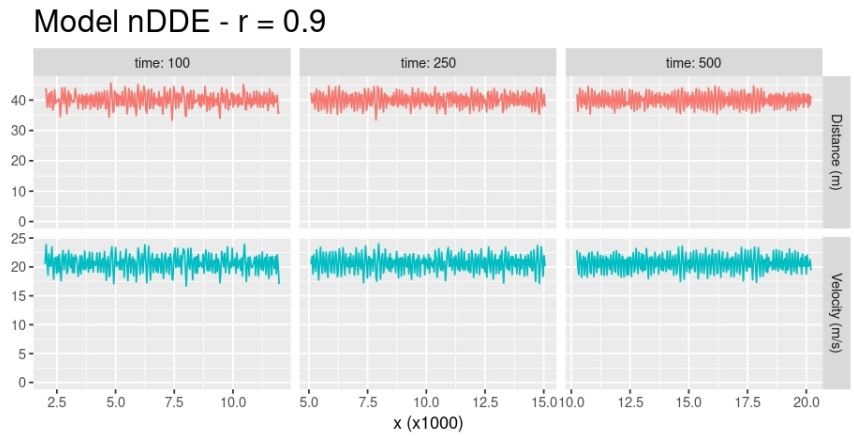


Figure 7.21: Evolution of distance and velocity of the vehicles with nDDE for $r = 0.9s$.

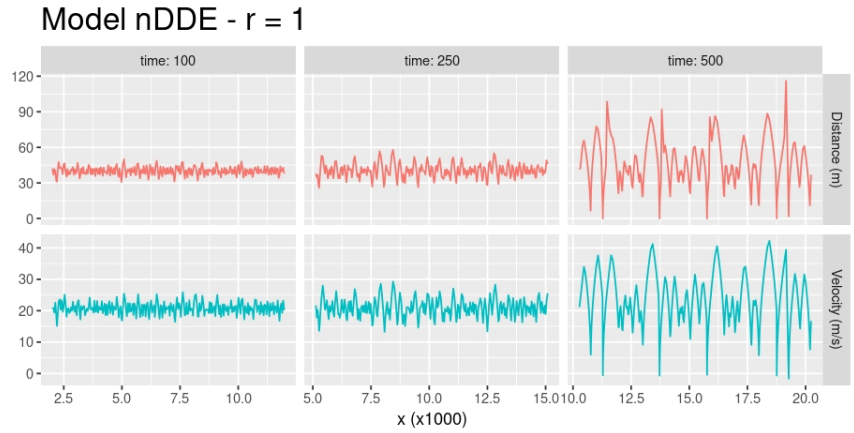


Figure 7.22: Evolution of distance and velocity of the vehicles with nDDE for $r = 1s$.

covering all the relevant spatial scales (*micro*, *meso* and *macro*). The main purpose has been to illustrate the general applicability of the methods starting from a single retarded acceleration equations, rather than to provide a detailed analysis of a specific model. It has been shown that this set of techniques can be usefully applied to any car following model that is based on standard kinetic variables (distance, velocity, relative velocity and relative acceleration).

It is also worth noting that the different models may behave in a different way at a specific scale. We have seen that some models are not amenable to be approximated by the CGLE in the mesoscopic scale (like the OVM and IDM, for different reasons), the OVM does not present macroscopic instability, and the IDM does not show metastability and passes directly from stable traffic to density waves traffic. This shows the importance of a careful evaluation of driving models at all scales to get a complete picture of their performance.

Finally , another purpose of this chapter has been to show the application of the mathematical techniques described in this thesis to general dynamic DDE/PDE problems, and, in this sense, we feel that these multiscale approach can be useful in other research fields.

Chapter 8

Conclusion

This thesis proposes new application methods of nonlinear analysis to study the instability introduced by reaction times and communication delays in road traffic processes. The research primarily aims to determine the limits of driver reaction times, vehicle dynamics, and algorithmic delays, and to quantify their impact on the emergence of traffic oscillations and density waves across various physical scales.

The research addresses this challenge by investigating traffic dynamics across multiple scales – micro, meso, and macro – recognizing the need for a holistic understanding that examines phenomena at each level. It establishes a formal definition of these scales, defining their spatial validity and the appropriate mathematical tools (Ordinary Differential Equations - ODEs and Partial Differential Equations - PDEs) for each. A key component is the integration of reaction times—the delay between a stimulus and a driver's response—into traffic models utilizing Retarded Functional Differential Equations (Delay Differential Equations).

Ultimately, this thesis, by combining established techniques with original methods, seeks to bridge the gap between individual vehicle behavior and the broader traffic flow, contributing to a more robust and accurate understanding of automated driving systems and their interaction with the road network.

Chapter 2 summarizes existing results in vehicular traffic analysis. Original contributions are detailed in Chapters 3, 4, 5, and 6, and are briefly reviewed in the following section. Chapter 7 provides a unified view of the application of the methods introduced in this thesis, studying well-known existing car-following models from a holistic perspective covering all relevant spatial scales (micro, meso, and macro).

8.1 Original contributions of the thesis

Chapter 3: this chapter presents a software simulation platform designed to validate the mathematical results of this thesis. The platform's accuracy is validated by comparing its results with previously published simulations and theoretical models, when available. Results indicate high accuracy and demonstrate the platform's capacity to simulate complex environments and interactions across micro and macro scales.

The platform's architecture enables the simulation of relatively large traffic networks – up to 500 vehicles – within approximately 60 minutes. Data analysis reveals the platform's resilience to variations in delay parameters, highlighting its ability to generate plausible density waves reflecting the inherent instability of traffic flow under uncertain conditions.

The validation results confirm the platform's accuracy and efficient computational performance. The platform successfully replicates key features of existing car-following models and effectively demonstrates the influence of variable delays on traffic behavior.

Chapter 4: this chapter introduces a comprehensive methodology for calculating precise series expansions for periodic solutions stemming from Hopf bifurcations in Delay Differential Equations (DDEs). This methodology extends the general methodology provided in [8], allowing implementation using modern symbolic and numerical computation systems, and enables calculations up to the desired order expansion, limited only by numerical precision and computing platform capacity.

This methodology offers significant advantages over existing numerical integration methods for calculating precise periodic solutions for Hopf bifurcations in DDEs: on one hand, numerical integration methods require additional checks to ensure a solution has reached a periodic phase, which can be time-consuming, particularly in systems where the frequency and amplitude converge slowly; on the other hand, this method provides instant calculation of frequency and amplitude of the steady-state solution using pre-computed coefficients.

The method is sufficiently general to be applied to a wide spectrum of complex problems, including examples provided in the chapter – a SIR epidemic model and a macroeconomic model. This methodology is particularly beneficial for scenarios requiring closed-form solutions for DDEs, especially when far from the bifurcation point.

Chapter 5: this chapter details a novel approach to analyze multi-vehicle scenarios in equilibrium near a bifurcation induced by an increase in the reaction delay of vehicles. The method searches for periodic solutions of the deviation from equilibrium using a perturbative method, translated into a system of retarded PDEs defined in a 4-dimensional $\mathbb{R}^4$ domain, but expressed as operations in $\mathbb{C}^4$ with complex conjugates. The difficulty of managing these functions is addressed through the use of Wirtinger calculus techniques, which allows the calculation of the neutral stability curve and the bifurcation point (in time and space).

In addition, the Complex Ginzburg-Landau Equation (CGLE) formalism is employed to gain further insight into the nature of the solution at the bifurcation (potentially metastable). Criteria for predicting periodic or modulated patterns in the metastable state are defined, and the impact of constant terms appearing in the solution, resulting from nonlinearities, is considered.

The strategy to solve this problem has not been previously proposed, and the usage of Wirtinger calculus and the CGLE frameworks represent original contributions of this work.

Chapter 6: this chapter generalizes existing methodologies for deriving macroscopic PDEs equations from microscopic equations, valid for large time and space scales. This approach can be applied to any car-following microscopic model based on standard variables (distance, velocity, relative velocity, and relative acceleration). Furthermore, a procedure to obtain a

non-retarded acceleration expression from the (normally) retarded original equation is defined. Based on this equation, a general expression for the final PDE system for the macroscopic process is provided.

Moreover, we have introduced an approximation, valid for large space scales (*long-wavelength*), which considerably simplifies the obtained PDE system to a 1-dimensional PDE on the macroscopic velocity (v) that yields a simple stability criterion for this scale. Until now, no such analysis exists in the literature that consistently addresses the conditions of density wave formation in different driving models.

8.2 Future directions of research

Finally, we would like to mention some research paths that could be taken to improve and extend the results of this thesis:

- **Application to scenarios with delay caused by V2X systems**: this was one of the main objectives at the beginning of the research, but has been postponed to prioritize the mathematical aspects of the research, specially in light of the necessity to invest more effort in the mesoscale analysis. It is the aim of the author to apply the methods developed to the analysis of car-following models that consider the intervention of V2X systems.
- **Introduction of stochastic terms and stochastic calculus**: the results of this thesis could be greatly improved if the stochastic nature of the reaction times is factored in. It is necessary to investigate the possibility of modelling the delay as a stochastic variable, and the application of stochastic calculus techniques to obtain more robust results.
- **Extension of Poincaré-Lindstedt method to delayed PDEs**: the methodology in Chapter 4 is applicable to ODEs and DDEs. It would be interesting to investigate the conditions under which this method could be applied to Hopf bifurcations in PDEs, and to explore extending the method to this type of bifurcation using a power expansion of the spatial frequency.
- **Conditions of existence of mesoscopic solutions in equilibrium traffic**: as demonstrated in the results of Chapter 7, even when the mesoscopic bifurcation point is determined, the existence of a metastable solution depends on the ability of the space of solutions to accommodate the "shift" in the equilibrium point resulting from the nonlinearity. A formal approach to this problem would be of value, not only for this field, but also generally for the delayed PDE bifurcation area.
- **Formalization of the CGLE calculation to delayed PDEs**: the CGLE formalism is normally defined in the context of Hopf bifurcations in non-retarded PDEs. The application of this method to delayed PDEs has revealed a singular structure of the approximate solutions (equation (5.35)) due to the peculiar power expansion in delayed equations (Poincaré-Lindstedt). The problem needs to be addressed more formally than the limited results included in this thesis.

References

[1] J. F. Padial A. C. Casal. "Some results in a nonlinear car-following model with reaction delay". In: *CEDYA+CMA 2017*.

[2] Norman Abramson. "The ALOHA system: Another alternative for computer communications". In: *Proceedings of the November 17-19, 1970, fall joint computer conference*. 1970, pp. 281–285.

[3] Igor S. Aranson and Lorenz Kramer. "The world of the complex Ginzburg-Landau equation". In: *Reviews of modern physics* 74.1 (2002), p. 99.

[4] M. Bando et al. "Dynamical model of traffic congestion and numerical simulation". In: *Physical review E : statistical physics, plasmas, fluids, and related interdisciplinary topics* 51.2 (1995), pp. 1035–1042.

[5] Cristiane M. Batistela et al. "SIRSi compartmental model for COVID-19 pandemic with immunity loss". In: *Chaos, Solitons and Fractals* 142 (2021), p. 110388.

[6] Fred Brauer, Carlos Castillo-Chavez, and Carlos Castillo-Chavez. *Mathematical models in population biology and epidemiology*. Vol. 2. 40. Springer, 2012.

[7] Adam Bridgewater, Benoit Huard, and Maia Angelova. "Amplitude and frequency variation in nonlinear glucose dynamics with multiple delays via periodic perturbation". In: *Journal of Nonlinear Science* 30.3 (2020), pp. 737–766.

[8] A. Casal and M. Freedman. "A Poincaré-Lindstedt approach to bifurcation problems for differential-delay equations". In: *IEEE Transactions on Automatic Control* 25.5 (1980), pp. 967–973.

[9] Robert E. Chandler, Robert Herman, and Elliott W. Montroll. "Traffic dynamics: studies in car following". In: *Operations research* 6.2 (1958), pp. 165–184.

[10] Mark C. Cross and Pierre C. Hohenberg. "Pattern formation outside of equilibrium". In: *Reviews of modern physics* 65.3 (1993), p. 851.

[11] Percy Deift, C. David Levermore, and C. Eugene Wayne. *Dynamical Systems and Probabilistic Methods in Partial Differential Equations: 1994 Summer Seminar on Dynamical Systems and Probabilistic Methods for Nonlinear Waves, June 20-July 1, 1994, MSRI, Berkeley, CA*. Vol. 31. American Mathematical Soc., 1996.

[12] Odo Diekmann, Johan Andre Peter Heesterbeek, and Johan AJ Metz. "On the definition and the computation of the basic reproduction ratio R0 in models for infectious diseases in heterogeneous populations". In: *Journal of mathematical biology* 28 (1990), pp. 365–382.

[13] Pauline Van den Driessche and James Watmough. "Reproduction numbers and subthreshold endemic equilibria for compartmental models of disease transmission". In: *Mathematical biosciences* 180.1-2 (2002), pp. 29–48.
[14] Leslie C. Edie. "Car-Following and Steady-State Theory for Noncongested Traffic". In: *Operations research* 9.1 (1961), pp. 66–76.
[15] Ericsson. *Ericsson Mobility Report*. 2021.
[16] Thomas Erneux. *Applied delay differential equations*. Vol. 3. Springer Science and Business Media, 2009.
[17] Noble B. Ferguson and Bruce A. Finlayson. "Error bounds for approximate solutions to nonlinear ordinary differential equations". In: *AIChE Journal* 18.5 (1972), pp. 1053–1059.
[18] Robert FH Fischer. *Precoding and signal shaping for digital transmission*. John Wiley and Sons, 2005.
[19] José Enríquez Gabeiras and Juan Francisco Padial Molina. "Evaluation of a general car-following model for micro/macro traffic modelling". In: *Proceedings XVII CMA/XXVII CEDYA*. Universidad de zaragoza, 2022, p. 39.
[20] José Enríquez Gabeiras and Juan Francisco Padial Molina. "Calculation of explicit expressions for the Hopf bifurcation limit cycles in delay-differential equations". In: *Opuscula Mathematica* 45.3 (2025), pp. 307–338.
[21] Mario H. Castaneda Garcia et al. "A tutorial on 5G NR V2X communications". In: *IEEE Communications Surveys and Tutorials* 23.3 (2021), pp. 1972–2026.
[22] Vladimir García-Morales and Katharina Krischer. "The complex Ginzburg–Landau equation: an introduction". In: *Contemporary Physics* 53.2 (2012), 79–95.
[23] Denos C. Gazis, Robert Herman, and Renfrey B. Potts. "Car-following theory of steady-state traffic flow". In: *Operations research* 7.4 (1959), pp. 499–505.
[24] Denos C. Gazis, Robert Herman, and Richard W. Rothery. "Nonlinear follow-the-leader models of traffic flow". In: *Operations research* 9.4 (1961), pp. 545–567.
[25] David E. Gilsinn. "On algorithms for estimating computable error bounds for approximate periodic solutions of an autonomous delay differential equation". In: *Communications in Nonlinear Science and Numerical Simulation* 14.4 (2009), pp. 1526–1550.
[26] Zhongjin Guo and Xiaoyan Ma. "Residue harmonic balance solution procedure to nonlinear delay differential systems". In: *Applied Mathematics and Computation* 237 (2014), pp. 20–30.
[27] K. A. Hafeez et al. "Performance analysis of broadcast messages in VANETs safety application". In: *IEEE GLOBECOM'2010* (2010).
[28] Khalid Abdel Hafeez et al. "Performance analysis and enhancement of the DSRC for VANET's safety applications". In: *IEEE Transactions on Vehicular Technology* 62.7 (2013), pp. 3069–3083.
[29] Jack K. Hale. *Theory of functional differential equations*. New York: New York Springer-Verlag, 1977.
[30] Jack K. Hale and Sjoerd M. Verduyn Lunel. *Introduction to functional differential equations*. Vol. 99. Springer Science and Business Media, 2013.
[31] Dirk Helbing. "Traffic and related self-driven many-particle systems". In: *Reviews of modern physics* 73.4 (2001), pp. 1067–1141. DOI: 10.1103/RevModPhys.73.1067.

[32] Herbert W. Hethcote. “The mathematics of infectious diseases”. In: *SIAM Review* 42.4 (2000), pp. 599–653.

[33] Pierre C. Hohenberg and Alexei P. Krekhov. “An introduction to the Ginzburg–Landau theory of phase transitions and nonequilibrium patterns”. In: *Physics Reports* 572 (2015), 1–42.

[34] R. Hunger. “An introduction to complex differentials and complex differentiability (2008)”. In: *URL https://mediatum.ub.tum.de/doc/631019/631019.pdf* ().

[35] Boris S. Kerner and Peter Konhäuser. “Cluster effect in initially homogeneous traffic flow”. In: *Physical review E* 48.4 (1993), R2335.

[36] Arne Kesting, Martin Treiber, and Dirk Helbing. “Enhanced intelligent driver model to access the impact of driving strategies on traffic capacity”. In: *Philosophical Transactions of the Royal Society A: Mathematical, Physical and Engineering Sciences* 368.1928 (2010), 4585–4605.

[37] Leonard Kleinrock and Fouad Tobagi. “Packet switching in radio channels: Part I-carrier sense multiple-access modes and their throughput-delay characteristics”. In: *IEEE Transactions on Communications* 23.12 (1975), pp. 1400–1416.

[38] Kelvin Koor et al. “A short tutorial on Wirtinger Calculus with applications in quantum information”. In: *arXiv preprint arXiv:2312.04858* (2023).

[39] Y. Kuramoto. *Chemical oscillations, waves, and turbulence*. Vol. 8. Springer-Verlag, 1984, p. 156.

[40] Peter D. Lax. “The formation and decay of shock waves”. In: *The American Mathematical Monthly* 79.3 (1972), pp. 227–241.

[41] H. K. Lee, H-W Lee, and D. Kim. “Macroscopic traffic models from microscopic car-following models”. In: *Physical Review E* 64.5 (2001), p. 056126.

[42] Michael James Lighthill and Gerald Beresford Whitham. “On kinematic waves II. A theory of traffic flow on long crowded roads”. In: *Proceedings of the Royal Society of London.Series A.Mathematical and Physical Sciences* 229.1178 (1955), pp. 317–345.

[43] Zimeng Lv et al. “Stability analysis of time-delayed SAIR model for duration of vaccine in the context of temporary immunity for COVID-19 situation”. In: *Electronic Research Archive* 31.2 (2023), pp. 1004–1030.

[44] Sven Maerivoet and Bart De Moor. “Cellular automata models of road traffic”. In: *Physics reports* 419.1 (2005), pp. 1–64.

[45] Maplesoft. *Numeric Delay Differential Equation Examples*. 2023.

[46] Jerrold E. Marsden and Marjorie McCracken. *The Hopf bifurcation and its applications*. Vol. 19. Springer Science and Business Media, 1976.

[47] Alexander Mielke. “The Ginzburg-Landau equation in its role as a modulation equation”. In: vol. 2. Handbook of dynamical systems. Elsevier, 1999, 759–834.

[48] Takashi Nagatani. “The physics of traffic jams”. In: *Reports on progress in physics* 65.9 (2002), p. 1331.

[49] Gaurang Naik, Biplav Choudhury, and Jung-Min Park. “IEEE 802.11 bd and 5G NR V2X: Evolution of radio access technologies for V2X communications”. In: *IEEE access* 7 (2019), pp. 70169–70184.

[50] Jorge Navarro-Ortiz et al. “A survey on 5G usage scenarios and traffic models”. In: *IEEE Communications Surveys and Tutorials* 22.2 (2020), pp. 905–929.

[51] Ali H. Nayfeh. *Perturbation methods*. John Wiley and Sons, 2004.

[52] Ali H. Nayfeh and Dean T. Mook. *Nonlinear oscillations*. John Wiley and Sons, 2008.
[53] Gordon Frank Newell. "Nonlinear effects in the dynamics of car following". In: *Operations research* 9.2 (1961), pp. 209–229.
[54] *ns-3 Conceptual Overview - https://www.nsnam.org/docs/tutorial/html/conceptual-overview.html*.
[55] *ns-3 Network Simulator - https://www.nsnam.org/*.
[56] J. F. Padial and A. Casal. "Bifurcation in car-following models with time delays and driver and mechanic sensitivities". In: *Revista de la Real Academia de Ciencias Exactas, Físicas y Naturales.Serie A, Matemáticas* 116.4 (2022).
[57] Harold J. Payne. "Model of freeway traffic and control". In: *Mathematical Model of Public System* (1971), pp. 51–61.
[58] Bruce Pell, Matthew D. Johnston, and Patrick Nelson. "A data-validated temporary immunity model of COVID-19 spread in Michigan". In: *Mathematical Biosciences and Engineering* 19.10 (2022), pp. 10122–10142.
[59] Ilya Prigogine and Robert Herman. "No title". In: *Kinetic theory of vehicular traffic* (1971).
[60] Richard Rand. "Differential-delay Equations". In: *Complex systems: fractionality, time-delay and synchronization*. Ed. by Albert CJ Luo and Jian-Qiao Sun. Springer Science & Business Media, 2011.
[61] Richard W. Rothery. "Car following models". In: *Trac Flow Theory* (1992).
[62] Wim Van Saarloos. "The complex Ginzburg-Landau equation for beginners". In: *SANTA FE INSTITUTE STUDIES IN THE SCIENCES OF COMPLEXITY-PROCEEDINGS VOLUME-*. Vol. 21. ADDISON-WESLEY PUBLISHING CO, 1995, p. 19.
[63] Stefania Santini et al. "A consensus-based approach for platooning with intervehicular communications and its validation in realistic scenarios". In: *IEEE Transactions on Vehicular Technology* 66.3 (2016), pp. 1985–1999.
[64] Mohammad Qaleh Shakhany and Khodakaram Salimifard. "Predicting the dynamical behavior of COVID-19 epidemic and the effect of control strategies". In: *Chaos, Solitons and Fractals* 146 (2021), p. 110823.
[65] B. Shayak et al. "Impact of reproduction number on the multiwave spreading dynamics of COVID-19 with temporary immunity: A mathematical model". In: *International Journal of Infectious Diseases* 104 (2021), pp. 649–654.
[66] Hal L. Smith. *An introduction to delay differential equations with applications to the life sciences*. New York: New York Springer, 2011.
[67] Fouad Tobagi and Leonard Kleinrock. "Packet switching in radio channels: Part II-The hidden terminal problem in carrier sense multiple-access and the busy-tone solution". In: *IEEE Transactions on Communications* 23.12 (1975), pp. 1417–1433.
[68] Martin Treiber, Ansgar Hennecke, and Dirk Helbing. "Congested traffic states in empirical observations and microscopic simulations". In: *Physical review E* 62.2 (2000), p. 1805.
[69] Martin Treiber, Ansgar Hennecke, and Dirk Helbing. "Microscopic simulation of congested traffic". In: Traffic and granular flow'99. Springer, 2000, pp. 365–376.
[70] Martin Treiber and Arne Kesting. *Traffic flow dynamics*. Vol. 1. Springer, 2013.
[71] Ferdinand Verhulst. *Nonlinear Differential Equations and Dynamical Systems*. Springer, 1990, pp. 130–144.

[72] Stephen Wolfram. *A new kind of science*. Vol. 5. Wolfram media Champaign, IL, 2002.
[73] Min Xiao and Jinde Cao. "Approximate expressions of the bifurcating periodic solutions in a neuron model with delay-dependent parameters by perturbation approach". In: *Cognitive neurodynamics* 4 (2010), pp. 241–250.
[74] Min Xiao et al. "Stability switches and Hopf bifurcations of an isolated population model with delay-dependent parameters". In: *Applied Mathematics and Computation* 264 (2015), pp. 99–115.
[75] Xuebing Zhang and Honglan Zhu. "Hopf bifurcation and chaos of a delayed finance system". In: *Complexity* 2019 (2019).

Appendix A

Simulator diagrams

The following diagrams contain the object-oriented programming structures (C++) that support the simulator programs used in the validation of this thesis results.

Figure A.1 provides the data structures and the functions implemented in the main simulator program, the active nodes data structure and the associated mobility model to each vehicle.

As explained in section 3, the mobility model is an extension of the standard mobility models provided by the *ns-3* platform, anf Figure A.2 shows the inheritance relationship with the standard mobility model from *ns-3*.

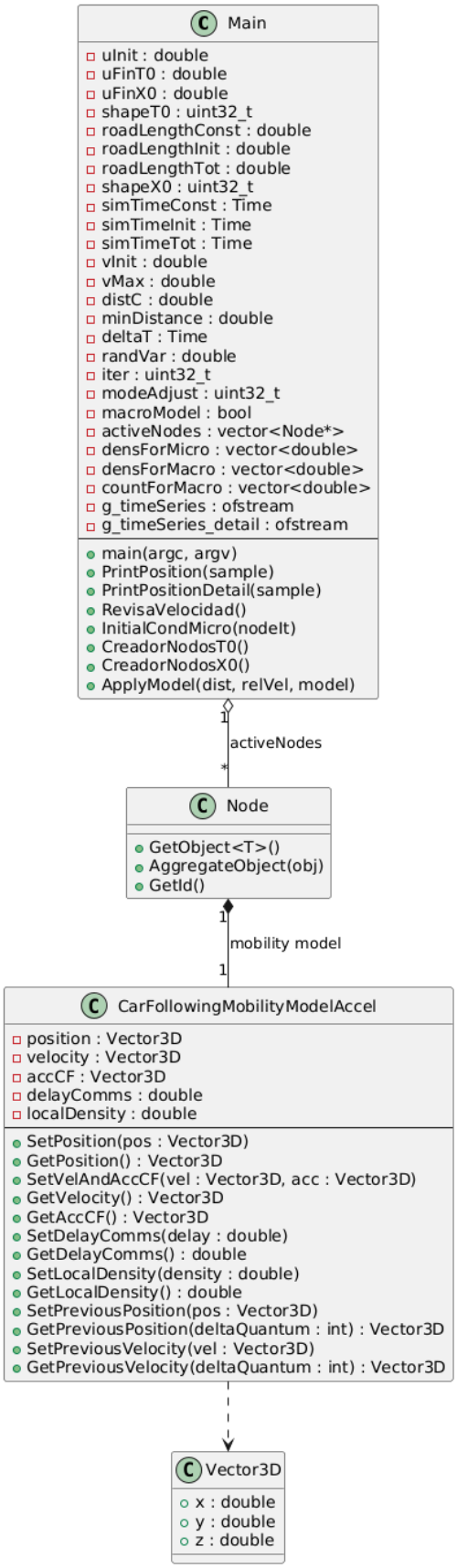


Figure A.1: C++ structure of the main simulator program

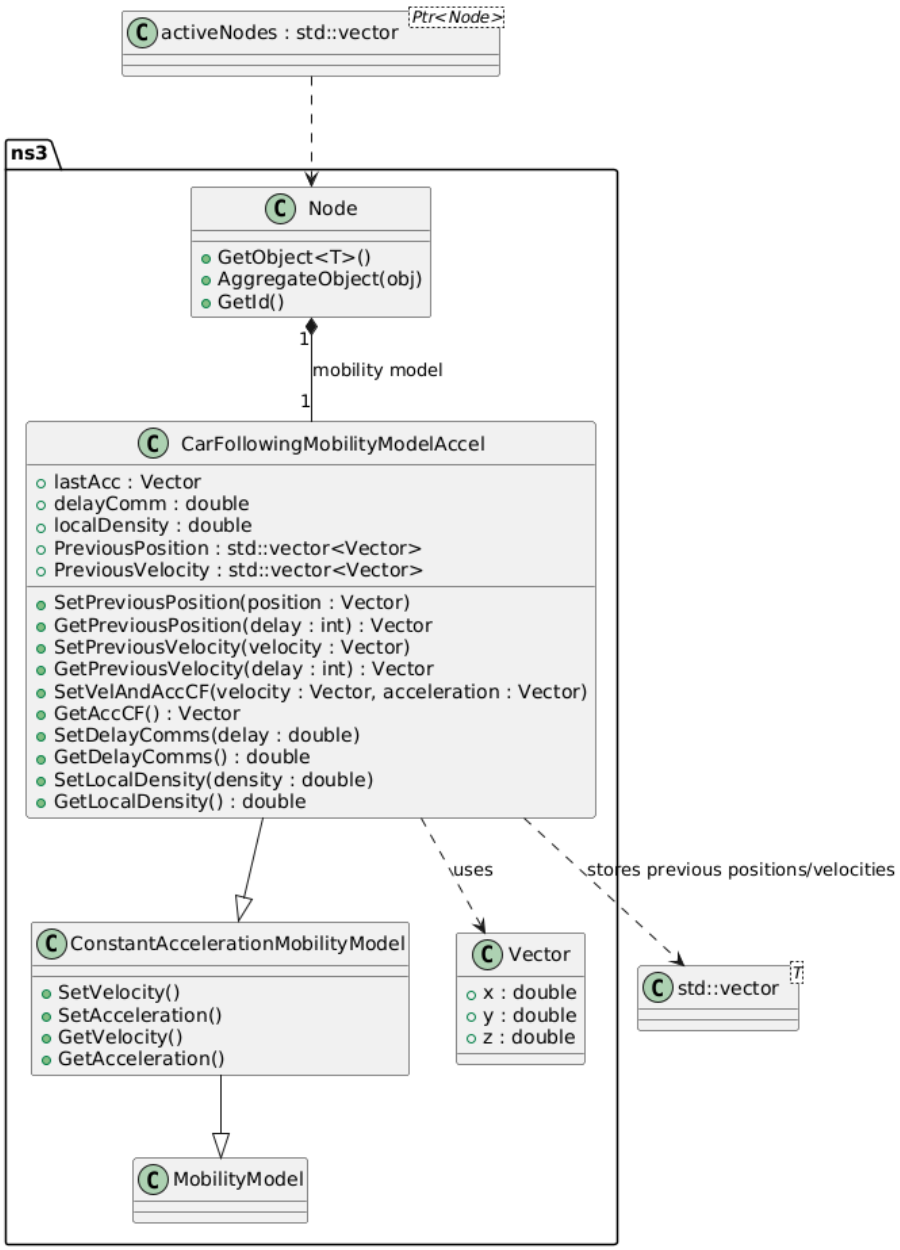


Figure A.2: C++ structure of the car-following model implementation.

Appendix B

Maple programs pseudocode

This annex contains the high level view of the programs developed in the Maple 2024 platform (https://www.maplesoft.com/) to perform the calculations for the different methods and algorithms introduced in this thesis. The diagrams represent the different calculation sections with pseudocode and indication of the relevant Maple packages and functions used, and an example of the output obtained.

B.1 Calculation of Hopf limit cycles in DDEs

The next two figures (Figure B.1 and Figure B.2) contain a pseudocode for the program implemented in the Maple 2024 platform for the methodology introduced in Chapter 4. It has to be noted that only the most general features of the program are described, and that the original program extends to more than 600 lines of code.

The pseudocode and sample results correspond to the nDDE microscopic car-following model scenario in Section 4.4.1, but has been programmed so that it can be easily adapted to the other problems with slight modifications, mostly the initial DDE equation and the dimensionality of the problem in the data structures.

B.2 Calculation of mesoscopic bifurcation and CGLE coefficients

In this case Figure B.3 and Figure B.4 contain the pseudocode for the program for the calculations in Chapter 5. Again, only the high level behaviour of the program is described. The original program extends to more than 600 lines of code.

The pseudocode and sample results correspond to the nDDE mesoscopic car-following model scenario in Section 5.3.4.

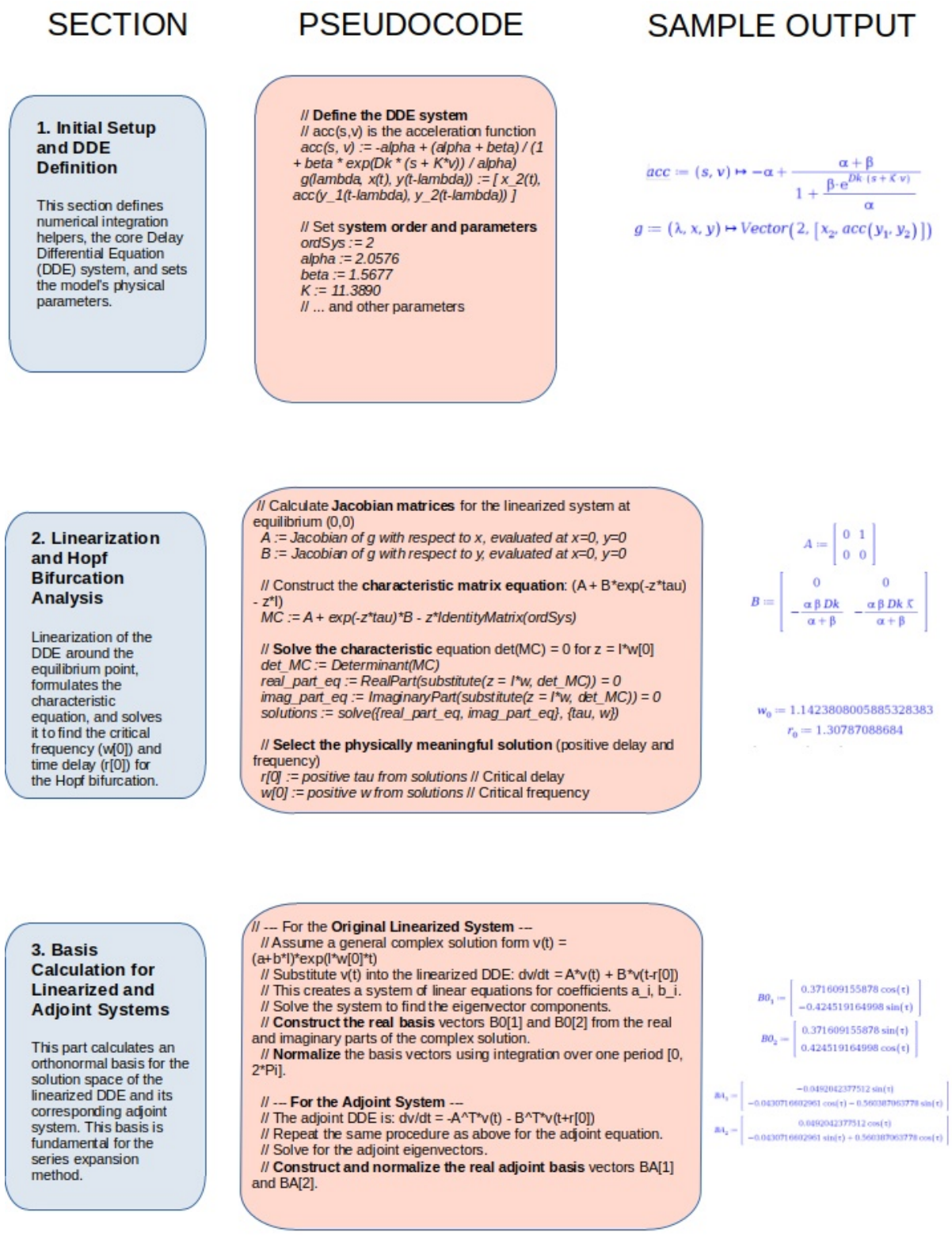


Figure B.1: Pseudocode of the Maple 2024 program for the calculation of limit cycles in Hopf bifurcation in DDEs (I).

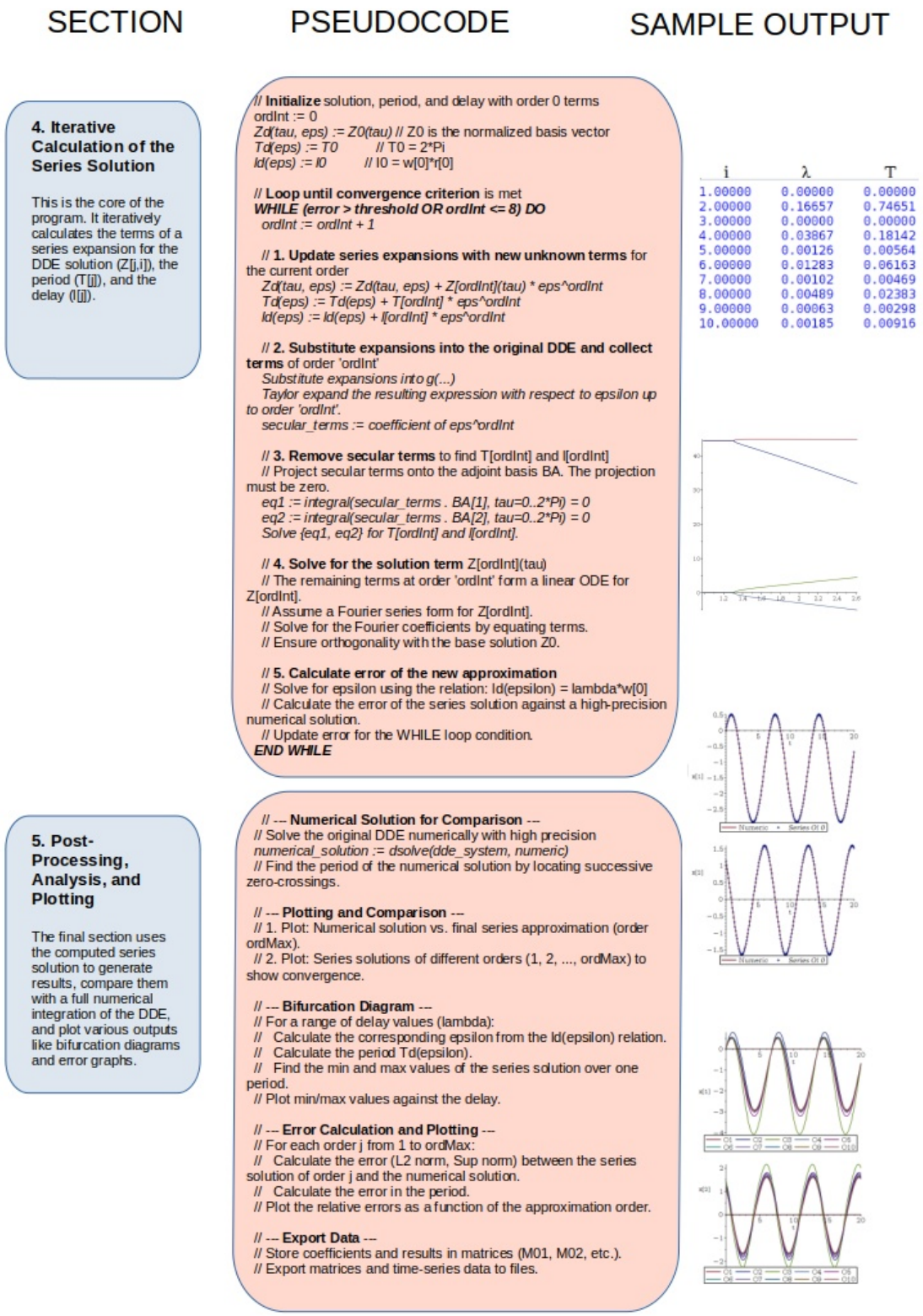


Figure B.2: Pseudocode of the Maple 2024 program for the calculation of limit cycles in Hopf bifurcation in DDEs (II).

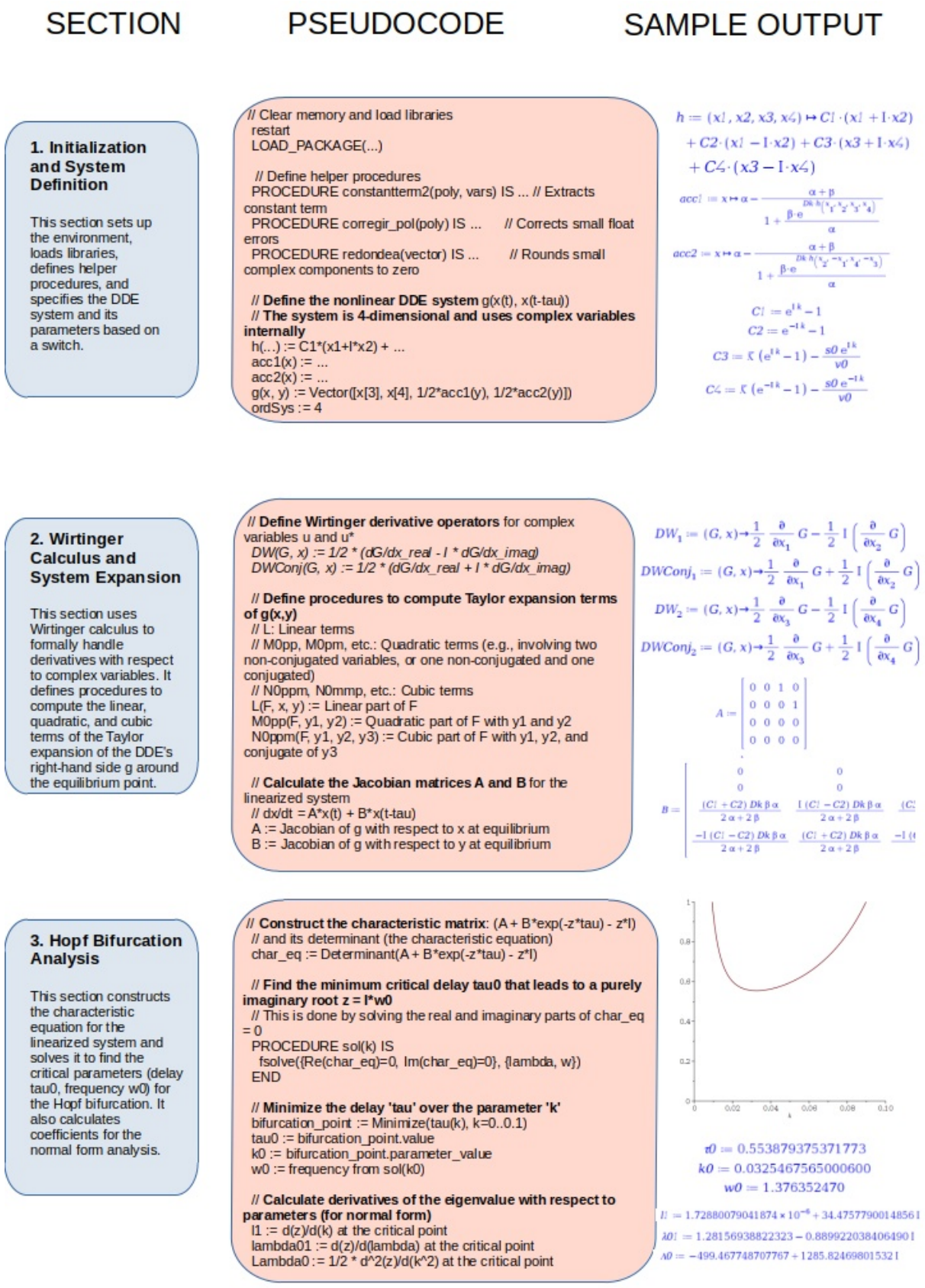


Figure B.3: Pseudocode of the Maple 2024 program for the calculation of the nDDE mesoscopic approximation (I).

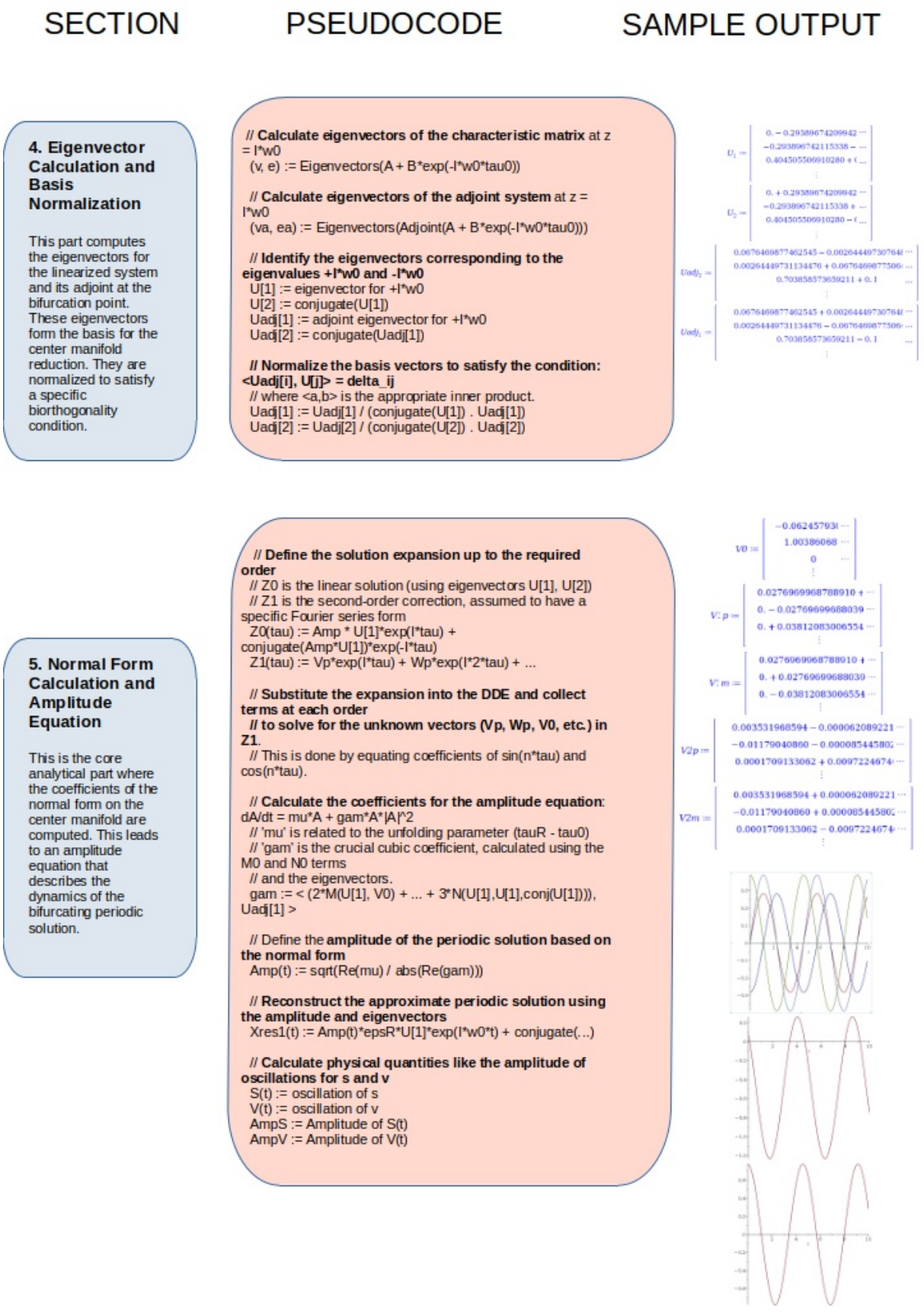


Figure B.4: Pseudocode of the Maple 2024 program for the calculation of the nDDE mesoscopic approximation (II).